# UC Riverside
## UC Riverside Electronic Theses and Dissertations

**Title**
Linking Anthropogenic Aerosols and Large-Scale Circulation Systems in Climate Models

**Permalink**
https://escholarship.org/uc/item/14z6p2qp

**Author**
Hassan Mozumder, Mohammad Taufiq

**Publication Date**
2021

Peer reviewed|Thesis/dissertation

UNIVERSITY OF CALIFORNIA
RIVERSIDE

Linking Anthropogenic Aerosols and Large-Scale Circulation Systems in Climate
Models

A Dissertation submitted in partial satisfaction
of the requirements for the degree of

Doctor of Philosophy

in

**Earth and Planetary Sciences**

by

Mohammad Taufiq Hassan Mozumder

December 2021

Dissertation Committee:

    Dr. Robert J. Allen, Chairperson
    Dr. Wei Liu
    Dr. Andy Ridgwell

The Dissertation of Mohammad Taufiq Hassan Mozumder is approved:

_____

_____

_____

Committee Chairperson

University of California, Riverside

## Acknowledgments

First and foremost, I would like to thank my advisor Dr. Robert J. Allen for his constant support and guidance. I am fortunate and grateful to be a part of his group here at UC Riverside. This work would not be possible without his continuous encouragement and generous patience. Thanks to his invaluable time and mentorship, I have grown as a scientist over the years.

I would also like to thank my collaborators, Dr. Cynthia Randles and Dr. Wei Liu for their support and helpful inputs in multiple projects. Dr. Liu was always available for a chat, which helped me immensely both personally and academically. Additionally, I would like to thank my other committee memeber, Dr. Andy Ridgwell, for his valuable feedbacks and insights. I want to acknowledge support from the Fellowships and Internships in Extremely Large Data Sets (FIELDS) Program, a NASA MUREP Institutional Research Opportunity (MIRO) Program, grant number NNX15AP99A.

Special Thanks to my parents Mohammad Shahjahan Mozumder and Hasina Begum for their support and patience throughout my career. I am especially thankful to my wife Samiha Binte Shahid for her continuous motivation and inspiration. Thank you for brightening my days with your beautiful smile.

Chapter 2 of this dissertation, in full, is a reprint of the material from the following publication: Allen, R. J., Hassan, T., Randles, C. A., & Su, H. (2019). Enhanced land–sea warming contrast elevates aerosol pollution in a warmer world. Nature Climate Change, 9(4), 300-305.

Chapter 3 of this dissertation, in full, is a reprint of the material from the following publication: Hassan, T., Allen, R. J., Liu, W., & Randles, C. A. (2021). Anthropogenic aerosol forcing of the Atlantic meridional overturning circulation and the associated mechanisms in CMIP6 models. Atmospheric Chemistry and Physics, 21(8), 5821-5846.

Chapter 4 of this dissertation, in part, is a reprint of the material from the submitted publication: Hassan, T., Allen, R. J., Liu, W., Shim, S., Noije, T. V., Sager, P. L., Oshima, N., Deushi, M., Randles, C. A., & O'Connor, F. M. (Submitted). The impact of air quality control efforts on the Atlantic Meridional Overturning Circulation.

To my wife−Samiha.

Thank you for your patience.

# ABSTRACT OF THE DISSERTATION

Linking Anthropogenic Aerosols and Large-Scale Circulation Systems in Climate Models

by

Mohammad Taufiq Hassan Mozumder

Doctor of Philosophy, Graduate Program in Earth and Planetary Sciences
University of California, Riverside, December 2021
Dr. Robert J. Allen, Chairperson

This dissertation is composed of three parts. In the first part, I investigate the anthropogenic aerosol burden response to future warming perturbations using climate models. Many climate models simulate an increase in anthropogenic aerosol species in response to warming. This is primarily due to a decrease in wet removal associated with reduced precipitation. The enhanced aerosol burden and hydrological changes are related to a robust climate change phenomenon—the land–sea warming contrast. Enhanced land warming is associated with continental reductions in lower-tropospheric humidity that drive decreases in low clouds, which leads to reduced large-scale precipitation and aerosol wet removal. Thus, unless anthropogenic emission reductions occur, a warmer world will be associated with enhanced aerosol pollution.

In the Second part, I explore the mechanisms that drive the Atlantic meridional overturning circulation (AMOC) based on the Coupled Model Intercomparison Project phase 6 (CMIP6) models. The CMIP6 all-forcing simulations show a robust AMOC strength-

ening during $\sim$1950$-$1990 and weakening afterwards ($\sim$1990$-$2020). These multi-decadal AMOC variations are related to changes in North Atlantic atmospheric circulation, which drive changes in the subpolar North Atlantic surface density flux. CMIP6 anthropogenic aerosol forced simulations yield a similar AMOC including associated atmospheric circulation responses. I conclude that the CMIP6 models yield robust, externally forced AMOC changes, the bulk of which are due to anthropogenic aerosols.

Finally, I quantify the impact of near-term climate forcer (NTCF) mitigation-including aerosols and chemically reactive gases such as tropospheric ozone and methane-on the AMOC using four chemistry-climate models. Non-methane NTCF mitigation, including aerosols, ozone and precursor gases alone, will amplify greenhouse gas-induced weakening of the AMOC. However, all-NTCF mitigation, which also includes methane reductions, more than offset this weakening. Thus, efforts to improve air quality must also target methane to avoid additional climate change, including weakening of world's major ocean circulation system.

# Contents

# List of Figures

# List of Tables

# Chapter 1

# Introduction

Lower tropospheric aerosols can affect air quality and human health. A recent study attributed 3.3 million premature deaths each year to aggravated aerosol pollution, led by fine particulate matter (PM2.5) [1], particularly in heavily polluted areas like India and China. Regardless of the emergent importance of atmospheric aerosol mitigation, there exists a large inconsistency among studies estimating aerosol response to climate change. This inconsistency is driven by our limited understanding of the physical processes and their complex interaction with aerosol particles. The optical properties of aerosols, which can influence the energy balance of the earth system by scattering or absorbing radiation, adds to the complexity. According to the report on the 5th Intergovernmental Panel on Climate Change (IPCC), the total effective aerosol radiative forcing is -0.9 Wm-2 (-1.9 to -0.1) [2], indicating aerosols have a net cooling effect. Both climatic and societal importance of air pollution has significantly enhanced by anthropogenic activities, as humans are responsible for a large part of the tropospheric aerosol burden increase since the pre-industrial era [3].

Continued greenhouse-gas induced global warming is expected to be associated with changes in physical, chemical and biological factors that control the lifetime, transport, chemistry, atmospheric burden and surface concentration of aerosols. Understanding the response of aerosol burden to robust physical perturbations is important to the context of future climate change. Chapter 2 presents a study that investigates the land-sea warming contrast, where continents warm more rapidly than ocean as a robust feature found in both observations and climate model simulations. Heat from the ocean surface is more readily transferred away from the surface due to turbulence and mixing. It is also found that if heat is being transferred by advection, the land-ocean warming contrast can be solely explained by the change in lapse rate over land and ocean [4, 5]. As a result, a significant land-ocean warming contrast is seen over most latitudes, while strongest over mid−high latitudes, which intensifies with continued global warming [6, 7].

The land specific humidity varies in concert with the specific humidity and saturation specific humidity over the sea. Thus, near-surface atmospheric moisture content is primarily controlled by the saturation specific humidity of the oceans. When a warming perturbation is applied according to future projections, the continents warm more rapidly than oceans due to land-ocean warming contrast. The rapidly warming continents can hold far more moisture compared to the increased moisture that is transported from the slowly warming ocean. The relative humidity (RH) over lands falls. Recent observational and climate model simulation studies have found a significant decrease in near-surface relative humidity over continents [?, 7].

Chapter 2 shows that the hydrological perturbations related to land-sea warming

contrasts will enhance aerosol burden, resulting in reduced air quality and an enhanced aerosol radiative effect. This is due to the fact a reduction in relative humidity over land has potentially important hydrological cycle implications. This impact is evident particularly in terms of large-scale precipitation. Most models parameterize large-scale precipitation based, in part, on a relative humidity threshold (e.g. air needs to be at saturated before precipitation can occur). To the extent that future warming drives decreases in RH over land, there is also a corresponding decrease in large-scale precipitation and wet deposition.

The Atlantic Meridional Overturning Circulation (AMOC) is one of the major ocean circulation system that can significantly impact our climate by globally transporting large amounts of heat, carbon and freshwater[8, 9]. Observations, proxies and climate model simulations of AMOC variability indicate a gradual weakening during the recent decades[10, 11, 12, 13]. Most climate models agree that the long-term gradual weakening in AMOC is a response to positive radiative forcing associated to gradually increasing greenhouse gases[14, 15, 16, 17, 18, 19]. By the end of the 21st century, for example, models estimate a 24-39% decline in the AMOC, with larger weakening under larger increases in future GHG emissions [20]. Although there is considerable uncertainty on the role of anthropogenic aerosols on North Atlantic climate variability, aerosols may impact the AMOC−including strengthening (weakening) the AMOC and increasing (decreasing) the northward cross-equatorial ocean heat transport[21, 22, 23, 24, 25, 26, 17]−since it can offset (reinforce) the positive radiative forcing exerted by the greenhouse gases.

Chapter 3 investigates the impact of atmospheric aerosol reduction using a multi-model approach. The Coupled Model Intercomparison Project phase 6 (CMIP6) models are

used to identify the AMOC responses during different periods as a response to the changes in North Atlantic atmospheric circulation. This study shows that a large suite of state-of-the-art climate models yield a robust strengthening (weakening) of the AMOC from ∼1950-1990 (∼1990-2020), and that this response is largely driven by anthropogenic aerosols. The multi-decadal AMOC variability is initiated by North Atlantic aerosol perturbations to net surface shortwave radiation and surface temperature (and hence sea surface density), which in turn affect sea level pressure gradient and surface wind−and via latent and sensible heat fluxes−sea surface density flux through its thermal component. AMOC-related feedbacks act to reinforce this aerosol-forced AMOC response, largely due to changes in sea surface salinity (and hence sea surface density), with temperature (and cloud) related feedbacks acting to mute the initial response.

Since there is an increasing demand of improved air quality−incorporating reduction in anthropogenic aerosols−and a substantial evidence that AMOC is weakening, understanding future changes in AMOC is of primary interest, in the context of climate mitigation policies. A strict policy is expected to be imposed to mitigate future ambient air pollution. However, an aggressive aerosol removal strategy could lead to additional surface warming, significant mean increase in precipitation and a significant weakening in AMOC[27, 13, 28]. Since methane can increase the radiative forcing by 20%–25% through shortwave absorption, methane emission reduction is highlighted−in addition to aerosol reduction−in recent studies for a 'win-win' policy to mitigate climate change and air pollution[29, 30, 31, 27, 28].

Near-term climate forcers (NTCFs)−chemical species whose impact on climate occurs primarily within the first decade after their emission−have received significant at-

tention, as they consider components that can affect both the air quality as well as the radiative balance of the Earth[32, 33]. NTCFs, also known as short-lived climate forcers (SLCFs), include aerosols, and chemically reactive gases including ozone, sulfur dioxide and methane ($CH_4$). Thus, future reduction in NTCFs−to improve air quality−can exhibit rapid climate response due to their short atmospheric lifetimes compared to GHGs. Policies that consider future reductions in emissions of NTCFs is therefore important to meet the United Nation's Sustainable Development Goals, as well as to mitigate the projected AMOC weakening, which is close to a point of critical transition[34, 35, 36, 37].

In chapter 4, I analyze simulations from the the Aerosol and Chemistry Model Intercomparison Project (AerChemMIP), part of the Coupled Model Intercomparison Project (CMIP6), with models that include an interactive representation of tropospheric aerosols and atmospheric chemistry, allowing for the quantification of chemistry-climate interactions[38, 39]. I found that relative to the Shared Socio-economic Pathway 3-7.0 (SSP3-7.0; with strong increases in GHGs and NTCFs), NMNTCF (aerosols and ozone precursors) mitigation in the SSP3-7.0-lowNTCF scenario leads to significant AMOC weakening in all AerChemMIP models. In contrast, NTCF (aerosols, ozone and precursor gases including methane) mitigation in the SSP3-7.0-lowNTCFCH4 scenario nullifies most of the projected weakening in NMNTCF due to the inclusion of methane mitigation.

# Chapter 2

# Enhanced land–sea warming contrast elevates aerosol pollution in a warmer world

## Abstract

Many climate models simulate an increase in anthropogenic aerosol species in response to warming1, particularly over the Northern Hemisphere mid-latitudes during June, July and August. Recently, it has been argued that this increase in anthropogenic aerosols can be linked to a decrease in wet removal associated with reduced precipitation, but the mechanisms remain uncertain. Here, using a state-of-the-art climate model (the Community Atmosphere Model version 5), we expand on this notion to demonstrate that the enhanced aerosol burden and hydrological changes are related to a robust climate

change phenomenon—the land–sea warming contrast. Enhanced land warming is associated with continental reductions in lower-tropospheric humidity that drive decreases in low clouds—particularly large scale (stratus) clouds—which, in turn, lead to reduced large-scale precipitation and aerosol wet removal. Idealized model simulations further show that muting the land–sea warming contrast weakens these hydrological changes, thereby suppressing the aerosol increase. Moreover, idealized simulations that only feature land warming yield enhanced continental aridity and an increase in aerosol burden. Thus, unless anthropogenic emission reductions occur, our results add confidence that a warmer world will be associated with enhanced aerosol pollution.

## 2.1  Introduction

Since the pre-industrial era, anthropogenic activities have resulted in a significant increase in anthropogenic aerosol burden5, which in turn has affected Earth's radiative balance. According to the Fifth Assessment Report of the IPCC, the total effective aerosol radiative forcing is $-0.9$ $W$ $m^{-2}$ (90% uncertainty range: $-1.9$ $to$ $-0.1$ $W$ $m^{-2}$) [40], indicating that aerosols cause a net cooling effect, which has probably offset 40% of GHG warming [41]. Aerosols can also adversely affect air quality and human health, with a recent study attributing 3.3 million premature deaths each year to aggravated aerosol pollution, led by fine particulate matter (PM2.5) [1], particularly in heavily polluted areas such as India and China. Continued GHG-induced global warming is expected to be associated with changes in the physical, chemical and biological factors that control the lifetime, transport, chemistry and atmospheric burden of aerosols [42, 43]. Considering the climatic and societal

importance of aerosol pollution, an improved understanding of how future climate change can influence the amount of aerosol is needed for climate and air pollution policy decisions.

Studies show a mixed aerosol response to GHG-induced warming, with some analyses yielding a decrease in aerosol burden, particularly SO4 [44, 45]. However, more recent studies show an increase in aerosols under warming [46, 47, 48]. State-of-the-art Atmospheric Chemistry Climate Model Intercomparison Project (ACCMIP) [49] models yield robust increases in most aerosol species, particularly over the Northern Hemisphere mid-latitudes during summer, which are largely due to a decrease in wet removal from reductions in large-scale precipitation (LSP) [47]. This results in a negative aerosol climate feedback, ranging from $-0.21 \; to \; -0.46 \; W \; m^{-2} \; K^{-1}$. Similarly, these same ACCMIP models yield a robust increase in PM2.5 and, in turn, an increase in premature mortality [50].

Uncertainty in the aerosol response to future warming is related to several factors, including uncertainty in the simulation of aerosol processes [51, 52], including transport, removal and chemistry. Furthermore, models must accurately simulate how GHG-induced warming impacts the climate system and, in turn, how these warming perturbations affect the important physical processes controlling aerosol burden. However, some climate warming responses are more robust than others. The land–sea warming contrast (LSWC), where continents warm more than the ocean [53, 54, 6, 55], is a robust feature found in both observations and climate model simulations. This phenomenon is caused by contrasts in surface sensible and latent fluxes over land [53], land–ocean contrasts in boundary-layer

lapse rate changes [56], boundary-layer relative humidity and associated low-level cloud cover changes over land [57], and soil moisture reductions [58]. Thus, enhanced continental warming is associated with an increase in land aridity, which in turn may affect the burden of anthropogenic aerosols. Here, we demonstrate, using novel simulations, that the LSWC is a dominant driver of the anthropogenic aerosol increase under future warming.

## 2.2  Results and Discussion

Figure 2.1 a,d,g,j shows that the Community Atmosphere Model version 5 (CAM5) [59] simulates a significant increase in all anthropogenic aerosol species in response to warming. Responses are estimated from the difference between a ten-year control simulation, based on the year 2000 climate and aerosol emissions, and a ten-year warming simulation, based on the year 2100 climate and year 2000 aerosol emissions (section 2.3). The significance of all of the responses was determined by Student's t-test for the difference of means, using the pooled variance. In all cases, the annual mean aerosol burden increases globally, with the maximum increase over the Northern Hemisphere mid-latitudes (30–60°N)—more specifically, over the Northern Hemisphere mid-latitude continents during summer (June through August (JJA)). For example, the annual mean sulphate ($SO_4$) burden increases 3.5% globally, 3.8% over the Northern Hemisphere mid-latitude land, and 9.8% over the Northern Hemisphere mid-latitude continents during JJA.

A similar sequence in decreasing wet deposition (Figure 2.1 b,e,h,k) is found from global annual to Northern Hemisphere mid-latitude continents during JJA. Wet deposition

is the primary removal mechanism for atmospheric aerosols and soluble gases [60]. Hence, the increase in burden is consistent with a reduction in wet deposition, and moreover, the maximum increase in aerosol burden over Northern Hemisphere mid-latitude continents during JJA is consistent with a corresponding maximum reduction in wet removal. Furthermore, most of this reduction in aerosol wet removal is driven by a decrease in wet deposition due to LSP (Figure 2.1 c,f,i,l). Over the oceans, the weaker decreases and increases in wet deposition, respectively, are consistent with: (1) the increase in aerosol burden over the continents, some of which gets transported over the ocean, leading to an increase in wet removal; and (2) increases in LSP (Figure A.1). These results agree with earlier findings based on ACCMIP models [47].

We now focus on what contributes to the reduction in aerosol wet deposition, most of which occurs over the continents of the Northern Hemisphere mid-latitudes during JJA. A decrease in wet deposition is in contrast with the expected global mean precipitation increase in response to warming10. CAM5 supports previous findings and simulates a 2.5% increase in global annual mean total precipitation, which becomes larger over the Northern Hemisphere mid-latitude continents (9.4% annual increase). Most of this annual mean increase over the Northern Hemisphere mid-latitude continents is driven by convective precipitation (a 21% annual increase) as opposed to LSP (a 2% annual increase; Figure A.1). During JJA, Northern Hemisphere midlatitude total precipitation increases slightly, which is decomposed into a 14% increase in convective precipitation, but an 18% decrease in LSP (Figure 2.2 a). Similar results exist across the CMIP5 models [47]. Despite this increase

in convective precipitation, the change in wet deposition due to convective precipitation is negligible over the Northern Hemisphere mid-latitudes during JJA under warming (Figure 2.2). The decrease in LSP is consistent with a maximum reduction in wet deposition due to large-scale (and total) precipitation over the Northern Hemisphere mid-latitude continents during JJA. Although the dominant role of LSP, and the corresponding wet removal, is consistent with ACCMIP models2, we acknowledge relatively large model diversity in terms of the proportion of wet removal due to convective precipitation16, as well as additional uncertainties in aerosol simulations (section 2.3).

Reductions in relative humidity and soil moisture are important components of the projected summer drying over the Northern Hemisphere mid-latitudes [61]. To a large extent, land moisture is dictated by the transport of moisture from the oceans [62]. When the continental lower tropospheric temperature warms more than that over the ocean, the air can hold more moisture relative to the amount of moisture advected from the oceans [7]. As a result, the relative humidity over the continents decreases. This relative humidity reduction promotes low-level cloud (CLOW) reductions over the land, causing further land warming, thus constituting a positive feedback that acts to further warm and dry out the land [57, 5]. Soil moisture is also a crucial factor for the positive land-drying feedback during the summer. Less soil moisture has been associated with less precipitation through atmospheric feedbacks [63].

CAM5 captures this summertime drying over the Northern Hemisphere mid-latitude continents (Figure A.3), including the reduction in relative humidity and CLOW, as well as a reduction in soil moisture, all of which are largest during JJA (Figure 2.3). The CLOW reduction is largely due to decreases in lowlevel large-scale (stratus) cloud (SCLOW; section 2.3). Furthermore, snow depth exhibits a maximum decrease during March through May (MAM), which implies less snow melt during the late spring and early summer, probably contributing to the decrease in soil moisture. Also consistent with the enhanced continental aridity is a decrease in surface runoff. These CAM5 hydrological changes are generally consistent across CMIP5 models (Figure A.4). However, some exceptions do exist, including the seasonal cycle of runoff and the magnitude of the snow depth response.

To evaluate the importance of enhanced land warming to the aforementioned hydrological responses, and the increase in aerosol burden under warming, a set of idealized simulations were performed to mute the land warming. These were identical to the default warming simulation, but the near-surface land temperature was nudged to the control simulation's near-surface land temperature (section 2.3). Three separate nudging simulations were performed, with nudging strengths of 1.0, 2.5 and 5.0%. These simulations successfully muted the enhanced land warming, with larger nudging producing a larger LSWC reduction (Figure A.5 and Table A.1). The LSWC amplitude can be measured in terms of the warming ratio, defined as the lower-tropospheric continental warming relative to that over the ocean [64]. In CAM5 simulations with 5.0% nudging, the global annual warming ratio drops from 1.46 to 1.08 (26% decrease). This warming ratio reduction oc-

curs at all latitudes, but the largest decrease ($\sim$41%) occurs over the Northern Hemisphere mid-latitudes during JJA. Hence, these nudging simulations successfully weaken the LSWC.

The importance of muted land warming was explored in two steps: (1) by analysing the hydrology changes; and (2) by investigating the aerosol burden and wet deposition changes. The muted land warming simulations weaken the decrease in all hydrology variables, particularly during JJA, including lower tropospheric relative humidity, soil moisture, surface runoff, low clouds and LSP (Figure 2.2). The decrease in MAM snow depth is also weakened. Thus, with a weaker LSWC, less Northern Hemisphere mid-latitude continental drying occurs, and this response generally scales with the magnitude of the nudging. However, we note possible nonlinearities with some aspects of the response, as the changes in LSP, soil moisture and runoff are similar for the 2.5 and 5.0% nudging experiments, despite clear separation of the change in aerosol burdens.

Figure 2.3 shows that muted land warming results in a weaker increase (or decrease) in anthropogenic aerosol species over the Northern Hemisphere mid-latitude continents, particularly during JJA. Consistently, the decrease in wet deposition due to LSP is also weakened. This weakening is consistent with the changes in hydrology and strength of the nudging—1.0% nudging yields the smallest reduction during JJA, and 5.0% nudging yields the largest reduction.

Climate change may also affect aerosol burden through modification of chemical production pathways, particularly in the context of SO4 and secondary organic aerosols (SOA). In CAM5, changes in chemical production act to mute the increase in SO4 and SOA burden over the Northern Hemisphere mid-latitude continents, especially during JJA (Figure A.6 and Figure A.7). The two primary chemical production pathways of SO4 are aqueous and gaseous production (section 2.3). In response to warming, CAM5 exhibits a decrease in aqueous SO4 production, consistent with the decrease in low clouds (Figure 2.2). This, in turn, results in more of the SO4 gaseous precursor SO2 (not shown), and a corresponding increase in SO4 gaseous production. However, the decrease in aqueous production dominates, and the total chemical production of SO4 decreases in response to warming (Figure A.6).

In CAM5, a relatively simple treatment of SOA is assumed (section 2.3). A gaseous precursor for SOA formation (SOAG) requires oversaturation to condense and form SOA. The SOAG partial pressure increases with enhanced warming, which decreases the condensation of SOAG to SOA under warming, resulting in less SOA (Figure A.7). Hence, changes in chemical production are not responsible for the increase in SO4 or SOA burden under warming— in fact, they act to weaken the increase. Furthermore, these conclusions are consistent across the muted warming simulations (Figure A.6 and Figure A.7).

Finally, a third set of simulations were performed to investigate the impact of increasing the LSWC. They were identical to the control simulation, but the near-surface land

14

temperature was nudged to that based on a future warming simulation, based on the year 2150 Representative Concentration Pathway (RCP) 8.5 climate conditions (section 2.3). Three different nudging strengths of 1.0, 2.5 and 5.0% were used. These simulations therefore enhance the LSWC (Figure A.8), and a larger contrast is obtained with a larger nudging strength. These simulations, which only feature enhanced land warming, yield an increase in all anthropogenic aerosol species, in addition to a decrease in wet removal by LSP, over the Northern Hemisphere mid-latitude continents (Figure 2.4). These simulations also show the expected hydrological changes, including decreases in lower-tropospheric relative humidity, soil moisture, low clouds and LSP, particularly during JJA (Figure A.9). Thus, land warming alone causes continental drying and an increase in aerosol burden, with more land warming yielding a larger response.

Now, we further elucidate the cause of the JJA LSP decrease over the Northern Hemisphere mid-latitude continents. Extratropical storm tracks play an important role in mid-latitude precipitation, and global warming may lead to a decrease in extratropical storm track activity [65, 66]. CAM5 simulations support this finding, yielding a decrease in JJA Northern Hemisphere mid-latitude storm track activity (Figure A.10). However, the decrease in JJA storm track activity occurs over both land and ocean, with similar magnitude, in opposition to the land–sea contrast in LSP, low cloud and other hydrological variables (for example, Figure A.3). Additional analyses also suggest that a decrease in storm track activity is not the dominant cause of the LSP decrease (Appendix A).

15

Instead, the LSP decrease is largely consistent with decreases in SCLOW. As with most models, CAM5 parameterizes largescale cloud cover based on relative humidity23. The JJA Northern Hemisphere mid-latitude decrease in continental relative humidity under warming is consistent with the decrease in large-scale cloud cover, particularly in the lower troposphere. Moreover, the net condensation rate of water vapour into liquid stratus droplets depends on the stratus cloud cover. This implies that a decrease in largescale cloud cover should be associated with a decrease in LSP. Thus, we suggest that the decrease in LSP is a direct consequence of the decrease in large-scale cloud cover.

Statistical analyses support this conclusion. The spatial (grid box) JJA Northern Hemisphere mid-latitude land correlation between SCLOW and low-level relative humidity (LSP) is 0.72 (0.55) in the control simulation. The corresponding correlation between the change in SCLOW and the change in low-level relative humidity (LSP) is 0.52 (0.43). In contrast, the corresponding correlations between LSP and storm track activity are much weaker, at 0.16 in the control simulation and 0.19 based on responses. Similar results are obtained in CMIP5 models (Appendix A). Furthermore, a regression model comprising SCLOW versus LSP values from the CAM5 control simulation predicts reasonably well the actual change in JJA Northern Hemisphere mid-latitude continental LSP (Figure A.11).

To further test the importance of SCLOW to LSP, we performed additional perturbed parameter experiments with CAM5 that involved reducing the sensitivity of SCLOW to relative humidity (section 2.3). When decreasing the sensitivity of SCLOW to relative

16

humidity, smaller (relative) decreases in SCLOW under warming are expected. Furthermore, if decreases in SCLOW drive decreases in LSP under warming, smaller (relative) decreases in LSP would also be expected. In the default warming simulation, the Northern Hemisphere mid-latitude JJA continental decrease in SCLOW is $-3.7\%$ and the decrease in LSP is $-3.3$ mm month1. The corresponding percentage changes are $-33.9$ and $-13.3\%$, respectively. In our sensitivity experiment, the corresponding decreases in SCLOW and LSP were $-2.5\%$ and $-2.6$ mm month$^{-1}$, respectively. More importantly, the percentage changes exhibited weaker decreases, at $-30.5$ and $-10.7\%$, respectively. Thus, as we reduce the sensitivity of SCLOW to relative humidity over land, warming results in a smaller SCLOW decrease, and a correspondingly smaller LSP decrease.

Similar to state-of-the-art ACCMIP models, CAM5 simulates a global annual mean increase in anthropogenic aerosols in response to GHG-induced warming, with a maximum increase over the Northern Hemisphere mid-latitude continents during JJA. Targeted CAM5 simulations show that this response is related to the LSWC and associated increases in continental aridity, which result in less aerosol wet removal. Muting the LSWC weakens the increase in aerosol burden, as well as the decrease in soil moisture, runoff, snow depth, lower tropospheric relative humidity, LSP and associated aerosol wet removal. Furthermore, land warming alone yields an increase in aerosol burden and the opposite hydrological changes. Additional analyses suggest that the reduction in LSP is largely due to decreases in SCLOW, which is consistent with reductions in continental relative humidity. Although aerosol simulations have uncertainty, we have related the increase in aerosol burden under warming to

a robust climate change phenomenon— the land warms more than the ocean, which leads to enhanced continental aridity, and less LSP and aerosol wet removal. Furthermore, although our results are based on a single climate model, a larger suite of CMIP5 models yields similar hydrological changes to CAM5. ACCMIP models also support the importance of reduced LSP and aerosol wet removal under warming. Since our default warming responses are (1) based on a business-as-usual warming scenario and (2) assume no reductions in anthropogenic aerosol emissions, they represent an upper bound on future aerosol increases in response to climate change. Unless emission reductions occur, our results add confidence that a warmer world will be associated with enhanced anthropogenic aerosol pollution, or alternatively, that larger emission reductions will be necessary to obtain a desired level of air quality.

## 2.3 Methods

All simulations for this study were performed with the state-of-the-art CAM5 (ref. [59])—the atmospheric component of the Community Earth System Model version 1.2.2, developed primarily at the National Center for Atmospheric Research. CAM5 incorporates the three-mode modal aerosol model (MAM3) [67], which provides internally mixed representations of number concentrations and mass for Aitken, accumulation and coarse aerosol modes. The simulated aerosols were composed of $SO_4$, black carbon, primary organic aerosols (POA), SOA, sea salt and mineral dust. Aerosol wet removal was based on ref. [68], but with modifications for the consistency with cloud macrophysics and microphysics. The routine treats both in-cloud and below-cloud scavenging. For in-cloud scavenging, cloud

water first-order loss rates (based on cloud water mixing ratios and precipitation production rates) were multiplied by 'solubility factors' to obtain aerosol first-order loss rates. The solubility factors can be interpreted as the aerosol fraction in cloud drops multiplied by the tuning factor. The stratiform in-cloud scavenging only affects the stratiform-cloud-borne aerosol particles, and these have solubility factors of 1.0 (0 for interstitial aerosols).

In CAM5 (and most models), two types of clouds were diagnosed: large-scale (stratus) and convective (cumulus). The large-scale cloud cover is derived from the assumed triangular distribution of total relative humidity. The cumulus cloud cover is a function of the convective mass flux from both the deep and shallow convection schemes.

The spatial correlation (JJA Northern Hemisphere mid-latitude land) between the change in CLOW and SCLOW is 0.98. Furthermore, the JJA Northern Hemisphere mid-latitude continental decreases in CLOW and SCLOW are $-4.1$ and $-3.7\%$, respectively (significant at the 99% confidence level). The corresponding decrease in low-level convective cloud cover is much weaker at $-0.4\%$. In terms of percentage changes, CLOW and SCLOW exhibit large responses at $-28.8$ and $-33.9\%$, respectively ($-11.5\%$ for low-level convective cloud cover). Thus, the bulk of the CLOW decrease is due to decreases in SCLOW, and the spatial patterns of the responses are very similar. Using CLOW as a surrogate for SCLOW is a reasonable approximation.

Furthermore, the change in SCLOW, as for most hydrological variables including LSP, exhibits a land–sea contrast (for example, Figure A.3). During JJA in the Northern Hemisphere mid-latitudes, SCLOW decreases by $-3.7\%$ over land, but increases by $1.5\%$ over sea (both significant at the 99% confidence level). This is consistent with the land–sea contrast in low-level relative humidity, which decreases by $-4.5\%$ (significant at the 99% confidence level) over land, but increases by $0.5\%$ (significant at the 95% confidence level) over the sea.

Uncertainty in the aerosol response to future warming is related to several factors, including uncertainty in the simulation of aerosol processes. For example, models parameterize aerosol removal processes differently, including both wet and dry removal. Based on AeroCom models, relatively large diversity exists in terms of the proportion of wet removal due to convective precipitation versus LSP. Across AeroCom models and aerosol species, the percentage of convective wet removal (relative to the total) ranges from 10-80% [51]. CAM5 falls in the middle of this relatively large range, with a percentage of removal by convective precipitation ranging from 43-52%, depending on the aerosol species. Over the Northern Hemisphere midlatitude continents during JJA, the numbers are a bit larger than the global annual mean values, with approximately 50-60% of wet removal due to convective precipitation. Thus, CAM5 does not lack a sensitivity of wet removal by convective precipitation.

Another source of uncertainty is how changes in precipitation intensity versus frequency impact aerosol wet removal [69]. During JJA, the CMIP5 multimodel mean shows a 6-7% decrease in the LSP frequency rate in the Northern Hemisphere mid-latitudes. The corresponding decrease in the intensity of precipitation is 13-14%. This indicates that a decrease in the intensity of LSP, as opposed to the frequency, is probably the most important driver of the decrease in LSP and the associated wet removal3. However, we note that models tend to overestimate the frequency of precipitation (rain almost every day), implying that they may underestimate the role of precipitation frequency in wet scavenging.

Similar results are obtained with CAM5, as the frequency of JJA LSP decreases by $-3.5\%$ in the default warming simulation over Northern Hemisphere midlatitude continents, whereas the intensity decreases by $-13.8\%$. Furthermore, the changes in LSP in the nudged simulations are driven by changes in the intensity, as opposed to the frequency, of LSP. For example, the frequency of JJA LSP decreases by $-3.5$, $-4.2$, $-3.1$ and $-2.7\%$ over the Northern Hemisphere mid-latitude continents in the default warming and 1.0, 2.5 and 5.0% nudged (muted land warming) simulations, respectively. The corresponding intensity of LSP decreases by $-13.8$, $-4.6$, $-1.0$ and $-0.6\%$. Similarly, in the enhanced land warming simulations, the frequency of LSP decreases by $-1.4$, $-1.3$ and $-1.8\%$ in the 1.0, 2.5 and 5.0% nudged (enhanced land warming) simulations, respectively. The corresponding intensity of LSP decreases by $-6.5$, $-15.5$ and $-17.3\%$. Thus, changes in the intensity, as opposed to the frequency, of LSP are driving the bulk of the LSP signal. We note that changes in precipitation frequency are probably more related to dynamics

(for example, changes in the frequency of storm tracks), whereas changes in precipitation intensity are probably more related to changes in thermodynamics (for example, enhanced land warming and aridity). Thus, the dominant role of the LSP intensity decrease in the overall LSP reduction supports the importance of thermodynamics, as opposed to dynamics.

Although we did not use the full chemistry version of CAM5 (CAM5-chem), simple on-line chemistry is included in CAM5. In terms of SOA, the most straightforward representation (which is used in many climate models) is to assume fixed mass yields for precursor volatile organic compounds and then emit this mass as primary aerosol particles. MAM adds one level of sophistication by simulating a single lumped gas phase SOA species (SOAG). MAM then simulates condensation or evaporation of the SOAG to or from several aerosol modes. This provides a realistic method for estimating the distribution of SOA among different modes, and a minimal representation of the temperature dependence of the gas/aerosol partitioning.

Simple gas-phase chemistry is included for SO4. This includes: dimethyl sulfide oxidation with OH and $NO_3$ to form $SO_2$; $SO_2$ oxidation with OH to form $H_2SO_4$ (gas); $H_2O_2$ production; and $H_2O_2$ loss. Rate coefficients and oxidant concentrations ($O_3$, OH, $HO_2$ and $NO_3$) are provided from the Model for Ozone and Related chemical Tracers [70].

CAM5 time-slice simulations were integrated for ten years and were based on climatological sea-surface temperatures and sea-ice concentrations, along with anthropogenic

aerosol and precursor gas emissions. Nearly identical results were obtained with a longer, 20-year integration. Sea-surface temperatures and sea-ice concentration anomalies (2090−2099 relative to 2006−2015) from CMIP5 RCP 8.5 models were added to the default warming simulation, along with endof- the-century RCP 8.5 GHG concentrations. The control and default warming simulations both have identical aerosol and precursor gas emissions, based on the year 2000. We note that our simulations lack additional climate warming–land feedbacks, including prognostic wildfire emissions and changes in vegetation that may be important for changes in aerosol burden under future warming.

Additional idealized ten-year time-slice simulations were performed to investigate the effect of the LSWC on aerosol burden. Muted land warming simulations are identical to the default warming simulation, but near-surface land temperatures are nudged to the control simulation. The simulated meteorological field (near-surface land temperature) T$_{nudged}$ is calculated in the following manner:

$$T_{nudged} = (1 - \alpha)T_{warming} + \alpha T_{control}$$

where T$_{warming}$ and T$_{control}$ are the near-surface land temperatures from the default warming simulation and control simulation, respectively. T$_{control}$ is fed every 6h and the nudging is applied at every model time step (that is, every 30 min). The fraction  denotes the strength of the nudging, which varies between 0.010, 0.025 and 0.050 (that is, 1.0, 2.5 and 5.0% nudging, respectively).

A series of ten-year time-slice simulations with enhanced land warming was also performed. These simulations are identical to the control simulation, but near-surface land temperatures are relaxed to a warming simulation, which is based on RCP 8.5 climate conditions in the year 2150. Thus, these simulations only feature enhanced land warming. Similar to most climate models, CAM5 diagnoses the liquid stratus cloud cover as a function of the grid box mean relative the humidity over water. There is also a critical relative humidity ($U_{cl}$) that must be exceeded for liquid stratus cloud cover to form (that is, stratus cloud only exists when the grid mean relative humidity exceeds $U_{cl}$). In CAM5, $U_{cl}$ is an externally specified function of height and surface properties. $U_{cl}$ is specified at 0.8875 in the layers below 700 hPa (SCLOW). However, for SCLOW over land with a water-equivalent snow depth less than $10^{-6}$ m, $U_{cl} = 0.7875$. Similarly, $U_{cl} = 0.80$ in the layers above 400 hPa (high-level stratus). Between 700 and 400 hPa (mid-level stratus), a linearly interpolated $U_{cl}$ value is used.

Sensitivity experiments were performed by increasing $U_{cl}$, in the layers below 700 hPa over land with a water-equivalent snow depth of less than $10^{-6}$ m, from 0.7875 to 0.8875 (both a new control and a new warming simulation). By increasing $U_{cl}$, the amount of SCLOW over land is reduced, particularly during the summer months when the snow depth is low. The JJA Northern Hemisphere mid-latitude climatological SCLOW over land decreases from 10.9% in the default simulation ($U_{cl} = 0.7875$) to 8.4% in the sensitivity simulation ($U_{cl} = 0.8875$). Corresponding values over the sea remain relatively unchanged at 32.3% (32.7%) in the default (sensitivity) simulation.

More importantly, the sensitivity of SCLOW to relative humidity is reduced. This is confirmed by regressing SCLOW versus low-level relative humidity using values from each control simulation. With $U_{cl} = 0.7875$, the regression slope ($\Delta$CLOW/$\Delta$RH (where RH stands for relative humidity); that is, the sensitivity of SCLOW to relative humidity) is 0.51, implying that a 1% decrease in relative humidity yields a 0.5% decrease in SCLOW (significant at the 99% confidence level). With $U_{cl} = 0.8875$, the regression slope decreases to 0.41, implying that a 1% decrease in relative humidity yields a 0.4% decrease in SCLOW (significant at the 99% confidence level). Thus, this perturbed parameter experiment reduces the sensitivity of SCLOW to relative humidity by 20%. Similar results are obtained using relative humidity at other levels (for example, 700 hPa).

In addition to smaller reductions in JJA Northern Hemisphere mid-latitude continental SCLOW and LSP in our sensitivity simulation, other hydrological variables change in a consistent way, which supports the idea that feedbacks exist between the hydrological variables. For example, there is less JJA Northern Hemisphere mid-latitude land warming (6.0 to 5.6 K), a smaller decrease in lowlevel relative humidity ( 4.5 to  4.3%) and a smaller decrease in soil moisture ( 0.85 to  0.46 kg m$^{-2}$). Similar conclusions exist based on percentage changes. Thus, with reduced sensitivity of SCLOW to relative humidity, there is reduced land warming, as well as smaller decreases in low-level relative humidity and soil moisture. In other words, there is a smaller increase in continental aridity.

Consistent with our default warming and nudged simulations, the decrease in LSP (as $U_{cl}$ is increased) is entirely dominated by decreases in LSP intensity. The change in the frequency of LSP remains essentially unchanged at $-3.5\%$. However, the intensity of LSP changes from $-13.8$ to $-6.8\%$ as $U_{cl}$ is increased from $0.7875$ to $0.8875$.
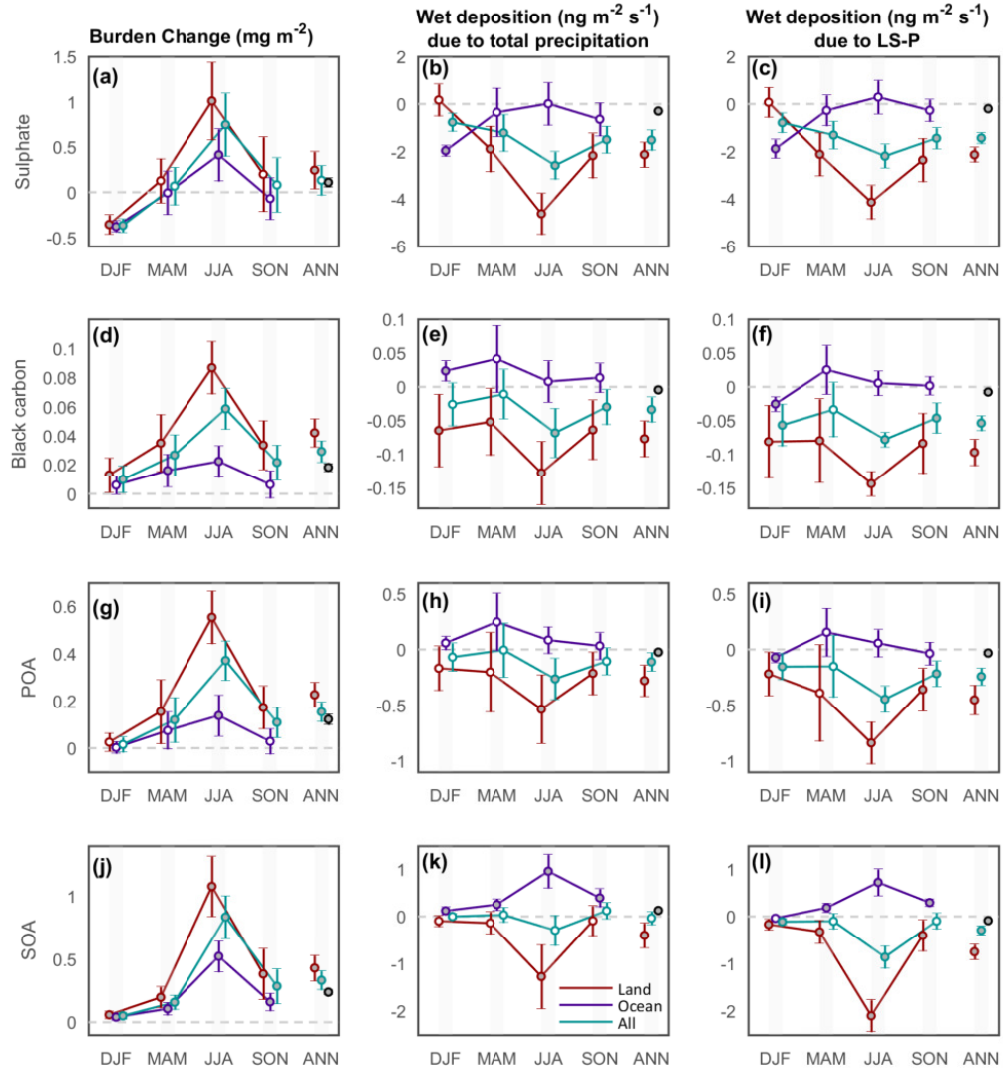
Figure 2.1: **CAM5 seasonal and annual mean aerosol burden and wet deposition response to climate change.** a–l, Changes in aerosol burden (a, d, g and j), and wet deposition due to total precipitation (b, e, h and k) and LSP (c, f, i and l) over the Northern Hemisphere mid-latitudes for SO4 (a–c), black carbon (d–f), POA (g–i) and SOA (j–l) stratified by all grid points (turquoise), land only (maroon) and ocean only (purple). Annual mean responses for the globe (black), Northern Hemisphere mid-latitudes (turquoise) and Northern Hemisphere mid-latitude continents (maroon) are shown to the right of each panel. Error bars represent the 99% confidence interval based on a Student's t-test for the difference of means, using the pooled variance. DJF, December through February; SON, September through November.
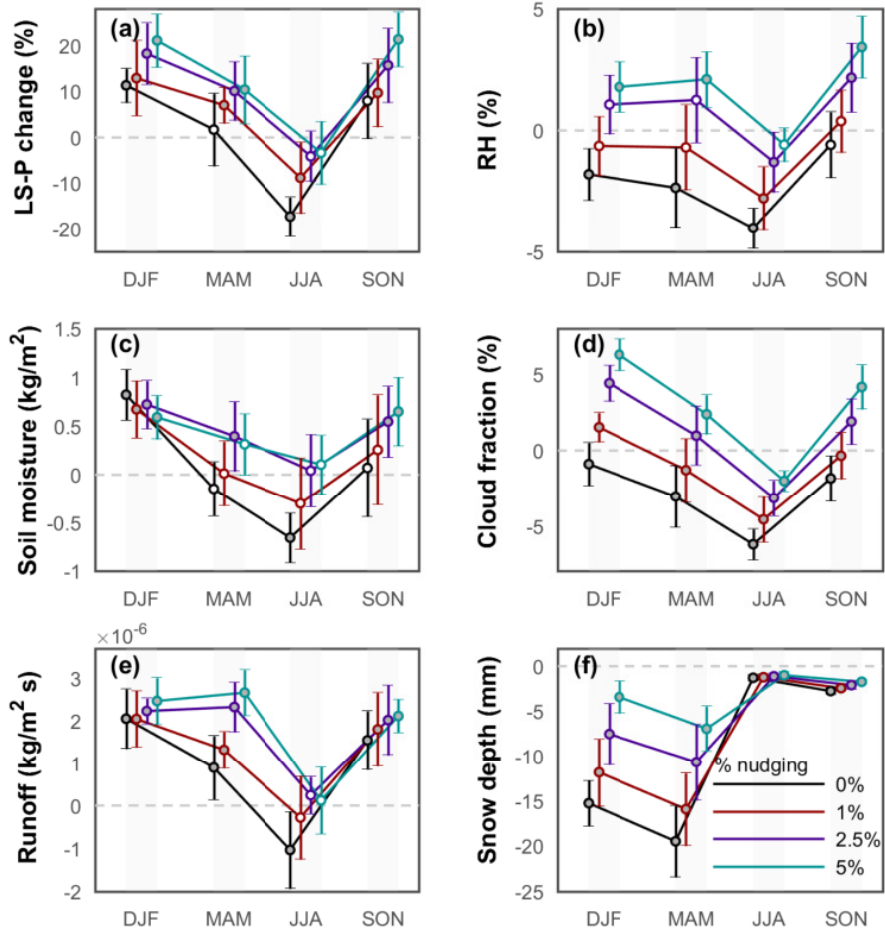
Figure 2.2: **CAM5 seasonal mean hydrology response for default warming and muted land warming simulations.** a–f, Changes for the Northern Hemisphere mid-latitudes over land for LSP (a), lower tropospheric relative humidity (b), 10 cm soil moisture (c), low cloud cover (d), surface runoff (e) and snow depth (f). Responses are shown for 0% nudging (that is, default warming; black), 1.0% nudging (maroon), 2.5% nudging (purple) and 5.0% nudging simulations (turquoise). Error bars represent the 99% confidence interval based on a Student's t-test for the difference of means, using the pooled variance. The low cloud cover response in d is nearly identical to the low-level, large-scale (stratus) cloud response.
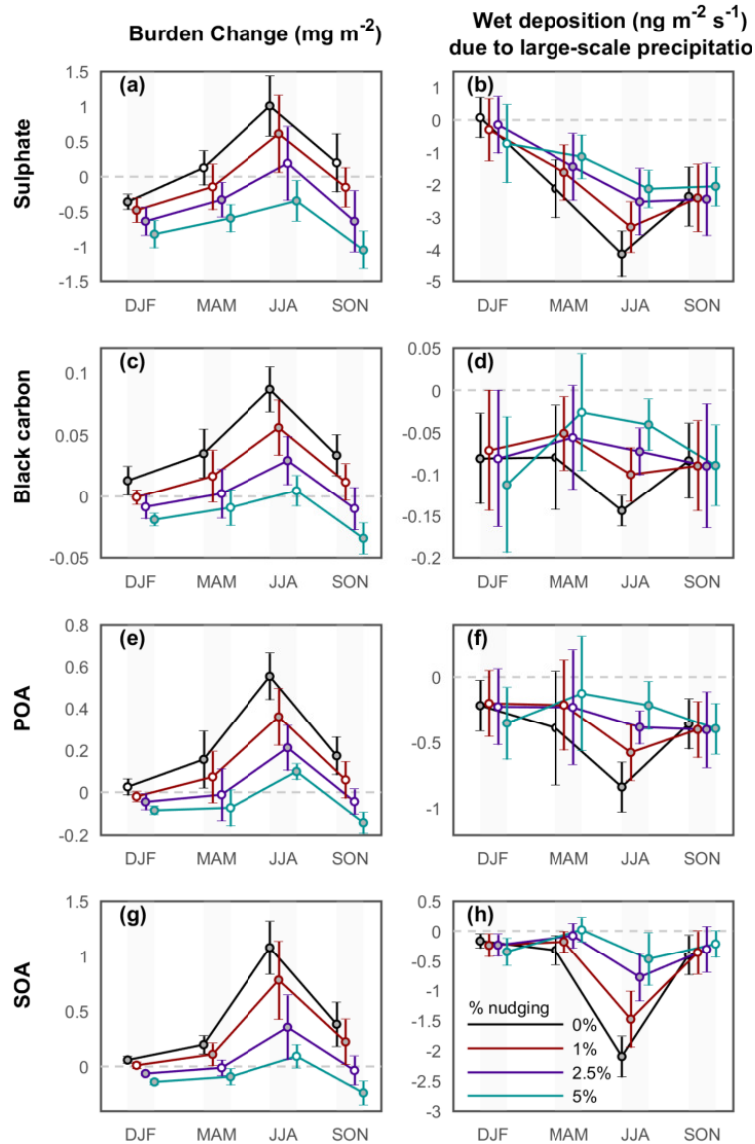
Figure 2.3: **CAM5 seasonal mean response of aerosol burden and wet deposition due to LSP for default warming and muted land warming simulations.** a–h, Changes in aerosol burden (a, c, e and g), and wet deposition due to LSP (b, d, f and h), for the Northern Hemisphere midlatitudes over land for SO4 (a and b), black carbon (c and d), POA (e and f) and SOA (g and h). Responses are shown for 0% nudging (that is, default warming; black), 1.0% nudging (maroon), 2.5% nudging (purple) and 5.0% nudging simulations (turquoise). Error bars represent the 99% confidence interval based on a Student's t-test for the difference of means, using the pooled variance.
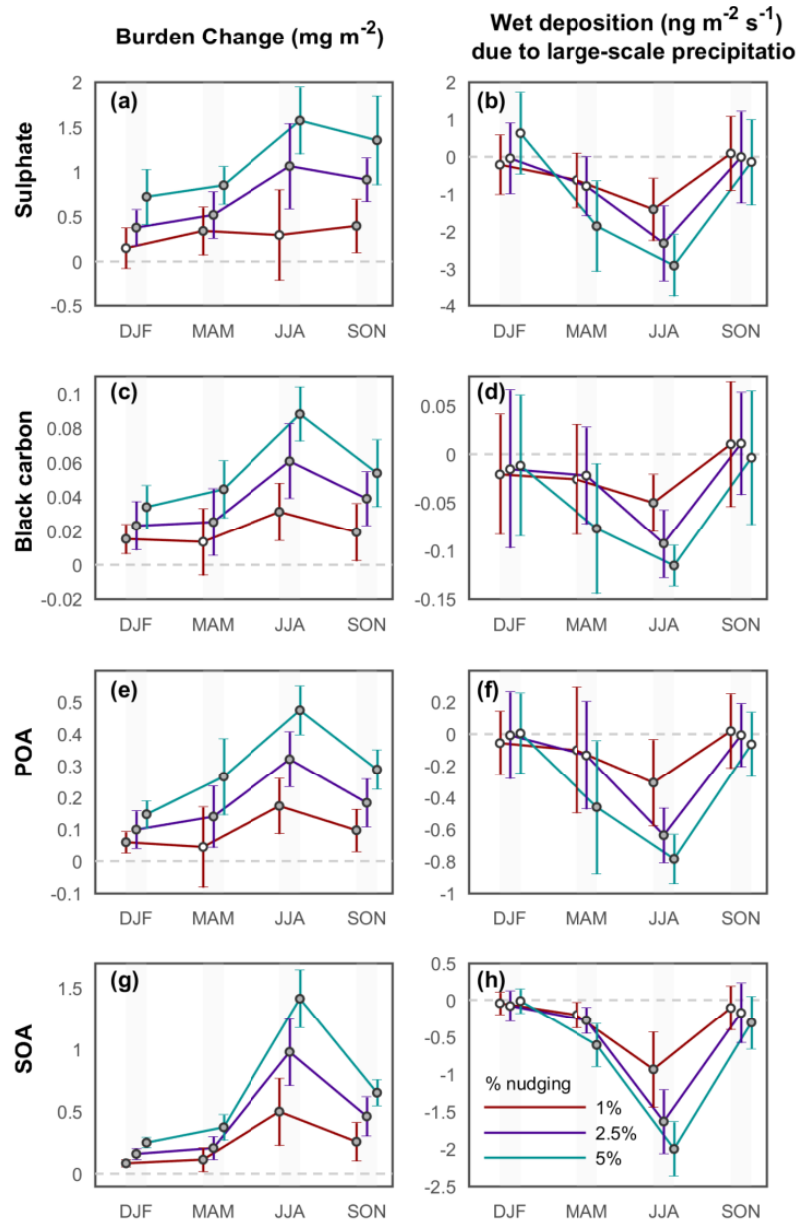
Figure 2.4: **CAM5 seasonal mean response of aerosol burden and wet deposition due to LSP for enhanced land warming simulations.** a–h, Changes in aerosol burden (a, c, e and g), and wet deposition due to LSP (b, d, f and h), are shown for the Northern Hemisphere mid-latitudes over land for SO4 (a and b), black carbon (c and d), POA (e and f) and SOA (g and h). Responses are shown for 1.0% nudging (maroon), 2.5% nudging (purple) and 5.0% nudging simulations (turquoise). Error bars represent the 99% confidence interval based on a Student's t-test for the difference of means, using the pooled variance.

# Chapter 3

# Anthropogenic aerosol forcing of the AMOC and the associated mechanisms in CMIP6 models

## Abstract

By regulating the global transport of heat, freshwater and carbon, the Atlantic Meridional Overturning Circulation (AMOC) serves as an important component of the climate system. During the late 20th and early 21st centuries, indirect observations and models suggest a weakening of the AMOC. Direct AMOC observations also suggest a weakening during the early 21st century, but with substantial interannual variability. Long-term weakening of the AMOC has been associated with increasing greenhouse gases (GHGs), but some modeling studies suggest the build up of anthropogenic aerosols (AAs) may have offset

part of the GHG-induced weakening. Here, we quantify 1900-2020 AMOC variations and assess the driving mechanisms in state-of-the-art climate models from the Coupled Model Intercomparison Project phase 6 (CMIP6). The CMIP6 all forcing (GHGs, anthropogenic and volcanic aerosols, solar variability, and land use/land change) multi-model mean shows negligible AMOC changes up to ~1950, followed by robust AMOC strengthening during the second half of the 20th century (~1950-1990), and weakening afterwards (1990-2020). These multi-decadal AMOC variations are related to changes in North Atlantic atmospheric circulation, including an altered sea level pressure gradient, storm track activity, surface winds and heat fluxes, which drive changes in the subpolar North Atlantic surface density flux. To further investigate these AMOC relationships, we perform a regression analysis and decompose these North Atlantic climate responses into an anthropogenic aerosol-forced component and a subsequent AMOC-related feedback. Similar to previous studies, CMIP6 GHG simulations yield robust AMOC weakening, particularly during the second half of the 20th century. Changes in natural forcings, including solar variability and volcanic aerosols, yield negligible AMOC changes. In contrast, CMIP6 AA simulations yield robust AMOC strengthening (weakening) in response to increasing (decreasing) anthropogenic aerosols. Moreover, the CMIP6 all-forcing AMOC variations and atmospheric circulation responses also occur in the CMIP6 AA simulations, which suggests these are largely driven by changes in anthropogenic aerosol emissions. More specifically, our results suggest that AMOC multi-decadal variability is initiated by North Atlantic aerosol optical thickness pertur-bations to net surface shortwave radiation and sea surface temperature (and hence sea surface density), which in turn affect sea level pressure gradient and surface wind−and

32

via latent and sensible heat fluxes—sea surface density flux through its thermal component. AMOC-related feedbacks act to reinforce this aerosol-forced AMOC response, largely due to changes in sea surface salinity (and hence sea surface density), with temperature (and cloud) related feedbacks acting to mute the initial response. Although aspects of the CMIP6 all-forcing multi-model mean response resembles observations, notable differences exist. This includes CMIP6 AMOC strengthening from ~1950-1990, when the indirect estimates suggest AMOC weakening. The CMIP6 multi-model mean also underestimates the observed increase in North Atlantic ocean heat content. And although the CMIP6 North Atlantic atmospheric circulation responses—particularly the overall patterns—are similar to observations, the simulated responses are weaker than those observed, implying they are only partially externally forced. The possible causes of these differences include internal climate variability, observational uncertainties and model shortcomings—including excessive aerosol forcing. A handful of CMIP6 realizations yield AMOC evolution since 1900 similar to the indirect observations, implying the inferred AMOC weakening from 1950-1990 (and even from 1930-1990) may have a significant contribution from internal (i.e., unforced) climate variability. Nonetheless, CMIP6 models yield robust, externally forced AMOC changes, the bulk of which are due to anthropogenic aerosols.

## 3.1   Introduction

The Atlantic Meridional Overturning Circulation (AMOC) is an important component of the climate system, transporting large amounts of heat and freshwater poleward [8, 9]. The AMOC exhibits variability on a range of timescales, impacting not only surface

temperature, but also precipitation and sea level in several regions [71, 72]. The AMOC plays a central role in the climate response to anthropogenic forcing [73, 74, 75, 19, 76, 77], and has also likely played a key role in past rapid climate change and paleoclimate shifts [78].

Since April 2004, the AMOC has been directly monitored at 26.5°N by the RAPID array [79]. The RAPID array shows a strong decline in the first part of the record and a slower increase afterwards. This record suggests an overall AMOC decline at a rate as high as 0.4 Sv yr$^{-1}$ (1 Sv = $10^6$ $m^3$ $s^{-1}$) [80, 81, 10, 11]. The causes of this recent AMOC slow-down remain highly debated, and may be related to natural decadal variability [82, 83, 84]. However, longer-term evidence, including sea surface temperature fingerprints and coral-based proxies, also suggest AMOC weakening−by about 0.2 Sv decade$^{-1}$ during the 20th century−as part of climate change [85, 12].

Although climate models disagree on the precise magnitude of the AMOC weakening−and differ substantially in their representation of the strength and depth of the AMOC−model simulations predict AMOC weakening in response to increasing greenhouse gases [14, 15, 16, 17, 18, 19]. By the end of the 21st century, for example, models estimate a 24-39% decline in the AMOC, with larger weakening under larger increases in future GHG emissions [20]. This has been related to reduced ocean heat loss, and secondarily through increased freshwater input at high latitudes, both of which decrease the density of sea water in the subpolar North Atlantic (i.e., the sinking region) [86]. For example, decreased Arctic sea-ice, via positive buoyancy anomalies caused by anomalous surface heat and freshwater fluxes, may help explain weakening of the AMOC [81, 87]. Warming of the tropical Indian Ocean−by

means of atmospheric teleconnections and changes in ocean salinity and circulation—may exert a stabilizing effect on the AMOC, attenuating its recent weakening [88]. Overall, our understanding of how anthropogenic perturbations impact the AMOC remains limited.

There is considerable debate on the role of anthropogenic aerosols in driving North Atlantic climate variability. One study argued anthropogenic aerosols are the dominant driver of Atlantic Multidecadal Variability (a broad term encompassing Atlantic climate variability), primarily through aerosol-cloud interactions and modification of net surface shortwave radiation [89]. However, this result was based on a single climate model, the Hadley Centre Global Environmental Model version 2, Earth System configuration (HadGEM2-ES). Subsurface inconsistencies between observations and HadGEM2-ES were also noted, and long-term trends in sea surface temperatures may be too sensitive to HadGEM2-ES' aerosol loading [90]. Others have also suggested a role of anthropogenic forcing, including aerosols, in driving Atlantic Multidecadal Variability [91, 92, 93, 94, 95, 96]. Anthropogenic aerosols may also impact the AMOC, including strengthening the AMOC and increasing the northward cross-equatorial ocean heat transport [21, 22, 23, 24, 25, 26, 17]. [26]—using the same HadGEM2-ES model discussed above—finds AMOC strengthening in response to increasing anthropogenic aerosols. They argue that this is primarily driven by increased salinification of the North Atlantic subpolar gyre via increased evaporation, decreased flux of ice through the Fram Strait and increased salt advection from the subtropical Atlantic. This study, like many of the earlier studies, relies on a single climate model. Very recently, however, [97] use the new Coupled Model Intercomparison Project phase 6 (CMIP6) [39] archive to show a ~10% AMOC strengthening from 1850-1985, which they

attribute to aerosol forcing. Furthermore, [98] find that the projected 21st century decline of anthropogenic aerosols in CMIP5 models induces AMOC weakening. This weakening of ocean circulation is associated with a divergence of meridional oceanic heat transport, which leads to enhanced ocean heat uptake but diminished storage of oceanic heat in the subpolar North Atlantic.

The newest generation of coupled climate and earth system models, CMIP6, represents a significant opportunity to evaluate the role of external forcing, including anthropogenic aerosols, on North Atlantic climate and the AMOC. Similar to the very recent results of [97], we show that a large suite of state-of-the-art climate models simulate robust strengthening of the AMOC from ∼1950-1990, and that this response is largely driven by anthropogenic aerosols. Furthermore, CMIP6 models yield robust AMOC weakening from 1990-2020, with anthropogenic aerosols again playing an important role. We show that this multi-decadal AMOC variability is initiated by North Atlantic aerosol perturbations to net surface shortwave radiation and surface temperature (and hence sea surface density), which in turn affect sea level pressure gradient and surface wind−and via latent and sensible heat fluxes−sea surface density flux through its thermal component. AMOC-related feedbacks act to reinforce this aerosol-forced AMOC response, largely due to changes in sea surface salinity (and hence sea surface density), with temperature (and cloud) related feedbacks acting to mute the initial response.

## 3.2 Methods

### 3.2.1 AMOC Calculation

The AMOC is defined as the maximum stream function ($\psi$) below 500 m at 28°N in the Atlantic Ocean. It is calculated by integrating the northward sea water velocity ($vo$) with depth, $z$, along the western ($x_w$) to the eastern boundaries ($x_e$) of the Atlantic Ocean:

$$\psi(z) = \int_z^0 \int_{x_w}^{x_e} vo(x, z')dxdz'. \tag{3.1}$$

The AMOC percent change is estimated from the least-squares regression slope ($r_s$) of the non-normalized AMOC time series using: $100 \times \frac{r_s \times N}{AMOC(N=1)}$, where $N$ is the number of years (e.g., 30 for 1990-2020) and $AMOC(N = 1)$ is the initial AMOC strength (e.g., in 1990 for 1990-2020). The quoted AMOC percent change uncertainties are estimated as the standard error, defined as $\frac{\sigma}{\sqrt{n_m}}$, where $\sigma$ represents the standard deviation across each model mean AMOC percent change and $n_m$ is the number of models.

Following prior work, we estimate an inferred AMOC as the subpolar North Atlantic (45-60°N and 0-50°W) minus the Northern Hemisphere (0-60°N and 0-360°) surface temperature anomaly, scaled by 2.3 Sv K$^{-1}$ [85]. Our inferred AMOC conclusions are qualitatively the same with alternative scalings [12], since we apply the same scaling to both observations and CMIP6.

### 3.2.2 SDF Calculation

The surface density flux (SDF) indicates the loss or gain of density (buoyancy) of the ocean surface due to thermal (radiation, sensible and latent heat) and haline (sea-ice

melting/freezing, brine rejection, precipitation minus evaporation) exchanges [99, 87]. An increase in subpolar North Atlantic SDF is associated with strengthening of the AMOC; a decrease in SDF is associated with weakening of the AMOC. Surface density flux is define as:

$$SDF = -\alpha \frac{SHF}{c_p} - \rho(0, SST)\beta \frac{SFWF \times SSS}{1 - SSS}, \tag{3.2}$$

where $c_p$, SST, and SSS are the specific heat capacity and sea surface temperature and salinity, respectively; $\alpha$ and $\beta$ are thermal expansion and haline contraction coefficients; and $\rho(0, SST)$ is the density of freshwater with a salinity of zero and the temperature of SST. SHF represents the net surface heat flux into ocean (positive downward), which is estimated as a sum of shortwave (SW) and longwave (LW) radiation, sensible (SHFLX) and latent (LHFLX) heat fluxes, and heat fluxes from sea ice melting and other minor sources. SFWF represents net surface freshwater flux into ocean (positive downward) and is estimated as precipitation + runoff + ice melting – evaporation. The first term $-\alpha \frac{SHF}{c_p}$ represents the thermal contribution (TSDF); the second term $-\rho(0, SST)\beta \frac{SFWF \times SSS}{1 - SSS}$ represents the haline contribution (HSDF) to the density flux.

### 3.2.3 OHC Calculation

The ocean heat content (OHC) is estimated from the ocean potential temperature for each model vertical level. It is derived by spatially integrating over the North Atlantic (0-60°N; 7.5-75°W) upper-ocean (0-700 m) [?, e.g.,]]Zhang13, and then multiplying by reference values for sea water density ($\rho$) and specific heat capacity ($C$) of 1025 kg m$^{-3}$ and 3985 J kg$^{-1}$ K$^{-1}$, respectively [100]. Ocean heat content is calculated for each vertical level

according to the following equation:

$$\Phi_z = \sum_{i,j} \rho C \theta_{i,j,z} V_{i,j,z},$$ (3.3)

where $\Phi_z$ is the ocean heat content for model vertical level, $z$; $\theta$ is the potential temperature at that vertical level; $V$ is the grid cell volume; and $i, j$ are the latitudes and longitudes that cover the North Atlantic. Equation (3.3) is subsequently integrated throughout the upper ocean (0-700 m) to get the North Atlantic upper ocean heat content, with units of Joules.

Observed OHC data comes from NOAA National Centers for Environmental Information (NCEI). This observed upper-ocean heat content is derived from a yearly averaged dataset of objectively analyzed ocean temperature anomalies since 1955 [101].

### 3.2.4 Regression Analysis

We decompose the 1940-2020 North Atlantic climate response into an anthropogenic aerosol-forced component and a subsequent AMOC-related feedback. The forced response is obtained by regressing the negative of the net downward subpolar North Atlantic surface shortwave radiation time series (-1xSW), which is a proxy for changes in anthropogenic aerosols, onto various fields including for example sea surface temperature (SST), surface wind speed (SFWD), sea level pressure (PSL) etc. Spatially dependent regression coefficients (e.g., $\frac{\delta SST}{\delta(-1 \times SW)}$), or sensitivities, are based on a linear least-squares regression analysis applied to the CMIP6 ensemble mean annual mean. To isolate the AMOC-related feedback, we first remove variability associated with the aforementioned forced response. This is accomplished by multiplying the sensitivity (for a given field) by the negative of the net downward subpolar North Atlantic surface shortwave radiation time series, and sub-

tracting this quantity from each field. We then perform a subsequent regression, where the AMOC time series is regressed onto this new field. To convert this feedback field to the same units as the forcing field, we multiply the feedback field by the regression slope between the AMOC time series and the negative of the net downward subpolar North Atlantic surface shortwave radiation time series. This latter regression slope has a value of 0.32 $\frac{Sv}{W\ m^{-2}}$ and is significant at the 95% confidence level. Similar results are obtained if the subpolar North Atlantic aerosol optical thickness time series is used (as opposed to -1xSW, not shown).

### 3.2.5   Decomposition of seawater density

The seawater density ($\rho$) is diagnosed offline using the CMIP6 models simulated temperature, salinity and pressure [102]. The same algorithm is used to calculate both surface and sub-surface seawater density. The density trend is decomposed into thermal and haline components according to:

$$\delta\rho = (\overline{\frac{d\rho}{dT}})\delta T + (\overline{\frac{d\rho}{dS}})\delta S, \tag{3.4}$$

where $\delta$ represents the trend and $\overline{\frac{d\rho}{dT}}$ and $\overline{\frac{d\rho}{dS}}$ represents the climatological partial derivative of temperature and salinity with respect to density at each grid box. For the time series, $\delta$ represents the anomaly and $\overline{\frac{d\rho}{dT}}$ and $\overline{\frac{d\rho}{dS}}$ represents the 1900-2020 annual area mean over the subpolar North Atlantic. $T$ is temperature in  and $S$ is salinity in PSU. $\frac{d\rho}{dT}$ is the temperature derivative of density and $\frac{d\rho}{dS}$ is the salinity derivative of the density. The derivatives are calculated based on the formulas from Unesco's joint panel on oceanographic tables and standards.

### 3.2.6 Decomposition of Latent and Sensible Heat Fluxes

Using Monin-Obukhov similarity theory [103], latent (LHFLX) and sensible (SHFLX) heat fluxes can be decomposed into wind, moisture and temperature components according to:

$$LHFLX = -L_v \rho_{air} u_* q_* \tag{3.5}$$

$$SHFLX = -c_{p,air} \rho_{air} u_* \theta_*, \tag{3.6}$$

where $L_v$ is the latent heat of vaporization; $c_{p,air}$ is the specific heat capacity of air at constant pressure; $\rho_{air}$ is the surface air density; $u_*$ is the surface velocity scale (m s$^{-1}$, also referred to as the surface friction velocity); $q_*$ is the surface humidity scale (kg kg$^{-1}$); and $\theta_*$ is the surface temperature scale (K) [104, 105]. The velocity scale can be estimated from observed or simulated surface wind stress ($\tau$) as $u_* = \sqrt{\frac{|\tau|}{\rho_{air}}}$. Given values for latent and sensible heat fluxes and Eqs. (7-8), the moisture and temperature scales can be calculated as the residual. The validity of this methodology has been verified in MERRA2, where all fields (e.g., $u_*$, $q_*$, $\theta_*$, and the surface heat fluxes) are archived.

LHFLX and SHFLX trends can then be decomposed into wind, moisture and temperature components according to:

$$\delta LHFLX \approx -L_v \rho_{air} (\overline{u_*} \delta q_* + \overline{q_*} \delta u_*) \tag{3.7}$$

$$\delta SHFLX \approx -c_{p,air} \rho_{air} (\overline{u_*} \delta \theta_* + \overline{\theta_*} \delta u_*) \tag{3.8}$$

where $\delta$ represents the trend and $\overline{u_*}$, $\overline{q_*}$ and $\overline{\theta_*}$ represent climatological values at each grid box. $\rho_{air}$ is assumed to be constant for each grid box. Cross checking the estimated and actual LHFLX and SHFLX trends shows very close agreement. The first (second) term in

Eq. (9) represents the moisture (wind) component of $\delta$LHFLX. Similarly, the first (second) term in Eq. (10) represents the temperature (wind) component of $\delta$SHFLX.

### 3.2.7 Storm Track Activity

We define the extratropical cyclone (storm track) activity using temporal variance statistics, band-pass filtered using a 24-hour difference filer [106, 107]:

$$pp = \overline{[PSL(t+24hour) - PSL(t)]^2}, \tag{3.9}$$

where PSL is the daily sea level pressure and $pp$ is the 24-hour difference filtered variance of sea level pressure. The overbar corresponds to time averaging over each year.

### 3.2.8 Anthropogenic Aerosol Effective Radiative Forcing

Anthropogenic aerosol Effective Radiative Forcing (ERF) is estimated from the net top-of-the-atmosphere (TOA) radiative fluxes (the sum of net longwave and shortwave fluxes) using ~30 years of data from fixed sea surface temperature (SST) simulations [108]. More specifically, anthropogenic aerosol ERF is the net TOA radiative flux difference between piClim-Control and piClim-aer simulations (i.e., piClim-aer−piClim-Control). These two simulations are identical in all ways except piClim-Control features preindustrial aerosol and precursor gas emissions whereas piClim-aer features present-day (i.e., 2014) aerosol and precursor gas emissions. Twelve models are available for the aerosol ERF calculation. The transient anthropogenic aerosol ERF is calculated in a similar fashion, using the histSST and histSST-piAer experiments. Only three models are available for the transient aerosol ERF calculation, including MIROC6, UKESM1-0-LL, and NorESM2-LM.

### 3.2.9 Trend and Correlation Significance

Multi-model ensemble mean trends are based on the ensemble mean time series for each model. All time series are normalized by subtracting each model's long-term (1900-2020) climatology. Trends are based on a least-squares regression and significance is based on a standard $t$-test. The lead-lag correlation analysis is based on Pearson's correlation coefficient. The 95% confidence intervals for the lead-lag correlations are estimated by first transforming the Pearson's correlation coefficient ($r$) to a Fisher's z-score ($r_z$). The corresponding standard error of the $z$ distribution is defined as: $\sigma_z = \frac{1}{\sqrt{N-3}}$, where N is the number of years. The confidence interval under the transformed system is calculated as: $r_z \pm z_{\frac{\alpha}{2}} \times \sigma_z$, where $z_{\frac{\alpha}{2}}$ is calculated from the inverse of the cumulative distribution function and $\alpha$ is 0.05 for a 95% confidence interval. The transformation is reversed to obtain the lower and upper bounds of the confidence interval. Similar lead-lag correlation results are obtained under detrended and non-detrended time series.

## 3.3 Results

### 3.3.1 CMIP6 All Forcing Simulations

**Time Series**

Figure 3.1a shows the 1900-2020 CMIP6 all forcing ensemble mean normalized AMOC time series based on 24 models and 95 realizations (Figure B.1 shows the models and number of realizations used). Relatively small change occurs up to ~1950, after which the AMOC strengthens through ~1990, and then rapidly weakens through present-day

(2020). 83% (92%) of the models yield a positive (negative) AMOC trend from 1950-1990 (1990-2020). The 1950-1990 (1990-2020) ensemble mean strengthening (weakening) represents a 7.7±1.6 (−11.4±1.8) percent change (Figure B.1). These and all subsequent percent changes are relative to the beginning year of the time period (Methods Section). As these multi-decadal AMOC variations are based on the ensemble mean from a relatively large number of models, they are not due to internal climate variability. Instead, they are driven by external forcing.

We note that the non-normalized climatological AMOC strength varies considerably across CMIP6 models Table B.1). Over the present-day (2005-2018), the CMIP6 simulated AMOC ranges from 9.1 Sv (NESM3) to 30.3 Sv (NorESM2-MM). The corresponding multi-model mean AMOC strength and one-sigma uncertainty across models is 19.8 and 5.6 Sv, respectively (similar values are obtained over the entire 1900-2020 time period at 20.5 an 5.8 Sv). This is similar to but somewhat larger than that from the RAPID array at 17.5 Sv with an interannual standard deviation of 1.4 Sv. Re-estimating Figure 3.1a using only those models that simulate a climatological AMOC strength within one standard deviation of the RAPID observations (i.e., 16.1 to 18.9 Sv) yields 8 models. This model subset yields similar 1950-2020 results, including AMOC strengthening from ~1950-1990, followed by weakening (not shown).

The AMOC is related to surface density fluxes in the subpolar North Atlantic [87, 99], which modulate deepwater formation in the deep convection region. We define the subpolar North Atlantic region as 45-60°N and 0-50°W. We get similar results with alternate definitions of the subpolar North Atlantic region (e.g. 45-65°N and 10-60°W).

Figure 3.1 also includes the corresponding time series for the subpolar North Atlantic surface density flux (SDF), thermal (TSDF) and haline (HSDF) components. The AMOC and SDF exhibit similar multi-decadal variations, including an increase (decrease) from ~1950-1990 (1990-2020). Moreover, most of the temporal variation in SDF is consistent with TSDF. The haline SDF component (HSDF) is an order of magnitude weaker (Figure 3.1l). Multi-decadal variations in TSDF are largely consistent with latent (LHFLX) and sensible (SHFLX) heat fluxes (Figure 3.1 d-e). Similar temporal evolution also occurs for the subpolar North Atlantic surface wind (SFWD), which is a component of both LHFLX and SHFLX. Moreover, the sea level pressure gradient (dPSL) between Europe (30-45°N and 0-30°E) and the subpolar North Atlantic also exhibits similar temporal evolution consistent with surface wind variations (Figure 3.1 g-h), as does the subpolar North Atlantic extratropical cyclone (storm track) activity, March mixed layer depth (MMLD) and sea surface density (SSD) (Figure 3.1 i-k). We also mention here that the multi-decadal evolution of these variables is generally out of phase with the subpolar North Atlantic net downward surface shortwave radiation (SW; Figure 3.1f).

**Lead-Lag Correlations**

Figure 3.2 shows subpolar North Atlantic lead-lag Pearson correlations ($r$; Methods Section) based on the CMIP6 all forcing annual mean ensemble mean. The subpolar North Atlantic 550 nm aerosol optical thickness (AOT; a measure of the extinction of radiation by aerosols) and SW exhibit the maximum correlation at $-0.89$ with zero lag (Figure 3.2a). The subpolar North Atlantic net surface shortwave radiation and AMOC exhibit maximum correlation at $-0.84$, with SW leading the AMOC by ~12 years (Figure 3.2b). Similarly, the

subpolar North Atlantic net surface shortwave radiation and surface temperature are maximally correlated at 0.90 with zero lag (Figure 3.2c); and surface temperature and AMOC have maximum correlation of $-0.85$, with AMOC lagging by $\sim$12 years (Figure 3.2d). Thus, the subpolar North Atlantic net surface shortwave radiation and surface temperature are temporally in sync with aerosol optical thickness, all three of which lead the AMOC by $\sim$12 years.

Figure 3.2e shows that the Europe-subpolar North Atlantic sea level pressure gradient and the subpolar North Atlantic surface wind have a maximum (and significant) correlation of 0.69 at zero lag, which is consistent with geostrophy. Similarly, maximum correlations at zero lag occur between the surface density flux and the subpolar North Atlantic surface wind; Europe-subpolar North Atlantic sea level pressure gradient; March mixed layer depth; and sea surface density ($r = 0.86$; 0.58; 0.85; and 0.92 respectively; Figure 3.2 g,i,k,m). Similar results exist between both the sea level pressure gradient and surface wind and the thermal component of the surface density flux; the thermal component of the surface density flux also shows a maximum and significant correlation at zero lag with latent ($r = 0.79$) and sensible ($r = 0.94$) heat fluxes (not shown). Thus, the Europe-subpolar North Atlantic pressure gradient, as well as the subpolar North Atlantic surface wind and surface density and heat fluxes are temporally in sync and significantly correlated. These responses are similar to, and generally consistent with, North Atlantic Oscillation (NAO)-like variability driving air-sea fluxes [109]. However, correlations between these variables (i.e., SDF, SFWD, and dPSL) and the AMOC all have maximum (and significant) correlations at a 4-5 year lead, ranging from 0.66 to 0.78 (Figure 3.2 f,h,j). The 5-year

lead correlation where the subpolar North Atlantic surface density flux leads and AMOC is likely related to signal propagation via Kelvin waves/boundary currents, which impact the AMOC in the lower latitudes (e.g., 28°N) [110, 111, 112, 113, 114]. We note that the TSDF leads the AMOC by 5 years (r = 0.80), while the HSDF lags the AMOC by 7 years (r = 0.54). Similarly, $SSD$ (Figure 3.2n) and $SSD_T$ (not shown) lead the AMOC, but by 10 years (similar to SST) at r = 0.84 and 0.68, respectively; $SSD_S$ (not shown) lags AMOC by 4 years (r =0.68). Thus, both surface density flux and sea surface density decompositions suggest that the thermal component leads AMOC changes whereas the haline component lags AMOC changes. This will be elaborated upon in Section 3.1.3.

Figure 3.3 shows that the Europe-subpolar North Atlantic sea level pressure gradient and the subpolar North Atlantic surface wind, and surface density are significantly correlated with the net downward surface shortwave radiation and surface temperature, with the latter two variables leading by 6-8 years. For example, the maximum correlation between the subpolar North Atlantic surface temperature and the Europe-subpolar North Atlantic sea level pressure gradient is −0.67 at a 6-year lag (FFigure 3.3a). Similarly, the maximum correlation between the subpolar North Atlantic net downward surface shortwave radiation and the Europe-subpolar North Atlantic sea level pressure gradient is −0.65 at a 6-year lag (Figure 3.3b). Similar, but somewhat stronger correlations exist between the subpolar North Atlantic surface temperature/net downward surface shortwave radiation and both surface wind and surface density flux.

To summarize these results, the subpolar North Atlantic net downward surface shortwave radiation, surface temperature and aerosol optical thickness lead the Europe-

47

subpolar North Atlantic sea level pressure gradient and the subpolar North Atlantic surface wind, surface density and heat fluxes by 6-8 years (and the AMOC by 12 years); the Europe-subpolar North Atlantic sea level pressure gradient and the North Atlantic surface wind and surface density and heat fluxes lead the AMOC by 4-5 years. Although a correlation analysis does not show causation, this analysis suggests that AMOC multi-decadal variability is initiated by North Atlantic aerosol optical thickness perturbations to net surface shortwave radiation and surface temperature, which subsequently affect the sea level pressure gradient and surface wind−and via latent and sensible heat fluxes−the surface density flux through its thermal component.

CMIP6 all forcing simulations show that multi-decadal variability of the subpolar North Atlantic net surface shortwave radiation and aerosol topical thickness lead the AMOC, as well as the atmospheric circulation (e.g., dPSL and SFWD) and SDF (Figure 3.2 & Figure 3.3). This suggests changes in anthropogenic aerosols are important drivers of North Atlantic atmospheric circulation and AMOC multi-decadal variability. Beginning near the middle of the 20th century and lasting for several decades, global anthropogenic and chemically reactive gas emissions grew quickly, particularly from North America and Europe [115]. In the later parts of the 20th century, while emissions from Asia continued to grow, European and North American sulfate emissions declined as a result of emission control policies. Figure B.2−Figure B.3 show a consistent evolution of North Atlantic SW, AOT and anthropogenic aerosol effective radiative forcing (ERF; Methods Section). This includes relatively rapid increases in AOT and corresponding decreases in SW and ERF beginning in ∼1940 and lasting until ∼1980, and opposite changes afterwards (i.e., about

10 years prior to the AMOC responses; Figure 3.2 a-b), particularly over Europe.

**Regression Decomposition into Aerosol-Forced and AMOC Feedback Components**

To further investigate these AMOC relationships, we perform a regression analysis and decompose the 1940-2020 North Atlantic climate response into an anthropogenic aerosol-forced component and a subsequent AMOC-related feedback. The negative of the net downward subpolar North Atlantic surface shortwave radiation time series (-1xSW) is used as a proxy for changes in anthropogenic aerosols (Section 2.4). Figure 3.4a shows the expected negative sensitivity (regression slope) between SST and the subpolar North Atlantic -1xSW (i.e., an increase in aerosols is associated with SST cooling and vice versa). The SST field also exhibits a strong AMOC-related feedback that is of opposite sign to the aerosol-forced component in the subpolar North Atlantic (Figure 3.4b). That is, AMOC strengthening (weakening) leads to subpolar North Atlantic SST warming (cooling), which is consistent with increases (decreases) in poleward ocean heat transport (not shown). This SST-AMOC feedback sensitivity is consistent with expectations, including previously identified AMOC-related SST fingerprints [12]. In particular, Figure 3.4b is consistent with the notion (if you flip the sign) that AMOC weakening is related to cooling in the subpolar North Atlantic (i.e., the "warming" hole) due to decreases in poleward ocean heat transport, as well as warming in the Gulf Stream region which is associated with a northwards and closer-to-the-shore shift of the Gulf Stream. Although we acknowledge that this regression decomposition may not completely separate the forced signal from the feedback, Figure 3.4 shows very good results that are consistent with expectations, and support this approach.

Figure 3.5 shows corresponding regression maps for SDF and its various components. An increase in aerosols (i.e., -1xSW) is associated with an increase in SDF (Figure 3.5a) and vice versa (i.e., positive aerosol forced sensitivity). This is largely related to the thermal SDF component (TSDF; Figure 3.5b), with smaller contributions from the haline SDF component (HSDF; Figure 3.6c). In each case, the AMOC feedback (Figure 3.5 c-f) acts to reinforce these aerosol forced SDF changes, with TSDF again dominating over HSDF.

The three dominant components of TSDF, including surface shortwave radiation (SWSDF), latent heat (LSDF) and sensible heat (SSDF) all contribute to its positive aerosol forced sensitivity (Figure 3.5 g-i). A positive sensitivity for SWSDF is expected, as aerosols decrease surface shortwave radiation which would act to increase SDF. We suggest the positive aerosol-forced sensitivities for LSDF and SSDF are related to aerosol-induced changes in surface winds, and in particular, an aerosol-induced increase in subpolar North Atlantic surface winds which enhances LSDF and HSDF (as previously suggested). We acknowledge that the aerosol-forced LSDF sensitivities exhibit a complex spatial pattern, including opposite signed regressions outside the subpolar North Atlantic. Thus, increases in aerosols are associated with increases in subpolar North Atlantic SWSDF, LSDF and SSDF that all contribute to the increase in TSDF (and vice versa). We note that in the case of HSDF (although of secondary importance to TSDF), evaporation is the most important component for both the aerosol-forced sensitivities as well as the AMOC feedback (not shown).

Figure 3.5 j-l shows that the corresponding AMOC feedback in the subpolar North Atlantic has opposite sign for SWSDF but similar sign for LSDF and SSDF (the LSDF

feedback sensitivity is also larger in magnitude than the forced sensitivity). Thus, the AMOC feedback acts to oppose the aerosol forced TSDF change through SWSDF (as will be discussed below, this is related to clouds, which in turn is related to SSTs). Aerosol forced TSDF changes, however, are reinforced through LSDF and HSDF AMOC-related feedbacks, which in turn are likely associated with the aforementioned positive SST AMOC feedback–that is, an increase in the AMOC is associated with subpolar North Atlantic SST warming, which would be expected to increase sensible heat flux, as well as latent heat flux as moisture is tied to temperature. These latter two feedbacks dominate, since the AMOC feedback for TSDF exhibits positive sensitivity.

Figure 3.6 shows a similar regression analysis for several additional climate variables. The aerosol-forced surface wind (SFWD; Figure 3.6a) sensitivity shows positive values in the subpolar North Atlantic. This is consistent with the corresponding sea level pressure (PSL; Figure 3.6b) sensitivity, which shows negative values near the Icelandic low and positive values over the continents, including Europe (i.e., strengthened pressure gradient). This continental PSL regression is consistent with decreases (increases) in net surface shortwave radiation enhancing surface cooling (warming), leading to an increase (decrease) in sea level pressure over the continents. This altered pressure gradient, in turn, impacts the subpolar North Atlantic surface winds. An increase in aerosols is associated with strengthening of the North Atlantic sea level pressure gradient, which in turn leads to an increase in surface winds (and vice versa). Furthermore, in both cases, the AMOC feedback (Figure 3.6 d-e) exhibits weaker sensitivities as compared to the aerosol-forced sensitivities. This implies the PSL-SFWD response is largely aerosol-forced, and not AMOC related feedback.

Figure 3.6c shows corresponding regressions for total cloud cover (CLT). The aerosol forced response exhibits large positive sensitivities over most of the North Atlantic and surrounding continents, which is consistent with aerosols leading to an increase in cloud cover. This aerosol-forced increase in subpolar North Atlantic CLT would act to enhance SST cooling, and hence, AMOC strengthening via enhanced sea surface density (discussed next). Interestingly, the AMOC feedback (Figure 3.6f) shows opposite signed sensitivities in the subpolar North Atlantic. This is likely related to the AMOC feedback on SST (positive sensitivities; Figure 3.4b), which impacts lower-tropospheric stability and in turn, low clouds [116]. In other words, when the AMOC strengthens, the subpolar North Atlantic SST warms (e.g., due to enhanced poleward ocean heat transport), which reduces lower tropospheric stability and likely low cloud cover. In contrast, AMOC weakening and the associated subpolar North Atlantic SST cooling may increase lower tropospheric stability and in turn, low clouds. As discussed above (Figure 3.5), this negative CLT-AMOC feedback weakens the positive TSDF-AMOC feedback via SWSDF (but this negative feedback is not large enough to offset the LSDF and SSDF AMOC feedbacks on TSDF).

Finally, we perform a similar regression analysis on sea surface density ($SSD$), as well as its thermal ($SSD_T$) and haline ($SSD_S$) components (see Methods Section 2.5). As expected, a positive aerosol-forced sensitivity exists for $SSD$ (Figure 3.7a). This is largely consistent with $SSD_T$ (Figure 3.7b) as opposed to $SSD_S$ (Figure 3.7c), although $SSD_S$ also contributes near the eastern boundary of the North Atlantic. Averaged over the subpolar North Atlantic, $SSD_T$ yields an aerosol-forced sensitivity of 0.042 $\frac{kg/m^3}{W/m^2}$, whereas $SSD_S$ yields a corresponding sensitivity of 0.007 $\frac{kg/m^3}{W/m^2}$ (the sum of these two yield

0.049 $\frac{kg/m^3}{W/m^2}$, which is similar to but not exactly the same as the overall SSD sensitivity of 0.044 $\frac{kg/m^3}{W/m^2}$). We note that the relative importance of salinity to the aerosol-forced $SSD$ regression (especially along the eastern boundary of the North Atlantic) is more important than the haline component was for the corresponding SDF regression (Figure 3.5c).

The AMOC feedback shows similar (but weaker) positive sensitivities for $SSD$ (Figure 3.7d), particularly along the eastern boundary of the North Atlantic, and this is consistent with $SSD_S$ (Figure 3.7f). Averaged over the subpolar North Atlantic, $SSD$ yields an AMOC feedback sensitivity of 0.006 $\frac{kg/m^3}{W/m^2}$, which is entirely due to the $SSD_S$ feedback sensitivity of 0.012 $\frac{kg/m^3}{W/m^2}$. The $SSD_T$ feedback sensitivity is of opposite sign, with a subpolar North Atlantic sensitivity of -0.008 $\frac{kg/m^3}{W/m^2}$, implying the temperature component of SSD acts to weaken the overall $SSD$ AMOC feedback. This is consistent with the previously discussed AMOC feedback on SST (positive sensitivities; Figure 3.4b). Thus, the AMOC feedback acts to strengthen the $SSD$ response to aerosols, and this feedback is largely due to salinity. Moreover, this salinity AMOC feedback is larger in magnitude than the aerosol-forced salinity sensitivities (0.012 versus 0.007 $\frac{kg/m^3}{W/m^2}$, respectively). This AMOC-salinity feedback is, to some extent, consistent with recent studies that have associated AMOC weakening to reduced salinity divergence and an increase in salinity in the subtropical Atlantic [117]. More detailed analysis of how the salinity changes occur are warranted. We note that no clear signals are found in the poleward ocean salt transport in the Atlantic integrated over depth (in contrast to the corresponding poleward heat transport), as individual models yield contrasting responses (not shown). As salinity appears to be of secondary importance, particularly with respect to the aerosol-forced component.

In addition to the surface seawater density, we perform a similar regression analysis on subsurface seawater density ($SD$) and its thermal ($SD_T$) and haline ($SD_S$) components. For this analysis, a subset of 6 CMIP6 ALL models are used. $SD$, $SD_T$, and $SD_S$ averaged over both 0-200 m and 0-1000 m show similar aerosol-forced and AMOC feedback sensitivities as in $SSD$, $SSD_T$, and $SSD_S$ (not shown). We also perform a regression analysis on zonal mean Atlantic $SD$, $SD_T$, and $SD_S$ (Figure 3.7 g-l). $SD$ yields significant and positive aerosol-forced sensitivities in depth-latitude space that are consistent with the $SSD$ results. These aerosol-forced SD sensitivities are largely consistent with $SD_T$ as opposed to $SD_S$. In terms of the corresponding AMOC feedback, $SD$ sensitivities are again significant and positive throughout most of the high-latitude North Atlantic (although weaker than the aerosol-forced sensitivities), which again supports a positive AMOC feedback. Furthermore, this feedback is largely consistent with $SD_S$, as $SD_T$ acts in the opposite direction (i.e., negative sensitivities poleward of 45N). In summary, the subsurface seawater density sensitivities yield conclusions similar to those based on the sea surface density sensitivities.

The aerosol-forced $SSD$, $SSD_T$ and $SSD_S$ results are generally consistent with those based on SDF, TSDF and HSDF (Figure 3.5). However, there are some differences with the AMOC feedback, including opposite signed subpolar North Atlantic sensitivities between $SSD_T$ (negative) and TSDF (positive). The $SSD_S$ AMOC feedback is also larger than that based on HSDF (but of the same sign). These differences are likely related to heat and salt advection, which are not directly included in the SDF calculations, but are implicitly included in $SSD$ calculations. Overall, however, we arrive at a similar picture: an increase in aerosols increases SDF and $SSD$ in the subpolar North Atlantic, and this

is largely associated with the thermal component. The AMOC feedback acts to reinforce the SDF and $SSD$ aerosol-forced response. The thermal SDF AMOC feedback is most important for the SDF, with the haline SDF feedback of smaller importance. Based on $SSD$, the $SSD_T$ AMOC feedback is of the opposite sign, which acts to weaken the positive sensitivities between the AMOC and $SSD$. The $SSD_S$ feedback is most important for $SSD$, which is likely related to changes in salt advection that are not captured by HSDF. Although not shown, we also note that the aerosol-forced March mixed layer depth (MMLD) exhibits significant positive sensitivities in the subpolar North Atlantic (implying enhanced deep convection in response to aerosol forcing), and the corresponding MMLD-AMOC feedback also exhibits positive (but somewhat weaker) sensitivities, which again implies that the AMOC induces changes that positively feedback onto the AMOC (e.g., the aforementioned salinity contribution to $SSD_S$; and the latent and sensible heat flux contributions to TSDF.

**Spatial Trend Maps**

Figure 3.8 shows the 1990-2020 CMIP6 all forcing ensemble mean annual mean spatial trend map, and the corresponding model agreement on the sign of the trend, for the surface density flux and its thermal component. Consistent with Figure 3.1, SDF significantly decreases from 1990-2020 in the subpolar North Atlantic, with high (80-100%) model agreement (Figure 3.8 a,b). Most of this SDF decrease is driven by the thermal component (Figure 3.8 c,d). The haline component yields a weak decrease (Figure B.4). Moreover, decomposing the thermal SDF into its respective components shows that latent and sensible heat fluxes are the dominant drivers (Figure B.4). Consistently, the CMIP6 all forcing 1990-2020 ensemble mean surface wind trend−a component of latent and sensible

heat fluxes—shows significant reductions with high (80-100%) model agreement in the sub-polar North Atlantic. These surface wind trends are consistent with the corresponding PSL trends, including a weakened Europe-subpolar North Atlantic pressure gradient (Figure 3.8 e-h), as well as a decrease in subpolar North Atlantic extratropical cyclone (storm track) activity (Figure 3.8 i-j). Near opposite changes occur from 1950-1990 (Figure B.5). March mixed layer depth (MMLD) is used to investigate North Atlantic deep convection, which is associated to deep water formation and the strength of the AMOC [118]. Our results suggest a consistent response in March mixed layer depth (Figure B.6). 1990-2020 CMIP6 all forcing ensemble mean annual mean show a significant decrease in wintertime deep convection in the North Atlantic. During the 1950-1990 time period, the CMIP6 all forcing ensemble mean shows an increase in deep convection (but not as statistically significant as the 1990-2020 decrease). Similar trend patterns from reanalyses and observations also exist, including the subpolar North Atlantic sea level pressure, surface winds and latent and sensible heat fluxes (Figure B.7—Figure B.9). However, dissimilarities in magnitude exist, suggesting these responses are only partially externally forced.

**Decomposition of Latent/Sensible Heat Fluxes**

Using Monin-Obukhov similarity theory [103], latent and sensible heat fluxes can be further decomposed into wind, moisture and temperature components (Methods Section). Figure B.10—Figure B.11 shows the importance of wind changes to latent and sensible heat fluxes, and in turn, the thermal component of the SDF. Thus, our results suggest that strengthening (weakening) of the AMOC from ∼1950-1990 (1990-2020) is in part due to strengthening (weakening) of the surface winds in the subpolar North Atlantic (consistent

with the altered sea level pressure gradient), which in turn leads to increases (decreases) in surface density flux through increases (decreases) in surface latent and sensible heat fluxes.

### 3.3.2   CMIP6 Anthropogenic Aerosol Simulations

Figure 3.9a shows the 1900-2020 CMIP6 anthropogenic aerosol (AA) ensemble mean normalized AMOC time series based on 8 models and 43 realizations (Figure B.12 shows the models and number of realizations used). The evolution of the AMOC in CMIP6 AA simulations is similar to that in the corresponding all forcing simulations, in particular the strengthening from ∼1950 to 1990, and weakening afterwards. 88% (100%) of the models yield a positive (negative) AMOC trend from 1950-1990 (1990-2020). The 1950-1990 (1990-2020) ensemble mean strengthening (weakening) represents a 8.8±2.3 (−7.1±1.6) percent change (Figure B.12). Figure 3.9 also shows that from ∼1950-2020, surface density and heat fluxes, as well as the sea level pressure gradient, storm track activity, and surface wind follow a similar evolution as in the CMIP6 all forcing simulations. CMIP6 AA experiments also exhibit similar lead-lag relationships as in the CMIP6 all forcing simulations (not shown).

We note that fewer CMIP6 AA (as compared to all forcing) models are available. Similar CMIP6 all forcing results as described above are generally obtained when the same 8 CMIP6 models in common between CMIP6 all forcing and CMIP6 AA are used. For example, the 1990-2020 AMOC weakening based on the original 24 all forcing models yields a percent change of −11.4±1.8. Using the 8 model subset yields similar results, at −12.9±2.4 (Figure B.13). The 8 model CMIP6 all forcing subset yields somewhat weaker 1950-1990 AMOC strengthening (6.1±1.6 versus 4.7±1.4 percent change; Figure B.13).

The close correspondence between the CMIP6 AA and all forcing ensemble mean

AMOC time series since ∼1950 again suggests anthropogenic aerosols are driving much of the response. This is further supported by looking at the CMIP6 greenhouse gas (GHG) and natural forcing ensemble mean AMOC time series. The CMIP6 GHG ensemble mean annual mean AMOC shows long-term weakening, whereas natural forcing yields negligible long-term change (Figure B.14−Figure B.15). Over 1990-2020, the CMIP6 GHG AMOC weakening represents a −6.7±0.8 percent change, which is comparable to the AMOC weakening under CMIP6 AA (−7.1±1.6; Figure B.12). Thus, ∼1950-1990 AMOC strengthening in CMIP6 all forcing simulations is largely controlled by anthropogenic aerosols; from 1990-2020, both anthropogenic aerosols and GHGs contribute to AMOC weakening.

Using this common set of models, we also look at the CMIP6 Atlantic meridional streamfunction in depth-latitude space, which is calculated from zonally integrated meridional velocity field (Figure 3.13). The 1990-2020 CMIP6 AMOC weakening is significant throughout most of the North Atlantic in all three forcing scenarios–ALL, AA and GHG– with GHG weakening larger than that due to AA. In contrast, the 1950-1990 time period features CMIP6 ALL and AA strengthening that is again significant throughout most of the North Atlantic; CMIP6 GHG forcing yields the opposite response (and weaker than the CMIP6 AA strengthening). Thus, the 1950-1990 AMOC strengthening in CMIP6 ALL is entirely dominated by AA, with GHGs acting to mute this strengthening. The 1990-2020 AMOC weakening in CMIP6 ALL is due to both GHGs and AAs, with GHGs driving a larger response. To measure the overall 1950-2020 impact of AA versus GHGs on the AMOC, we calculate the difference of the trends (1990-2020 minus 1950-1990). Figure 3.13 (j-l) shows that this trend "shift" is largely due to aerosols, as opposed to GHGs.

Figure 3.10 shows the 1990-2020 CMIP6 AA ensemble mean annual mean trends and the model agreement on the sign of the trend for the surface density flux and its thermal component, as well as the atmospheric variables (e.g., SFWD). Responses are again very similar to the corresponding CMIP6 all forcing simulations, further supporting the importance of anthropogenic aerosols. The CMIP6 AA ensemble mean shows a decrease in SDF that is largely driven by TSDF (Figure 3.10 a-d), weakening of the Europe-subpolar North Atlantic pressure gradient (Figure 3.10 e,f), a corresponding decrease in the subpolar North Atlantic surface wind (Figure 3.10 g-h), a decrease in the subpolar North Atlantic storm track activity. Also consistent with CMIP6 all forcing simulations are near opposite changes in these variables from 1950-1990 (Figure B.16; see also Figure B.7−Figure B.8). The CMIP6 AA ensemble mean March mixed layer depth responses are similar to the corresponding CMIP6 all forcing simulations (Figure B.6), with MMLD increases (decreases) in the subpolar North Atlantic from 1950-1990 (1990-2020). And furthermore, Figure B.10−Figure B.11 shows the importance of wind changes to latent and sensible heat fluxes, and in turn, the thermal component of the SDF in CMIP6 AA simulations. The AMOC strengthening in response to increasing anthropogenic aerosol forcing is consistent with prior studies [21, 22, 23, 24, 25, 26, 17]. However, unlike [26] who used the HadGEM2-ES model, we do not find strong evidence that increased salinification is the dominant driving factor.

## 3.4 Discussion

Models will continue to have uncertainties, including those relevant to the AMOC and North Atlantic climate. These include biases in the mean state, as well as their repre-

sentation of the strength and depth of the AMOC (e.g., Table B.1) and ocean freshwater transport [119, 120, 121, 19, 122]. For example, in many CMIP3/5 models, the AMOC imports freshwater into the Atlantic, in opposition to observations, likely resulting in an artificially stable AMOC [99]. Models also lack realistic melting of the Greenland ice sheet and the corresponding freshening of the North Atlantic [123].

The CMIP6 AMOC response may be too sensitive to anthropogenic aerosol forcing [90] and CMIP6 models may also overestimate aerosol indirect effects [?]. However, anthropogenic aerosol ERF estimates are consistent between CMIP6 and recent observational estimates, with 90% confidence intervals of $-1.5$ to $-0.6$ and $-2.0$ to $-0.4$ W m$^{-2}$, respectively [124, 125]. It is also notable that the aerosol ERF in CMIP5 models, with a 90% confidence interval of $-1.8$ to $-0.2$ W m$^{-2}$ [126], is similar to that (but with a larger range) in CMIP6 models. The mean and standard deviation of the anthropogenic aerosol ERF in 12 CMIP6 models (Table B.2) are $-0.98$ and $0.24$ W m$^{-2}$, respectively. The corresponding values in 18 CMIP5 models are $-1.0$ and $0.44$ W m$^{-2}$, respectively [126]. In contrast, [97] argues the larger 1850-1985 AMOC weakening in CMIP6 models, relative to CMIP5, is due to stronger anthropogenic aerosol forcing in CMIP6. There, they show a robust relationship between AMOC strength and a proxy for aerosol forcing—the interhemispheric difference of net top-of-the-atmosphere shortwave radiation. A model's transient climate response (TCR)–the surface temperature warming around the time of $CO_2$ doubling in a 1% per year $CO_2$ increase simulation–may also be important, and CMIP6 models yield a relatively large range of 1.3 to 3.0°C [127]. Although we find the expected positive inter-model relationship between 1900-1985 AMOC changes and TCR, the correlation is only 0.28 (p = 0.18).

There is some evidence that the magnitude of the AMOC trends in CMIP6 models is related to a model's anthropogenic aerosol ERF−particularly over Europe−which again supports the importance of changes in European aerosols. The correlation (over model means and using the 12 models with aerosol ERF; Table B.2) between the global mean aerosol ERF and AMOC trend yields the expected negative (positive) correlation from 1950-1990 (1990-2020), implying models with a larger global mean aerosol ERF yield larger AMOC strengthening (weakening). However, these correlations are not significant at the 95% confidence level, at −0.29 for 1950-1990 and 0.11 for 1990-2020. Somewhat larger, but still non-significant, correlations between European aerosol ERF and AMOC trends exist at −0.38 for 1950-1990 and 0.26 for 1990-2020. Ideally, the transient aerosol ERF should be used for this calculation, but this quantity is only available for 3 models. Similar conclusions are also obtained if we divide the CMIP6 models into two groups, one with a larger (absolute value) global mean anthropogenic aerosol ERF (ERF$_{HI}$; 7 model mean aerosol ERF of −1.17 W m$^{-2}$), and the other with a smaller global mean aerosol ERF (ERF$_{LO}$; 5 model mean aerosol ERF of −0.72 W m$^{-2}$). From 1950-1990, ERF$_{HI}$ (ERF$_{LO}$) models yield AMOC strengthening that represents a 7.4±1.4 (4.7±2.1) percent change. From 1990-2020, ERF$_{HI}$ (ERF$_{LO}$) models yield AMOC weakening that represents a −14.6±1.6 (−11.3±2.6) percent change (Table B.2).

The CMIP6 all forcing ensemble mean reproduces the observed Northern Hemisphere (0-60°N; 0-360°E) and the North Atlantic (0-60°N; 0-75°W) surface temperature evolution, particularly from 1950-2020 (Figure 3.11 a,b). However, discrepancies exist in the evolution of the subpolar North Atlantic surface temperature, most notably from ∼1970-

1990 (Figure 3.11c). This may not be surprising, since this also overlaps with the 1950-1990 time period, when evolution of the CMIP6 AMOC differs from inferred (i.e., surface temperature based) AMOC observations (Methods Section). Consistently, similar discrepancies exist between inferred AMOC trends in CMIP6 and observations (Figure 3.11d). The CMIP6 multi-model mean shows significant 1950-1990 strengthening (0.03 Sv year$^{-1}$) whereas observations show significant weakening ($-0.03$ Sv year$^{-1}$). The sign of the inferred AMOC trend after 1990 is in better agreement between CMIP6 ($-0.07$ Sv year$^{-1}$) and observations ($-0.02$ Sv year$^{-1}$), where both show weakening. However, the observed 1990-2020 AMOC trends are weaker than the CMIP6 multi-model mean and not-significant (at the 95% confidence interval), due in part to a brief strengthening in the early to mid-1990s.

Although these CMIP6 inferred AMOC trends are comparable to the actual CMIP6 AMOC trends, there are also notable differences. The CMIP6 all forcing ensemble mean 1950-1990 inferred AMOC trend is weaker than the actual CMIP6 AMOC trend (25% weaker, 0.03 versus 0.04 Sv year$^{-1}$). And moreover, there is less model agreement for the CMIP6 1950-1990 inferred AMOC strengthening, as compared to the actual AMOC (62 versus 83%, respectively). CMIP6 1990-2020 inferred and actual AMOC trends are both significant and similar in magnitude ($-0.07$ versus $-0.08$ Sv year$^{-1}$, respectively), as is the model agreement (92% for both).

Thus, CMIP6 and observations both suggest AMOC weakening after 1990. However, disagreement exists for 1950-1990, where inferred AMOC observations show significant weakening, but CMIP6 shows significant strengthening. Moreover, disagreement exists between the CMIP6 1950-1990 actual and inferred AMOC trend, with the inferred AMOC

yielding weaker and less robust strengthening. These discrepancies warrant further clarification, but they suggest that the 1950-1990 inferred AMOC in observations may yield excessive weakening (relative to the actual AMOC). A recent study suggests that the North Atlantic cooling is not only related to a weaker AMOC, but also northward heat transport. So, inferred AMOC estimates from sea surface temperature are prone to error, and they are not solely a measure of the AMOC [128]. We do note, however, that multiple proxy observations, support AMOC weakening during 1950-1990 [129]. In addition to these AMOC differences, the CMIP6 multi-model mean also underestimates the magnitude of observed increase in North Atlantic upper ocean heat content (Figure 3.11e).

The inferred AMOC weakening from 1950-1990 (and even from 1930-1990) may have a significant contribution from internal (i.e., unforced) climate variability. Figure 3.12a shows CMIP6 AMOC trends for each individual model realization for four time periods, 1950-1990, 1990-2020, 1930-2020, as well as 1930-1990. Also included are the corresponding inferred AMOC trends based on surface temperature observations. Some individual model realizations are able to reproduce the inferred AMOC trends, including the 1950-1990 weakening, as well as weakening over the longer 1930-1990 time period. 8.6% (8 of 92) and 13% (12 of 92) of the model realizations yield 1950-1990 and 1930-1990 AMOC weakening that falls within the observational uncertainty (which includes 5 and 12 different models, respectively). For the inferred AMOC strengthening from 1990-2020, 41.3% (38 of 92) of the model realizations are within the observational uncertainty (which includes 13 models).

There are 5 realizations from two different CMIP6 models (CanESM5 and IPSL-CM6A-LR) that yield AMOC trends that fall within the observational uncertainty for all

four time periods. Figure 3.12b shows that the corresponding ensemble mean AMOC for these 5 realizations better resembles the inferred AMOC evolution since 1900, including strengthening during the first few decades, followed by a prolonged weakening, a relatively brief strengthening, and then subsequent weakening. Furthermore, these 5 realizations also better simulate the increase in North Atlantic upper ocean heat content (Figure 3.12c). Differences remain, however, including a ~decade delay in the initial AMOC weakening (inferred weakening begins in the 1930s but these models show weakening commences in the 1940s), as well as an earlier (and brief) strengthening during the late-20th century (inferred strengthening begins in the 1990s but these models show weakening commences in the 1980s). We note that both of these models underestimate the climatological AMOC strength relative to RAPID observations (17.5±1-standard deviation of 1.4 Sv versus 11.6 Sv for IPSL-CM6A-LR and 13.1 Sv for CanESM5; Table B.1). Although no significant AMOC differences were found between the $ERF_{HI}$ and $ERF_{LOW}$ subsets, it is interesting to note that IPSL-CM6A-LR and CanESM5 have 2 of the lowest 5 CMIP6 anthropogenic aerosol ERFs (Table B.2). It is also possible that the reason why these two models stand out is because they have a relatively large number of realizations (11 and 10, respectively; Figure B.1), which simply increases the chances of a simulated AMOC evolution comparable to that observed.

CMIP6 models yield consistent multi-decadal AMOC variability, including strengthening from ~1950-1990, followed by weakening from 1990-2020. These AMOC variations are initiated by North Atlantic aerosol optical thickness perturbations to net surface short-wave radiation and surface temperature (i.e., sea surface density), which in turn affect the

sea level pressure gradient and surface wind–and via latent and sensible heat fluxes–the sea surface density flux through its thermal component. AMOC-related feedbacks act to reinforce this aerosol-forced AMOC response, largely due to changes in sea surface salinity and its corresponding impacts on sea surface density, with temperature (and cloud) related feedbacks acting to mute the initial response. Anthropogenic aerosol forcing alone reproduces the bulk of the multi-decadal AMOC responses. Moreover, reanalyses and observations yield similar patterns of the North Atlantic atmospheric circulation response, suggesting part of this signal is externally forced. However, other aspects of the CMIP6 AMOC response are at odds with observations. This includes the inferred ∼1950-1990 weakening of the AMOC based on surface temperature observations [85], when the CMIP6 multi-model mean yields strengthening. Moreover, the CMIP6 multi-model mean underestimates the observed increase in North Atlantic ocean heat content since ∼1955. Some of these discrepancies could be due to model shortcomings, such as excessive anthropogenic aerosol forcing [97]. A handful of CMIP6 realizations (5 of 92) yield AMOC evolution since 1900 similar to the indirect observations, implying the inferred AMOC weakening from 1950-1990 (and even from 1930-1990) may have a significant contribution from internal (i.e., unforced) climate variability.

Consistent with the recent decreases in anthropogenic aerosol emissions, nearly all of the future emission scenarios (Shared Socio-economic Pathways, SSPs) [130] yield large reductions in future anthropogenic aerosol emissions, with global sulfate emissions projected to decrease by up to 80% by 2050. Thus, anthropogenic aerosol emissions, including those around the North Atlantic, will likely continue to rapidly decline over the next few decades.

Our results suggest that the continued decrease in anthropogenic aerosol emissions that accompany efforts to reduce air pollution will reinforce GHG-induced AMOC weakening over the next few decades−with the caveat that internal AMOC variability will also be important.
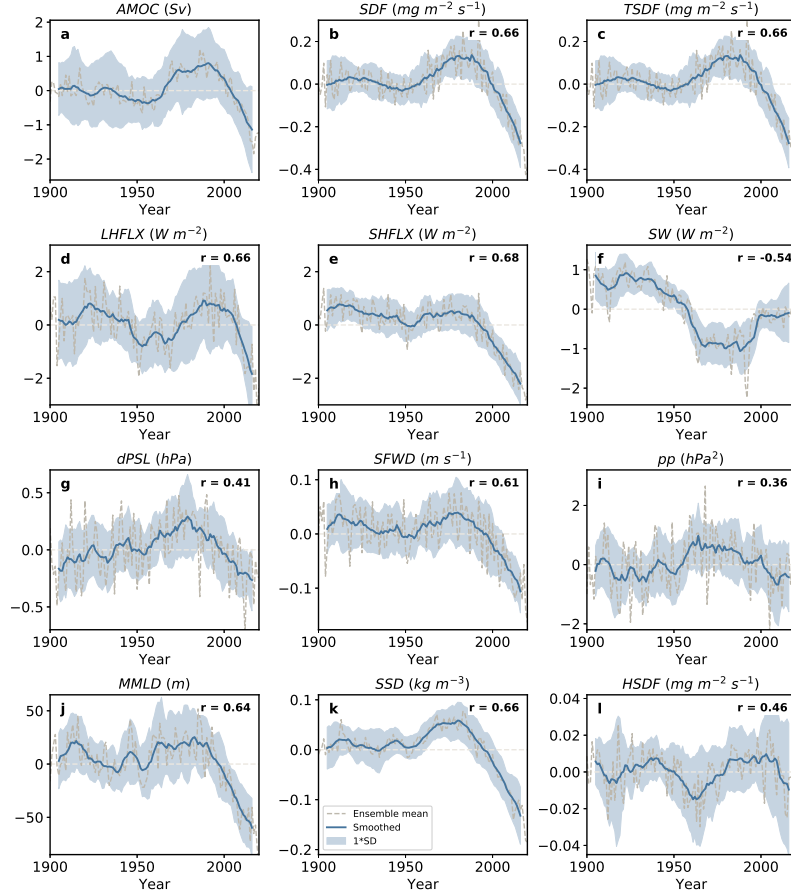
Figure 3.1: **1900-2020 ensemble mean annual mean all forcing Coupled Model Intercomparison Project phase 6 normalized time series.** (a) Atlantic Meridional Overturning Circulation (AMOC) and subpolar North Atlantic (b) surface density flux (SDF); (c) thermal SDF (TSDF); (d) latent heat flux (LHFLX); (e) sensible heat flux (SHFLX); (f) net downward surface shortwave radiation (SW); (g) sea level pressure gradient (dPSL); (h) surface wind (SFWD); (i) storm track activity (pp); (j) March mixed layer depth (MMLD); (k) sea surface density (SSD); and (l) haline SDF (HSDF). The 1950-2020 correlation coefficient (r) between the time series of each variable and the AMOC is shown in the upper right-hand side of each panel, all of which are significant at the 95% confidence level. SDF, TSDF and HSDF units are $\frac{mg}{m^2-s}$. SHFLX, LHFLX and SW units are W m$^{-2}$. dPSL units are hPa, pp units are hPa$^2$, MMLD units are m, SSD units are kg m$^{-3}$ and SFWD units are m s$^{-1}$. The subpolar North Atlantic region is defined as 45-60°N and 0-50°W. dPSL is the Europe-subpolar North Atlantic PSL gradient defined as 30-45°N and 0-30°E minus 45-60°N and 0-50°W.
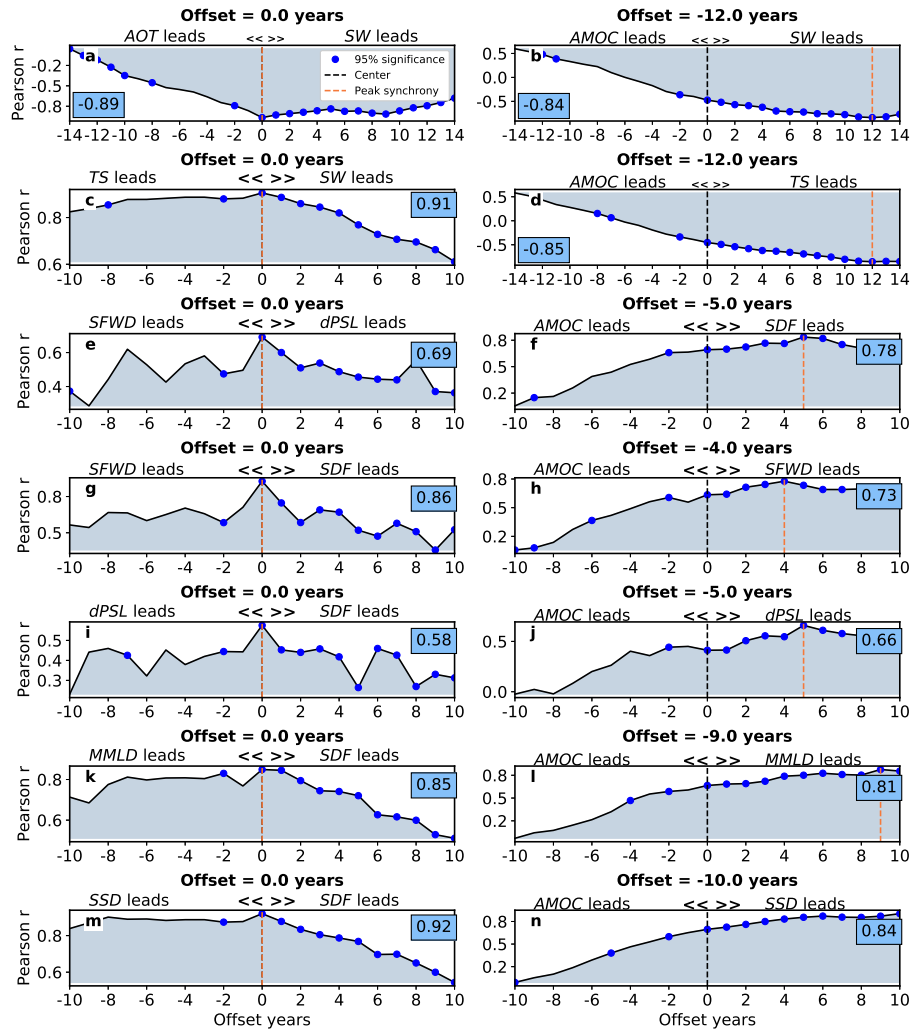
Figure 3.2: **1950-2020 lead-lag AMOC correlations based on the ensemble mean annual mean all forcing Coupled Model Intercomparison Project phase 6.** (Left panels) The subpolar North Atlantic (a) aerosol optical thickness at 550 nm (AOT) versus net downward surface shortwave radiation (SW); (c) surface temperature (TS) versus SW; (e) surface wind (SFWD) versus sea level pressure gradient (dPSL); (g) SFWD versus surface density flux (SDF); (i) dPSL versus SDF; (k) March mixed layer depth (MMLD) versus SDF; and (m) sea surface density (SSD) versus SDF. (Right panels) The Atlantic Meridional Overturning Circulation (AMOC) versus the subpolar North Atlantic (b) SW; (d) TS; (f) SDF; (h) SFWD; (j) dPSL; (l) MMLD; and (n) SSD. The maximum correlation is denoted by text in the blue box. Blue filled circles denote correlations that are significant at the 95% confidence level. The corresponding offset in years is denoted by the vertical dashed red line.
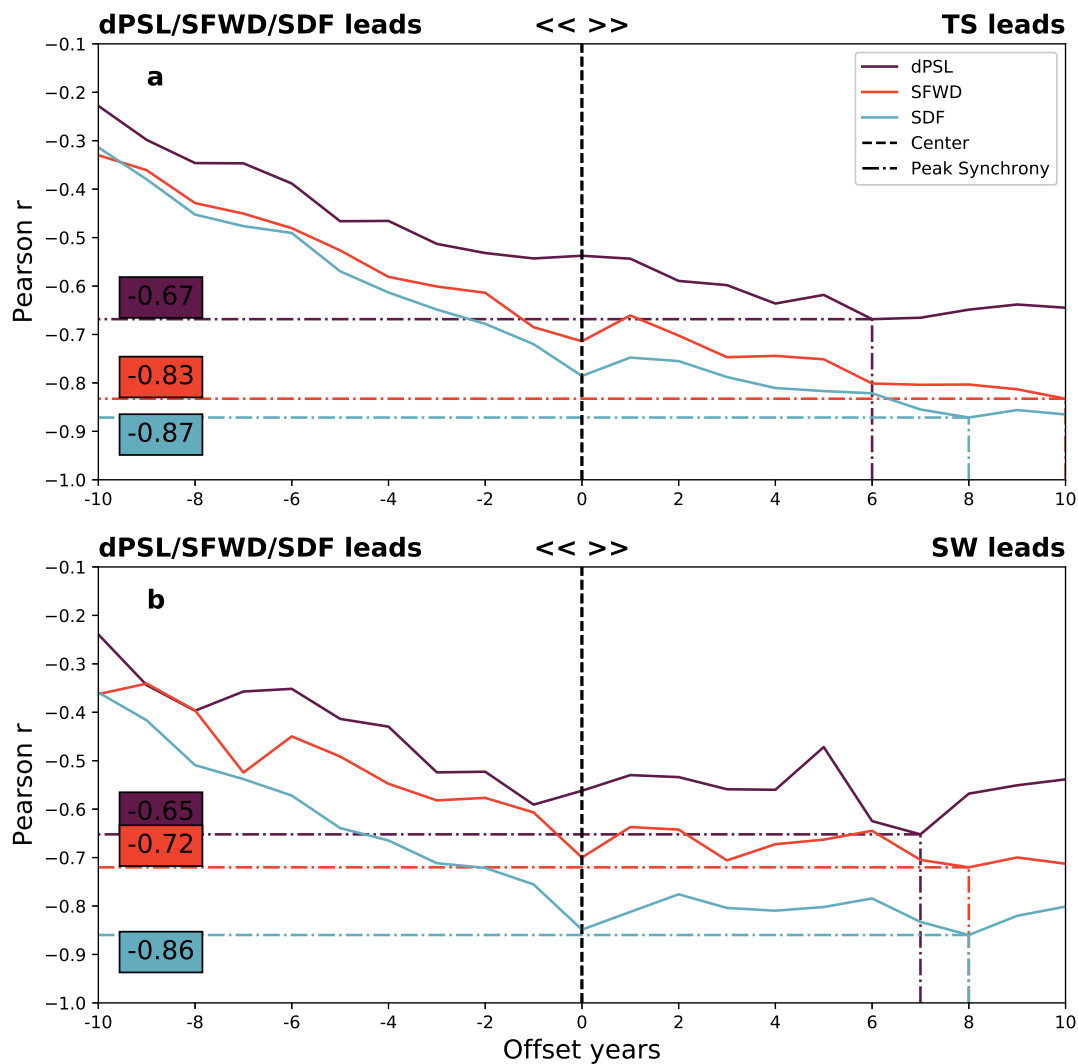
Figure 3.3: **1950-2020 lead-lag atmospheric circulation correlations based on the ensemble mean annual mean all forcing Coupled Model Intercomparison Project phase 6.** The subpolar North Atlantic (a) surface temperature (TS) and (b) net downward surface shortwave radiation (SW) versus sea level pressure gradient (dPSL; purple); surface wind (SFWD; red); and surface density flux (SDF; cyan). The maximum correlations are denoted by the horizontal dashed lines and as text in the color-coded boxes, all of which are significant at the 95% confidence level. The corresponding offsets in years are denoted by the vertical dashed color-coded lines.

Figure 3.4: **1940-2020 ensemble mean annual mean CMIP6 all forcing regression analysis.** Decomposition of sea surface temperature (SST) into (a) aerosol forced and (b) AMOC feedback components. The forced response is obtained by regressing the subpolar North Atlantic -1xSW time series (a proxy for anthropogenic aerosols) onto each field. The AMOC-related feedback is obtained by removing the variability associated with the forced response, and then regressing the AMOC time series onto this new field. The feedback field is converted to the same units as the aerosol-forced field by multiplying the feedback field by the regression slope between the AMOC and -1xSW subpolar North Atlantic time series $\frac{\delta(AMOC)}{\delta(-1\times SW)} = 0.32 \frac{Sv}{W\ m^{-2}}$, significant at the 95% confidence level). The units for the SST regression maps are K/W m$^{-2}$. Symbols denote regression significance at the 95% confidence level.

Figure 3.5: **1940-2020 ensemble mean annual mean CMIP6 all forcing regression analysis.** Decomposition of (a,d) surface density flux (SDF); (b,e) thermal component of SDF (TSDF); (c,f) haline component of SDF (HSDF); (g,j) net surface shortwave radiation driven SDF (SWSDF); (h,k) latent heat flux driven SDF (LSDF); and (i,l) sensible heat flux driven SDF (SSDF) into (a-c,g-i) aerosol forced and (d-f,j-l) AMOC feedback components. The forced response is obtained by regressing the subpolar North Atlantic -1xSW time series (a proxy for anthropogenic aerosols) onto each field. The AMOC-related feedback is obtained by removing the variability associated with the forced response, and then regressing the AMOC time series onto this new field. The feedback field is converted to the same units as the aerosol-forced field by multiplying the feedback field by the regression slope between the AMOC and -1xSW subpolar North Atlantic time series $\frac{\delta(AMOC)}{\delta(-1 \times SW)} = 0.32$ $\frac{Sv}{W\ m^{-2}}$, significant at the 95% confidence level). The units for all SDF regression maps are $mg\ m^{-2}\ s^{-1}/W\ m^{-2}$. Symbols denote regression significance at the 95% confidence level.
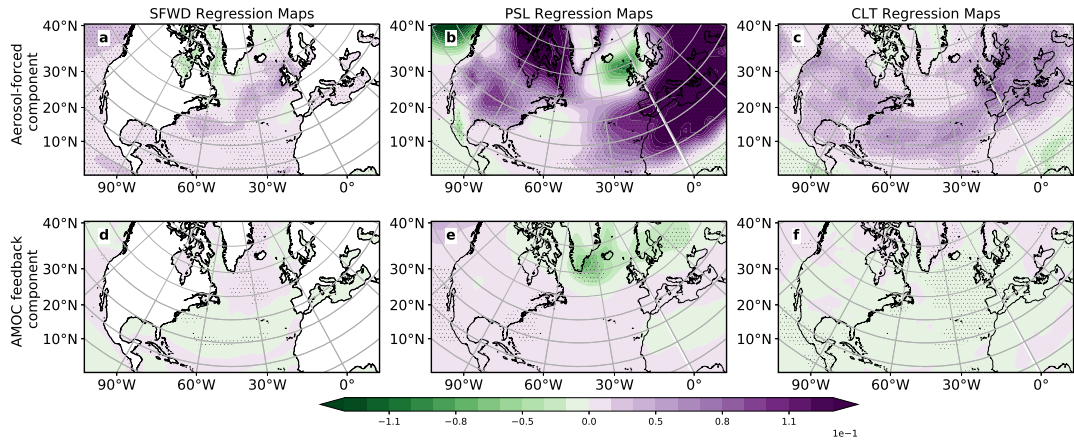
Figure 3.6: **1940-2020 ensemble mean annual mean CMIP6 all forcing regression analysis.** Decomposition of (a,d) surface wind speed (SFWD); (b,e) sea level pressure (PSL); and (c,f) total cloud cover (CLT) into (top panels) aerosol forced and (bottom panels) AMOC feedback components. The forced response is obtained by regressing the subpolar North Atlantic -1xSW time series (a proxy for anthropogenic aerosols) onto each field. The AMOC-related feedback is obtained by removing the variability associated with the forced response, and then regressing the AMOC time series onto this new field. The feedback field is converted to the same units as the aerosol-forced field by multiplying the feedback field by the regression slope between the AMOC and -1xSW subpolar North Atlantic time series $\frac{\delta(AMOC)}{\delta(-1 \times SW)} = 0.32 \ \frac{Sv}{W \ m^{-2}}$, significant at the 95% confidence level). The units for SFWD, PSL and CLT regression maps are m s$^{-1}$/W m$^{-2}$, hPa/W m$^{-2}$ and fraction/W m$^{-2}$ respectively. Symbols denote regression significance at the 95% confidence level.
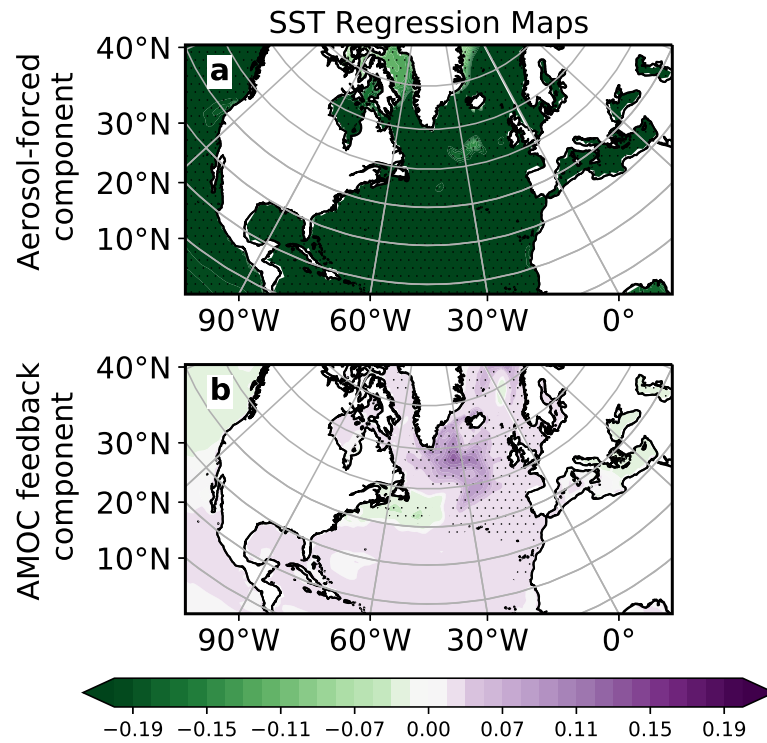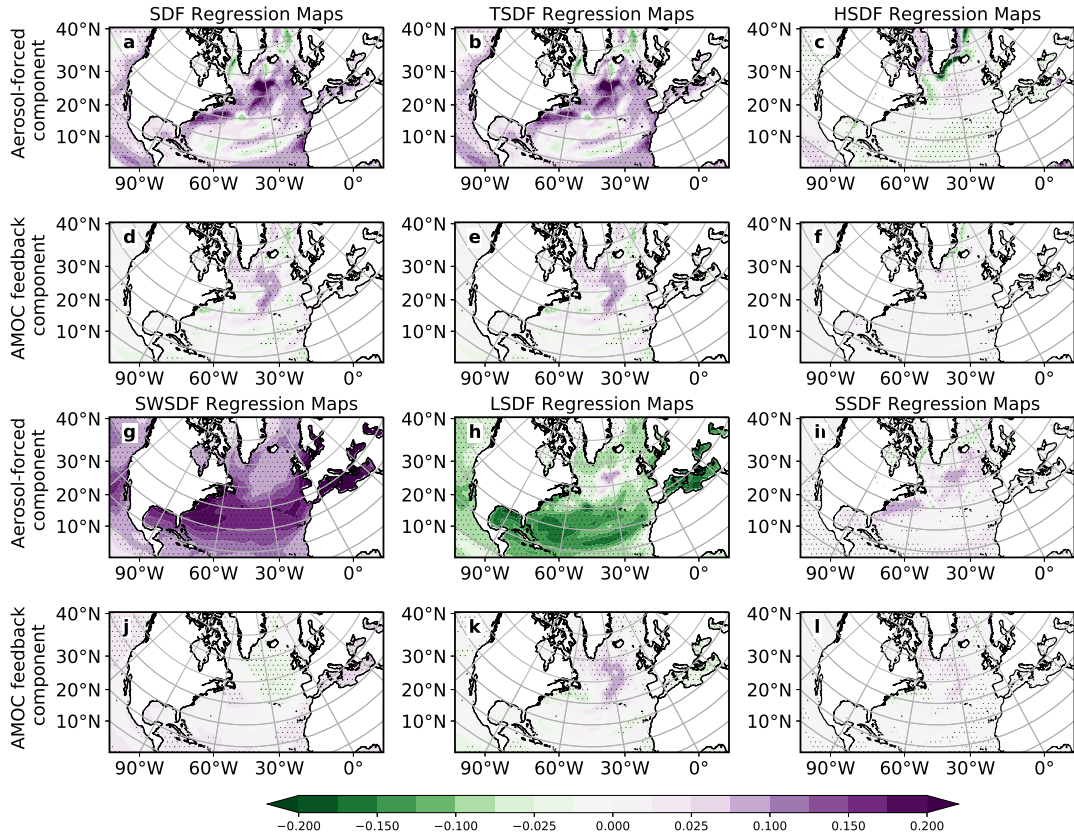
72
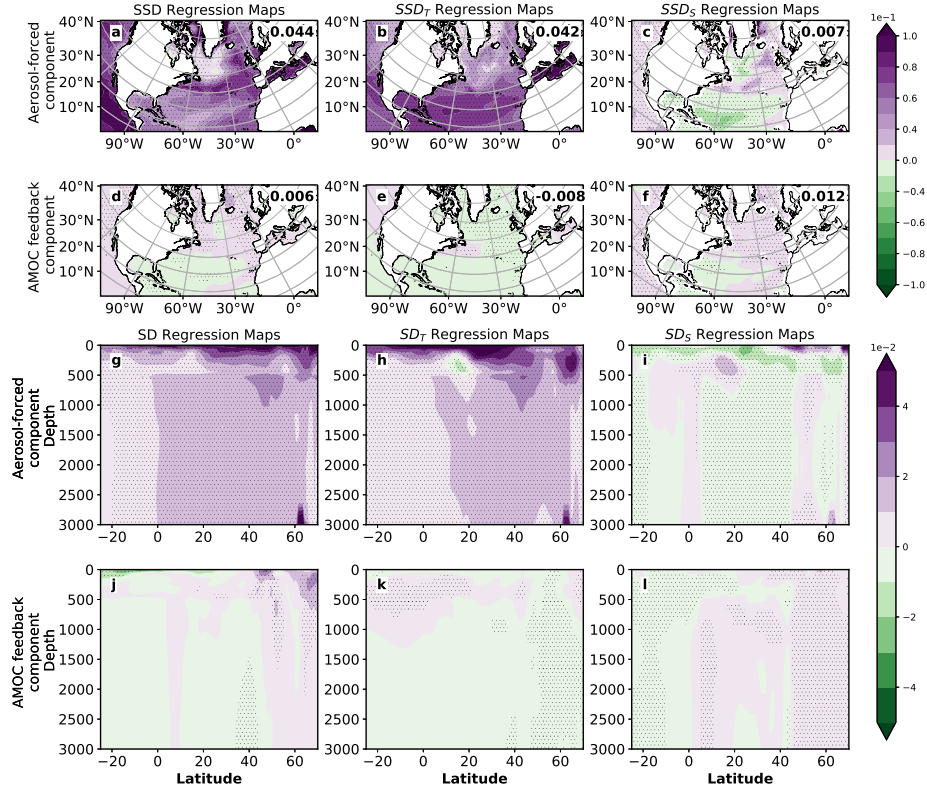
Figure 3.7: **1940-2020 ensemble mean annual mean CMIP6 all forcing regression analysis.** Decomposition of (a,d) sea surface density ($SSD$); (b,e) thermal component of SSD ($SSD_T$); (c,f) haline component of SSD ($SSD_S$); (g,j) zonal mean Atlantic seawater density ($SD$); (h,k) thermal component of SD ($SD_T$); and (i,l) haline component of SD ($SD_S$) into (a-c,g-i) aerosol forced and (d-f,j-l) AMOC feedback components. The forced response is obtained by regressing the subpolar North Atlantic -1xSW time series (a proxy for anthropogenic aerosols) onto each field. The AMOC-related feedback is obtained by removing the variability associated with the forced response, and then regressing the AMOC time series onto this new field. The feedback field is converted to the same units as the aerosol-forced field by multiplying the feedback field by the regression slope between the AMOC and -1xSW subpolar North Atlantic time series $\frac{\delta(AMOC)}{\delta(-1\times SW)} = 0.32 \frac{Sv}{W\ m^{-2}}$, significant at the 95% confidence level). Numbers in the top right of each panel show the subpolar North Atlantic averaged regression coefficients (in units of kg m$^{-3}$/W m$^{-2}$). The units for all SSD regression maps are kg m$^{-3}$/W m$^{-2}$. Symbols denote regression significance at the 95% confidence level. For the SD analysis (panels g-l), a subset of 6 CMIP6 ALL models are used, including BCC-CSM2-MR, CESM2, CNRM-CM6-1, CanESM5, HadGEM3-GC31-LL, and IPSL-CM6A-LR.

73
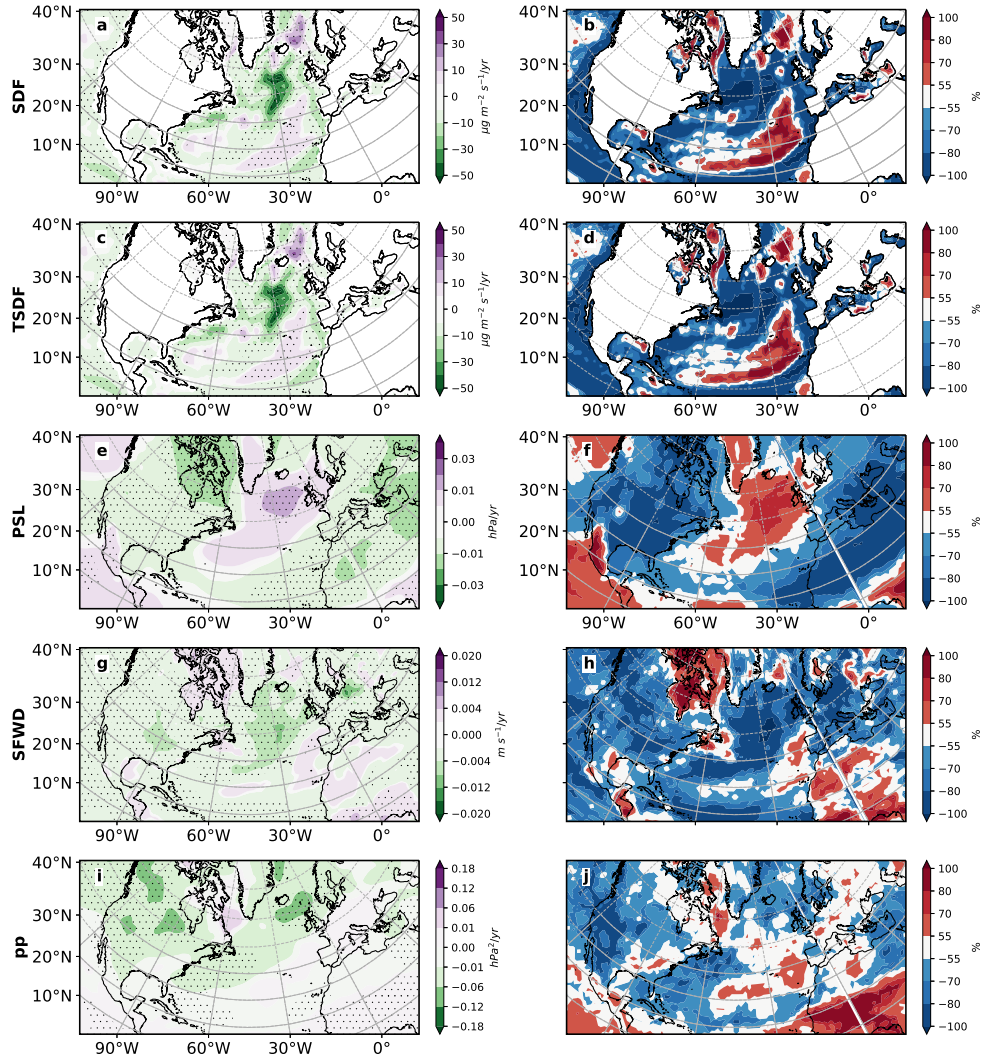
Figure 3.8: **1990-2020 annual mean all forcing Coupled Model Intercomparison Project phase 6 ensemble mean trends and model agreement on the sign of the trend.** (a-b) surface density flux (SDF); (c-d) thermal SDF (TSDF); (e-f) sea level pressure (PSL); (g-h) surface winds (SFWD); and (i-j) storm track activity (pp). Left panels show the ensemble mean trend; right panels show model agreement on the sign of the trend for each model's ensemble mean. Symbols in left panels designate trend significance at the 95% confidence level based on a $t$-test. SDF and TSDF trend units are $\frac{\mu g}{m^2 - s}$ year$^{-1}$. PSL, pp, and SFWD trend units are hPa year$^{-1}$, hPa$^2$ year$^{-1}$, and m s$^{-1}$ year$^{-1}$, respectively. Trend realization agreement units are %. Red (blue) colors indicate model agreement on a positive (negative) trend.

Figure 3.9: **1900-2020 ensemble mean annual mean anthropogenic aerosol forcing Coupled Model Intercomparison Project phase 6 normalized time series.** (a) Atlantic Meridional Overturning Circulation (AMOC) and subpolar North Atlantic (b) surface density flux (SDF); (c) thermal SDF (TSDF); (d) latent heat flux (LHFLX); (e) sensible heat flux (SHFLX); (f) net downward surface shortwave radiation (SW); (g) sea level pressure gradient (dPSL); (h) surface wind (SFWD); (i) storm track activity (pp); (j) March mixed layer depth (MMLD); (k) sea surface density (SSD); and (l) haline SDF (HSDF). 1950-2020 correlation coefficient against AMOC is shown at the upper right-hand side of each panel, all of which are significant at the 95% confidence level except for those correlations marked with an asterisk. SDF, TSDF and HSDF units are $\frac{mg}{m^2-s}$. SHFLX, LHFLX and SW units are W m$^{-2}$. dPSL units are hPa, pp units are hPa$^2$, MMLD units are m, SSD units are kg m$^{-3}$ and SFWD units are m s$^{-1}$. The subpolar North Atlantic region is defined as 45-60°N and 0-50°W. dPSL is the Europe-subpolar North Atlantic PSL gradient defined as 30-45°N and 0-30°E minus 45-60°N and 0-50°W.

75
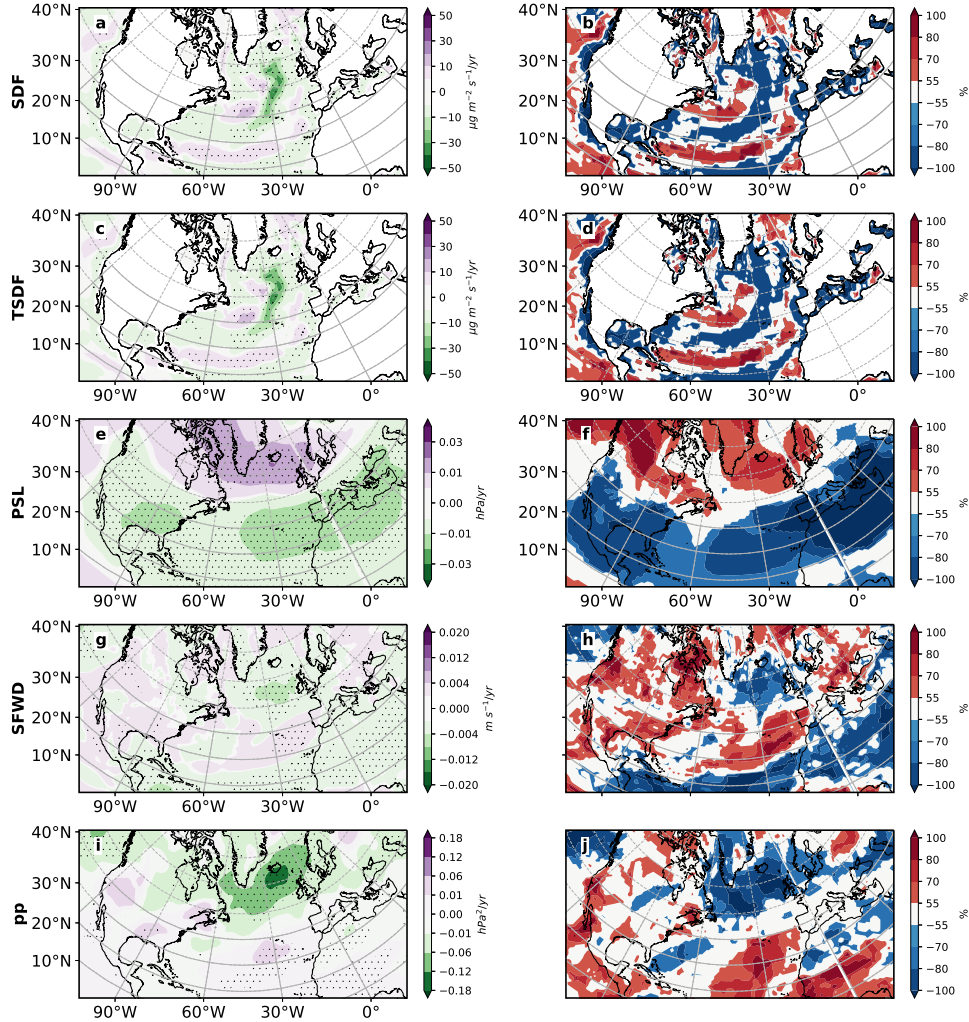
Figure 3.10: **1990-2020 annual mean anthropogenic aerosol forcing Coupled Model Intercomparison Project phase 6 ensemble mean trends and model agreement on the sign of the trend.** (a-b) surface density flux (SDF); (c-d) thermal SDF (TSDF); (e-f) sea level pressure (PSL); (g-h) surface winds (SFWD); and (i-j) storm track activity (pp). Left panels show the ensemble mean trend; right panels show model agreement on the sign of the trend for each model's ensemble mean. Symbols in left panels designate trend significance at the 95% confidence level based on a $t$-test. SDF and TSDF trend units are $\frac{\mu g}{m^2 - s}$ year$^{-1}$. PSL, pp, and SFWD trend units are hPa year$^{-1}$, hPa$^2$ year$^{-1}$, and m s$^{-1}$ year$^{-1}$, respectively. Trend realization agreement units are %. Red (blue) colors indicate model agreement on a positive (negative) trend.

Figure 3.11: **Ensemble mean annual mean all forcing Coupled Model Intercomparison Project phase 6 and observed surface temperature, inferred AMOC and ocean heat content time series.** 1900-2020 (a) Northern Hemisphere (0-60°N; 0-360°E); (b) North Atlantic (0-60°N; 7.5-75°W); and (c) subpolar North Atlantic (45-60°N; 0-50°W) surface temperature (TS); (d) inferred AMOC; and (e) 1955-2014 North Atlantic upper-ocean (0-700 m) ocean heat content (OHC). Results are shown for the CMIP6 all forcing ensemble mean (solid black) and observations (ending in 2019), including NASA GISS (GISTEMPv4; dashed light blue), NOAA (NOAAGlobalTempv4.0.1; dashed orange) and CRU (CRUTEM4; dashed green) for TS. Also included in panel (d) is the April 2004-July 2019 directly observed AMOC from the RAPID array (dash-dot dark blue). Light blue shading shows the CMIP6 inter-model standard deviation. AMOC units are Sv; OHC units are $10^{22}$ Joules. Inferred AMOC trends for 1950-1990 are **−0.03**, **−0.03**, **−0.03** and **0.03** Sv year$^{-1}$ for GISS, NOAA, CRU and CMIP6, respectively. The corresponding 1990-2020 inferred AMOC trends are −0.02, −0.02, −0.02 and −**0.07** Sv year$^{-1}$. The CMIP6 all forcing actual AMOC trends are **0.04** and −**0.08** Sv year$^{-1}$ for 1950-1990 and 1990-2020, respectively. Bold trends are significant at the 95% confidence level.
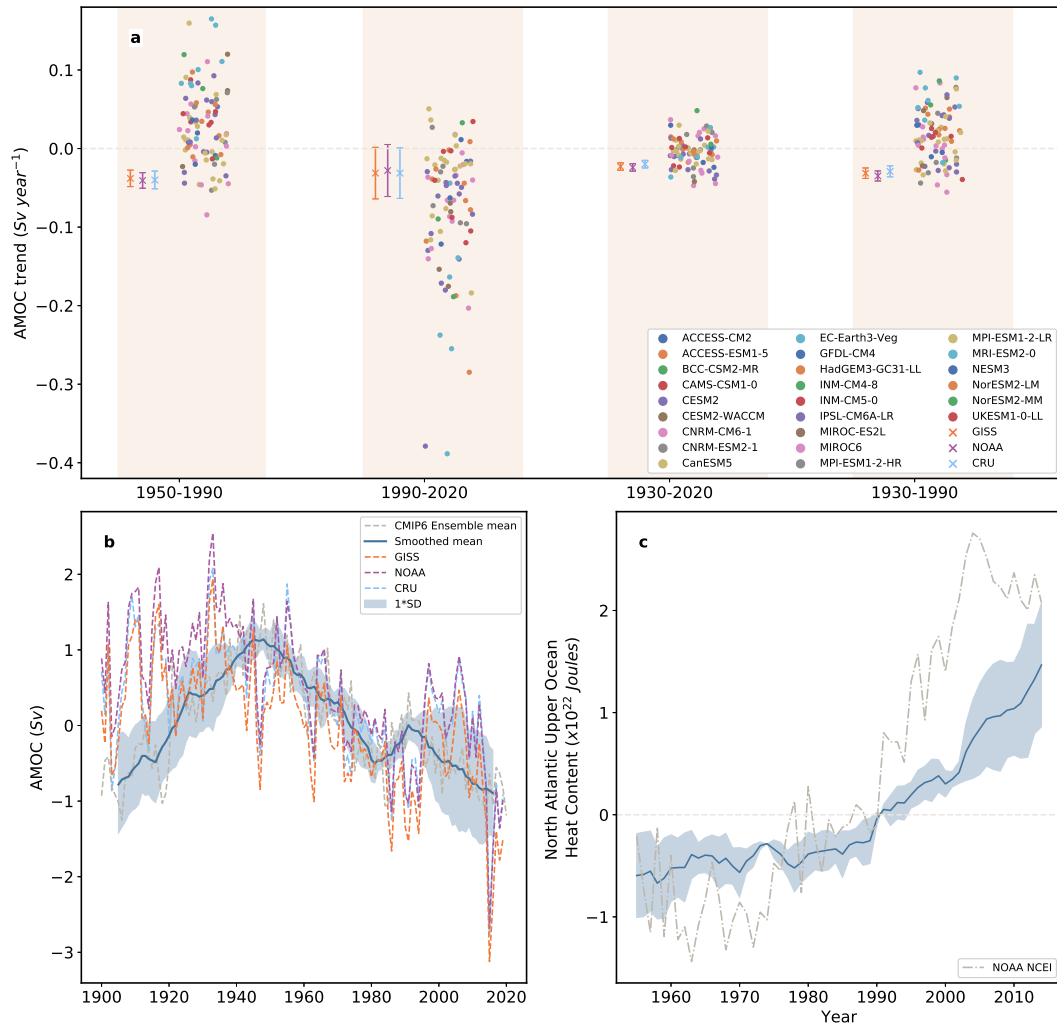
Figure 3.12: **Coupled Model Intercomparison Project phase 6 all forcing annual mean AMOC and OHC for individual model realizations.** (a) AMOC trends [Sv year$^{-1}$] are shown for four time periods, including 1950-1990, 1990-2020, 1930-2020, and 1930-1990. Each individual model realization is shown with a symbol. Also included (X's) are the corresponding inferred AMOC trends (ending in 2019) based on surface temperature observations. Error bars on inferred AMOC trends represent the 95% confidence interval of the trend. (b) Ensemble mean annual mean normalized AMOC [Sv] time series (gray dashed) and 10-year running mean (solid blue line) based on the two CMIP6 models (CanESM5 and IPSL-CM6A-LR; 5 realizations in total) that yield AMOC trends that fall within the observational uncertainty for all four time periods. (c) As in (b), but for the 1955-2014 North Atlantic upper-ocean (0-700 m) ocean heat content (OHC). Also included in (c) is the corresponding observed OHC (gray dashed) from NOAA National Centers for Environmental Information (NOAA NCEI) .

78
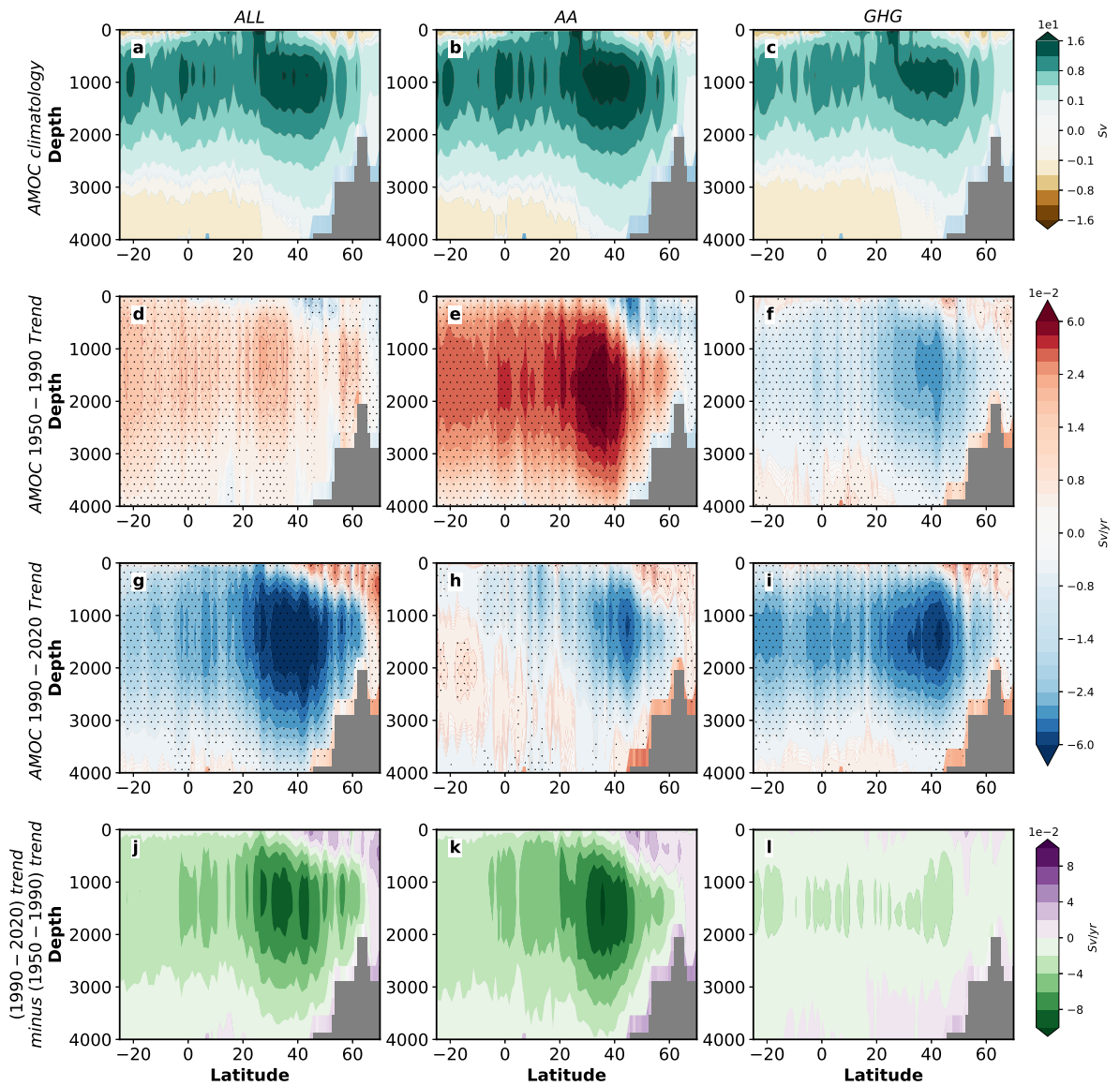
Figure 3.13: **1950-2020 ensemble mean annual mean Coupled Model Intercomparison Project phase 6 Atlantic meridional streamfunction in depth-latitude space.** Zonal mean (a-c) 1950-1990 climatology; (d-f) 1950-1990 trends; (g-i) 1990-2020 trends; and (j-l) trend "shift" (1990-2020 trend minus 1950-1990 trend) for (left column) all forcing; (middle column) anthropogenic aerosol forcing; and (right column) GHG forcing. Symbols designate trend significance at 95% confidence level based on a t-test. Streamfunction trend units are in Sv/year.

# Chapter 4

# The impact of air quality control efforts on the Atlantic Meridional Overturning Circulation

## Abstract

Observations indicate the Atlantic Meridional Overturning Circulation (AMOC)—a fundamental component of the ocean's global conveyor belt—is weakening. Although causes remain uncertain, AMOC weakening is consistent with increasing greenhouse gases (GHGs). Recent studies also suggest that anthropogenic emissions associated with air pollution, such as aerosols, can significantly impact the AMOC. Here, we use four state-of-the-art chemistry-climate models to quantify how efforts to improve future air quality via near-term climate forcer (NTCF) mitigation will impact the AMOC. Non-methane NTCF (NM-

NTCF) mitigation, which includes aerosols, ozone and precursor gases alone, induces end-of-century AMOC weakening by up to 10%. However, all-NTCF mitigation, which also includes methane reductions, offsets this weakening. The AMOC responses, particularly under all-NTCF mitigation, are best explained by the cumulative North Atlantic radiative forcing. Thus, efforts to improve air quality must also target methane and other GHGs to avoid additional climate change, including weakening of the world's major ocean circulation system.

## 4.1    Introduction

The Atlantic Meridional Overturning Circulation (AMOC) is the key circulation system of the Atlantic Ocean, significantly impacting climate by transporting large amounts of heat, carbon and freshwater[8, 9]. Indirect evidence, including sea surface temperature (SST) fingerprints and coral-based proxies, show that the AMOC has weakened throughout this past century[85, 12]. Although these indirect methods have been questioned[131, 132], additional observational indicators including a "salinity pile-up" in the South Atlantic[133] support AMOC weakening, including a possible transition from a strong to a weak mode[134]. Such AMOC weakening is a robust feature of GHG-forced climate model simulations, thereby suggesting a likely cause[135, 14, 17, 136, 77, 137]. Several studies have also shown the importance of anthropogenic aerosols (AAs) to multi-decadal AMOC variations[138, 21, 26, 24, 25, 17]. Coupled Model Intercomparison Project phase 6 (CMIP6)[39] models show 20th century AMOC strengthening up to ∼1985, which was attributed to the build up of AAs; and AMOC weakening from ∼1985-2020, consistent with

reduced AA emissions in Europe and the US[97, 139].

Atmospheric aerosols, as well as chemically reactive gases such as ozone and methane ($CH_4$), are commonly referred to as near-term (or short-term) climate forcers (NTCFs) as their impact occurs within the first decade after emission[32]. NTCF mitigation has received considerable attention, as aerosols and ozone are sources of air pollution[140], which is associated with adverse human health and ecosystem impacts[141, 142, 143]. Although air quality is improved in response to removal of AAs, relatively large near-term increases in surface temperature and precipitation also occur[144, 145, 146]. The importance of reducing methane emissions to simultaneously mitigate climate change and improve air quality has also been investigated[147, 148, 149, 150]. Simulations from the the Aerosol and Chemistry Model Intercomparison Project (AerChemMIP)[38] show that non-methane NTCF (NMNTCF; aerosols, ozone and precursor gases) mitigation leads to mid- and end-of-the-century warming and wetting; NTCF reductions that also include methane (all-NTCF), however, compensate for this warming by mid-century and more than offset this warming by end-of-the-century[151, 152]. No studies, however, have investigated the impacts of future NTCF mitigation on the AMOC. Here, we analyze a suite of 2015-2100 air quality (AQ) control simulations from four AerChemMIP models, which include interactive representations of tropospheric aerosols and atmospheric chemistry, allowing for the quantification of chemistry-climate interactions.

## 4.2 Results

### 4.2.1 AMOC Response in Air Quality Control Experiments

Under the three AQ control experiments (section 4.4; Table C.1), AerChemMIP models yield large and significant 21st century AMOC weakening−but with relatively large inter-model spread on the magnitude of the weakening (Figure C.1 & Figure C.2). This AMOC weakening is consistent with the large increase in $CO_2$ in these experiments, and several prior studies that have shown GHGs drive AMOC weakening[153, 135, 14, 17, 136, 77, 137]. In particular, $CO_2$ increases by more than 100% by end-of-the-century in all three experiments, from ∼400 ppm in 2015 to more than 850 ppm by 2100 (Figure C.3). Strong non-$CH_4$ AQ control, which features large increases in both $CO_2$ and $CH_4$ (and decreases in aerosol and ozone precursor gases), yields the largest AMOC weakening, with a multi-model mean (MMM) decrease of 63% and an inter-model range of −45 to −78%. Based on raw AMOC trends, the MMM weakening is −0.139 Sv year$^{-1}$, with a range of −0.103 to −0.195 Sv year$^{-1}$. Strong AQ control, which is also driven by the large increase in $CO_2$, but reductions in $CH_4$, aerosol and ozone precursor gases, yields the weakest MMM AMOC decrease at 53%, ranging from −45 to −65% (−0.112 Sv year $^{-1}$ with a range of −0.084 to −0.136 Sv year$^{-1}$).

GISS-E2-1-G yields the largest AMOC weakening for weak AQ and strong non-$CH_4$ AQ control. This suggests that the GISS-E2-1-G AMOC is more sensitive to $CO_2$ than the other models, which is consistent with a prior study[137]. There, under abrupt quadrupling of $CO_2$, GISS-E2-1-G is a clear outlier, yielding by far the largest and swiftest AMOC weakening (−15 Sv in ∼25 years, compared to the MMM of less than −5 Sv).

Although the reasons are unclear, models with a stronger climatological AMOC—such as GISS-E2-1-G—tend to have larger AMOC weakening under increasing $CO_2$[14, 136, 137]. Based on our four models, GISS-E2-1-G has the largest climatological (2005-2018) AMOC at 22.5 Sv. The other models yield 17.0, 17.2 and 18.6 Sv for UKESM1-0-LL, EC-Earth3-AerChem and MRI-ESM2-0, respectively.

### 4.2.2 AMOC Response Under NTCF Mitigation

Figure 4.1 shows 21st century depth-latitude trends in the Atlantic meridional stream function (section 4.4) based on NTCF mitigation (i.e., differences between AQ control experiments; section 4.4; Table C.1), including NMNTCF, all-NTCF, and $CH_4$ mitigation for each model. Under NMNTCF mitigation, significant weakening of this circulation occurs throughout the North Atlantic in all models. In contrast, $CH_4$ mitigation yields significant strengthening of the circulation. Under all-NTCF mitigation, most models yield relatively weak, non-significant changes—the exception is GISS-E2-1-G where the circulation significantly strengthens.

The 2015-2100 AMOC (section 4.4) time series and trends for the three NTCF signals are included in Figure 4.2. We note that internal climate variability remains in most of the model's time series, particularly GISS-E2-1-G and EC-Earth3-AerChem. Three realizations (one in the case of EC-Earth3-AerChem) is not sufficient to remove all of the internal climate variability. Nonetheless, NMNTCF mitigation leads to significant AMOC weakening in all four models ranging from 5-10% ($-0.013$ to $-0.021$ Sv year$^{-1}$) by end-of-the-century (Figure 4.2 a,d). Although the trend uncertainty bars overlap, UKESM1-0-LL yields the largest AMOC strengthening at 10±3% and GISS-E2-1-G yields the smallest

AMOC strengthening at 5±4%. This result is consistent with modeling studies that have linked anthropogenic aerosols to AMOC perturbations, including AMOC weakening from ~1990-2020 in response to aerosol and precursor gas emission reductions[97, 139].

In contrast to NMNTCF mitigation, all-NTCF mitigation yields AMOC trends that range from −2% to 19% (−0.004 to 0.048 Sv year$^{-1}$) and three of the four models yield negligible AMOC change (Figure 4.2 b,e). GISS-E2-1-G is the lone model that yields a significant AMOC trend under all-NTCF mitigation−a strengthening of nearly 19% by end-of-the-century, which dominates the all-NTCF MMM signal. Removing GISS-E2-1-G from the MMM results in a non-significant three model mean AMOC trend of 0.01%. Methane mitigation alone (Figure 4.2 c,f) yields significant AMOC strengthening in all four models by end-of-the-century, ranging from 6-24% (0.011 to 0.061 Sv year$^{-1}$). Similar to all-NTCF mitigation, GISS-E2-1-G yields the largest response (24% strengthening), suggesting this model's AMOC response is very sensitive to not only $CO_2$ (e.g., Section 2.1), but also methane. Thus, these results show that inclusion of $CH_4$ reductions (i.e., all-NTCF mitigation) offsets AMOC weakening under NMNTCF mitigation.

### 4.2.3 Mechanisms of AMOC Response

Little consensus exists on the mechanisms responsible for low-frequency AMOC variability. Several studies, however, show the importance of changes in deep convection due to both thermal- and haline-induced buoyancy anomalies in the subpolar North Atlantic (SPNA; defined here as 45-60°N and 0-60°W), which modulates deep water formation[154, 114, 155, 99, 87]. This signal is subsequently propagated via Kelvin waves/boundary currents, which impact the AMOC in the lower latitudes[110, 111, 112, 113, 114]. In the

context of external forcing of the AMOC, GHG-induced AMOC weakening is consistent with reduced ocean heat loss, as well as increased freshwater input at high latitudes, both of which decrease sea surface density (SSD) in the sinking region of the subpolar North Atlantic[153, 135, 14, 156]. AMOC-related feedbacks are also likely important, including for example AMOC-induced changes in poleward Atlantic ocean heat transport (OHT)[153, 135, 157, 139]. This feedback is consistent with the aforementioned AMOC-related SST fingerprints[12], including the notion that 20th century AMOC weakening is related to cooling in the subpolar North Atlantic (i.e., the "warming" hole) due to decreases in poleward OHT (which may also involve other processes[131, 132]).

### 4.2.4 AMOC and Effective Radiative Forcing

From a fundamental point of view, the AMOC responses under NTCF mitigation should be related to the change in net top-of-the-atmosphere radiative fluxes, i.e., an increase will warm the North Atlantic Ocean and promote a decrease in SSD and SPNA deep water formation (and vice versa). Figure 4.3 (a,c,e) shows the North Atlantic (NA; 0-65°N; 0-60°W) effective radiative forcing (ERF; section 4.4) time series, which quantifies the change in net top-of-the-atmosphere energy due to both instantaneous radiative forcing and rapid (i.e., independent of sea surface temperature) adjustments[108]. Positive NA ERF trends exist for NMNTCF mitigation (particularly to mid-century), which is consistent with the strong decrease in aerosols and gaseous precursors (e.g., $SO_2$ decreases ~50% by mid-century) under strong AQ control, and minimal changes under weak AQ control (Figure C.3). In contrast, the corresponding ERF trends for all-NTCF and $CH_4$ mitigation are negative. This is driven by the decrease in $CH_4$ concentrations under strong AQ control

(i.e., 26% decrease by mid-century), coupled with the continued increase in $CH_4$ concentrations under weak AQ control. The NA MMM 2015-2100 ERF trends are 0.008, $-0.012$ and $-0.021$ W m$^{-2}$ per year for NMNTCF, all-NTCF and $CH_4$ mitigation, respectively, and all are significant at the 95% confidence level. All models exhibit qualitatively similar NA ERF trends (i.e., positive trends under NMNTCF mitigation; negative trends under all-NTCF and $CH_4$ mitigation).

Regressing the AMOC and NA ERF trends across all models and the three mitigation signals yields a significant negative slope (m) of $-1.39$ Sv per W m$^{-2}$ and a Pearson's correlation coefficient (r) of $-0.69$ (Figure 4.4a). Without GISS-E2-1-G, the correlation coefficient increases to $-0.94$ (regression slope of $-1.00$ Sv per W m$^{-2}$). Thus, as expected, a decrease in NA ERF is associated with AMOC strengthening and vice versa. Under all-NTCF mitigation, however, the NA ERF trend does not explain the lack of AMOC strengthening in three of four models (i.e., non-GISS-E2-1-G models). Based on this three model subset, the MMM all-NTCF NA ERF trend is significant and negative at $-0.011$ W m$^{-2}$ year$^{-1}$, but the corresponding MMM AMOC trend is negligible (Figure 4.2e). Similarly, in the same three models, the NA ERF trend is twice as large in magnitude under $CH_4$ as opposed to NMNTCF mitigation at $-0.022$ and 0.011 W m$^{-2}$ year$^{-1}$, respectively. However, the corresponding AMOC response is similar (in magnitude) at 0.017 and $-0.016$ Sv year$^{-1}$ (Figure 4.2 d,f). Thus, NA ERF fails to capture several features of the AMOC response. We note that we do not find evidence for the importance of the inter-hemispheric forcing gradient[97].

This implies the AMOC may be more sensitive (per unit NA ERF) to NMNTCFs as opposed to methane (up to twice as sensitive, based on the three model subset). Such a notion seems reasonable if surface forcing is more important to the AMOC, as opposed to top-of-the-atmosphere forcing (i.e., ERF, which is the sum of surface and atmospheric forcing). Aerosol forcing—particularly non-absorbing aerosols—largely impact the surface radiative fluxes, whereas GHGs like methane impact both the surface and the atmosphere. Examination of the NA surface ERF does show some improvements (relative to NA ERF) in accounting for the AMOC trends under mitigation (not shown). However, this leads to the opposite result—the $CH_4$ mitigation surface ERF is now weaker in magnitude than that for NMNTCF mitigation (e.g., $-0.008$ versus $0.020$ W m$^{-2}$ year$^{-1}$, respectively)—which once again does not account for the AMOC response under these two mitigation signals.

Outside of ERF, another (initially attractive) explanation for the lack of an AMOC response under all-NTCF mitigation in the three models (except for GISS-E2-1-G) is related to precipitation (P). Aerosols have a larger apparent hydrological sensitivity than GHGs (i.e., the change in precipitation per unit change in global surface temperature). So even though the all-NTCF mitigation ERF trend is negative, the decrease in aerosols may still dominate the precipitation response (i.e. they could promote an increase). However, we do not find strong evidence to support aerosol-hydrological considerations as a universal mechanism under all-NTCF mitigation (Appendix C; Table C.2 & Table C.3).

Recent studies have shown the importance of cumulative carbon emissions to global mean temperature change and other climate parameters, such as Arctic sea ice[158, 159]. Given the novelty of the transient ERF simulations as conducted for AerChemMIP (sec-

88

tion 4.4), in a somewhat similar manner, we calculate the cumulative NA ERF and inves-tigate it's role in accounting for the AMOC responses under mitigation. Figure 4.3 (b,d,f) shows the time series of the cumulative NA ERF. Under NMNTCF mitigation, an accumu-lation of energy occurs in the North Atlantic by end-of-the-century, ranging from 15.4 W $m^{-2}$ year in GISS-E2-1-G to 78.5 W $m^{-2}$ year in UKESM1-0-LL. The opposite occurs under $CH_4$ mitigation by end-of-the-century, where the cumulative NA ERF decreases from $-55.5$ W $m^{-2}$ year in MRI-ESM2-0 to $-88.0$ W $m^{-2}$ year in UKESM1-0-LL. Under all-NTCF mitigation, most models yield much smaller changes in cumulative NA ERF by end-of-the-century. Energy builds up in the first few decades for most models, due to the reduction in NMNTCFs. There is then a decrease in cumulative ERF (due to the decrease in $CH_4$), but this decrease is relatively small by $2100-$except for GISS-E2-1-G. For example, EC-Earth3-AerChem, UKESM1-0-LL and MRI-ESM2-0 yield $-4.2$, $-9.4$ and $-23.7$ W $m^{-2}$ year. GISS-E2-1-G yields the largest change in cumulative NA ERF at $-42.1$ W $m^{-2}$ year.

Figure 4.4b shows the scatter plot between the AMOC trend and the end-of-century cumulative NA ERF. A similar, but somewhat better relationship exists than with the NA ERF trend. Over all four models, the correlation improves from $-0.69$ with NA ERF to $-0.73$ with end-of-century cumulative NA ERF. The results are also improved when GISS-E2-1-G is removed from the calculation$-$from a correlation of $-0.94$ with NA ERF to $-0.97$ with cumulative NA ERF. Thus, the relatively large all-NTCF AMOC response (0.048 Sv year$^{-1}$) in GISS-E2-1-G is consistent with its relatively large (negative) cumulative ERF ($-42.1$ W $m^{-2}$ year); the negligible all-NTCF AMOC trends in the other three models are consistent with their smaller accumulated ERF ($<$0.001 Sv year$^{-1}$ and $-12.4$ W $m^{-2}$ year,

respectively). Furthermore, both $CH_4$ and NMNTCF mitigation yield similar accumulated NA ERFs ($-72.9$ versus $60.4$ W m$^{-2}$ year, respectively) in the non-GISS-E2-1-G models, consistent with the similar (in magnitude) AMOC trends under these two mitigation signals ($0.017$ versus $-0.016$ Sv year$^{-1}$). GISS-E2-1-G, however, still appears to be an outlier under $CH_4$ and all-NTCF mitigation (and even to some extent NMNTCF mitigation), yielding a relatively strong AMOC response relative to both ERF and even cumulative ERF (consistent with the above discussion).

### 4.2.5 Sea Surface Density

We now focus more specifically on the AMOC mechanisms in those experiments that yield a significant AMOC response, including NMNTCF and $CH_4$ mitigation, and weak AQ control (which is representative of the other two AQ control experiments). The most robust mechanism-related AMOC signals—particularly under mitigation—are changes in SPNA SSD, including its thermal ($SSD_T$) and haline ($SSD_S$) components (section 4.4). In particular, 2015-2100 SPNA SSD and $SSD_S$ increase under $CH_4$ mitigation and decrease under NMNTCF mitigation for all models (as well as AQ control experiments; Table C.4). The increase in SSD and $SSD_S$ under $CH_4$ mitigation is consistent with enhanced buoyancy anomalies and AMOC strengthening; the decrease in SSD and $SSD_S$ under NMNTCF mitigation and AQ control experiments is consistent with reduced buoyancy anomalies and AMOC weakening. Similar signed SPNA $SSD_T$ trends also occur, except for GISS-E2-1-G as well as MRI-ESM2-0 under AQ control experiments. We note that the 2015-2100 SSD trends under all-NTCF mitigation are less robust than the other two mitigation signals, with two models (MRI-ESM2-0 and EC-Earth3-AerChem) yielding non-significant all-NTCF SSD

trends. Furthermore, the 2015-2100 increase in SSD under all-NTCF mitigation largely occurs in the second half of the century (when the $CH_4$ forcing becomes more important). From 2015-2055, for example, most models lack significant SPNA SSD trends under all-NTCF mitigation (Table C.5). This agrees well with the cumulative NA ERF time series (Figure 4.3 d).

To better quantify how multi-decadal SSD variations are related to the AMOC, Figure 4.5 shows 21st century regression maps of the AMOC regressed onto $SSD_T$ (i.e., $\delta\,SSD_T / \delta\,AMOC$; section 4.4) for the two NTCF signals that yield significant AMOC changes−NMNTCF and $CH_4$ mitigation. We also include the weak AQ control experiment (which is representative of the other two AQ control experiments), because the signal is not only larger, but because it shares similarities to the mitigation cases (particularly for a given model). Based on the above discussion, we would expect positive SPNA sensitivities, i.e., an increase in $SSD_T$ due to SST cooling is associated with AMOC strengthening and vice versa. However, this is often not the case. Negative SPNA regression coefficients exist for GISS-E2-1-G, as well as MRI-ESM2-0. The MRI-ESM2-0 signal is weaker under the two mitigation signals, with the negative sensitivities largely confined near Iceland. In contrast, UKESM-1-0-LL yields positive $\delta SSD_T/\delta AMOC$ SPNA regression coefficients. EC-Earth3-AerChem yields both positive and negative sensitivities under NMNTCF and $CH_4$ mitigation (positive to the west of Iceland and negative to the east, but with small significance). Under weak AQ control, EC-Earth3-AerChem is similar to UKESM1-0-LL, with positive SPNA sensitivities (but less positive near Iceland). The negative SPNA $\delta SSD_T/\delta AMOC$ sensitivities (and less positive relative to the broader NA region under AQ control) are consistent with changes in

AMOC-induced poleward Atlantic OHT (Figure C.4 & Figure C.5), which in turn impacts the SSTs in a way that offsets the expected response due to the imposed radiative forcing. Weakening of the AMOC under positive radiative forcing (e.g., NMNTCF mitigation and AQ control experiments) is associated with a decrease in poleward Atlantic OHT, which promotes SPNA SST cooling and a increase in $SSD_T$; AMOC strengthening under negative radiative forcing (e.g., $CH_4$ mitigation) is associated with an increase in poleward Atlantic OHT, which promotes SPNA SST warming and a decrease in $SSD_T$.

Figure 4.6 shows the corresponding regression maps of the AMOC regressed onto the haline component of SSD ($SSD_S$). Significant positive $\delta SSD_S/\delta AMOC$ SPNA sensitivities exist for nearly all models, across both mitigation signals and the weak AQ control experiment. Thus an increase in $SSD_S$ is associated with strengthening of the AMOC, whereas a decrease is associated with weakening of the AMOC. The exception is UKESM1-0-LL for NMNTCF mitigation, where $\delta SSD_S/\delta AMOC$ is positive, but generally lacks significance. These $\delta SSD_S/\delta AMOC$ sensitivities are similar to those based on SSD (Figure C.6), particularly for GISS-E2-1-G and MRI-ESM2-0 (i.e., they are all positive), which suggests AMOC variations are largely associated with $SSD_S$ as opposed to $SSD_T$. We note that under all-NTCF mitigation, the AMOC versus SSD, $SSD_S$ and $SSD_T$ regressions are weak and lack significance, except in the case of GISS-E2-1-G where the results are very similar to $CH_4$ mitigation (not shown). Additional analyses, investigating the ratio of the 2015-2100 SPNA SSD trend to the SPNA $SSD_S$ trend (Table C.6; Appendix C) further supports the importance of $SSD_S$.

### 4.2.6  Freshwater Flux & Mixed Layer Depth

Ultimately, changes is $SSD_S$ can only be driven by changes in surface net freshwater flux (FF) or changes in ocean circulation. Non-SSD variables, such as FF, generally exhibit non-significant trends under mitigation over the entire SPNA, particularly relative to the AQ experiments (Table C.2). Thus, to further explore the causes of the changes in $SSD_S$, Figure C.7−Figure C.10 shows 2015-2100 spatial trend maps of several variables, including the surface net freshwater flux, as well as its main components including precipitation (P) and the negative of surface evaporation (i.e., −E, like FF and P represents the gain of fresh water to the surface) for NMNTCF and $CH_4$ mitigation, as well as the weak AQ control experiment (which is representative of the other two). In GISS-E2-1-G and MRI-ESM2-0, an increase in SPNA $SSD_S$ is consistent with a decrease in FF, which is largely related to an increase in evaporation (and vice versa). The change in SPNA evaporation is consistent with the change in SSTs. That is, warming SPNA SST under $CH_4$ mitigation (due to enhanced poleward Atlantic OHT; Figure C.4 & Figure C.5) is associated with more evaporation; cooling SSTs under NMNTCF mitigation and weak AQ control (due to reduced poleward Atlantic OHT) is associated with less evaporation. These changes in SSTs are particularly prominent for GISS-E2-1-G. For MRI-ESM2-0, the SST change is more subtle, especially for $CH_4$ mitigation, which is perhaps better described as a lack of SPNA cooling. For EC-Earth3-AerChem and UKESM1-0-LL, changes in both SPNA P and −E appear to be important to FF under mitigation, with −E becoming more important under larger forcing (i.e., weak AQ control). Similar conclusions generally exist when regressing SPNA FF, as well as P and −E onto $SSD_S$ (Figure C.11−Figure C.14). Thus, we suggest that $SSD_S$ is

largely driven by evaporation via changes in SSTs, which in turn are consistent with changes in poleward Atlantic OHT (Appendix C).

Changes in SSD can impact mixing and deep convection in the SPNA. March mixed-layer depth (MMLD) is used to investigate North Atlantic deep convection, which is associated with deep water formation and the strength of the AMOC[160]. All models show maximum climatological MMLD in the SPNA, particularly in the Labrador Sea extending around the southern tip of Greenland to Iceland, and then extending through the Norwegian Sea, up to Svalbard i.e., the Greenland-Iceland-Norway (GIN) sea. The $\delta$MMLD/$\delta$AMOC sensitivities for NMNTCF and $CH_4$ mitigation, as well as weak AQ control for each model are included in Figure C.15. Positive SPNA sensitivities generally exist between the AMOC and MMLD, supporting the notion that enhanced deep convection (as represented by increases MMLD) is associated with AMOC strengthening, and vice versa. GISS-E2-1-G tends to show the largest sensitivity under mitigation relative to the other models, especially for $CH_4$ mitigation. In general, most models show both positive and negative sensitivities in the SPNA under mitigation, implying the importance of regional changes in deep convection. For example, EC-Earth3-AerChem shows significant positive sensitivities under $CH_4$ mitigation largely in the GIN sea. Under NMNTCF mitigation, MRI-ESM2-0 shows positive values in the Labrador and Norwegian sea; UKESM1-0-LL yields positive sensitivities in the Greenland sea alone. Weak AQ control shows robust positive sensitivities throughout most of the SPNA (consistent with the larger forcing) in all models.

### 4.2.7 Clouds

As discussed above, GISS-E2-1-G yields a relatively large AMOC response in nearly all situations. To some extent, this is even true for NMNTCF mitigation, where the GISS-E2-1-G AMOC trend is $-0.013$ Sv year$^{-1}$ (comparable to other models), but GISS-E2-1-G NMNTCF cumulative NA ERF (and NA ERF) is quite small at 15.4 W m$^{-2}$ year (Appendix C). Although this may be related to GISS-E2-1-G's large climatological AMOC, we suggest that part of GISS-E2-1-G's large AMOC response is due to a stronger AMOC-cloud feedback[139] (i.e., larger cloud response per unit of AMOC change). Figure C.16 shows the total cloud cover (CLT) regressed onto the AMOC time series for NMNTCF mitigation, CH$_4$ mitigation and weak AQ control. For each of these, GISS-E2-1-G exhibits significant and relatively large negative regression coefficients in the SPNA, ranging from $-0.5$ to $-1.0$ % Sv$^{-1}$.

Similar results exist under all-NTCF mitigation, as well as with the other AQ control experiments (not shown). The other models do not consistently exhibit this feature, and in some cases, show the opposite sensitivity (which is possibly a CLT-global warming response under AQ control). The negative regression coefficients in GISS-E2-1-G suggest that AMOC weakening, which is associated with a decrease in poleward Atlantic OHT and SPNA cooling, yields an increase in cloud cover (and vice versa). The cloud cover response, in turn, will further promote SPNA SST cooling. On one hand, this could drive an increase in SSD$_T$ (muting AMOC weakening), but on the other hand, it could promote less evaporation and a net increase in freshwater flux, yielding a decrease in SSD$_S$, which acts to reinforce AMOC weakening. Give the prior discussion, the SST-evaporation-SSD$_S$

pathway appears to be dominant in this model. Thus, the strong AMOC-CLT feedback helps to account for the large AMOC response in GISS-E2-1-G.

## 4.3 Discussion and Conclusion

Models will continue to have uncertainties, including those relevant to the AMOC and North Atlantic climate, including biases in the mean state, as well as the strength and depth of the AMOC and ocean freshwater transport[119, 120, 121, 19, 122] CMIP6 models, however, well simulate the observed present-day (2005-2018) AMOC strength. For example, the multi-model mean AMOC strength and one-sigma uncertainty across 24 CMIP6 models is 19.8±5.6 Sv, which is similar to that from the RAPID array at 17.5±1.4 Sv[139]. The four models used here yield a similar MMM AMOC climatology of 18.8±2.6 Sv. Furthermore, the CMIP6 AMOC response may be too sensitive to anthropogenic aerosol forcing[90, 97] and CMIP6 models may also overestimate aerosol indirect effects[161]. However, anthropogenic aerosol ERF estimates are consistent between CMIP6 and recent observational estimates, with 90% confidence intervals of $-1.5$ to $-0.6$ and $-2.0$ to $-0.4$ W m$^{-2}$, respectively[162, 163]. The models used here yield corresponding aerosol ERFs of $-1.21$ W m$^{-2}$ for MRI-ESM2-0; $-1.11$ for UKESM1-0-LL; $-0.93$ for GISS-E2-1-G (p3); and $-0.8$ W m$^{-2}$ for EC-Earth3-AerChem[163, 164].

Our analysis is the first to investigate the impacts of near-term climate forcer mitigation on the AMOC. NMNTCF mitigation weakens the AMOC, which reinforces GHG-induced AMOC weakening. Including methane reductions, along with the aerosol and ozone precursor gas reductions (i.e., all-NTCF mitigation), however, offsets NMNTCF

96

AMOC weakening. AMOC trends are significantly (anti-)correlated with the net top-of-the-atmosphere North Atlantic effective radiative forcing trends, and in particular, the cumulative NA ERF. An increase in cumulative NA ERF by end-of-the-century is associated with AMOC weakening, whereas a decrease is associated with AMOC strengthening. Furthermore, unlike NA ERF trends, the cumulative ERF better accounts for the AMOC responses, particularly under all-NTCF mitigation. GISS-E2-1-G, however, remains an outlier (i.e., it has a relatively large AMOC response relative to the forcing), but this appears to be related to a strong AMOC-CLT feedback.

To first order, the ERF or cumulative ERF will perturb SSTs and the thermal component of sea surface density, which will then impact the AMOC. Although radiative forcing can also impact the climate in additional ways (e.g., precipitation, evaporation), which could also impact the AMOC, most of the hydrological changes appear to be directly related to changes in the AMOC itself (i.e., a feedback related to changes in poleward Atlantic OHT and SPNA SSTs). However, we are unable to clearly separate cause and effect in fully-coupled simulations. Due to the smaller forcing under mitigation (and relatively small number of realizations), the AMOC mechanisms are "noisier" as compared to the AQ control experiments. Nonetheless, our analysis shows that AMOC variations are associated with SPNA SSD variations, and that this is related to both the thermal and haline component of SSD, with the relative importance of $SSD_S$ more important under larger forcing (and larger AMOC signal). In some models, even with relatively weak forcing (e.g., GISS-E2-1-G), $SSD_S$ is the dominant driver of SSD.

97

This study ads to the growing number of analyses that suggest clean air policies need to address methane, in addition to aerosol and ozone precursor gases. NMNTCF mitigation alone will reinforce $CO_2$ driven warming and the associated climate impacts, including weakening of the AMOC. This unintended climate change, however, can be offset by simultaneously incorporating methane (and $CO_2$) reductions.

## 4.4  Methods

**Future Emission Scenarios and NTCF Experiments**

As part of ScenarioMIP, a set of Shared Socio-economic Pathways (SSPs) have been developed for CMIP6[130, 165, 39, 166]. To detect the impact of air quality pollutants, AerChemMIP uses SSP3-7.0 ( 7.0 W m$^{-2}$ at 2100) as the reference scenario, which lacks climate policy, has "weak" levels of air quality control measures and thus the highest levels of NTCFs[130, 167, 168]. To isolate the effects of air quality controls, the SSP3-7.0-lowNTCF scenario was developed, using the same socio-economic scenario and the same emissions drivers (e.g. population, GDP, energy and land-use), but with "strong" levels of air quality control measures[166]. In the case of air pollutant species (e.g. sulfur, BC, OC, NOx), the emissions factors assumed in SSP1, a sustainability pathway, are adopted. Here, the decrease in air pollutant species emissions is due to swift ramping up of end-of-pipe measures for air pollution control (rather than a transition to non-fossil-based fuels). This assumption implicitly assumes that SSP1's air pollutant legislation and technological progress can be achieved in the SSP3 world. Thus, the decrease in air pollutant species emissions is due to the aggressive air pollution policy alone. In the case of $CH_4$, the $CH_4$ emissions reduction

rates in SSP1-2.6 relative to the SSP1 baseline are adopted to SSP3-7.0. This implicitly assumes that a SSP3-7.0-lowNTCF world can reduce $CH_4$ as if SSP1's stringent climate mitigation policy is implemented in the SSP3 world. We acknowledge that the lowNTCF pathway is unlikely to occur in reality, and that our results likely represent an upper bound as the baseline scenario (SSP3-7.0) contains the highest levels of NTCFs.

In addition to the SSP3-7.0 reference experiment, two sets of experiments were run based on the SSP3-7.0-lowNTCF scenario[169]. The first low NTCF experiment, SSP3-7.0-lowNTCF, excludes the methane changes[38, 151]. An additional experiment, SSP3-7.0-lowNTCFCH4, was also performed that includes both methane and NMNTCFs. Thus, the SSP3-7.0-lowNTCF experiment, which we henceforth refer to as strong non-methane air quality (AQ) control, allows quantification of the climate and air quality impacts due to NM-NTCFs. The SSP3-7.0-lowNTCFCH4 experiment, which we henceforth refer to as strong AQ control, allows the impacts of all NTCFs (including methane) to be quantified. Furthermore, we define NMNTCF mitigation as the difference between the strong non-methane AQ control experiment and the weak AQ control experiment (SSP3-7.0-lowNTCF−SSP3-7.0). Similarly, all-NTCF mitigation is defined as the difference between the strong and weak AQ control experiment (SSP3-7.0-lowNTCFCH4−SSP3-7.0). Finally, methane mitigation alone is defined as the difference between the two strong air quality control experiments (with and without methane reductions, SSP3-7.0-lowNTCFCH4−SSP3-7.0-lowNTCF). Table C.1 lists the experiments and mitigation signals used in this study.

Under weak air quality control (Figure C.3), global mean atmospheric $CO_2$ and $CH_4$ concentrations (models are concentration-driven for these species) increase by ∼35%

by mid-century, with continued increases of 116% and 83%, respectively, by 2100 (relative to 2015). Global emissions of all aerosols and gaseous precursors (models are emission-driven for these species) also increase by 7-13% by mid-century (except $SO_2$), but then decrease afterwards due to end-of-pipe measures for air pollution control. By 2100, most of these species have decreased relative to 2015, ranging from $\sim$0 (for volatile organic compounds, VOCs) to $-22\%$ (for $SO_2$). In contrast, strong air quality control yields emission reductions in all aerosol and gaseous precursors, particularly during the first half of the century, ranging from $-26\%$ for VOCs to $-54\%$ for $SO_2$. This decrease under strong air quality control continues (although more weakly) through 2100, with aerosol and gaseous precursor emissions decreasing by $-52$ to $-68\%$. Similarly, $CH_4$ concentrations decrease by $-26\%$ and $-34\%$ by mid-century and end-of-the-century, respectively ($CO_2$ concentrations are identical to those under weak air quality control).

**AerChemMIP Models and ERF**

Four coupled ocean-atmosphere-chemistry climate models performed the necessary 21st century AerChemMIP simulations, including UKESM1-0-LL[170, 171, 172], MRI-ESM2-0[173, 174], EC-Earth3-AerChem[175, 164] and GISS-E2-1-G[176]. UKESM1-0-LL, MRI-ESM2-0 and GISS-E2-1-G performing three 2015-2100 realizations for each of the three experiments described above; EC-Earth3-AerChem performed one realization for each of the experiments. These models also performed analogous experiments with fixed sea surface temperatures (SSTs) to quantify the transient effective radiative forcing (ERF). The three coupled ocean-atmosphere-chemistry integrations are repeated with prescribed SSTs

and sea ice, taken from the monthly mean evolving values from the base SSP3-7.0 cou-
pled simulation[38]. Although this experimental design does not technically yield an ERF,
each experiment (for a given model) has identical evolution of SSTs and sea-ice such that
when the experiments are subtracted to obtain the NTCF signal, the SSTs and sea-ice can-
cel out. That is, the ERF is estimated as the difference in the net top-of-the-atmosphere
(TOA) shortwave and longwave radiative fluxes (e.g., weak AQ control minus strong AQ
control in the fixed SST experiments yields the all-NTCF ERF). All analyses are based on
archived monthly mean data, which is subsequently averaged to obtain annual means. All
data is spatially interpolated to a 2.5°x2.5° grid using bilinear interpolation. The multi-
model mean (MMM) is obtained by averaging each model's mean response so that each
model has the same weight.

**AMOC Calculation**

The AMOC is defined as the maximum stream function ($\psi$) below 500 m at 28°N in the
Atlantic Ocean. It is calculated by integrating the northward sea water velocity ($vo$) with
depth, $z$, from the western ($x_w$) to the eastern boundaries ($x_e$) of the Atlantic Ocean:

$$\psi(z) = \int_z^0 \int_{x_w}^{x_e} vo(x, z')dxdz'. \tag{4.1}$$

The AMOC percent change is estimated from the least-squares regression slope ($m$) of the
non-normalized AMOC time series using: $100 \times \frac{m \times N}{AMOC(N=1)}$, where $N$ is the number of
years (e.g., 86 for 2015-2100) and $AMOC(N = 1)$ is the initial AMOC strength (e.g., in
2015 for 2015-2100 trends).

The quoted AMOC percent change uncertainties are estimated as the standard error, defined as $\frac{\sigma}{\sqrt{n_m}}$, where $\sigma$ represents the standard deviation across each model mean AMOC percent change and $n_m$ is the number of models.

**Trend Significance and Regression Analysis**

Multi-model ensemble mean trends are based on the ensemble mean time series for each model. All time series are normalized by subtracting each model's long-term (2015-2100) climatology. Trends are based on a least-squares regression and significance is based on a standard $t$-test. To isolate multi-decadal variability in common between two variables, we linearly regress the 10-year smoothed and non-detrended time series of one variable (e.g., AMOC) onto various fields, including for example SSD, $\text{SSD}_S$ and $\text{SSD}_T$. This yields spatially dependent regression coefficients (e.g., $\delta\text{SSD}/\delta\text{AMOC}$) or "sensitivities", based on a linear least-squares regression analysis. In this study, the subpolar North Atlantic (SPNA) is defined as 45-60°N and 0-60°W. The North Atlantic (NA) is defined as 0-65°N; 0-60°W. Similar results are generally obtained with slightly different definitions of the SPNA (e.g., 45-60°N and 0-70°W) and NA.

**Decomposition of seawater density**

The surface seawater density (SSD) is calculated using each model's simulated temperature, salinity and pressure. The density trend is decomposed into thermal and haline components according to:

$$\delta SSD = (\overline{\frac{dSSD}{dT}})\delta T + (\overline{\frac{dSSD}{dS}})\delta S, \tag{4.2}$$

where $\delta$ represents the trend and $\overline{\frac{dSSD}{dT}}$ and $\overline{\frac{dSSD}{dS}}$ represents the climatological partial derivative of temperature and salinity with respect to density at each grid box. $T$ is temperature in °C and $S$ is salinity in PSU. $\frac{dSSD}{dT}$ is the temperature derivative of density and $\frac{dSSD}{dS}$ is the salinity derivative of the density. The derivatives are calculated based on the formulas from Unesco's joint panel on oceanographic tables and standards. The first term on the right hand side of Eq. 4.2 represents the thermal component and the second term on the right hand side of Eq. 4.2 represents the haline component of $\delta$SSD.
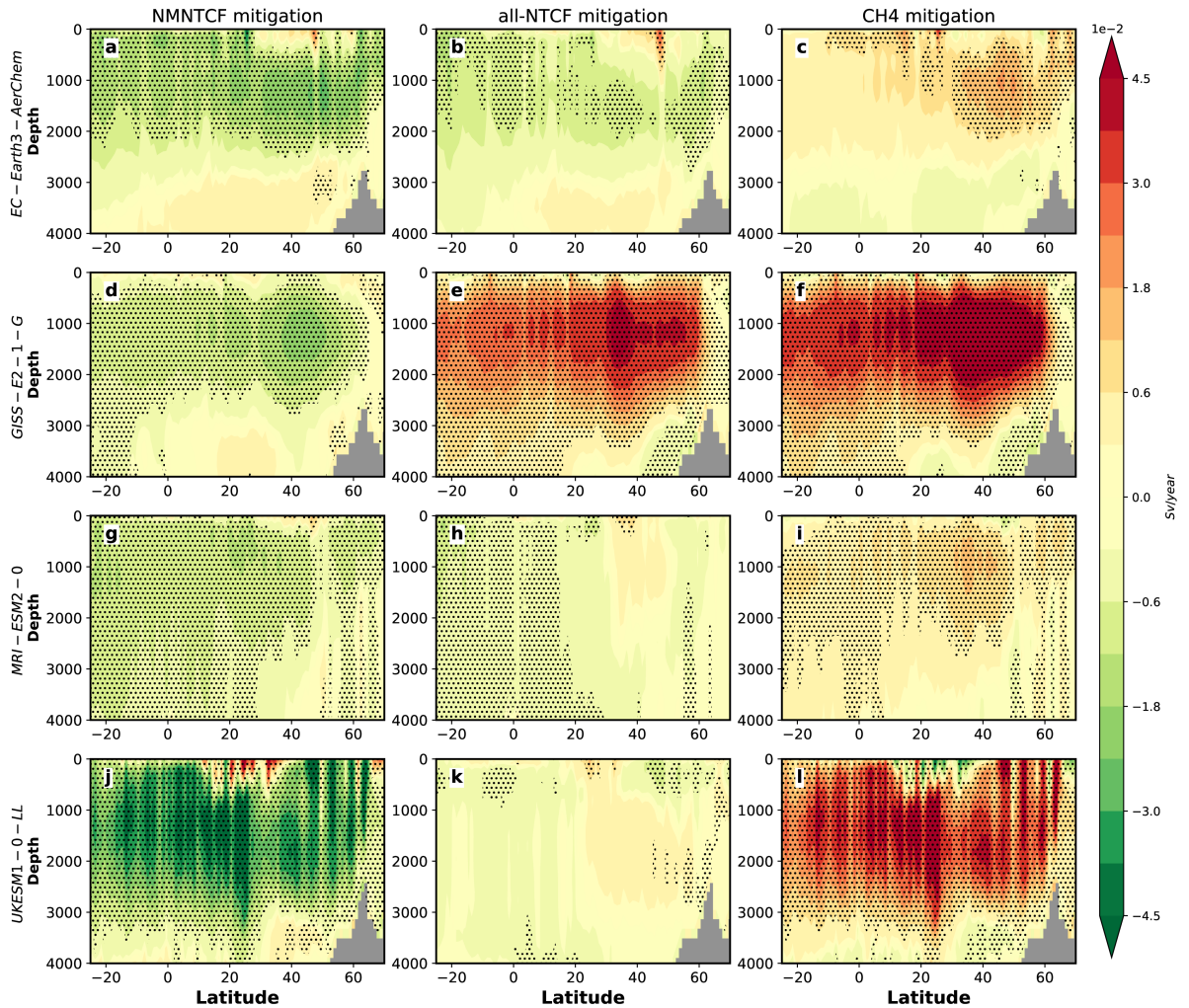
Figure 4.1: **2015-2100 annual mean depth-latitude trends in the Atlantic meridional stream function for the three mitigation signals.** (a, d, g, j) NMNTCF, (b, e, h, k) all-NTCF, and (c, f, i, l) CH$_4$ mitigation for (a-c) EC-Earth3-AerChem, (d-f) GISS-E2-1-G, (g-i) MRI-ESM2-0, and (j-l) UKESM1-0-LL. Trend units are $10^{-2}$ Sverdrups yr$^{-1}$, where Sverdrups (Sv) = $10^6$ m$^3$ s$^{-1}$. Symbols designate trend significance at 95% confidence level based on a standard $t$-test. Strengthening of the circulation is represented by red shading; weakening is represented by green shading.

104
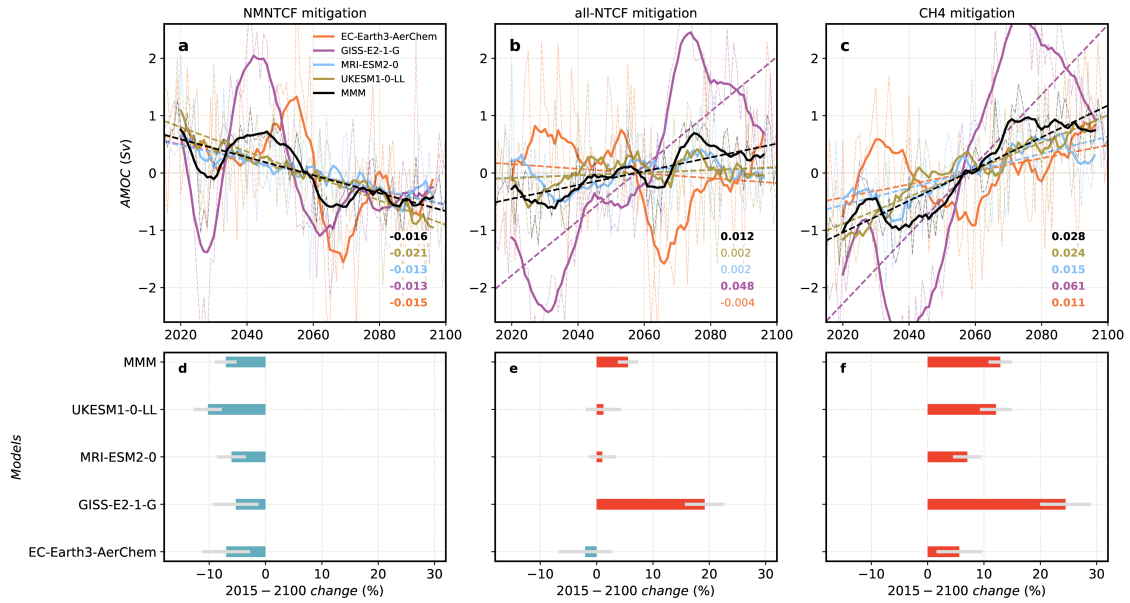
Figure 4.2: **2015-2100 changes in the annual mean Atlantic Meridional Overturning Circulation (AMOC) for the three mitigation signals.** (a-c) Normalized (relative to the long-term 2015-2100 climatology) AMOC time series and trends, (d-f) AMOC percent change (relative to 2015) for each model, including the multi-model mean (MMM) for (a, d) NMNTCF, (b, e) all-NTCF, and (c, f) $CH_4$ mitigation. In (a-c), thick lines show the smoothed AMOC time series using a 10-year running mean. Also included in (a-c) is the slope of the least-squares trend line (units of Sv year$^{-1}$), color coded by model as defined in the legend. AMOC trends significant at the 95% confidence level are bold. In (d-f), AMOC weakening (strengthening) is shown with blue (red) bars. The gray thin lines over the percent change bars represent the 95% confidence level.

105
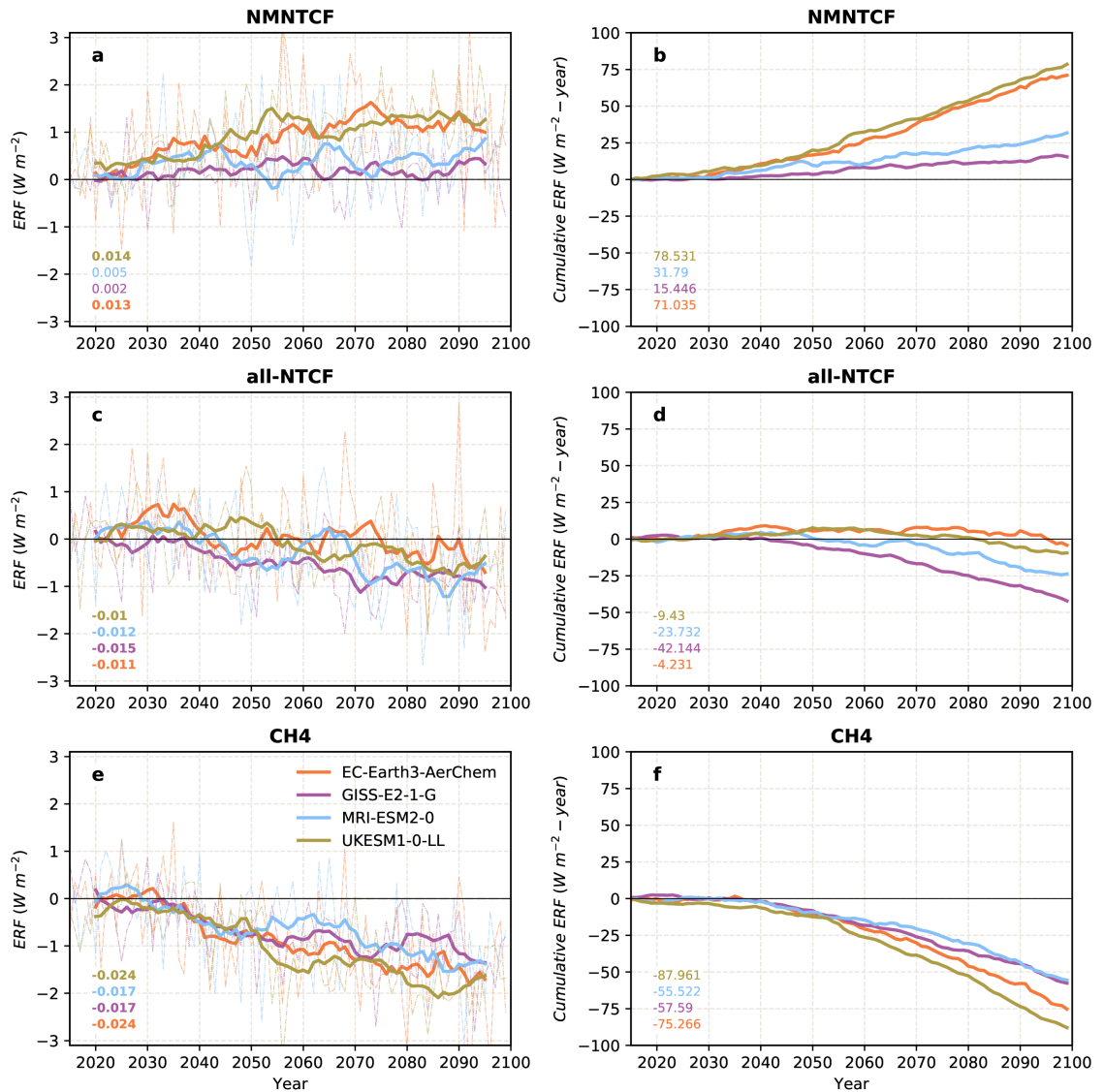
Figure 4.3: **2015-2100 North Atlantic effective radiative forcing for the three mitigation signals.** North Atlantic (a, c, e) annual mean effective radiative forcing (ERF) and (b, d, f) cumulative ERF time series for each model for (a, b) NMNTCF, (c, d) all-NTCF, and (e, f) $CH_4$ mitigation. Thick lines show the smoothed time series using a 10-year running mean. Also included in (a, c, e) is the slope of the least-squares trend line (units of W m$^{-2}$ year$^{-1}$), color coded by model as defined in the legend. Bold trends are significant at the 95% confidence level, based on a standard $t$-test. The end-of-century cumulative NA ERF (units of W m$^{-2}$ year) is included in (b, d, f), color coded by model.
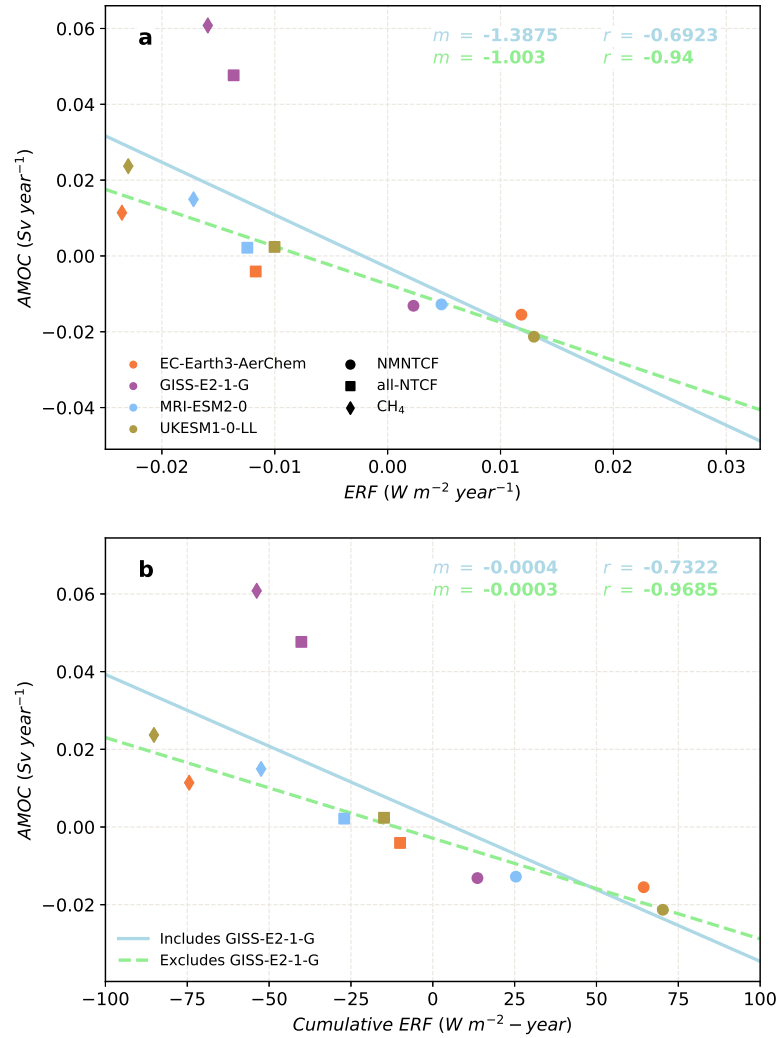
Figure 4.4: **AMOC versus effective radiative forcing scatter plot.** AMOC trend [Sv year$^{-1}$] versus North Atlantic (a) annual mean effective radiative forcing (ERF) trend [W m$^{-2}$ year$^{-1}$] and (b) cumulative ERF [W m$^{-2}$ year] for all models and mitigation signals. Also included is the slope of the least-squares trend line (m) and the correlation coefficient (r). Bold indicates significance at the 95% confidence level (all are significant). Light blue statistics and trend line is for all models; light green statistics and trend line is for all models without GISS-E2-1-G.
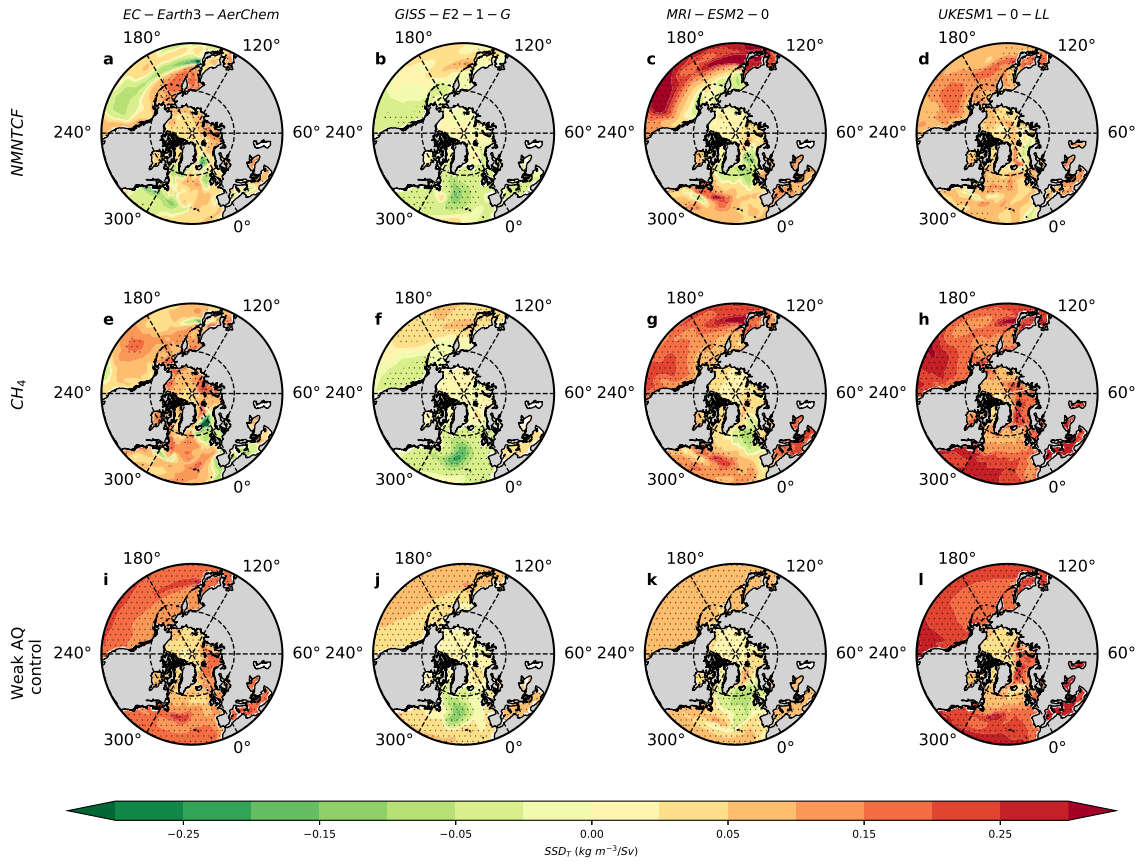
Figure 4.5: **2015-2100 annual mean thermal component of sea surface density (SSD$_T$) regression analysis.** Spatial maps of the AMOC time series regressed onto SSD$_T$ under (a-d) NMNTCF mitigation; (e-h) CH$_4$ mitigation; and (i-l) the weak air quality (AQ) control experiment for (a, e, i) EC-Earth3-AerChem; (b, f, j) GISS-E2-1-G; (c, g, k) MRI-ESM2-0; and (d, h, l) UKESM1-0-LL. Units are kg m$^{-3}$ per Sv. Symbols denote significant at the 95% confidence level based on a standard $t$-test.
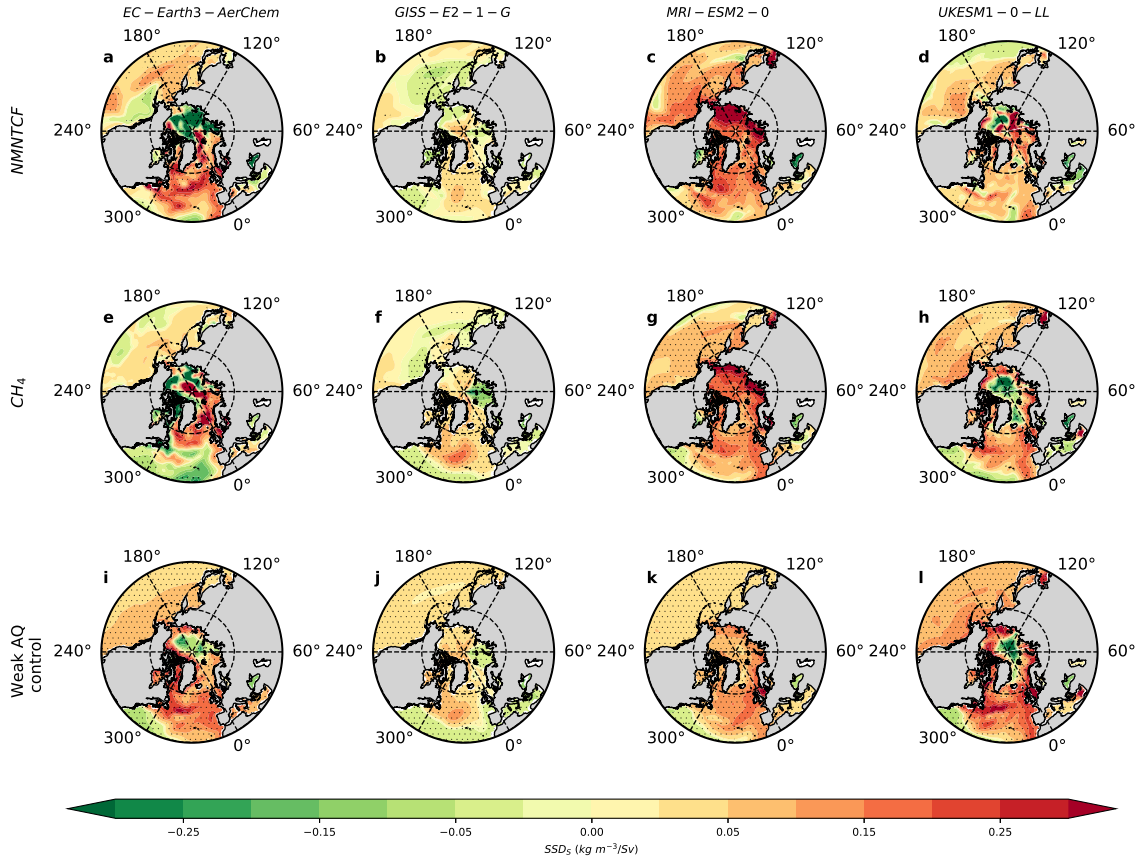
Figure 4.6: **2015-2100 annual mean haline component of sea surface density (SSD$_S$) regression analysis.** Spatial maps of the AMOC time series regressed onto SSD$_S$ under (a-d) NMNTCF mitigation; (e-h) CH$_4$ mitigation; and (i-l) the weak air quality (AQ) control experiment for (a, e, i) EC-Earth3-AerChem; (b, f, j) GISS-E2-1-G; (c, g, k) MRI-ESM2-0; and (d, h, l) UKESM1-0-LL. Units are kg m$^{-3}$ per Sv. Symbols denote significant at the 95% confidence level based on a standard $t$-test.

# Chapter 5

# Conclusions

Overall, this dissertation investigates the mechanisms that drive the large-scale circulations, aerosol interactions and their climate feedback using climate models. Chapter 2 results show that CAM5 simulates a global annual mean increase in anthropogenic aerosols in response to GHG-induced warming, with a maximum increase over the Northern Hemisphere mid-latitude continents during June, July and August (JJA). Targeted CAM5 simulations show that this response is related to the land-sea warming contrast (LSWC) and associated increases in continental aridity, which result in less aerosol wet removal. Muting the LSWC weakens the increase in aerosol burden, as well as the decrease in soil moisture, runoff, snow depth, lower tropospheric relative humidity, large-scale precipitation (LSP) and associated aerosol wet removal. Furthermore, land warming alone yields an increase in aerosol burden and the opposite hydrological changes. Unless emission reductions occur, these results add confidence that a warmer world will be associated with enhanced anthropogenic aerosol pollution.

In the multi-model analysis of the multi-decadal AMOC variability, I found that CMIP6 models yield consistent AMOC responses over different time periods. This includes a strengthening from ~1950-1990, followed by a weakening from 1990-2020. These AMOC variations are initiated by North Atlantic aerosol optical thickness perturbations to net surface shortwave radiation and surface temperature (i.e., sea surface density), which in turn affect the sea level pressure gradient and surface wind–and via latent and sensible heat fluxes–the sea surface density flux through its thermal component. AMOC-related feedbacks act to reinforce this aerosol-forced AMOC response, largely due to changes in sea surface salinity and its corresponding impacts on sea surface density, with temperature (and cloud) related feedbacks acting to mute the initial response. Anthropogenic aerosol forcing alone reproduces the bulk of the multi-decadal AMOC responses. Chapter 3 results suggest that the continued decrease in anthropogenic aerosol emissions that accompany efforts to reduce air pollution will reinforce GHG-induced AMOC weakening over the next few decades.

Non-methane near-term climate forcer (NMNTCF) mitigation weakens the AMOC, which reinforces GHG-induced AMOC weakening. Including methane reductions, along with the aerosol and ozone precursor gas reductions, however, offsets NMNTCF AMOC weakening. AMOC trends are significantly (anti-)correlated with the net top-of-the-atmosphere North Atlantic effective radiative forcing (ERF) trends, and in particular, the cumulative North Atlantic (NA) ERF. An increase in cumulative NA ERF by end-of-the-century is associated with AMOC weakening, whereas a decrease is associated with AMOC strengthening. Chapter 4 analysis shows that AMOC variations are associated with subpolar North Atlantic sea surface density (SSD) variations, and that this is related to both the thermal

($SSD_T$) and haline ($SSD_S$) component of SSD, with the relative importance of $SSD_S$ more important under larger forcing (and larger AMOC signal). This adds to the growing number of analyses that suggest clean air policies need to address methane, in addition to aerosol and ozone precursor gases. NMNTCF mitigation alone will reinforce $CO_2$ driven warming and the associated climate impacts, including weakening of the AMOC. This unintended climate change, however, can be offset by simultaneously incorporating methane (and $CO_2$) reductions.

# Bibliography

[1] Lelieveld, J., Evans, J. S., Fnais, M., Giannadaki, D. & Pozzer, A. The contribution of outdoor air pollution sources to premature mortality on a global scale. *Nature* **525**, 367–371 (2015).

[2] Boucher, O. *et al.* Clouds and Aerosols. In: Climate Change 2013: The Physical Science Basis. Contribution of Working Group I to the Fifth Assessment Report of the Intergovernmental Panel on Climate Change [Stocker, T.F., D. Qin, G.-K. Plattner, M. Tignor, S.K. Allen, J. Boschung, A. Nauels, Y. Xia, V. Bex and P.M. Midgley (eds.)]. Tech. Rep., Cambridge University Press, Cambridge, United Kingdom and New York, NY, USA, pp. 571-657 (2013).

[3] Bond, T. C. *et al.* Historical emissions of black and organic carbon aerosol from energy related combustion, 1850-2000. *Glob. Biogeochem. Cyc.* **21**, doi:10.1029/2006GB002840 (2007).

[4] Sutton, R. T., Dong, B. & Gregory, J. M. Land/sea warming ratio in response to climate change: IPCC AR4 model results and comparison with observations. *Geophys. Res. Lett.* **34**, L02701, doi:10.1029/2006GL028164 (2007).

[5] Joshi, M., Lambert, F. & Webb, M. An explanation for the difference between twentieth and twenty-first century land–sea warming ratio in climate models. *Climate dynamics* **41**, 1853–1869 (2013).

[6] Byrne, M. P. & O'gorman, P. A. Land–ocean warming contrast over a wide range of climates: Convective quasi-equilibrium theory and idealized simulations. *Journal of Climate* **26**, 4000–4016 (2013).

[7] Byrne, M. P. & O'gorman, P. A. Understanding decreases in land relative humidity with global warming: Conceptual model and gcm simulations. *Journal of Climate* **29**, 9045–9061 (2016).

[8] Talley, L. D. Freshwater transport estimates and the global overturning circulation: Shallow, deep and throughflow components. *Progress in Oceanography* **78**, 257–303, doi: 10.1016/j.pocean.2008.05.001 (2008).

[9] Buckley, M. W. & Marshall, J. Observations, inferences, and mechanisms of the Atlantic Meridional Overturning Circulation: A review. *Reviews of Geophysics* **54**, 5–63, doi: 10.1002/2015RG000493 (2016).

[10] Smeed, D. A. *et al.* The North Atlantic Ocean is in a state of reduced overturning. *Geophysical Research Letters* **45**, 1527–1533, doi: 10.1002/2017GL076350 (2018).

[11] Frajka-Williams, E. *et al.* Atlantic Meridional Overturning Circulation: Observed transport and variability. *Frontiers in Marine Science* **6**, 260, doi: 10.3389/fmars.2019.00260 (2019).

[12] Caesar, L., Rahmstorf, S., Robinson, A., Feulner, G. & Saba, V. Observed fingerprint of a weakening Atlantic Ocean overturning circulation. *Nature* **556**, 191–196, doi: 10.1038/s41586–018–0006–5 (2018).

[13] Hassan, T., Allen, R. J., Liu, W. & Randles, C. Anthropogenic aerosol forcing of the amoc and the associated mechanisms in cmip6 models. *Atmospheric Chemistry and Physics Discussions* **2020**, 1–28 (2020).

[14] Gregory, J. M. *et al.* A model intercomparison of changes in the Atlantic thermohaline circulation in response to increasing atmospheric $CO_2$ concentration. *Geophysical Research Letters* **32**, doi: 10.1029/2005GL023209 (2005).

[15] Solomon, S. *et al.* (eds.) *Climate Change 2007: The Physical Science Basis. Contribution of Working Group I to the Fourth Assessment Report of the Intergovernmental Panel on Climate Change* (Cambridge University Press, New York, pp. 996, 2007).

[16] Drijfhout, S. S. & Hazeleger, W. Detecting Atlantic MOC changes in an ensemble of climate change simulations. *Journal of Climate* **20**, 1571–1582, doi: 10.1175/JCLI4104.1 (2007).

[17] Cheng, W., Chiang, J. C. H. & Zhang, D. Atlantic Meridional Overturning Circulation (AMOC) in CMIP5 Models: RCP and Historical Simulations. *Journal of Climate* **26**, 7187–7197, doi: 10.1175/JCLI–D–12–00496.1 (2013).

[18] Kirtman, B. *et al.* Near-term Climate Change: Projections and Predictability. In: Climate Change 2013: The Physical Science Basis. Contribution of Working Group I to the Fifth Assessment Report of the Intergovernmental Panel on Climate Change [Stocker, T.F., D. Qin, G.-K. Plattner, M. Tignor, S.K. Allen, J. Boschung, A. Nauels, Y. Xia, V. Bex and P.M. Midgley (eds.)]. Tech. Rep., Cambridge University Press, Cambridge, United Kingdom and New York, NY, USA, pp. 953-1028 (2013).

[19] Kostov, Y., Armour, K. C. & Marshall, J. Impact of the Atlantic meridional overturning circulation on ocean heat storage and transient climate change. *Geophysical Research Letters* **41**, 2108–2116, doi: 10.1002/2013GL058998 (2014).

[20] Weijer, W., Cheng, W., Garuba, O., Hu, A. & Nadiga, B. Cmip6 models predict significant 21st century decline of the atlantic meridional overturning circulation. *Geophysical Research Letters* e2019GL086075 (2020).

[21] Delworth, T. L. & Dixon, K. W. Have anthropogenic aerosols delayed a greenhouse gas-induced weakening of the North Atlantic thermohaline circulation? *Geophysical Research Letters* **33**, L02606, doi: 10.1029/2005GL024980 (2006).

[22] Cai, W. *et al.* Pan-oceanic response to increasing anthropogenic aerosols: Impacts on the Southern Hemisphere oceanic circulation. *Geophysical Research Letters* **33**, L21707, doi: 10.1029/2006GL027513 (2006).

[23] Cai, W. *et al.* Anthropogenic aerosol forcing and the structure of temperature trends in the southern Indian Ocean. *Geophysical Research Letters* **34**, L14611, doi: 10.1029/2007GL030380 (2007).

[24] Cowan, T. & Cai, W. The response of the large-scale ocean circulation to 20th century Asian and non-Asian aerosols. *Geophysical Research Letters* **40**, 2761–2767, doi: 10.1002/grl.50587 (2013).

[25] Collier, M. A., Rotstayn, L. D., Kim, K.-Y., Hirst, A. C. & Jeffrey, S. J. Ocean circulation response to anthropogenic aerosol and greenhouse gas forcing in the CSIRO-Mk3.6 coupled climate model. *Australian Meteorological and Oceanographic Journal* **63**, 27–39, doi: 10.22499/2.6301.003 (2013).

[26] Menary, M. B. *et al.* Mechanisms of aerosol-forced AMOC variability in a state of the art climate model. *Journal of Geophysical Research: Oceans* **118**, 2087–2096, doi: 10.1002/jgrc.20178 (2013).

[27] Allen, R. J. *et al.* Climate and air quality impacts due to mitigation of non-methane near-term climate forcers. *Atmospheric Chemistry and Physics* **20**, 9641–9663 (2020).

[28] Allen, R. J. *et al.* Significant climate benefits from near-term climate forcer mitigation in spite of aerosol reductions. *Environmental Research Letters* **16**, 034010 (2021).

[29] Shindell, D. T., Voulgarakis, A., Faluvegi, G. & Milly, G. Precipitation response to regional radiative forcing. *Atmospheric Chemistry and Physics* **12**, 6969–6982, doi: 10.5194/acp–12–6969–2012 (2012).

[30] Etminan, M., Myhre, G., Highwood, E. & Shine, K. Radiative forcing of carbon dioxide, methane, and nitrous oxide: A significant revision of the methane radiative forcing. *Geophysical Research Letters* **43**, 12–614 (2016).

[31] Modak, A., Bala, G., Caldeira, K. & Cao, L. Does shortwave absorption by methane influence its effectiveness? *Climate Dynamics* **51**, 3653–3672 (2018).

[32] Myhre, G. *et al.* Anthropogenic and Natural Radiative Forcing. In: Climate Change 2013: The Physical Science Basis. Contribution of Working Group I to the Fifth Assessment Report of the Intergovernmental Panel on Climate Change [Stocker, T.F., D. Qin, G.-K. Plattner, M. Tignor, S.K. Allen, J. Boschung, A. Nauels, Y. Xia, V. Bex and P.M. Midgley (eds.)]. Tech. Rep., Cambridge University Press, Cambridge, United Kingdom and New York, NY, USA (2013).

[33] Shindell, D. T. *et al.* Radiative forcing in the ACCMIP historical and future climate simulations. *Atmospheric Chemistry and Physics* **13**, 2939–2974, doi:10.5194/acp–13–2939–2013 (2013).

[34] Haines, A. *et al.* Short-lived climate pollutant mitigation and the sustainable development goals. *Nature Climate Change* **7**, 863–869 (2017).

[35] Lelieveld, J. Clean air in the anthropocene. *Faraday discussions* **200**, 693–703 (2017).

[36] Shindell, D. *et al.* A climate policy pathway for near-and long-term benefits. *Science* **356**, 493–494 (2017).

[37] Boers, N. Observation-based early-warning signals for a collapse of the atlantic meridional overturning circulation. *Nature Climate Change* **11**, 680–688, doi: 10.1038/s41558–021–01097–4 (2021).

[38] Collins, W. J. *et al.* AerChemMIP: quantifying the effects of chemistry and aerosols in CMIP6. *Geoscientific Model Development* **10**, 585–607, doi: 10.5194/gmd–10–585–2017 (2017).

[39] Eyring, V. *et al.* Overview of the Coupled Model Intercomparison Project Phase 6 (CMIP6) experimental design and organization. *Geoscientific Model Development* **9**, 1937–1958, doi: 10.5194/gmd–9–1937–2016 (2016).

[40] Change, I. C. The physical science basis, summary for policymakers, contribution of wgi to the fifth assessment report of the intergovernmental panel on climate change (2013).

[41] Ramanathan, V., Crutzen, P. J., Kiehl, J. & Rosenfeld, D. Aerosols, climate, and the hydrological cycle. *science* **294**, 2119–2124 (2001).

[42] Vecchi, G. A. & Soden, B. J. Global warming and the weakening of the tropical circulation. *Journal of Climate* **20**, 4316–4340 (2007).

[43] Held, I. M. & Soden, B. J. Robust responses of the hydrological cycle to global warming. *Journal of climate* **19**, 5686–5699 (2006).

[44] Pye, H. *et al.* Effect of changes in climate and emissions on future sulfate-nitrate-ammonium aerosol levels in the united states. *Journal of Geophysical Research: Atmospheres* **114** (2009).

[45] Racherla, P. N. & Adams, P. J. Sensitivity of global tropospheric ozone and fine particulate matter concentrations to climate change. *Journal of Geophysical Research: Atmospheres* **111** (2006).

[46] Westervelt, D. *et al.* Quantifying pm2. 5-meteorology sensitivities in a global climate model. *Atmospheric environment* **142**, 43–56 (2016).

[47] Allen, R. J., Landuyt, W. & Rumbold, S. T. An increase in aerosol burden and radiative effects in a warmer world. *Nature Climate Change* **6**, 269–274 (2016).

[48] Fang, Y. *et al.* The impacts of changing transport and precipitation on pollutant distributions in a future climate. *Journal of Geophysical Research: Atmospheres* **116** (2011).

[49] Lamarque, J.-F. *et al.* The atmospheric chemistry and climate model intercomparison project (accmip): Overview and description of models, simulations and climate diagnostics. *Geoscientific Model Development* **6**, 179–206 (2013).

[50] Silva, R. A. *et al.* Future global mortality from changes in air pollution attributable to climate change. *Nature climate change* **7**, 647–651 (2017).

[51] Textor, C. *et al.* Analysis and quantification of the diversities of aerosol life cycles within aerocom. *Atmospheric Chemistry and Physics* **6**, 1777–1813 (2006).

[52] Allen, R. J. & Landuyt, W. The vertical distribution of black carbon in cmip5 models: Comparison to observations and the importance of convective transport. *Journal of Geophysical Research: Atmospheres* **119**, 4808–4835 (2014).

[53] Sutton, R. T., Dong, B. & Gregory, J. M. Land/sea warming ratio in response to climate change: Ipcc ar4 model results and comparison with observations. *Geophysical research letters* **34** (2007).

[54] Boer, G. The ratio of land to ocean temperature change under global warming. *Climate dynamics* **37**, 2253–2270 (2011).

[55] Byrne, M. P. & O'Gorman, P. A. Link between land-ocean warming contrast and surface relative humidities in simulations with coupled climate models. *Geophysical Research Letters* **40**, 5223–5227 (2013).

[56] Joshi, M. & Gregory, J. Dependence of the land-sea contrast in surface climate response on the nature of the forcing. *Geophysical Research Letters* **35** (2008).

[57] Fasullo, J. T. Robust land–ocean contrasts in energy and water cycle feedbacks. *Journal of Climate* **23**, 4677–4693 (2010).

[58] Clark, R. T., Murphy, J. M. & Brown, S. J. Do global warming targets limit heatwave risk? *Geophysical Research Letters* **37** (2010).

[59] Neale, R. B. *et al.* Description of the ncar community atmosphere model (cam 5.0). *NCAR Tech. Note NCAR/TN-486+ STR* **1**, 1–12 (2010).

[60] Atlas, E. & Giam, C. Ambient concentration and precipitation scavenging of atmospheric organic pollutants. *Water, air, and soil pollution* **38**, 19–36 (1988).

[61] Rowell, D. P. & Jones, R. G. Causes and uncertainty of future summer drying over europe. *Climate Dynamics* **27**, 281–299 (2006).

[62] Simmons, A., Willett, K., Jones, P., Thorne, P. & Dee, D. Low-frequency variations in surface atmospheric humidity, temperature, and precipitation: Inferences from reanalyses and monthly gridded observational data sets. *Journal of Geophysical Research: Atmospheres* **115** (2010).

[63] Allen, R. & Zender, C. The role of eastern siberian snow and soil moisture anomalies in quasi-biennial persistence of the arctic and north atlantic oscillations. *Journal of Geophysical Research: Atmospheres* **116** (2011).

[64] Sejas, S. A., Albert, O. S., Cai, M. & Deng, Y. Feedback attribution of the land-sea warming contrast in a global warming simulation of the ncar ccsm4. *Environmental Research Letters* **9**, 124005 (2014).

[65] Chang, E. K., Guo, Y., Xia, X. & Zheng, M. Storm-track activity in ipcc ar4/cmip3 model simulations. *Journal of climate* **26**, 246–260 (2013).

[66] Chang, E. K., Guo, Y. & Xia, X. Cmip5 multimodel ensemble projection of storm track change under global warming. *Journal of Geophysical Research: Atmospheres* **117** (2012).

[67] Liu, X. *et al.* Toward a minimal representation of aerosols in climate models: Description and evaluation in the community atmosphere model cam5. *Geoscientific Model Development* **5**, 709–739 (2012).

[68] Rasch, P. *et al.* A comparison of scavenging and deposition processes in global models: results from the wcrp cambridge workshop of 1995. *Tellus B* **52**, 1025–1056 (2000).

[69] Hou, P., Wu, S., McCarty, J. L. & Gao, Y. Sensitivity of atmospheric aerosol scavenging to precipitation intensity and frequency in the context of global climate change. *Atmospheric Chemistry and Physics* **18**, 8173–8182 (2018).

[70] Emmons, L. K. *et al.* Description and evaluation of the model for ozone and related chemical tracers, version 4 (mozart-4). *Geoscientific Model Development* **3**, 43–67 (2010).

[71] Delworth, T. L. & Mann, M. E. Observed and simulated multidecadal variability in the Northern Hemisphere. *Climate Dynamics* **16**, 661–676, doi: 10.1007/s003820000075 (2000).

[72] Knight, J. R., Allan, R. J., Folland, C. K., Vellinga, M. & Mann, M. E. A signature of persistent natural thermohaline circulation cycles in observed climate. *Geophysical Research Letters* **32**, L20708, doi: 10.1029/2005GL024233 (2005).

[73] Drijfhout, S., van Oldenborgh, G. J. & Cimatoribus, A. Is a decline of AMOC causing the warming hole above the North Atlantic in observed and modeled warming patterns? *Journal of Climate* **25**, 8373–8379, doi: 10.1175/JCLI–D–12–00490.1 (2012).

[74] Winton, M., Griffies, S. M., Samuels, B. L., Sarmiento, J. L. & Frölicher, T. L. Connecting changing ocean circulation with changing climate. *Journal of Climate* **26**, 2268–2278, doi: 10.1175/JCLI–D–12–00296.1 (2013).

[75] Marshall, J., Donohoe, A., Ferreira, D. & McGee, D. The ocean's role in setting the mean position of the Inter-Tropical Convergence Zone. *Climate Dynamics* **42**, 1967–1979, doi: 10.1007/s00382–013–1767–z (2014).

[76] Marshall, J. *et al.* The ocean's role in the transient response of climate to abrupt greenhouse gas forcing. *Climate Dynamics* **44**, 2287–2299, doi: 10.1007/s00382–014–2308–0 (2015).

[77] Liu, W., Fedorov, A. V., Xie, S.-P. & Hu, S. Climate impacts of a weakened Atlantic Meridional Overturning Circulation in a warming climate. *Science Advances* **6**, doi: 10.1126/sciadv.aaz4876 (2020).

[78] Broecker, W. S. Thermohaline circulation, the achilles heel of our climate system: Will man-made co2 upset the current balance? *Science* **278**, 1582–1588, doi: 10.1126/science.278.5343.1582 (1997).

[79] McCarthy, G. *et al.* Observed interannual variability of the Atlantic meridional overturning circulation at 26.5 °N. *Geophysical Research Letters* **39**, L19609, doi: 10.1029/2012GL052933 (2012).

[80] Smeed, D. A. *et al.* Observed decline of the Atlantic meridional overturning circulation 2004–2012. *Ocean Science* **10**, 29–38, doi: 10.5194/os–10–29–2014 (2014).

[81] Sévellec, F., Fedorov, A. V. & Liu, W. Arctic sea-ice decline weakens the Atlantic Meridional Overturning Circulation. *Nature Climate Change* **7**, 604–610, doi: 10.1038/nclimate3353 (2017).

[82] Zhao, J. & Johns, W. Wind-forced interannual variability of the Atlantic Meridional Overturning Circulation at 26.5 °N. *Journal of Geophysical Research: Oceans* **119**, 2403–2419, doi: 10.1002/2013JC009407 (2014).

[83] Jackson, L. C., Peterson, K. A., Roberts, C. D. & Wood, R. A. Recent slowing of Atlantic overturning circulation as a recovery from earlier strengthening. *Nature Geoscience* **9**, 518–522, doi: 10.1038/ngeo2715 (2016).

[84] Yan, X., Zhang, R. & Knutson, T. R. Underestimated AMOC variability and implications for AMV and predictability in CMIP models. *Geophysical Research Letters* **45**, 4319–4328, doi: 10.1029/2018GL077378 (2018).

[85] Rahmstorf, S. *et al.* Exceptional twentieth-century slowdown in Atlantic Ocean overturning circulation. *Nature Climate Change* **5**, 475–480, doi: 10.1038/nclimate2554 (2015).

[86] Thorpe, R., Gregory, J. M., Johns, T., Wood, R. & Mitchell, J. Mechanisms determining the atlantic thermohaline circulation response to greenhouse gas forcing in a non-flux-adjusted coupled climate model. *Journal of Climate* **14**, 3102–3116 (2001).

[87] Liu, W., Fedorov, A. & Sévellec, F. The mechanisms of the Atlantic Meridional Overturning Circulation slowdown induced by Arctic sea ice decline. *Journal of Climate* **32**, 977–996, doi: 10.1175/JCLI–D–18–0231.1 (2019).

[88] Hu, S. & Fedorov, A. V. Indian Ocean warming can strengthen the Atlantic meridional overturning circulation. *Nature Climate Change* **9**, 747–751, doi: 10.1038/s41558–019–0566–x (2019).

[89] Booth, B. B. B., Dunstone, N. J., Halloran, P. R., Andrews, T. & Bellouin, N. Aerosols implicated as a prime driver of twentieth-century North Atlantic climate variability. *Nature* **484**, 228–232, doi: 10.1038/nature10946 (2012).

[90] Zhang, R. *et al.* Have aerosols caused the observed Atlantic multidecadal variability? *Journal of the Atmospheric Sciences* **70**, 1135–1144, doi: 10.1175/JAS–D–12–0331.1 (2013).

[91] Evan, A. T., Vimont, D. J., Heidinger, A. K., Kossin, J. P. & Bennartz, R. The role of aerosols in the evolution of tropical North Atlantic Ocean temperature anomalies. *Science* **324**, 778–781 (2009).

[92] Otterå, O. H., Bentsen, M., Drange, H. & Suo, L. External forcing as a metronome for Atlantic multidecadal variability. *Nature Geoscience* **3**, 688–694, doi: 10.1038/ngeo955 (2010).

[93] Chang, C.-Y., Chiang, J. C. H., Wehner, M. F., Friedman, A. R. & Ruedy, R. Sulfate aerosol control of tropical Atlantic climate over the Twentieth century. *Journal of Climate* **24**, 2540–2555, doi: 10.1175/2010JCLI4065.1 (2011).

[94] Allen, R. J., Evan, A. T. & Booth, B. B. B. Interhemispheric aerosol radiative forcing and tropical precipitation shifts during the late twentieth century. *Journal of Climate* **28**, 8219–8246, doi: 10.1175/JCLI–D–15–0148.1 (2015).

[95] Murphy, L. N., Bellomo, K., Cane, M. & Clement, A. The role of historical forcings in simulating the observed Atlantic multidecadal oscillation. *Geophysical Research Letters* **44**, 2472–2480, doi: 10.1002/2016GL071337 (2017).

[96] Bellomo, K., Murphy, L. N., Cane, M. A., Clement, A. C. & Polvani, L. M. Historical forcings as main drivers of the Atlantic multidecadal variability in the CESM large ensemble. *Climate Dynamics* **50**, 3687–3698, doi: 10.1007/s00382–017–3834–3 (2018).

[97] Menary, M. B. *et al.* Aerosol-forced AMOC changes in CMIP6 historical simulations. *Geophysical Research Letters* **47**, e2020GL088166, doi: 10.1029/2020GL088166 (2020).

[98] Ma, X., Liu, W., Allen, R. J., Huang, G. & Li, X. Dependence of regional ocean heat uptake on anthropogenic warming scenarios. *Science advances* **6**, eabc0303 (2020).

[99] Liu, W., Xie, S.-P., Liu, Z. & Zhu, J. Overlooked possibility of a collapsed Atlantic Meridional Overturning Circulation in warming climate. *Science Advances* **3**, doi: 10.1126/sciadv.1601666 (2017).

[100] Palmer, M. D. & McNeall, D. J. Internal variability of earth's energy budget simulated by CMIP5 climate models. *Environmental Research Letters* **9**, 034016, doi: 10.1088/1748–9326/9/3/034016 (2014).

[101] Levitus, S. *et al.* World ocean heat content and thermosteric sea level change (0–2000 m), 1955–2010. *Geophysical Research Letters* **39**, doi: 10.1029/2012GL051106 (2012).

[102] Fofonoff, N. P. & Millard Jr, R. Algorithms for the computation of fundamental properties of seawater. (1983).

[103] Monin, A. S. & Obukhov, A. M. Basic laws of turbulent mixing in the surface layer of the atmosphere. *Contributions of the Geophysical Institute of the Slovak Academy of Sciences* **24**, 163–187 (1954).

[104] Grachev, A. A. & Fairall, C. W. Dependence of the Monin–Obukhov Stability Parameter on the Bulk Richardson Number over the Ocean. *Journal of Applied Meteorology* **36**, 406–414, doi: 10.1175/1520–0450(1997)036¡0406:DOTMOS¿2.0.CO;2 (1997).

[105] Maronga, B. Monin–obukhov similarity functions for the structure parameters of temperature and humidity in the unstable surface layer: Results from high-resolution large-eddy simulations. *Journal of the Atmospheric Sciences* **71**, 716–733, doi: 10.1175/JAS–D–13–0135.1 (2014).

[106] Chang, E. K. M., Zheng, C., Lanigan, P., Yau, A. M. W. & Neelin, J. D. Significant modulation of variability and projected change in California winter precipitation by extratropical cyclone activity. *Geophys. Res. Lett.* **42**, 5983–5991, DOI: 10.1002/2015GL064424 (2015).

[107] Allen, R. J. & Luptowitz, R. El Niño-like teleconnection increases California precipitation in response to warming. *Nature Communications* **8**, 16055, doi: 10.1038/ncomms16055 (2017).

[108] Forster, P. M. *et al.* Recommendations for diagnosing effective radiative forcing from climate models for CMIP6. *Journal of Geophysical Research: Atmospheres* **121**, 12,460–12,475, doi: 10.1002/2016JD025320 (2016).

[109] Eden, C. & Jung, T. North Atlantic interdecadal variability: Oceanic response to the North Atlantic Oscillation (1865–1997). *Journal of Climate* **14**, 676–691, doi: 10.1175/1520–0442(2001)014¡0676:NAIVOR¿2.0.CO;2 (2001).

[110] Kawase, M. Establishment of deep ocean circulation driven by deep-water production. *Journal of Physical Oceanography* **17**, 2294–2317, doi: 10.1175/1520–0485(1987)017¡2294:EODOCD¿2.0.CO;2 (1987).

[111] Huang, R. X., Cane, M. A., Naik, N. & Goodman, P. Global adjustment of the thermocline in response to deepwater formation. *Geophysical Research Letters* **27**, 759–762, doi: 10.1029/1999GL002365 (2000).

[112] Johnson, H. L. & Marshall, D. P. A theory for the surface Atlantic response to thermohaline variability. *Journal of Physical Oceanography* **32**, 1121–1132, doi: 10.1175/1520–0485(2002)032¡1121:ATFTSA¿2.0.CO;2 (2002).

[113] Cessi, P., Bryan, K. & Zhang, R. Global seiching of thermocline waters between the Atlantic and the Indian-Pacific Ocean Basins. *Geophysical Research Letters* **31**, doi: 10.1029/2003GL019091 (2004).

[114] Zhang, R. Latitudinal dependence of Atlantic meridional overturning circulation (AMOC) variations. *Geophysical Research Letters* **37**, doi: 10.1029/2010GL044474 (2010).

[115] Hoesly, R. M. *et al.* Historical (1750–2014) anthropogenic emissions of reactive gases and aerosols from the Community Emissions Data System (CEDS). *Geoscientific Model Development* **11**, 369–408, doi: 10.5194/gmd–11–369–2018 (2018).

[116] Klein, S. A. & Hartmann, D. L. The seasonal cycle of low stratiform clouds. *J. Climate* **6**, 1587–1606 (1993).

[117] Zhu, C. & Liu, Z. Weakening atlantic overturning circulation causes south atlantic salinity pile-up. *Nature Climate Change* **10**, 998–1003 (2020).

[118] Liu, W. & Liu, Z. A diagnostic indicator of the stability of the atlantic meridional overturning circulation in ccsm3. *Journal of Climate* **26**, 1926–1938 (2013).

[119] Rahmstorf, S. On the freshwater forcing and transport of the Atlantic thermohaline circulation. *Climate Dynamics* **12**, 799–811, doi: 10.1007/s003820050144 (1996).

[120] Drijfhout, S. S., Weber, S. L. & van der Swaluw, E. The stability of the MOC as diagnosed from model projections for pre-industrial, present and future climates. *Climate Dynamics* **37**, 1575–1586, doi: 10.1007/s00382–010–0930–z (2011).

[121] Danabasoglu, G. *et al.* North Atlantic simulations in Coordinated Ocean-ice Reference Experiments phase II (CORE-II). Part I: Mean states. *Ocean Modelling* **73**, 76–107, doi: 10.1016/j.ocemod.2013.10.005 (2014).

[122] Danabasoglu, G. *et al.* North Atlantic simulations in Coordinated Ocean-ice Reference Experiments phase II (CORE-II). Part II: Inter-annual to decadal variability. *Ocean Modelling* **97**, 65–90, doi: 10.1016/j.ocemod.2015.11.007 (2016).

[123] Bakker, P. *et al.* Fate of the Atlantic Meridional Overturning Circulation: Strong decline under continued warming and Greenland melting. *Geophysical Research Letters* **43**, 12,252–12,260, doi: 10.1002/2016GL070457 (2016).

[124] Bellouin, N. *et al.* Bounding global aerosol radiative forcing of climate change. *Reviews of Geophysics* **58**, e2019RG000660 (2020).

[125] Smith, C. *et al.* Effective radiative forcing and adjustments in cmip6 models. *Atmos. Chem. Phys. Discuss., https://doi. org/10.5194/acp-2019-1212* **885** (2020).

[126] Allen, R. J. A 21st century northward tropical precipitation shift caused by future anthropogenic aerosol reductions. *Journal of Geophysical Research: Atmospheres* **120**, 9087–9102, doi: 10.1002/2015JD023623 (2015).

[127] Meehl, G. A. *et al.* Context for interpreting equilibrium climate sensitivity and transient climate response from the cmip6 earth system models. *Science Advances* **6**, eaba1981 (2020).

[128] Keil, P. *et al.* Multiple drivers of the north atlantic warming hole. *Nature Climate Change* 1–5 (2020).

[129] Chen, X. & Tung, K.-K. Global surface warming enhanced by weak atlantic overturning circulation. *Nature* **559**, 387–391 (2018).

[130] O'Neill, B. C. *et al.* A new scenario framework for climate change research: the concept of shared socioeconomic pathways. *Climatic Change* **122**, 387–400, doi: 10.1007/s10584–013–0905–2 (2014).

[131] Jackson, L. C. & Wood, R. A. Fingerprints for early detection of changes in the AMOC. *Journal of Climate* **33**, 7027–7044, doi: 10.1175/JCLI–D–20–0034.1 (2020).

[132] Keil, P. *et al.* Multiple drivers of the North Atlantic warming hole. *Nature Climate Change* **10**, 667–671, doi: 10.1038/s41558–020–0819–8 (2020).

[133] Zhu, C. & Liu, Z. Weakening Atlantic overturning circulation causes South Atlantic salinity pile-up. *Nature Climate Change* **10**, 998–1003, doi: 10.1038/s41558–020–0897–7 (2020).

[134] Boers, N. Observation-based early-warning signals for a collapse of the Atlantic Meridional Overturning Circulation. *Nature Climate Change* **11**, 680–688, doi: 10.1038/s41558–021–01097–4 (2021).

[135] Mikolajewicz, U. & Voss, R. The role of the individual air-sea flux components in $CO_2$-induced changes of the ocean's circulation and climate. *Climate Dynamics* **16**, 627–642, doi: 10.1007/s003820000066 (2000).

[136] Weijer, W., Cheng, W., Garuba, O. A., Hu, A. & Nadiga, B. T. CMIP6 models predict significant 21st century decline of the Atlantic Meridional Overturning Circulation. *Geophysical Research Letters* **47**, e2019GL086075, doi: 10.1029/2019GL086075 (2020).

[137] Bellomo, K., Angeloni, M., Corti, S. & von Hardenberg, J. Future climate change shaped by inter-model differences in Atlantic meridional overturning circulation response. *Nature Communications* **12**, 3659, doi: 10.1038/s41467–021–24015–w (2021).

[138] Delworth, T. L., Ramaswamy, V. & Stenchikov, G. L. The impact of aerosols on simulated ocean temperature and heat content in the 20th century. *Geophysical Research Letters* **32**, L24709, doi: 10.1029/2005GL024457 (2005).

[139] Hassan, T., Allen, R. J., Liu, W. & Randles, C. A. Anthropogenic aerosol forcing of the Atlantic meridional overturning circulation and the associated mechanisms in CMIP6 models. *Atmospheric Chemistry and Physics* **21**, 5821–5846, doi: 10.5194/acp–21–5821–2021 (2021).

[140] Fiore, A. M. *et al.* Global air quality and climate. *Chem. Soc. Rev.* **41**, 6663–6683, doi: 10.1039/C2CS35095E (2012).

[141] WHO. Ambient air pollution: A global assessment of exposture and burden of disease. Tech. Rep. ISBN: 9789241511353, World Health Organization (2016).

[142] Cohen, A. J. *et al.* Estimates and 25-year trends of the global burden of disease attributable to ambient air pollution: an analysis of data from the Global Burden of Diseases Study 2015. *The Lancet* **389**, 1907–1918, doi: 10.1016/S0140–6736(17)30505–6 (2017).

[143] Butt, E. W. *et al.* Global and regional trends in particulate air pollution and attributable health burden over the past 50 years. *Environmental Research Letters* **12**, 104017, doi: 10.1088/1748–9326/aa87be (2017).

[144] Rotstayn, L. D., Collier, M. A., Chrastansky, A., Jeffrey, S. J. & Luo, J. J. Projected effects of declining aerosol in RCP4.5: unmasking global warming? *Atmos. Chem. Phys.* **13**, 10883–10905 (2013).

[145] Westervelt, D. M., Horowitz, L. W., Naik, V., Golaz, J.-C. & Mauzerall, D. L. Radiative forcing and climate response to projected 21st century aerosol decreases. *Atmospheric Chemistry and Physics* **15**, 12681–12703, doi: 10.5194/acp–15–12681–2015 (2015).

[146] Samset, B. H. *et al.* Climate impacts from a removal of anthropogenic aerosol emissions. *Geophysical Research Letters* **45**, 1020–1029, doi: 10.1002/2017GL076079 (2018).

[147] Shindell, D. T. *et al.* Simultaneously mitigating near-term climate change and improving human health and food security. *Science* **335**, 183–189, doi: 10.1126/science.1210026 (2012).

[148] Stohl, A. *et al.* Evaluating the climate and air quality impacts of short-lived pollutants. *Atmospheric Chemistry and Physics* **15**, 10529–10566, doi: 10.5194/acp–15–10529–2015 (2015).

[149] Lelieveld, J. *et al.* Effects of fossil fuel and total anthropogenic emission removal on public health and climate. *Proceedings of the National Academy of Sciences* **116**, 7192–7197, doi: 10.1073/pnas.1819989116 (2019).

[150] Shindell, D. & Smith, C. J. Climate and air-quality benefits of a realistic phase-out of fossil fuels. *Nature* **573**, 408–411, doi: 10.1038/s41586–019–1554–z (2019).

[151] Allen, R. J. *et al.* Climate and air quality impacts due to mitigation of non-methane near-term climate forcers. *Atmospheric Chemistry and Physics* doi: 10.5194/acp–2019–1209 (2020 (accepted)).

[152] Allen, R. J. *et al.* Significant climate benefits from near-term climate forcer mitigation in spite of aerosol reductions. *Environmental Research Letters* doi: 10.1088/1748–9326/abe06b (2021).

[153] Dixon, K. W., Delworth, T. L., Spelman, M. J. & Stouffer, R. J. The influence of transient surface fluxes on North Atlantic overturning in a coupled GCM climate change experiment. *Geophysical Research Letters* **26**, 2749–2752, doi: 10.1029/1999GL900571 (1999).

[154] Biastoch, A., Böning, C. W., Getzlaff, J., Molines, J.-M. & Madec, G. Causes of interannual-decadal variability in the meridional overturning circulation of the midlatitude North Atlantic Ocean. *Journal of Climate* **21**, 6599–6615, doi: 10.1175/2008JCLI2404.1 (2008).

[155] Yeager, S. & Danabasoglu, G. The origins of late-twentieth-century variations in the large-scale North Atlantic circulation. *Journal of Climate* **27**, 3222–3247, doi: 10.1175/JCLI–D–13–00125.1 (2014).

[156] Dima, M., Nichita, D. R., Lohmann, G., Ionita, M. & Voiculescu, M. Early-onset of Atlantic Meridional Overturning Circulation weakening in response to atmospheric $CO_2$ concentration. *npj Climate and Atmospheric Science* **4**, 27, doi: 10.1038/s41612–021–00182–x (2021).

[157] Ma, X., Liu, W., Allen, R. J., Huang, G. & Li, X. Dependence of regional ocean heat uptake on anthropogenic warming scenarios. *Science Advances* **6**, doi: 10.1126/sciadv.abc0303 (2020).

[158] Steinacher, M. & Joos, F. Transient earth system responses to cumulative carbon dioxide emissions: linearities, uncertainties, and probabilities in an observation-constrained model ensemble. *Biogeosciences* **13**, 1071–1103, doi: 10.5194/bg–13–1071–2016 (2016).

[159] Notz, D. & Stroeve, J. Observed Arctic sea-ice loss directly follows anthropogenic $CO_2$ emission. *Science* **354**, 747–750, doi: 10.1126/science.aag2345 (2016).

[160] Liu, W. & Liu, Z. A diagnostic indicator of the stability of the Atlantic meridional overturning circulation in CCSM3. *J. Climate* **26**, 1926–1938 (2013).

[161] Toll, V., Christensen, M., Quaas, J. & Bellouin, N. Weak average liquid-cloud-water response to anthropogenic aerosols. *Nature* **572**, 51–55, doi: 10.1038/s41586–019–1423–9 (2019).

[162] Bellouin, N. *et al.* Bounding global aerosol radiative forcing of climate change. *Reviews of Geophysics* **58**, e2019RG000660, doi: 10.1029/2019RG000660 (2020).

[163] Smith, C. J. *et al.* Effective radiative forcing and adjustments in CMIP6 models. *Atmospheric Chemistry and Physics Discussions* **2020**, 1–37, doi: 10.5194/acp–2019–1212 (2020).

[164] van Noije, T. *et al.* EC-Earth3-AerChem: a global climate model with interactive aerosols and atmospheric chemistry participating in CMIP6. *Geoscientific Model Development* **14**, 5637–5668, doi: 10.5194/gmd–14–5637–2021 (2021).

[165] van Vuuren, D. P. *et al.* A new scenario framework for climate change research: scenario matrix architecture. *Climatic Change* **122**, 373–386, doi: 10.1007/s10584–013–0906–1 (2014).

[166] Gidden, M. J. *et al.* Global emissions pathways under different socioeconomic scenarios for use in CMIP6: a dataset of harmonized emissions trajectories through the end of the century. *Geoscientific Model Development* **12**, 1443–1475, doi: 10.5194/gmd–12–1443–2019 (2019).

[167] Rao, S. *et al.* Future air pollution in the shared socio-economic pathways. *Global Environmental Change* **42**, 346–358, doi: 10.1016/j.gloenvcha.2016.05.012 (2017).

[168] Fujimori, S. *et al.* SSP3: AIM implementation of Shared Socioeconomic Pathways. *Global Environmental Change* **42**, 268–283, doi: 10.1016/j.gloenvcha.2016.06.009 (2017).

[169] O'Neill, B. C. *et al.* The Scenario Model Intercomparison Project (ScenarioMIP) for CMIP6. *Geoscientific Model Development* **9**, 3461–3482, doi: 10.5194/gmd–9–3461–2016 (2016).

[170] Sellar, A. A. *et al.* UKESM1: Description and Evaluation of the U.K. Earth System Model. *Journal of Advances in Modeling Earth Systems* **11**, 4513–4558, doi: 10.1029/2019MS001739 (2019).

[171] Archibald, A. T. *et al.* Description and evaluation of the UKCA stratosphere–troposphere chemistry scheme (StratTrop vn 1.0) implemented in UKESM1. *Geoscientific Model Development* **13**, 1223–1266, doi: 10.5194/gmd–13–1223–2020 (2020).

[172] Mulcahy, J. P. *et al.* Description and evaluation of aerosol in UKESM1 and HadGEM3-GC3.1 CMIP6 historical simulations. *Geoscientific Model Development* **13**, 6383–6423, doi: 10.5194/gmd–13–6383–2020 (2020).

[173] Yukimoto, S. *et al.* The meteorological research institute earth system model version 2.0, mri-esm2.0: Description and basic evaluation of the physical component. *J. Meteor. Soc. Japan* **97**, 931–965, doi: 10.2151/jmsj.2019–051 (2019).

[174] Oshima, N. *et al.* Global and Arctic effective radiative forcing of anthropogenic gases and aerosols in MRI-ESM2.0. *Progress in Earth and Planetary Science* **7**, 38, doi: 10.1186/s40645–020–00348–w (2020).

[175] van Noije, T. P. C. *et al.* Simulation of tropospheric chemistry and aerosols with the climate model EC-Earth. *Geoscientific Model Development* **7**, 2435–2475, doi: 10.5194/gmd–7–2435–2014 (2014).

[176] Bauer, S. E. *et al.* Historical (1850–2014) aerosol evolution and role on climate forcing using the GISS ModelE2.1 contribution to CMIP6. *Journal of Advances in Modeling Earth Systems* **12**, e2019MS001978, doi: 10.1029/2019MS001978 (2020).

[177] Vickers, D. & Mahrt, L. Evaluation of the air-sea bulk formula and sea-surface temperature variability from observations. *Journal of Geophysical Research: Oceans* **111**, doi: 10.1029/2005JC003323 (2006).

# Appendix A

# Appendix to Enhanced land–sea warming contrast elevates aerosol pollution in a warmer world

## A.1 Appendix A Text

### A.1.1 Storm Track Activity Analysis

Storm track activity (zz), based on daily 500 hPa heights (Z), is calculated using a 24-hour difference filter:

$$zz = \overline{[Z(t + 24\ hour) - Z(t)]^2}, \tag{A.1}$$

The overbar corresponds to time averaging over each season (e.g., JJA). We focus on daily data, but 6- hourly data yields similar results. Moreover, similar results are obtained with sea-level pressure (not shown).

Consistent with prior results, CAM5 warming simulations yield a decrease in NH mid-latitude storm track activity during most seasons, including JJA. However, the JJA storm track activity decrease occurs over both land and ocean, with similar magnitude (Supplementary Figure 10). This is in opposition to the land-sea contrast in LSP, low cloud and other hydrological variables (e.g., Supplementary Figure 3). In the NH mid-latitudes, JJA LSP significantly decreases over land, but significantly increases over sea. If changes in storm track activity drive LSP changes, the decrease in storm track activity over land and sea would imply decreases in LSP over both. But this is not the case, which suggests the decrease in storm track activity is not the dominant driver of the JJA decrease in LSP over land in the NH mid-latitudes.

CAM5 muted warming simulations (not included) show that as the land warming is initially muted (going from 0% to 1%), there is a smaller decrease in JJA storm track activity, which is consistent with the weaker decrease in LSP (e.g., Supplementary Figure 1). However, this occurs over both land and sea, which is again in disagreement with the land-sea contrast in LSP in the muted warming simulations. Furthermore, there are minimal differences in the storm track activity response in the 1%, 2.5% and 5% muted warming simulations (with 2.5% yielding a weaker decrease then 5%), particularly over land.

### A.1.2 Spatial Correlation and Composite Difference Analysis

In CAM5, the spatial (grid box by grid box) JJA NH mid-latitude land correlation between the change in storm track activity and the change in LSP is weak at 0.16. The corresponding correlation in the control simulation is also relatively weak at 0.19. Based on CMIP5 RCP8.5 models (17 models with 25 realizations), the corresponding inter-model JJA NH mid-latitude land-based correlation between the change (2090-2099 relative to 2006-2015) in LSP and storm track activity is also weak and not significant at the 90% confidence level, at -0.21 (it is also of the wrong sign).

However, the CAM5 spatial JJA NH mid-latitude land correlation between SCLOW and low-level RH (LSP) is 0.72 (0.55) in the control simulation. The corresponding correlation between the change in SCLOW and the change in low-level RH (LSP) is 0.52 (0.43). The corresponding CMIP5 inter-model correlation between the change in low-level RH and total cloud cover is stronger at 0.33 (significant at the 90% confidence level), as is the corresponding correlation between the change in cloud cover and LSP at 0.41 (significant at the 95% confidence level). Thus, the correlation between LSP and SCLOW is larger than that based on storm track activity, of the expected sign, and statistically significant.

The above correlations are based on grid box by grid box relationships, which may not accurately reflect the role of the storm track on LSP (e.g., over larger spatial scales). Thus, we also analyze composite differences of the storm track activity response (2090-2099 relative to 2006-2015) between CMIP5 models that yield the largest decrease in NH mid-

latitude JJA continental LSP and the models that yield the smallest decrease (or increase). More specifically, models are subdivided into two groups, one that simulates a LSP change that falls below the mean LSP change minus one standard deviation and one that simulates a LSP change that falls above the mean LSP change plus one standard deviation. This results in 10 realizations with relatively large LSP decreases ("LG_LSP_DEC" subset) and 12 realizations with relatively small decreases (or increases) in LSP ("SM_LSP_DEC" subset). This yields a LSP composite difference (LG_LSP_DEC minus SM_LSP_DEC) of -18.8%, significant at the 99% confidence level.

This composite difference does not show a clear signal that would be indicative of a significant storm track role in dictating LSP changes (i.e., larger decrease in the storm track activity response in models that simulate a larger decrease in LSP, relative to those that simulate a weak decrease in LSP). The corresponding storm track activity composite difference is actually positive and not significant at 19.2 m$^2$ (1.1% percent change). The corresponding cloud cover difference is -2.0% (-5.4% percent change) significant at the 99% confidence level. Thus, as with the grid box correlations, there is minimal evidence that changes in storm track activity drive significant changes in LSP; however, there is evidence that decreases in LSP are related to decreases in cloud cover.

### A.1.3 Regression Model Analysis

Further investigation of the JJA NH mid-latitude continental change in the distribution of daily LSP shows that all of the decrease occurs at percentiles less than or equal to the 99th percentile (percentiles are based on the control simulation and are calculated at

131

each grid box). Here, LSP decreases by -5.2 mm month$^{-1}$. In contrast, LSP increases by 1.9 mm month-1 on days exceeding the 99th percentile. This increase is likely associated with more atmospheric water vapor under warming, which leads to an increase in the frequency of extreme precipitation (e.g., JJA NH mid-latitude continental precipitable water increases by 35.4% in the default warming simulation).

Using a regression model comprised of SCLOW versus LSP values from the control simulation ($R^2$=0.30) predicts reasonably well the actual change in JJA NH mid-latitude continental LSP. Using the entire distribution of LSP, this model overestimates the LSP reduction (-6.4 versus the actual -3.3 mm month$^{-1}$). However, using LSP restricted to days less than or equal to the 99th percentile, the corresponding estimate is in better agreement to the actual LSP decrease (-5.5 versus -5.2 mm month$^{-1}$; Supplementary Figure 11). A similar regression model based on lower-tropospheric RH (R2=0.46) also performs well, yielding an estimated LSP reduction of -5.6 mm month$^{-1}$. However, storm track activity underestimates the LSP decrease using both the entire LSP distribution (-1.3 mm month$^{-1}$) and that confined to less than or equal to the 99th percentile (-1.1 mm month$^{-1}$). Moreover, as previously stated, the LSP versus storm track regression model is poor ($R^2 = 0.03$).

## A.2    Appendix A Tables

Table A.1: **Land-Sea warming ratio based on CAM5 simulations.** Columns show the warming ratio (lower-tropospheric land warming divided by that over the ocean) calculated over the globe, NH mid-latitudes (30-60°N) and tropics (30°S-30°N). The first four rows show the warming ratio for the default warming simulation, and the three muted land warming (i.e., nudged) simulations. The last row shows the warming ratio percent change between the 5% nudged simulation and the default warming simulation. The lower troposphere extends from the surface to 900 hPa.

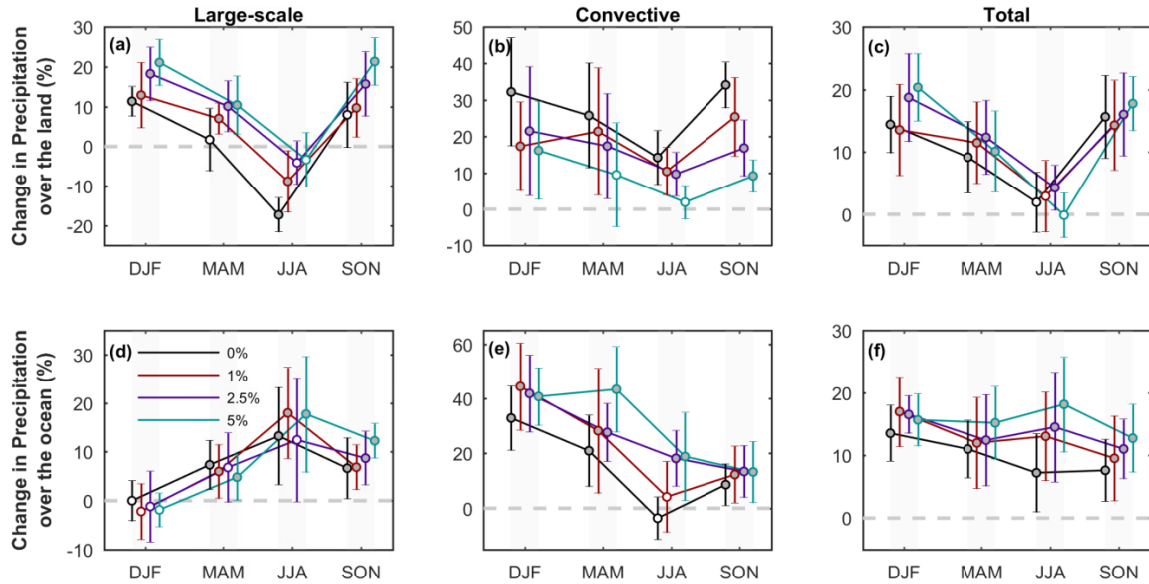| Warming Ratio | Global | | NH-mid-latitudes | | Tropics | |
|---|---|---|---|---|---|---|
| | Annual | JJA | Annual | JJA | Annual | JJA |
| Default Warming | 1.46 | 1.65 | 1.39 | 1.79 | 1.38 | 1.59 |
| 1% Nudged | 1.34 | 1.49 | 1.25 | 1.57 | 1.32 | 1.53 |
| 2.5% Nudged | 1.21 | 1.34 | 1.09 | 1.28 | 1.23 | 1.45 |
| 5% Nudged | 1.08 | 1.16 | 0.93 | 1.05 | 1.14 | 1.29 |
| Percent change from Default Warming to 5% Nudged | 25.78 | 29.5 | 33.21 | 41.38 | 17.81 | 18.77 |

## A.3   Appendix A Figures



Figure A.1: **CAM5 seasonal mean precipitation response for default warming and muted land warming simulations.** Percent changes are shown for the NH mid-latitudes over land (a-c) and ocean (d-f) for large-scale (left panels); convective (center panels) and total precipitation (right panels). Responses are shown for 0% Nudging (i.e., default warming; black); 1% Nudging (maroon); 2.5% Nudging (purple); and 5% Nudging (turquoise) simulations. Error bars represent the 99% confidence interval based on a t-test for the difference of means, using the pooled variance.
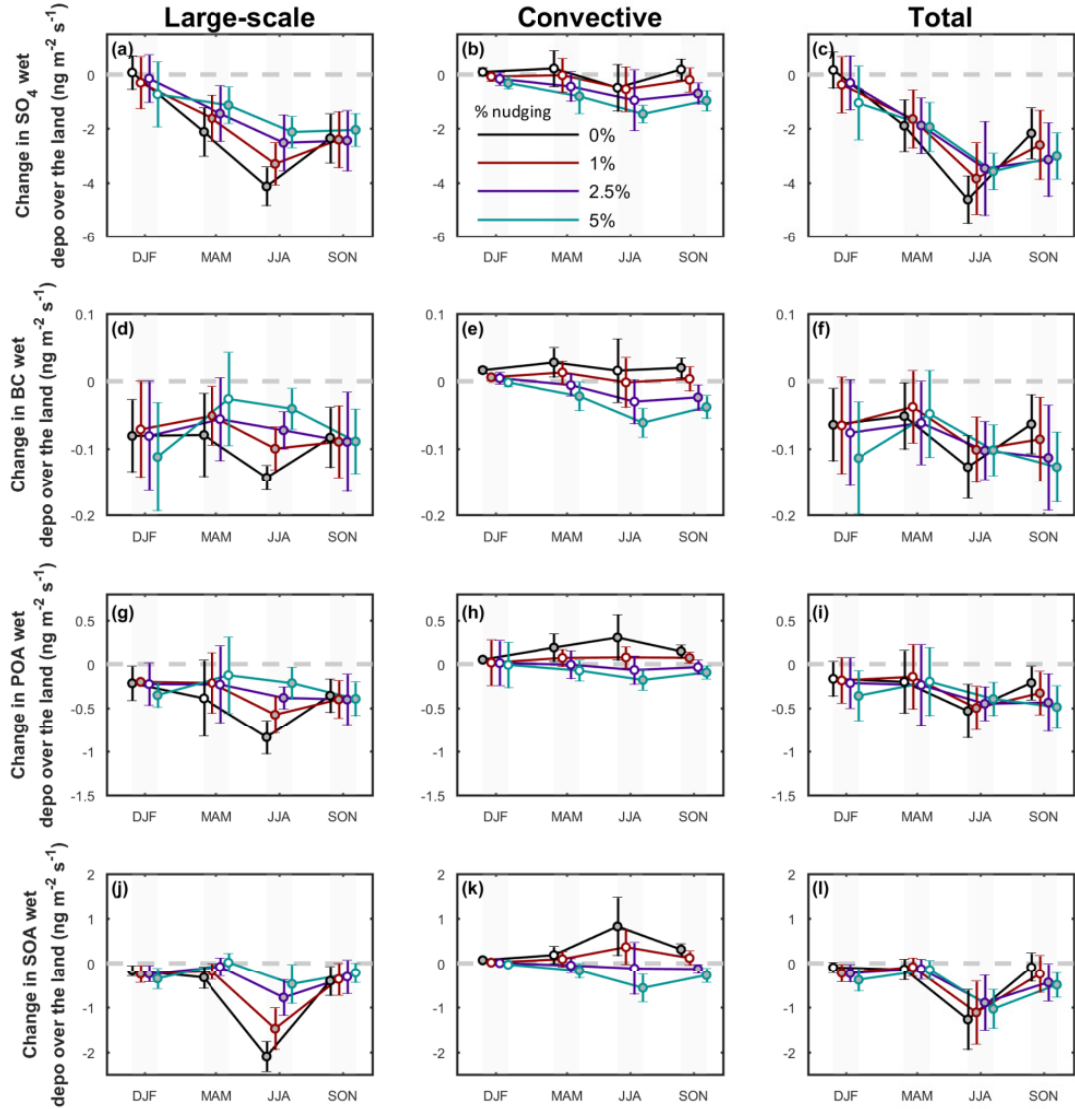
Figure A.2: **CAM5 seasonal mean response of aerosol wet deposition for default warming and muted land warming simulations.** Changes are shown for the NH mid-latitudes over land for (a-c) sulphate; (d-f) black carbon; (g-i) primary organic matter; (j-l) secondary organic aerosol due to large-scale (left panels); convective (center panels) and total precipitation (right panels). Responses are shown for 0% Nudging (i.e., default warming; black); 1% Nudging (maroon); 2.5% Nudging (purple); and 5% Nudging (turquoise) simulations. Error bars represent the 99% confidence interval based on a t-test for the difference of means, using the pooled variance.
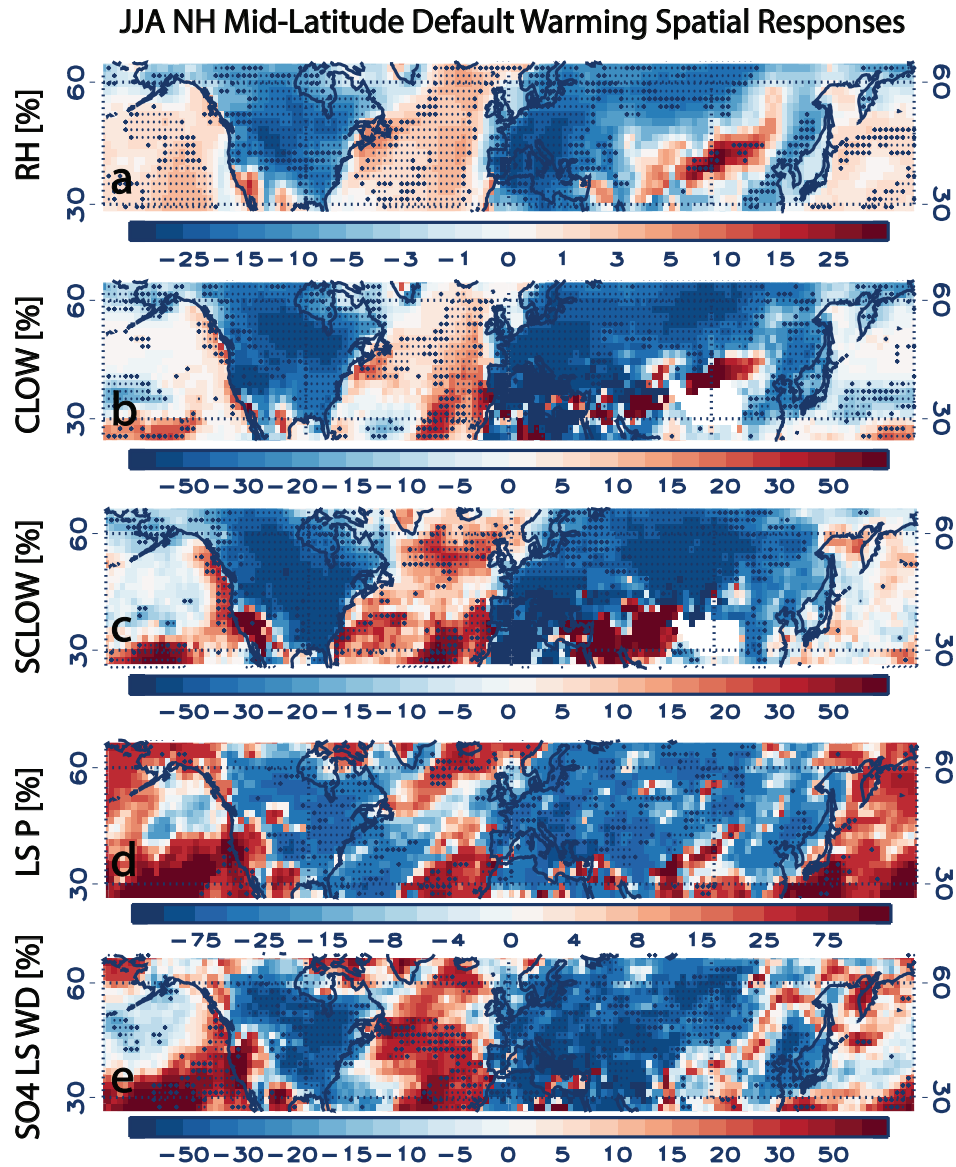
Figure A.3: **CAM5 Northern Hemisphere mid-latitude June-July-August mean response of select hydrological variables for the default warming simulation.** Percent change [%] in (a) lowertropospheric relative humidity (RH); (b) low-cloud cover (CLOW); (c) low-level large-scale (stratus) cloud cover (SCLOW); (d) large-scale precipitation (LSP); (e) sulfate ($SO_4$) large-scale precipitation wet deposition. Symbols represent significance at the 95% confidence interval based on a t-test for the difference of means, using the pooled variance. The panels illustrate a land-sea contrast in all variables, including decreases over land and increases over sea.
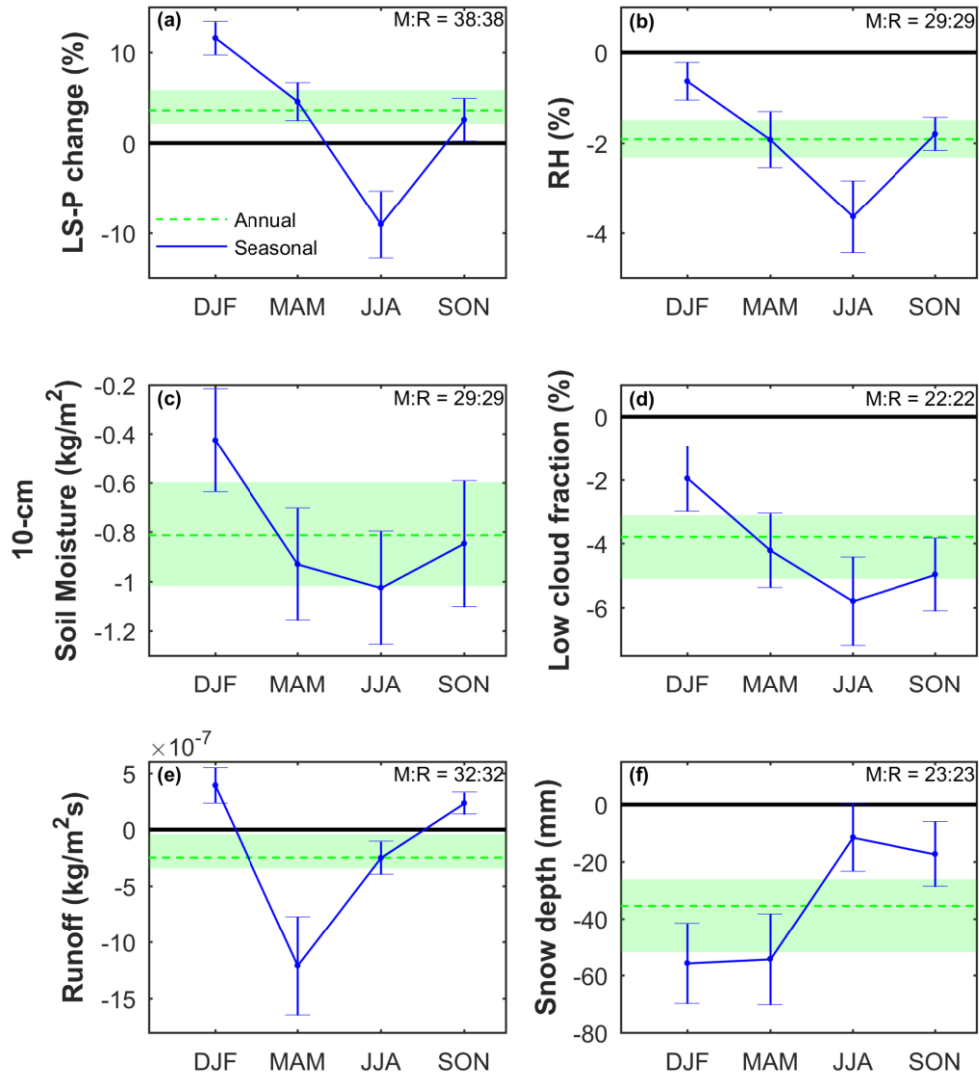
Figure A.4: **CMIP5 seasonal mean hydrology response for RCP8.5 warming simulations.** Changes (2090-2099 minus 2015-2006) are shown for the NH mid-latitudes over land for (a) large-scale precipitation [%]; (b) lower tropospheric relative humidity [%]; (c) 10-cm soil moisture [kg m$^{-2}$]; (d) cloud cover [%]; (e) surface runoff [$10^{-7}$ kg m$^{-2}$ s$^{-1}$]; and (f) snow depth [mm]. The green lines show the corresponding annual mean response. The M:R values depict the number of models (M), and the number of realizations (R) used. Uncertainty of the mean change is shown as blue error bars for seasonal mean values, and as the green shaded region for the annual mean. It is estimated as twice the standard error, $2\sigma/\text{sqrt(n)}$, where  is the standard deviation of the responses and n is the number of model-realizations.
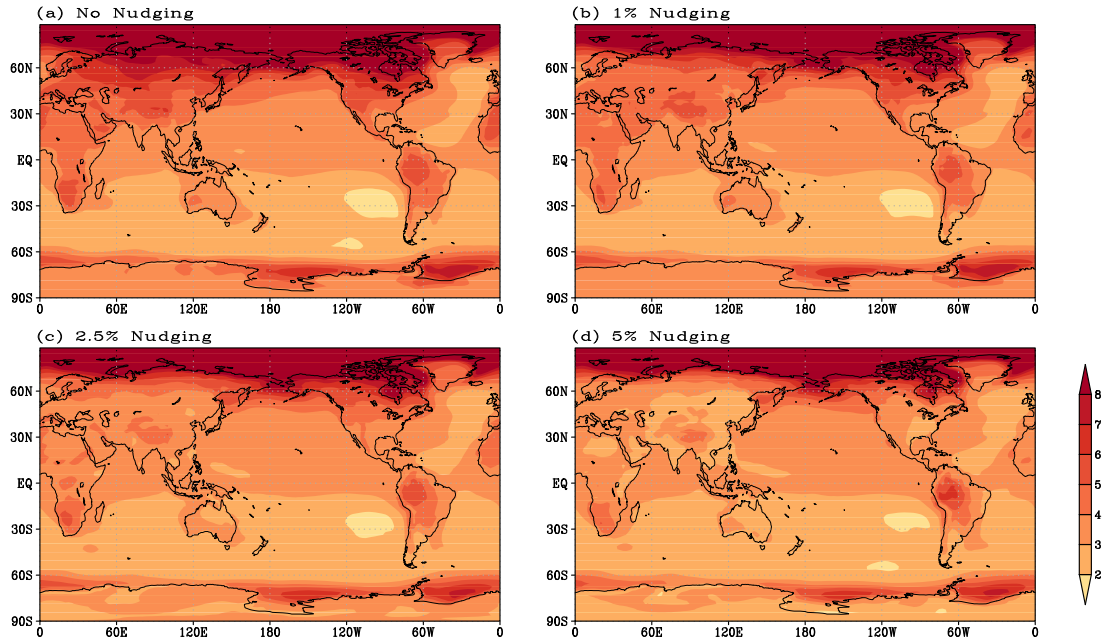
Figure A.5: **CAM5 annual mean lower-tropospheric temperature response for default warming and muted land warming simulations.** (a) 0% Nudging (i.e., default warming); (b) 1% Nudging; (c) 2.5% Nudging; and (d) 5% Nudging. The lower troposphere extends from the surface to 900 hPa. Units are K.
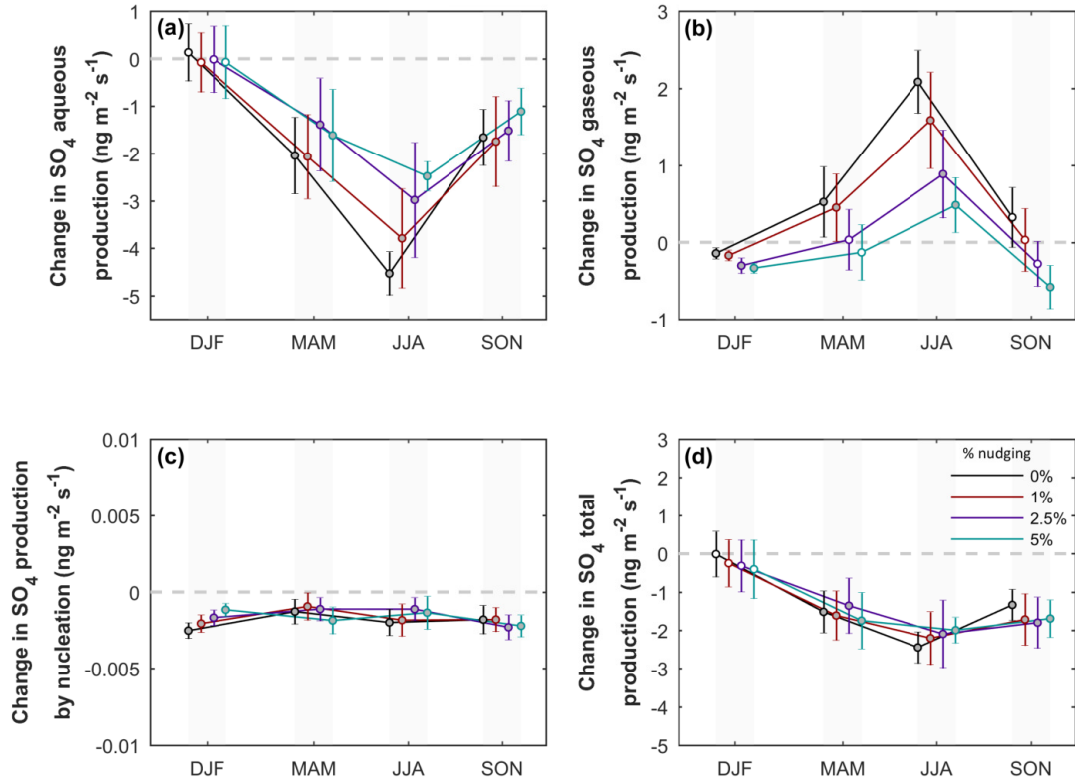
Figure A.6: **CAM5 seasonal mean SO4 chemistry response for default warming and muted land warming simulations.** Changes are shown for the NH mid-latitudes over land for (a) aqueous production; (b) gaseous production; (c) nucleation and (d) total $SO_4$ aerosol production (the sum of aqueous and gaseous production, and nucleation). Units are ng m$^{-2}$ s$^{-1}$. Responses are shown for 0% Nudging (i.e., default warming; black); 1% Nudging (maroon); 2.5% Nudging (purple); and 5% Nudging (turquoise) simulations. Error bars represent the 99% confidence interval based on a t-test for the difference of means, using the pooled variance.
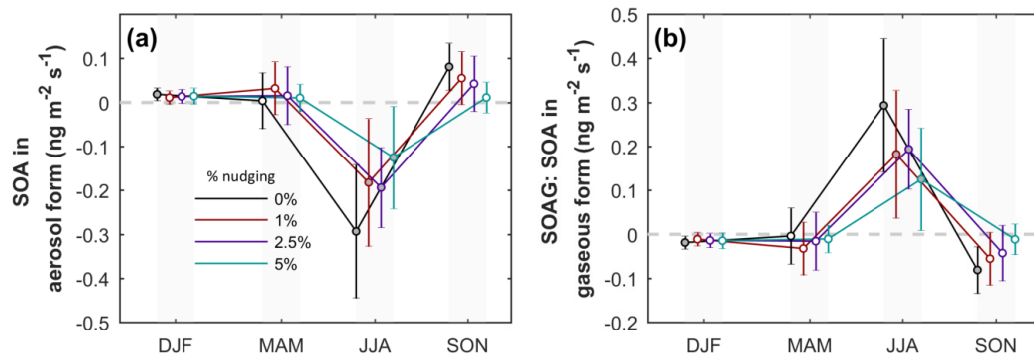
Figure A.7: **CAM5 seasonal mean response for SOA chemistry for default warming and muted land warming simulations.** Changes are shown for the NH mid-latitudes over land for SOA as an (a) aerosol and (b) gas. Units are ng m$^{-2}$ s$^{-1}$. Responses are shown for 0% Nudging (i.e., default warming; black); 1% Nudging (maroon); 2.5% Nudging (purple); and 5% Nudging (turquoise) simulations. Error bars represent the 99% confidence interval based on a t-test for the difference of means, using the pooled variance.
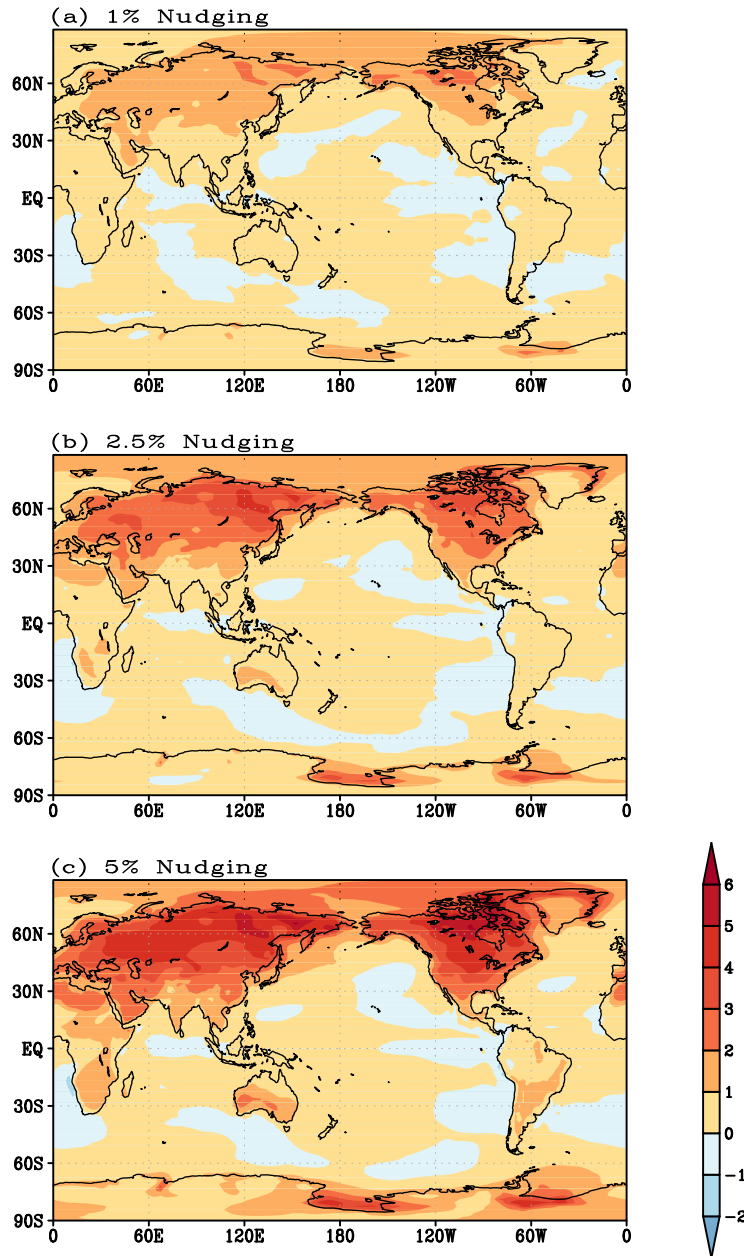
Figure A.8: **CAM5 annual mean lower-tropospheric temperature response for enhanced land warming simulations.** (A) 1% Nudging; (B) 2.5% Nudging; and (C) 5% Nudging. The lower troposphere extends from the surface to ~900 hPa. Units are K.
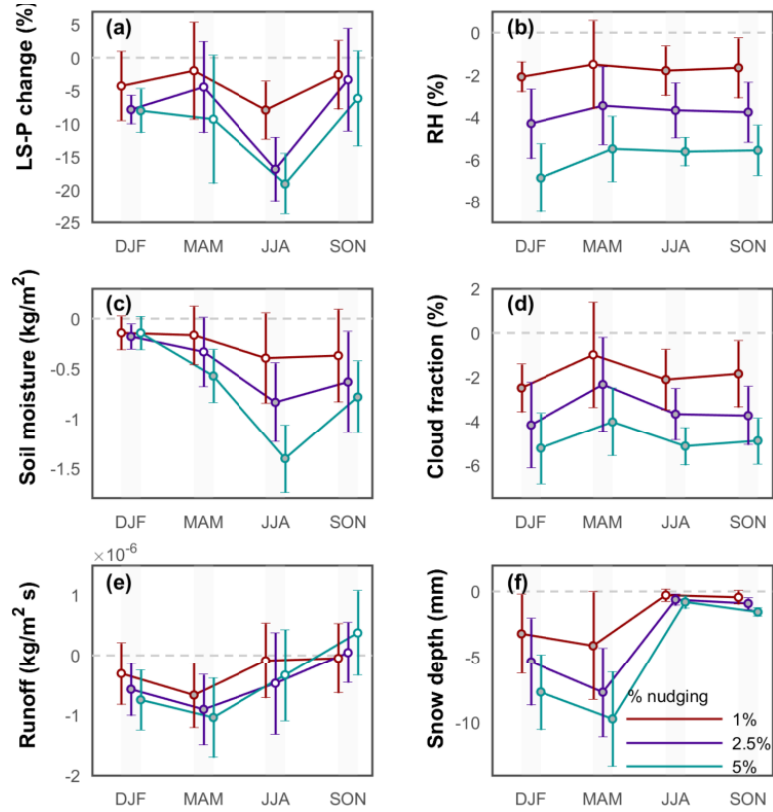
Figure A.9: **CAM5 seasonal mean hydrology response for enhanced land warming simulations.** Changes are shown for the NH mid-latitudes over land for (a) large-scale precipitation [%]; (b) lower tropospheric relative humidity [%]; (c) 10-cm soil moisture [kg m-2]; (d) low cloud cover [%]; (e) surface runoff [$10^{-7}$ kg m$^{-2}$ s$^{-1}$]; and (f) snow depth [mm]. Responses are shown for 1% Nudging (maroon); 2.5% Nudging (purple); and 5% Nudging (turquoise) simulations. Error bars represent the 99% confidence interval based on a t-test for the difference of means, using the pooled variance.
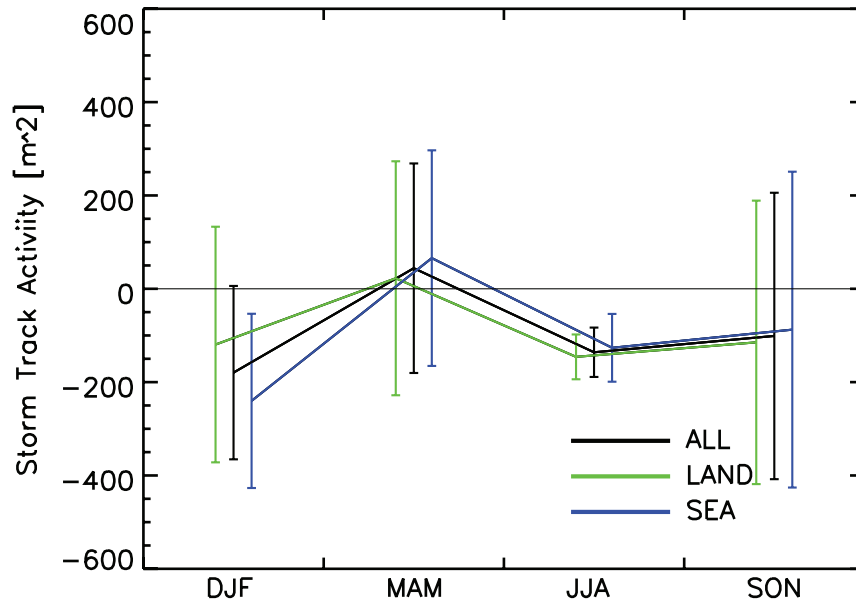
Figure A.10: **CAM5 seasonal mean storm track activity response for the default warming simulation.** Changes are shown for the NH mid-latitudes, over both land (green) and sea (blue). Error bars represent the 99% confidence interval based on a t-test for the difference of means, using the pooled variance. Storm track activity units are m$^2$.
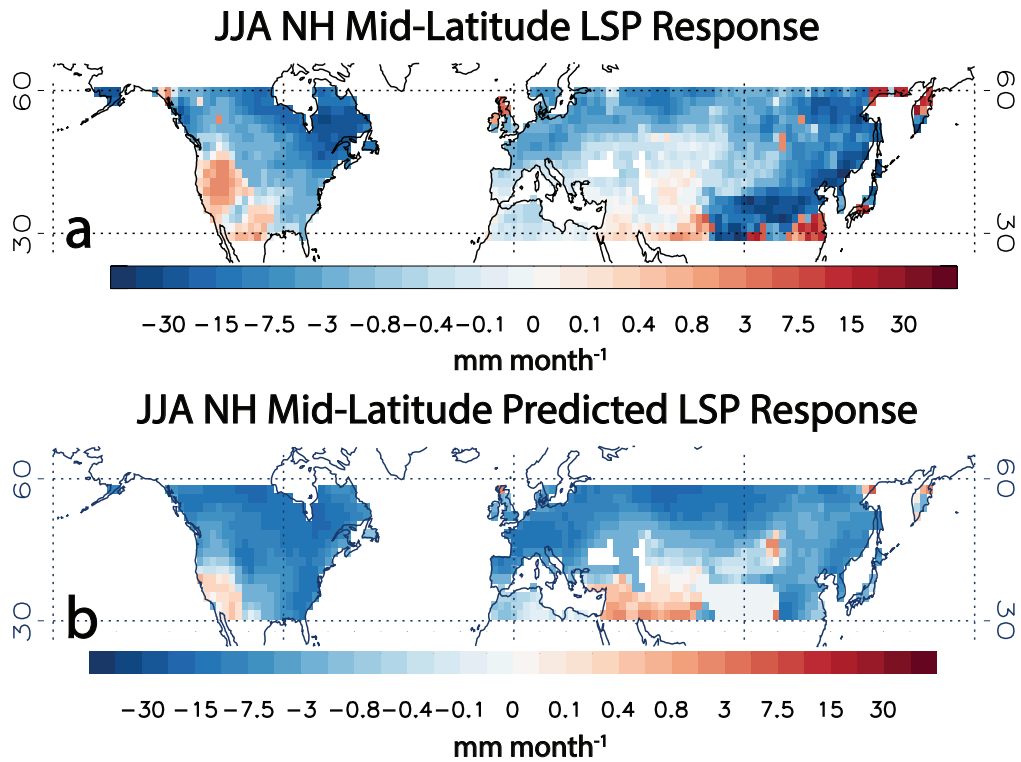
Figure A.11: **CAM5 JJA NH mid-latitude large-scale precipitation response and estimated response for the default warming simulation.** Large-scale precipitation response (LSP) and estimated response are based on days less than or equal to the 99th percentile (i.e., not including days exceeding the 99th percentile). Estimated response is based on a regression model using JJA NH mid-latitude continental LSP and low-level large-scale (stratus) cloud cover (SCLOW) from the control simulation. The change in SCLOW at each grid box is then multiplied by the slope of this regression model to obtain the estimated change in LSP.

# Appendix B

# Appendix to Anthropogenic aerosol forcing of the AMOC and the associated mechanisms in CMIP6 models

## B.1 Appendix B Tables

Table B.1: **Present-day (2005-2018) climatological AMOC strength based on RAPID observations and Coupled Model Intercomparison Project phase 6 all forcing models.** The AMOC is defined as the maximum stream function below 500 m in the Atlantic. AMOC units are Sverdrups (Sv), where 1 Sv is equal to $10^6$ m$^3$ s$^{-1}$.

| Model | AMOC Mean (Sv) |
|---|---|
| CAMS-CSM1-0 | 13.0 |
| MPI-ESM1-2-HR | 29.1 |
| ACCESS-CM2 | 18.8 |
| NESM3 | 9.1 |
| MIROC6 | 18.1 |
| CESM2 | 22.0 |
| MPI-ESM1-2-LR | 25.3 |
| IPSL-CM6A-LR | 11.6 |
| CNRM-CM6-1 | 15.4 |
| MIROC-ES2L | 18.8 |
| HadGEM3-GC31-LL | 16.8 |
| ACCESS-ESM1-5 | 20.3 |
| CESM2-WACCM | 22.8 |
| BCC-CSM2-MR | 25.4 |
| INM-CM5-0 | 18.3 |
| NorESM2-MM | 30.3 |
| CNRM-ESM2-1 | 15.4 |
| INM-CM4-8 | 25.4 |
| NorESM2-LM | 28.3 |
| MRI-ESM2-0 | 18.6 |
| EC-Earth3-Veg | 17.0 |
| UKESM1-0-LL | 17.0 |
| GFDL-CM4 | 21.8 |
| CanESM5 | 13.1 |
| RAPID | 17.5 |

Table B.2: **Anthropogenic aerosol Effective Radiative Forcing (ERF) and AMOC percent change in CMIP6 models.** Aerosol ERF is calculated for the globe (GL), Europe (EU; 30-45°N; 0-30°E) and the subpolar North Atlantic (sNA; 45-60°N; 0-50°W)). AMOC percent change is shown for both time periods, 1950-1990 and 1990-2020. Aerosol ERF is calculated as the net TOA radiative flux difference between piClim-Control and piClim-aer simulations (i.e., piClim-aer−piClim-Control). Models are arranged from largest (absolute value) global mean aerosol ERF to lowest. Aerosol ERF units are W m$^{-2}$ and AMOC percent change units are %.

| 2*Model | Aerosol ERF | | | AMOC | |
|---|---|---|---|---|---|
| | GL | sNA | EU | 1950-1990 | 1990-2020 |
| NorESM2-LM | -1.31 | -2.35 | -0.70 | 4.9 | -8.1 |
| NorESM2-MM | -1.26 | -2.22 | -0.72 | 8.9 | -15.7 |
| MRI-ESM2-0 | -1.19 | -0.22 | -2.56 | 21.8 | -29.6 |
| CNRM-CM6-1 | -1.15 | 0.26 | -1.48 | 3.3 | -9.0 |
| UKESM1-0-LL | -1.11 | -2.01 | -0.79 | 6.8 | -6.2 |
| HadGEM3-GC31-LL | -1.10 | -1.24 | -0.96 | 3.3 | -8.5 |
| MIROC6 | -1.04 | -0.64 | -1.06 | 0.1 | -20.9 |
| CanESM5 | -0.85 | -2.20 | -1.07 | 0.7 | -5.5 |
| CNRM-ESM2-1 | -0.74 | 0.23 | -1.08 | 2.6 | -7.2 |
| GFDL-CM4 | -0.73 | -0.76 | -1.20 | 3.1 | -2.3 |
| CESM2 | -0.65 | -0.38 | -0.09 | 11.3 | -23.9 |
| IPSL-CM6A-LR | -0.64 | -0.14 | -1.39 | 1.9 | -12.9 |
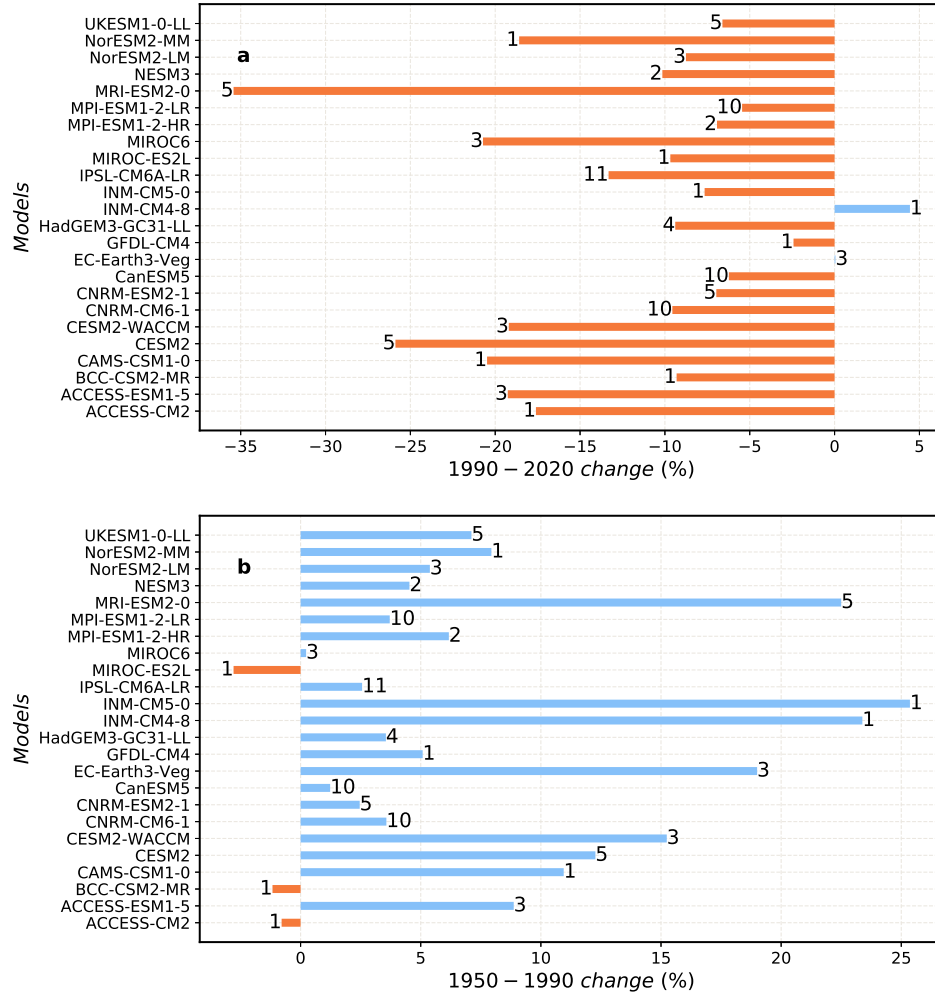
Figure B.1: **Ensemble mean AMOC percent change in all forcing Coupled Model Intercomparison Project phase 6 models.** Ensemble mean (a) 1990-2020 and (b) 1950-1990 AMOC percent change [%] for each model. AMOC weakening (strengthening) is shown with orange (blue) bars. Numbers in front of each bar represent the number of simulations used for that model. The AMOC percent change is estimated from the least-squares regression slope ($r_s$) of the non-normalized AMOC time series using: $100 \times \frac{r_s \times N}{AMOC(N=1)}$, where $N$ is the number of years (e.g.,∼30 for 1990−2020) and $AMOC(N=1)$ is the initial AMOC strength (e.g., in 1990 for 1990-2020).
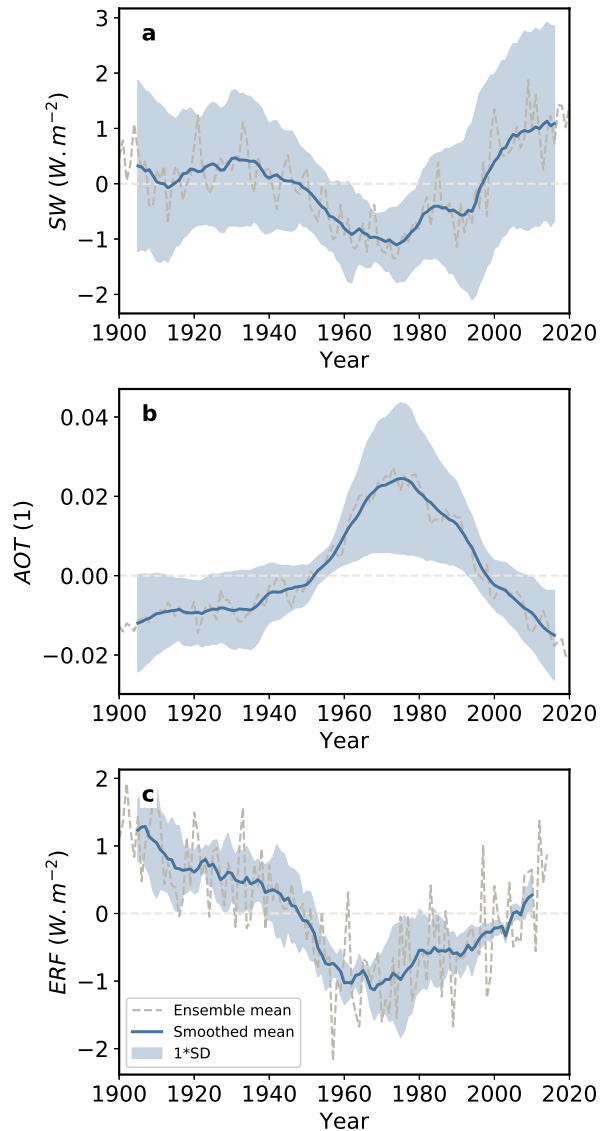
148

Figure B.2: **1900-2020 ensemble mean annual mean Coupled Model Intercomparison Project phase 6 normalized time series.** (a) net downward surface shortwave radiation (SW); (b) 550 nm aerosol optical thickness (AOT); and (c) anthropogenic aerosol effective radiative forcing (ERF). SW and AOT are based on CMIP6 anthropogenic aerosol forcing simulations. ERF is calculated from the histSST and histSST-piAer experiments, using the net top-of-the-atmosphere radiative flux. Only three models are available for the aerosol ERF calculation, including MIROC6, UKESM1-0-LL, and NorESM2-LM, and these simulations end in 2014. Values are averaged over the subpolar North Atlantic (45°N to 60°N and 0°W to 50°W). Units for SW and ERF are W m$^{-2}$. AOT is dimensionless.
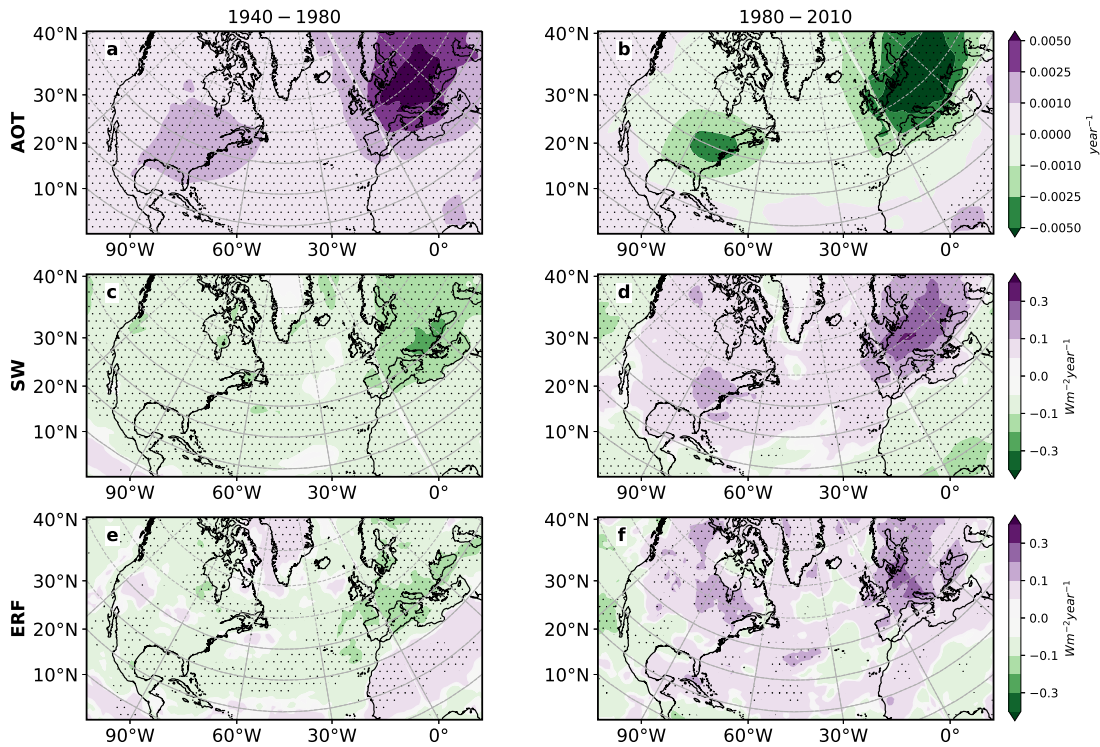
Figure B.3: **Ensemble mean annual mean Coupled Model Intercomparison Project phase 6 trends.** (left panels) 1940-1980 and (right panels) 1980-2010 (a-b) 550 nm aerosol optical thickness (AOT); (c-d) net downward surface shortwave radiation (SW); and (e-f) anthropogenic aerosol effective radiative forcing (ERF). Trends here have been shifted by 10 years earlier, due to the ∼10 year lead correlation with the AMOC. SW and AOT are based on CMIP6 anthropogenic aerosol forcing simulations. ERF is calculated from the histSST and histSST-piAer experiments, using the net top-of-the-atmosphere radiative flux. Only three models are available for the aerosol ERF calculation, including including MIROC6, UKESM1-0-LL, and NorESM2-LM. Symbols designate trend significance at the 95% confidence level based on a $t$-test. Trend units for AOT are year$^{-1}$ and W m$^{-2}$ year$^{-1}$ for SW and ERF.

Figure B.4: **1990-2020 annual mean all forcing Coupled Model Intercomparison Project phase 6 ensemble mean trends and model agreement on the sign of the trend.** (a-b) haline surface density flux (HSDF); (c-d) latent heat induced surface density flux (LSDF); and (e-f) sensible heat induced surface density flux (SSDF). Left panels show the ensemble mean trend; right panels show model agreement on the sign of the trend for each model's ensemble mean. Symbols in left panels designate trend significance at the 95% confidence level based on a $t$-test. Trend units are $\frac{\mu g}{m^2-s}$ year$^{-1}$. Trend realization agreement units are %. Red (blue) colors indicate model agreement on a positive (negative) trend.
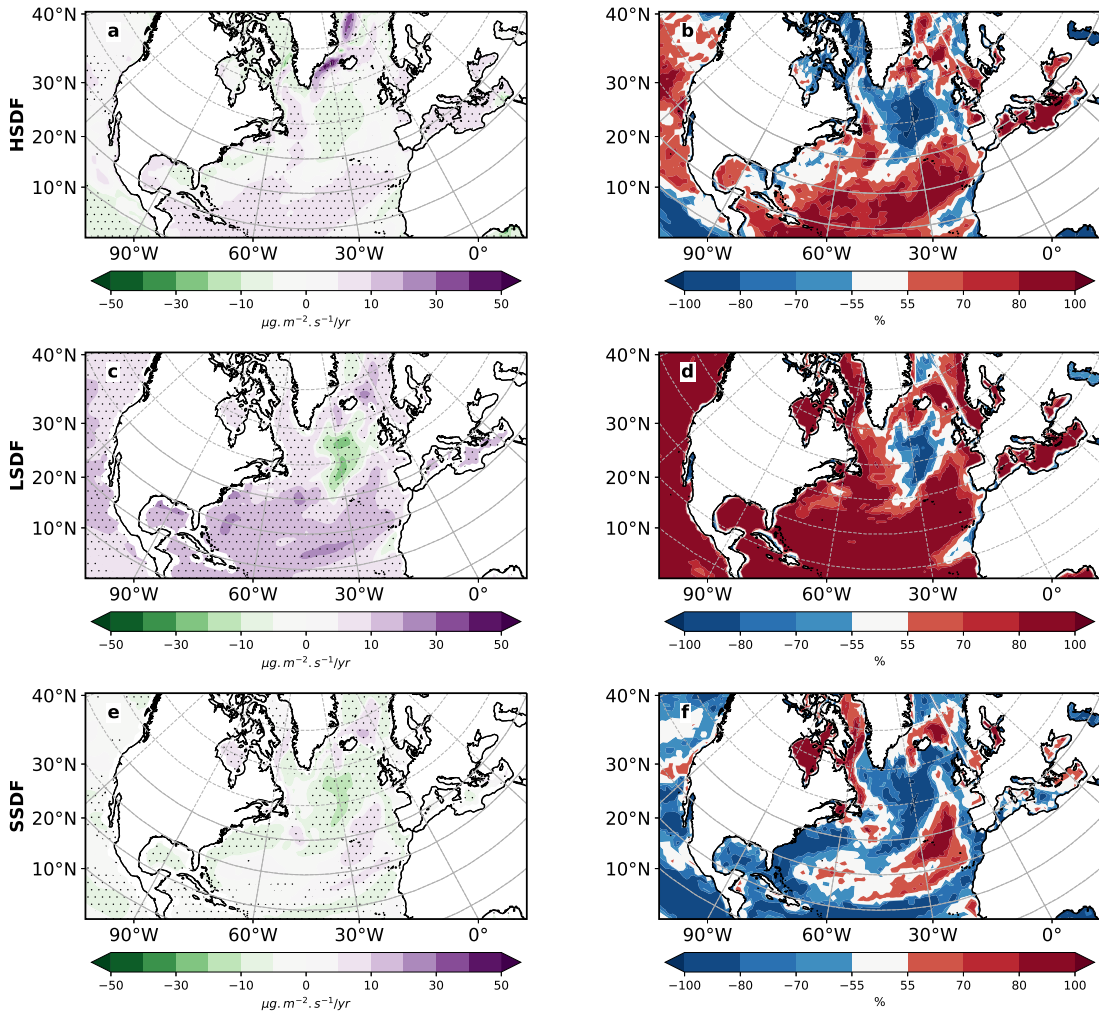
Figure B.5: **1950-1990 annual mean all forcing Coupled Model Intercomparison Project phase 6 ensemble mean trends and model agreement on the sign of the trend.** (a-b) surface density flux (SDF); (c-d) thermal SDF (TSDF); (e-f) sea level pressure (PSL); (g-h) surface winds (SFWD); and (i-j) storm track activity (pp). Left panels show the ensemble mean trend; right panels show model agreement on the sign of the trend for each model's ensemble mean. Symbols in left panels designate trend significance at the 95% confidence level based on a $t$-test. SDF and TSDF trend units are $\frac{\mu g}{m^2-s}$ year$^{-1}$. PSL, pp, and SFWD trend units are hPa year$^{-1}$, hPa$^2$ year$^{-1}$, and m s$^{-1}$ year$^{-1}$, respectively. Trend realization agreement units are %. Red (blue) colors indicate model agreement on a positive (negative) trend.
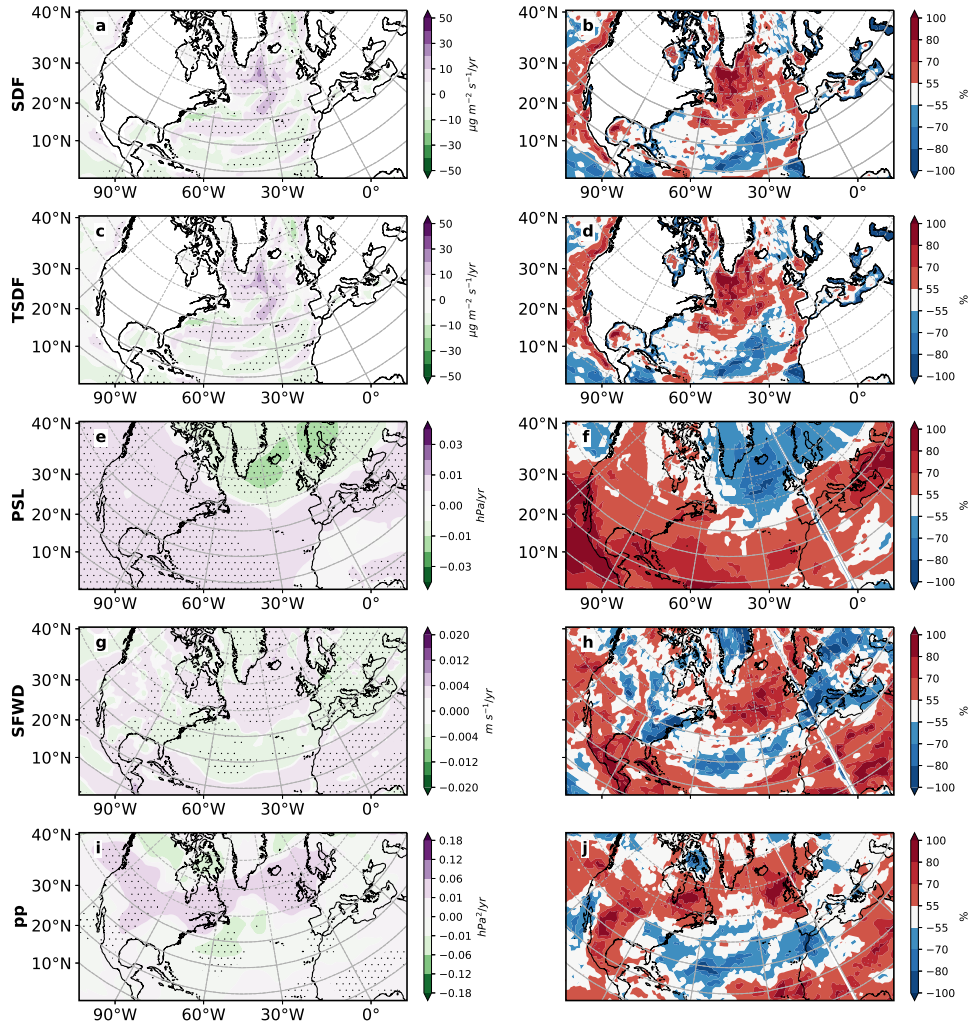
Figure B.6: **Ensemble mean annual mean Coupled Model Intercomparison Project phase 6 time series and trends.** (a, c, d) all forcing and (b, e, f) anthropogenic aerosol forcing March Mixed Layer Depth (MMLD). (a, b) subpolar North Atlantic time series; (c, e) 1950-1990 trend maps and (d, f) 1990-2020 trend maps. The ensemble mean time series (gray dashed) is smoothed using a 10-year running mean (solid blue line). Shading shows the corresponding inter-model standard deviation. Each model is normalized by subtracting its long-term (1900-2020) climatology. Symbols in bottom panels designate trend significance at 95% confidence level based on a t-test. MMLD trend units are in m/year.

Figure B.7: **Annual mean Coupled Model Intercomparison Project phase 6 ensemble mean and observed heat flux trends.** 1950-1990 CMIP6 ensemble mean (top panels) all forcing (a) latent heat flux (LHFLX) and (b) sensible heat flux (SHFLX) trends; (top middle panels) anthropogenic aerosol (AA) forcing (c) LHFLX and (d) SHFLX trends; and (bottom middle panels) greenhouse gas (GHG) forcing (e) LHFLX and (f) SHFLX trends. 1958-1990 (bottom panels) Objectively Analyzed air-sea Fluxes (OAFlux) (g) LHFLX and (h) SHFLX trends. Symbols in panels designate trend significance at the 95% confidence level based on a $t$-test. Trend units are W m$^{-2}$ year$^{-1}$.
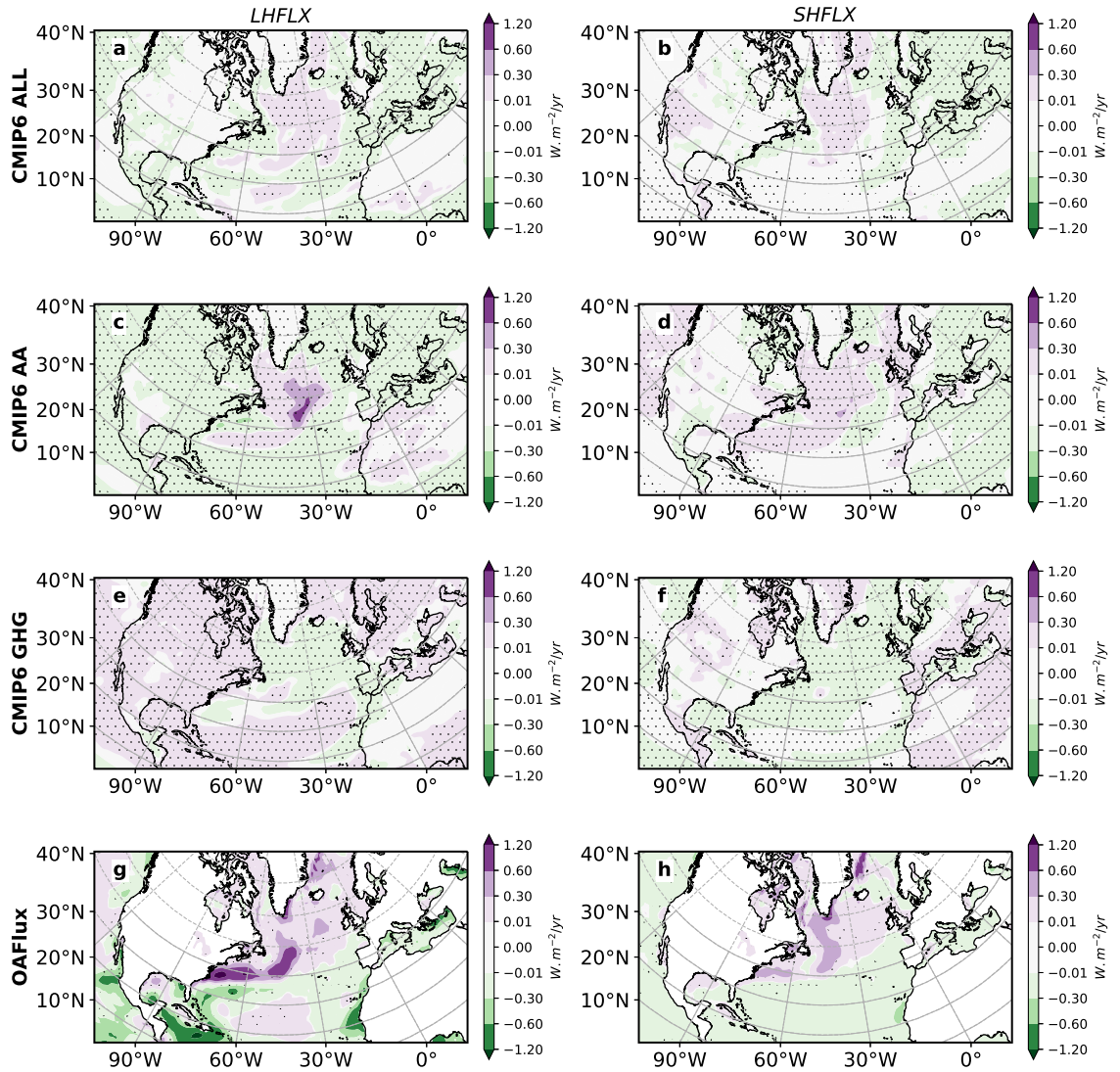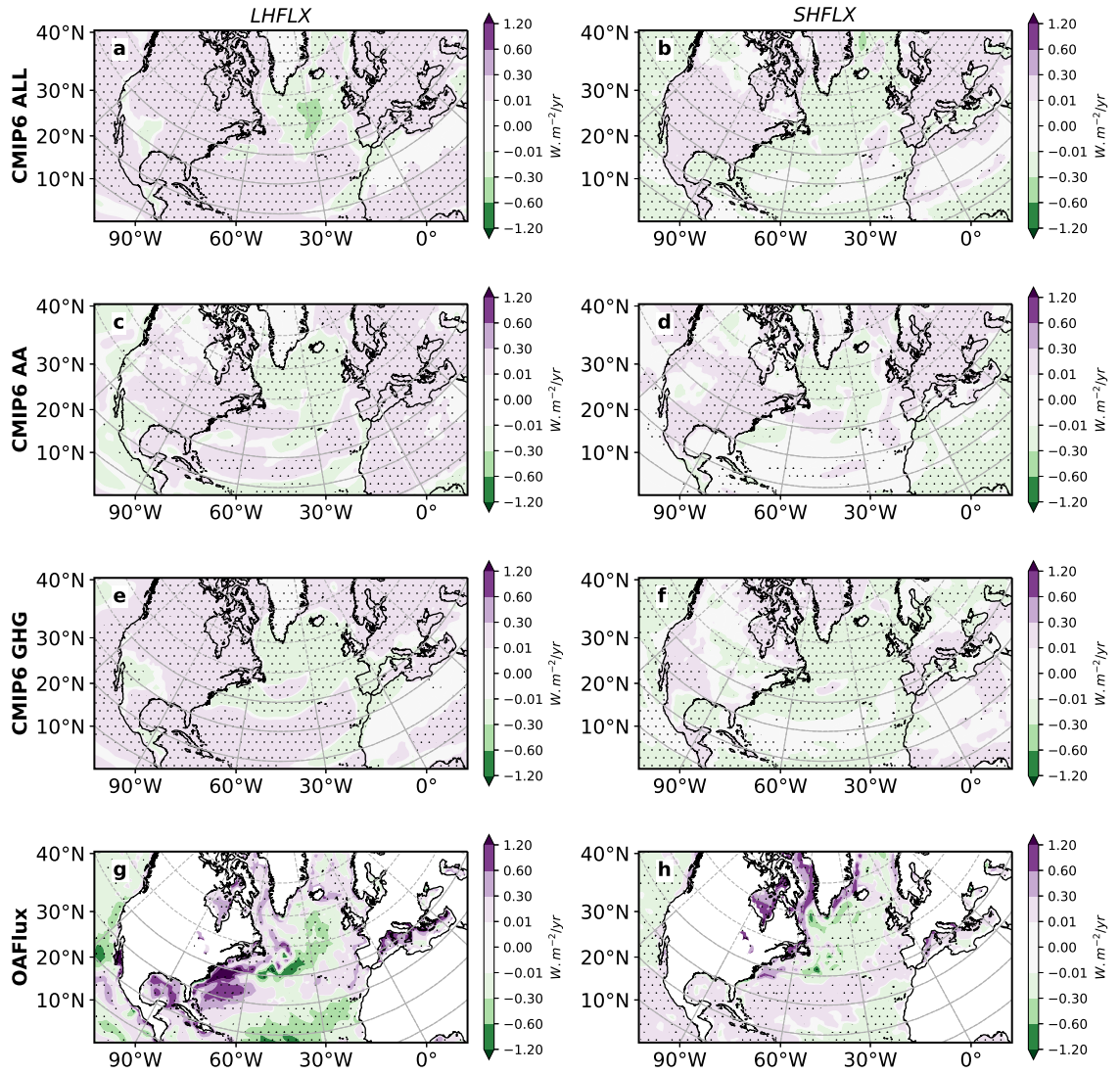
Figure B.8: **Annual mean Coupled Model Intercomparison Project phase 6 ensemble mean and observed heat flux trends.** 1990-2020 CMIP6 ensemble mean (top panels) all forcing (a) latent heat flux (LHFLX) and (b) sensible heat flux (SHFLX) trends; (top middle panels) anthropogenic aerosol (AA) forcing (c) LHFLX and (d) SHFLX trends; and (bottom middle panels) greenhouse gas (GHG) forcing (e) LHFLX and (f) SHFLX trends. 1990-2018 (bottom panels) Objectively Analyzed air-sea Fluxes (OAFlux) (g) LHFLX and (h) SHFLX trends. Symbols in panels designate trend significance at the 95% confidence level based on a $t$-test. Trend units are W m$^{-2}$ year$^{-1}$.
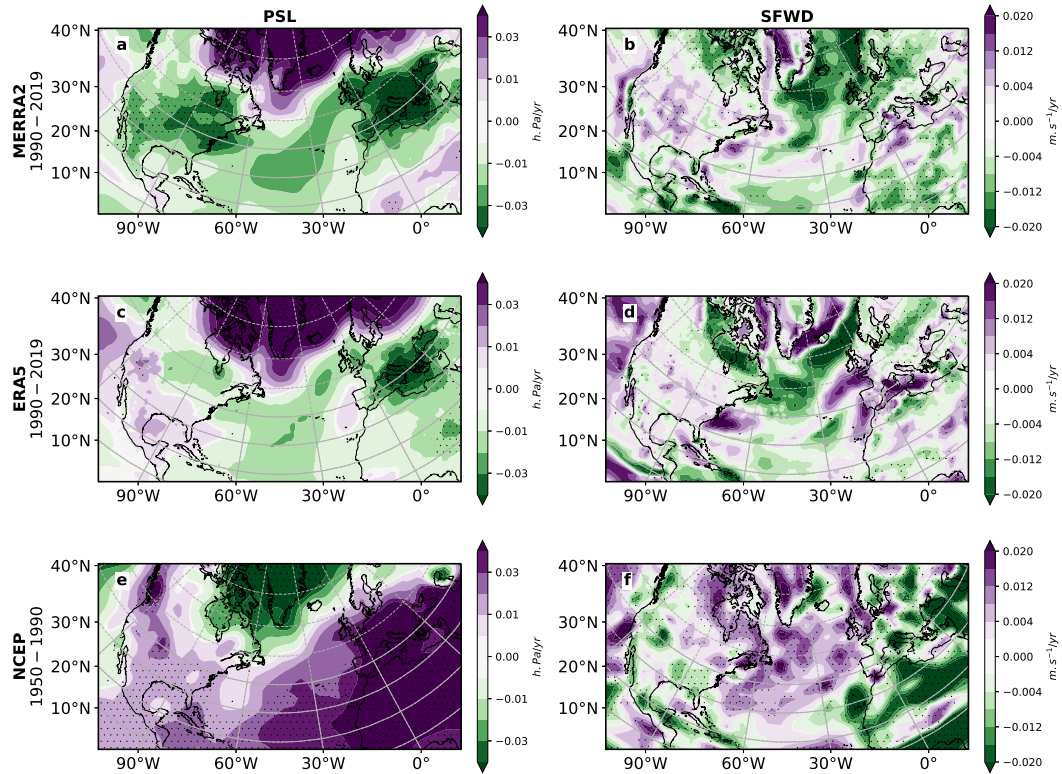
Figure B.9: **Annual mean sea level pressure and surface wind trends in reanalyses.**
1990-2019 (top panels) Modern Era Retrospective-Analysis for Research and Applications
version 2 Reanalysis (MERRA2) (a) sea level pressure (PSL) and (b) surface wind speed
(SFWD) trends; and (middle panels) European Centre for Medium-Range Weather Fore-
casts (ECMWF) Reanalyses (ERA5) (c) SLP and (d) SFWD. (bottom panels) 1950-1990
National Center for Environmental Prediction (NCEP) Reanalysis version 1 (e) PSL and
(f) SFWD trends. Symbols in panels designate trend significance at the 95% confidence
level based on a $t$-test. Trend units for PSL and SFWD are hPa year$^{-1}$ and m s$^{-1}$ year$^{-1}$,
respectively.
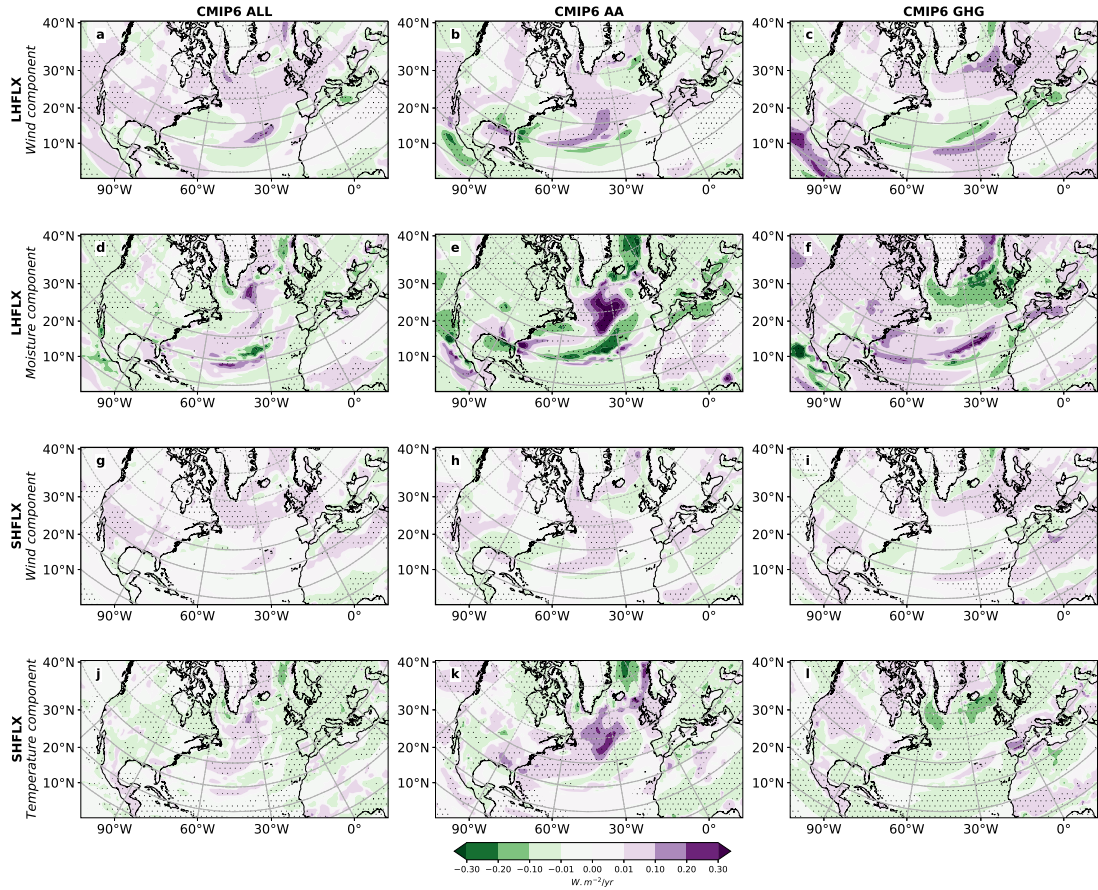
Figure B.10: **1950-1990 annual mean Coupled Model Intercomparison Project phase 6 ensemble mean heat flux decomposition trends.** CMIP6 (left column) all forcing, (middle column) anthropogenic aerosol (AA) forcing, and (right column) greenhouse gas (GHG) forcing ensemble mean trends for the decomposition of (top panels) latent heat flux (LHFLX) into its (a-c) wind and (d-f) moisture components; and (bottom panels) sensible heat flux (SHFLX) into its (g-i) wind and (j-l) temperature components. Symbols designate trend significance at the 95% confidence level based on a *t*-test. Trend units are W m$^{-2}$ year$^{-1}$.
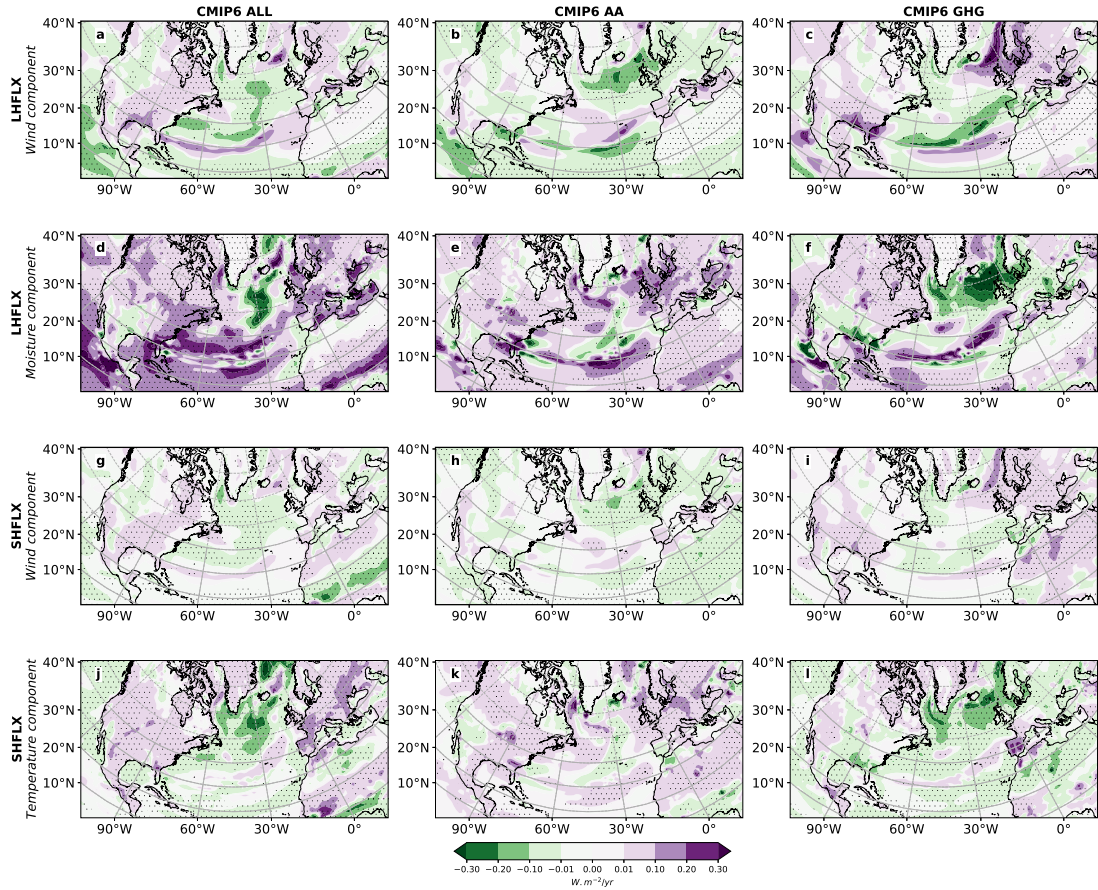
Figure B.11: **1990-2020 annual mean Coupled Model Intercomparison Project phase 6 ensemble mean heat flux decomposition trends.** CMIP6 (left column) all forcing, (middle column) anthropogenic aerosol (AA) forcing, and (right column) greenhouse gas (GHG) forcing ensemble mean trends for the decomposition of (top panels) latent heat flux (LHFLX) into its (a-c) wind and (d-f) moisture components; and (bottom panels) sensible heat flux (SHFLX) into its (g-i) wind and (j-l) temperature components. Symbols designate trend significance at the 95% confidence level based on a $t$-test. Trend units are W m$^{-2}$ year$^{-1}$.
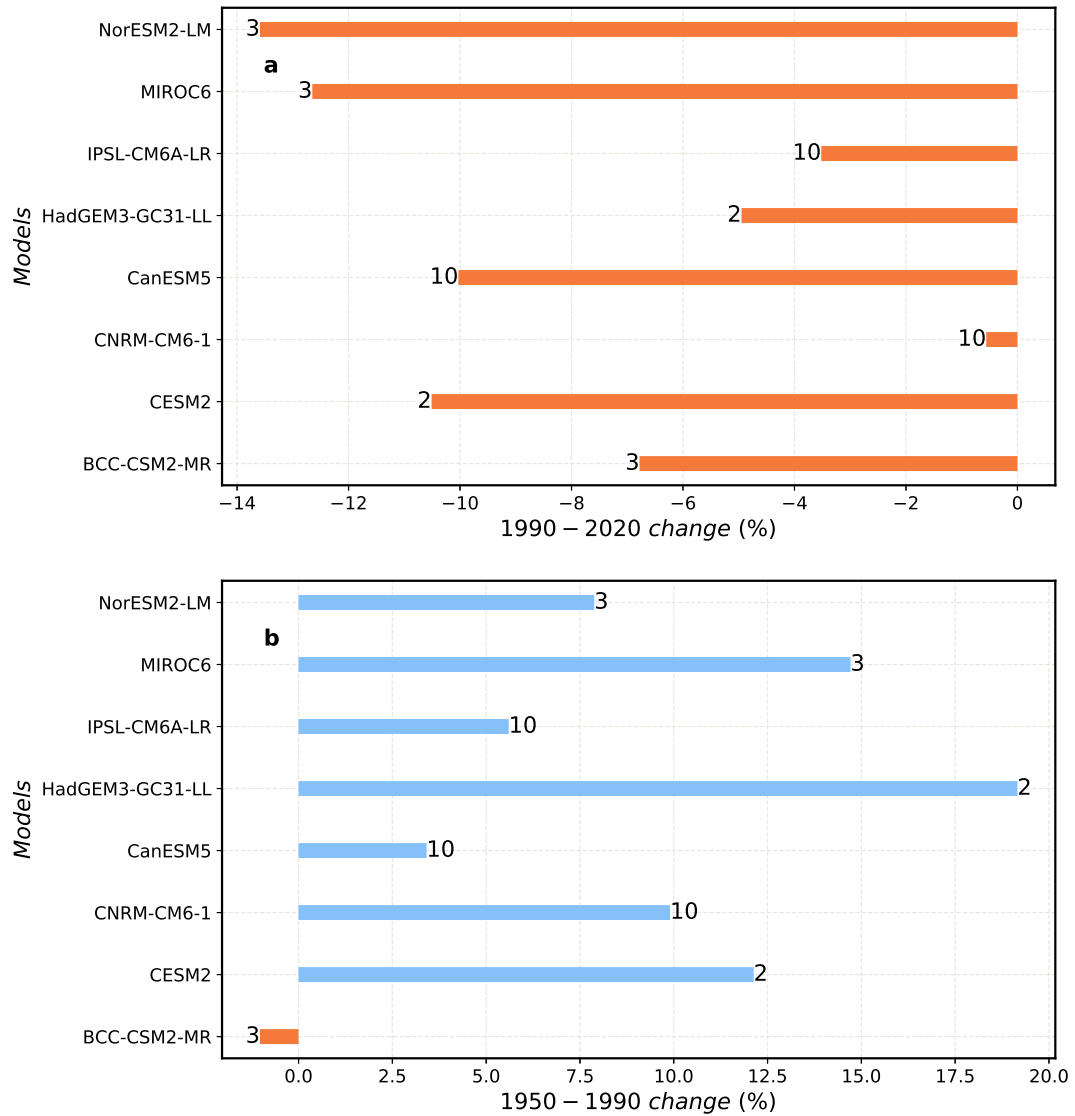
Figure B.12: **Ensemble mean AMOC percent change in anthropogenic aerosol forcing Coupled Model Intercomparison Project phase 6 models.** Ensemble mean (a) 1990-2020 and (b) 1950-1990 AMOC percent change [%] for each model. AMOC weakening (strengthening) is shown with orange (blue) bars. Numbers in front of each bar represent the number of simulations used for that model. The AMOC percent change is estimated from the least-squares regression slope ($r_s$) of the non-normalized AMOC time series using: $100 \times \frac{r_s \times N}{AMOC(N=1)}$, where $N$ is the number of years (e.g., 30 for 1990-2020) and $AMOC(N=1)$ is the initial AMOC strength (e.g., in 1990 for 1990-2020).

Figure B.13: **Atlantic Meridional Overturning Circulation using the 8 model subset of all forcing Coupled Model Intercomparison Project phase 6 models.** (a) 1900-2020 annual mean ensemble mean AMOC normalized time series. This is based on the same 8 models as are available for the CMIP6 anthropogenic aerosol (and greenhouse gas and natural forcing) simulations. The ensemble mean time series (gray dashed) is smoothed using a 10-year running mean (solid blue line). Shading shows the corresponding inter-model standard deviation. Each model is normalized by its long-term (1900-2020) climatology. Units are Sverdrups (Sv), where 1 Sv is equal to $10^6$ m$^3$ s$^{-1}$. Ensemble mean (b) 1990-2020 and (c) 1950-1990 AMOC percent change [%] for each model. AMOC weakening (strengthening) is shown with orange (blue) bars. Numbers in front of each bar represent the number of simulations used for that model.
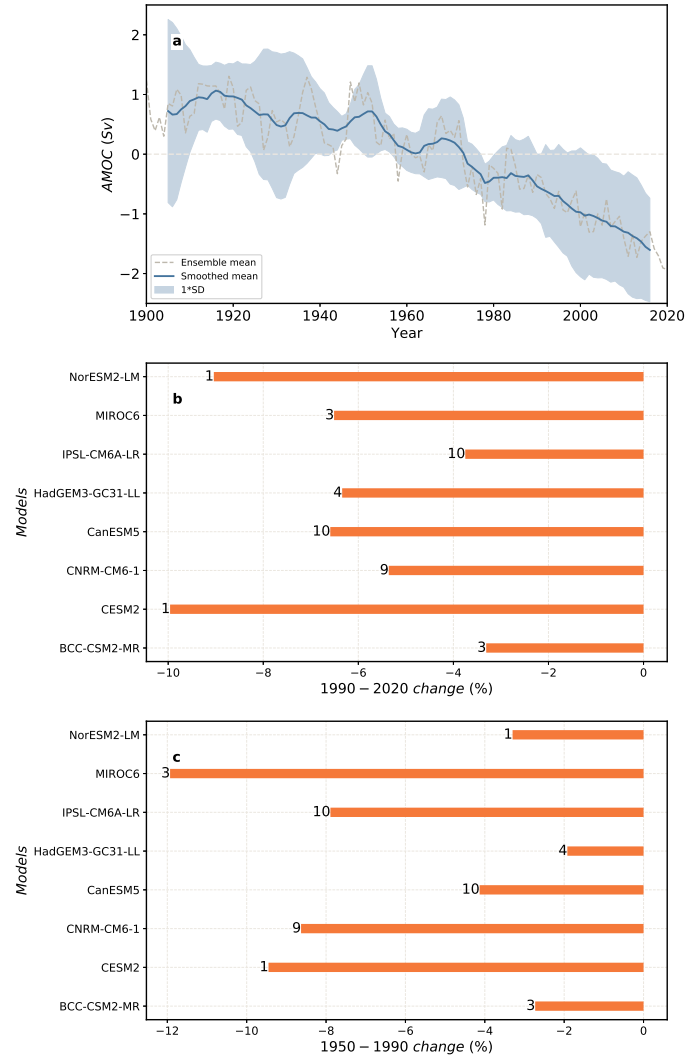
Figure B.14: **Atlantic Meridional Overturning Circulation in greenhouse gas forcing Coupled Model Intercomparison Project phase 6 models.** (a) 1900-2020 annual mean ensemble mean AMOC normalized time series. The ensemble mean time series (gray dashed) is smoothed using a 10-year running mean (solid blue line). Shading shows the corresponding inter-model standard deviation. Each model is normalized by its long-term (1900-2020) climatology. Units are Sverdrups (Sv), where 1 Sv is equal to $10^6$ m$^3$ s$^{-1}$. Ensemble mean (b) 1990-2020 and (c) 1950-1990 AMOC percent change [%] for each model. AMOC weakening (strengthening) is shown with orange (blue) bars. Numbers in front of each bar represent the number of simulations used for that model.
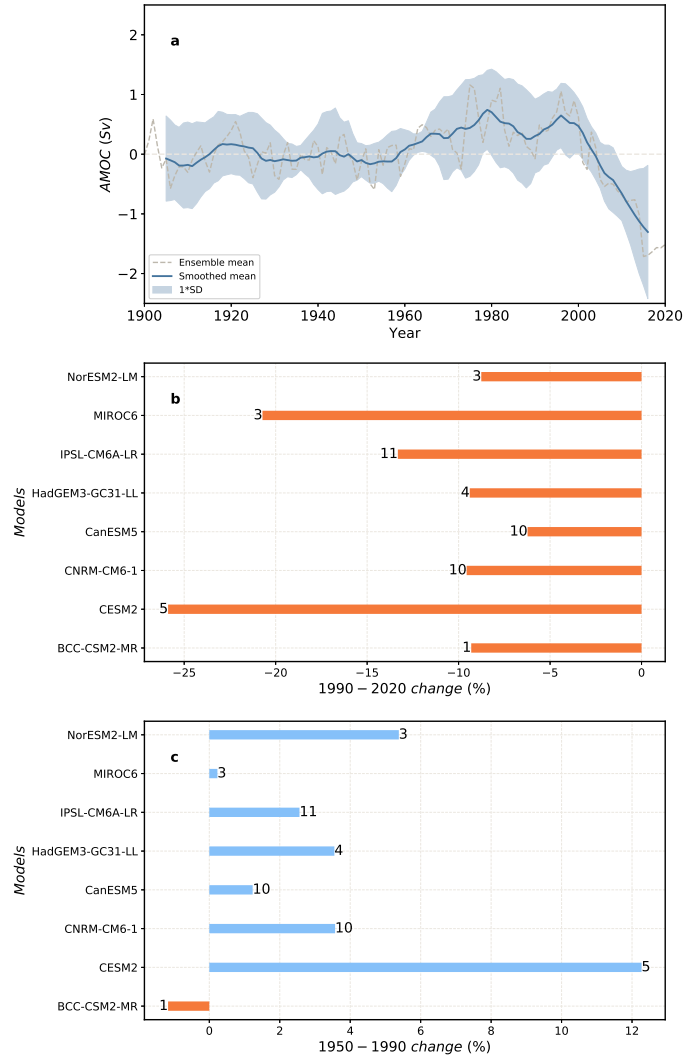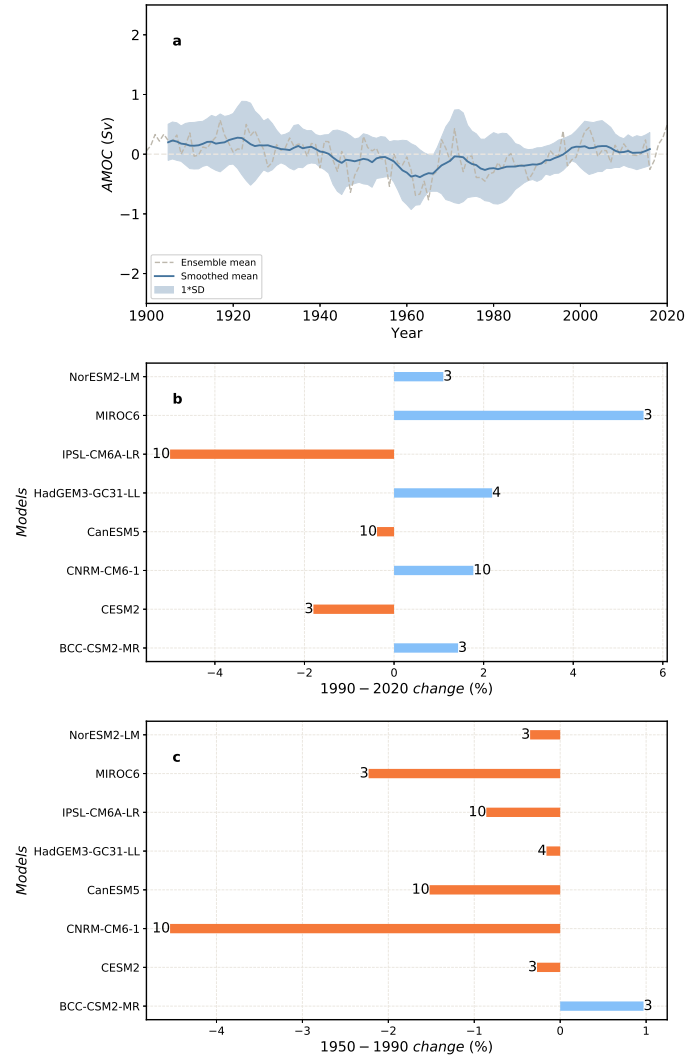
Figure B.15: **Atlantic Meridional Overturning Circulation in natural forcing Coupled Model Intercomparison Project phase 6 models.** (a) 1900-2020 annual mean ensemble mean AMOC normalized time series. The ensemble mean time series (gray dashed) is smoothed using a 10-year running mean (solid blue line). Shading shows the corresponding inter-model standard deviation. Each model is normalized by its long-term (1900-2020) climatology. Units are Sverdrups (Sv), where 1 Sv is equal to $10^6$ m$^3$ s$^{-1}$. Ensemble mean (b) 1990-2020 and (c) 1950-1990 AMOC percent change [%] for each model. AMOC weakening (strengthening) is shown with orange (blue) bars. Numbers in front of each bar represent the number of simulations used for that model.
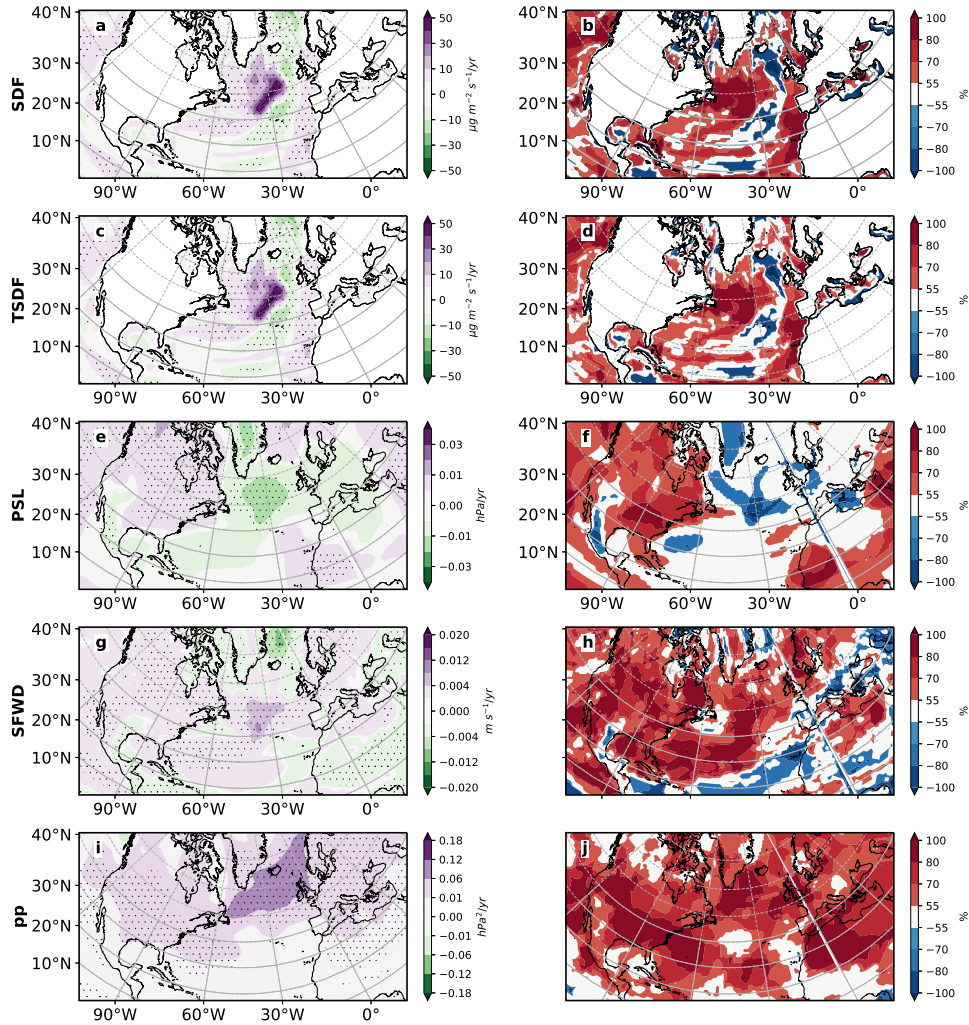
Figure B.16: **1950-1990 annual mean anthropogenic aerosol forcing Coupled Model Intercomparison Project phase 6 ensemble mean trends and model agreement on the sign of the trend.** (a-b) surface density flux (SDF); (c-d) thermal SDF; (e-f) sea level pressure (PSL); (g-h) surface winds (SFWD); and (i-j) storm track activity (pp). Left panels show the ensemble mean trend; right panels show model agreement on the sign of the trend for each model's ensemble mean. Symbols in left panels designate trend significance at the 95% confidence level based on a $t$-test. SDF and TSDF trend units are $\frac{\mu g}{m^2-s}$ year$^{-1}$. PSL, pp, and SFWD trend units are hPa year$^{-1}$, hPa$^2$ year$^{-1}$, and m s$^{-1}$ year$^{-1}$, respectively. Trend realization agreement units are %. Red (blue) colors indicate model agreement on a positive (negative) trend.

# Appendix C

# The impact of air quality control efforts on the Atlantic Meridional Overturning Circulation

## C.1 Appendix C Text

### C.1.1 Aerosol-Related Hydrological Considerations

As discussed in the main text, aerosols have a larger apparent hydrological sensitivity than GHGs (i.e., the change in precipitation per unit change in global surface temperature). So even though the 2015-2100 all-NTCF mitigation ERF trend is negative (less so for the cumulative ERF) and the surface cools, the decrease in aerosols may still dominate the precipitation response (i.e., they could promote an increase in P). An increase in P in the SPNA would favor an increase in freshwater flux and a decrease $SSD_S$, weakening the AMOC and potentially offsetting any AMOC strengthening due to SST cooling. Furthermore, changes in P may be important under NMNTCF mitigation. Here, any potential freshening due to SPNA P increases would act to reinforce SST warming, and both would promote a decrease in SSD and potentially weakening of the AMOC.

Under NMNTCF mitigation, the MMM Northern Hemisphere (NH) P trends are 0.21 and 0.14 mg m$^{-2}$ s$^{-1}$ decade$^{-1}$ from 2015-2055 and 2015-2100, respectively. In the North Atlantic, these trends are 0.14 and 0.08 mg m$^{-2}$ s$^{-1}$ decade$^{-1}$. All are significant at the 95% confidence level. Similarly, under all-NTCF mitigation, the MMM NH P trends are also significant at 0.19 and 0.04 mg m$^{-2}$ s$^{-1}$ decade$^{-1}$ from 2015-2055 and 2015-2100, respectively. Similar results exist in the North Atlantic, where the trends are 0.20 and 0.06 mg m$^{-2}$ s$^{-1}$ decade$^{-1}$. Thus, the reduction is aerosols is driving significant increases in P (particularly by mid-century), even under all-NTCF mitigation.

These P trends, however, are largely offset by decreases in −E (i.e., increases in E). The MMM NH P−E trends under NMNTCF mitigation are 0.004 and 0.049 mg m$^{-2}$

s$^{-1}$ decade$^{-1}$ from 2015-2055 and 2015-2100, respectively (the latter is significant at the 95% confidence level). In the North Atlantic, these trends are $-0.013$ and $0.004$ mg m$^{-2}$ s$^{-1}$ decade$^{-1}$ (neither are significant at the 95% confidence level). Similarly, under all-NTCF mitigation, the MMM NH P$-$E trends are $0.07$ and $0.04$ mg m$^{-2}$ s$^{-1}$ decade$^{-1}$ from 2015-2055 and 2015-2100, respectively (the latter is significant at the 95% confidence level). In the North Atlantic, these trends are $0.10$ and $0.02$ mg m$^{-2}$ s$^{-1}$ decade$^{-1}$ (neither significant at the 95% confidence level). Thus, neither NMNTCF or all-NTCF mitigation exhibit significant P$-$E trends in the North Atlantic, due to an increase in E offsetting the increase in P.

Similar results generally exist in the SPNA, although the trends are less significant (Supplementary Tables 2-3). Under all-NTCF mitigation, the 2015-2100 SPNA P trends are generally negative (except for GISS-E2-1-G; Supplementary Table 2). Over the 2015-2055 time period (when the aerosol forcing is larger; Supplementary Table 3), however, the corresponding P trends are positive for all models ranging from $0.13$ mg m$^{-2}$ s$^{-1}$ decade$^{-1}$ in MRI-ESM2-0 to $0.26$ mg m$^{-2}$ s$^{-1}$ decade$^{-1}$ in UKESM1-0-LL, with a significant MMM trend of $0.22$ mg m$^{-2}$ s$^{-1}$ decade$^{-1}$. However, these are partially offset by a decrease in $-$E, which decreases in all models ranging from $-0.07$ mg m$^{-2}$ s$^{-1}$ decade$^{-1}$ in EC-Earth3-AerChem to $-0.19$ mg m$^{-2}$ s$^{-1}$ decade$^{-1}$ in GISS-E2-1-G, with a significant MMM trend of $-0.12$ mg m$^{-2}$ s$^{-1}$ decade$^{-1}$. The corresponding 2015-2055 P$-$E trends remain positive for all models, ranging from $0.02$ mg m$^{-2}$ s$^{-1}$ decade$^{-1}$ in GISS-E2-1-G to $0.19$ mg m$^{-2}$ s$^{-1}$ decade$^{-1}$ in EC-Earth3-AerChem, but lack significance (as with the MMM at $0.11$ mg m$^{-2}$ s$^{-1}$ decade$^{-1}$).

Furthermore, if hydrological changes are important to the all-NTCF AMOC (particularly to mid-century, when all models yield a SPNA P and P−E increase), then we might expect negative 2015-2055 SPNA $SSD_S$ trends under all-NTCF mitigation. This is not the case as the corresponding $SSD_S$ trends (Supplementary Table 5) range from $-0.013$ kg m$^{-3}$ decade$^{-1}$ in EC-Earth3-AerChem to 0.033 kg m$^{-3}$ decade$^{-1}$ in UKESM1-0-LL, with a non-significant MMM trend of 0.005 kg m$^{-3}$ decade$^{-1}$. Thus, we do not find strong evidence that the lack of AMOC weakening under all-NTCF mitigation (in three of the four models) is due to aerosol-related hydrological considerations.

Under NMNTCF mitigation, three of four models yield a 2015-2100 increase in SPNA P, including a significant MMM P increase of 0.05 mg m$^{-2}$ s$^{-1}$ decade$^{-1}$ (Supplementary Table 2). However, this is only significant in one model−UKESM1-0-LL. Similar results exist from 2015-2055−three of four models yield a 2015-2055 increase in SPNA P, including a significant MMM P increase of 0.17 mg m$^{-2}$ s$^{-1}$ decade$^{-1}$ (Supplementary Table 3). Again, however, this is only significant in one model−in this case, GISS-E2-1-G. In contrast to the NH and North Atlantic, SPNA NMNTCF −E trends are positive in three of the four models for both time periods; again, however, these trends are not significant. The corresponding SPNA P−E trends are positive (but with minimal significance) for all models; the corresponding MMM trends are significant at 0.17 and 0.08 mg m$^{-2}$ s$^{-1}$ decade$^{-1}$ for 2015-2055 and 2015-2100, respectively. Thus, individual models generally yield non-significant P and −E trends under NMNTCF mitigation for the SPNA region as a whole, but the MMM does show a significant increase in P−E.

### C.1.2 Importance of $SSD_S$ to SSD

The ratio of the 2015-2100 SPNA SSD trend to the SPNA $SSD_S$ trend is shown in Supplementary Table 6. Both MRI-ESM2-0 and GISS-E2-1-G show that $SSD_S$ is more important than $SSD_T$ for NMNTCF and $CH_4$ mitigation, as well as for the AQ control experiments. For example, under NMNTCF mitigation, the ratio of the SSD trend to the $SSD_S$ trend is 90% and 114% in MRI-ESM2-0 and GISS-E2-G, respectively. Under AQ control experiments, this exceeds 100% in both models (due to the opposing effects of $SSD_T$ on SSD). The only instance where the $SSD_S$ trend is less than 50% of the SSD trend is for UKESM1-0-LL under the mitigation signals, at 47-48%. Under AQ control, this increases to 65-70%, comparable to EC-Earth3-AerChem at 65-74%. Thus, changes in SPNA SSD are largely due to changes in $SSD_S$ in GISS-E2-1-G and MRI-ESM2-0; in UKESM1-0-LL and EC-Earth3-AerChem, $SSD_T$ and $SSD_S$ changes are of similar importance (the exception being EC-Earth3-AerChem under NMNTCF mitigation), but $SSD_S$ becomes more important under the AQ control experiments.

### C.1.3 Additional Details on Freshwater Flux

Averaging hydrological variables over the entire SPNA, as done above, likely masks smaller scale changes that may be important. A more thorough evaluation of P, $-E$ and FF, focused on spatial trend maps as well as spatial regression analysis, is included here.

In GISS-E2-1-G and MRI-ESM2-0, positive 2015-2100 FF trends exist in the SPNA under NMNTCF mitigation and weak AQ control; negative trends occur under $CH_4$ miti-

gation (Supplementary Figures 9-10). These trends are particularly strong and ubiquitous for GISS-E2-1-G; in MRI-ESM2-0 under mitigation, these trends are confined to certain regions of the SPNA. For example, under $CH_4$ mitigation, the negative FF trends in MRI-ESM2-0 are located south and east of Iceland. For both models, the FF trends are largely consistent with $-E$ trends. In the case of GISS-E2-1-G under $CH_4$ mitigation, and for both models under AQ control, a significant trend in P exists, which acts to mute the change in FF due to $-E$. The changes in $-E$ (and P) are related to the change in SPNA SST. In GISS-E2-1-G, for example, SPNA SSTs cool under NMNTCF mitigation and weak AQ control; SPNA SSTs warm under $CH_4$ mitigation (consistent with AMOC-induced changes in poleward Atlantic OHT; Supplementary Figures 4-5). Warming SSTs promote a decrease in $-E$ (i.e., increase in E) and an increase in P (e.g., due to reduced atmospheric stability) and vice versa for SST cooling. For MRI-ESM2-0 under mitigation, the SPNA SST response is relatively weak and is better described as a lack of SPNA SST cooling under $CH_4$ mitigation, and a lack of SPNA SST warming under NMNTCF mitigation. However, as will be discussed below, this still promotes changes in $-E$, due to changes in the vertical gradient of specific humidity. We also note that based on lead-lag plots (not shown), GISS-E2-1-G clearly shows the AMOC leads both $SSD_T$ and $SSD_S$ (by about 3 years), particularly under the mitigation signals. Results are less clear with the other models.

For EC-Earth3-AerChem and UKESM1-0-LL (Supplementary Figures 7-8), changes in both P and $-E$ are important to changes in FF. Under NMNTCF mitigation, EC-Earth3-AerChem yields increasing FF in the western SPNA, extending up to Iceland. This is consistent with both an increase in P, as well as an increase in $-E$ near Iceland. Under $CH_4$

mitigation, FF decreases around Iceland, which is largely consistent with a decrease in $-$E. As with MRI-ESM2-0, the changes in $-$E near Iceland are related to SST changes that are opposite the broader SPNA region (i.e., cooling/lack of warming under NMNTCF mitigation; warming/lack of cooling under $CH_4$ mitigation). For UKESM1-0-LL under NMNTCF mitigation, a (weak) increase in FF occurs south of Iceland and off the western European coast, which is consistent with an increase in P (consistently, UKESM1-0-LL NMNTCF $SSD_S$ yields only a small decrease). Similarly, under $CH_4$ mitigation, UKESM1-0-LL shows decreases in FF south of Iceland and off the western European coast, which is again consistent with a decrease in P.

For both EC-Earth3-AerChem and UKESM1-0-LL under weak AQ control, the increase in FF is again related to an increase in P and an increase in $-$E. The increase in P is consistent with overall warming of the SPNA; the decrease in evaporation would at first seem to be inconsistent with these SST changes. However, both models show a warming hole near Iceland under weak AQ control. If the atmosphere just above the surface warms more, due to atmospheric transport of heat from outside the SPNA (which warms substantially more), the vertical gradient in specific humidity will be reduced, which would promote a decrease in evaporation. For example, the latent heat flux between the sea surface and the atmosphere can be estimated using standard flux-gradient relationships, $LE = \rho L_v C_q U(q_s - q)$, where $C_q$ is a roughness length dependent exchange coefficient, U is wind speed, q is specific humidity and $q_s$ is saturated specific humidity at the sea surface [177]. Except for $q_s$, variables are evaluated above the surface, typically at 10 m. We find that $(q_s - q)$ decreases in the SPNA for all four models under all three AQ experiments,

including the two models (UKESM1-0-LL and EC-Earth3-AerChem) that lack SPNA SST

cooling (not shown). We also find that $(q_s-q)$ changes in a way consistent with the change in

E for MRI-ESM2-0 and EC-Earth3-AerChem under NMNTCF and $CH_4$ mitigation. That

is, the warming minimum under NMNTCF mitigation near Iceland is associated with a

decrease in $q_s - q$ (similar to E); the cooling minimum under $CH_4$ mitigation near Iceland

is associated with an increase in $q_s - q$ (similar to E).

Thus, SPNA increases in $-E$ are a robust feature in all four models under AQ

control experiments, and these changes are related to the SPNA warming hole. We also

note a (weak) decrease in P near Iceland (where the warming hole exists) in UKESM1-0-LL

and EC-Earth3-AerChem, which is likely due to a similar argument, i.e., enhanced warming

aloft, which would promote an increase in atmospheric stability and reduced convection. As

discussed above, both GISS-E2-1-G and MRI-ESM2-0 have a stronger decrease in SPNA P,

consistent with SST cooling.

Similar conclusions generally exist when regressing FF, as well as P and $-E$, onto

SPNA $SSD_S$ (Supplementary Figures 11-14). We note that the regressions show a larger

role for $-E$ under mitigation in UKESM1-0-LL.

## C.1.4 Additional Details on AMOC Mechanisms Under AQ Control Experiments

As mentioned in the main text, similar AMOC mechanisms exist across the AQ

control experiments and NTCF mitigation signals. Due to the larger forcing and AMOC

response in the AQ control experiments, however, larger and more robust mechanism-related

changes occur. Given the large increase in $CO_2$ in common to each of these experiments (i.e., $CO_2$ increases from $\sim$400 ppm in 2015 to more than 850 ppm by 2100), similar results are obtained across the three AQ control experiments.

Twenty-first century SPNA SSD significantly decreases in all models for all three AQ control experiments (Supplementary Table 4). The MMM SPNA SSD decrease is $-0.17$, $-0.20$ and $-0.15$ kg m$^{-3}$ per decade for weak, strong non-$CH_4$ and strong AQ control. Most of this decrease is associated with a decrease in $SSD_S$, as opposed to $SSD_T$. For example, significant SPNA $SSD_S$ decreases occur in all models, with MMM trends that are nearly as large as those based on SSD at $-0.15$, $-0.17$ and $-0.13$ kg m$^{-3}$ per decade for weak, strong non-$CH_4$ and strong AQ control. As a percentage of the overall MMM SSD trend, the MMM $SSD_S$ trends are 87-90% as large (Supplementary Table 6). The two models with the weakest decrease in SPNA SSD$-$MRI-ESM2-0 and in particular, GISS-E2-1-G$-$also feature an increase in SPNA $SSD_T$ (the other two models show a decrease in $SSD_T$). The increase in SPNA $SSD_T$ acts to mute the overall decrease in SSD (which is driven by the decrease in $SSD_S$). We note that GISS-E2-1-G and MRI-ESM2-0 feature the largest AMOC weakening in each of the three AQ control experiments (Supplementary Figures 1-2), which again supports the importance of SPNA $SSD_S$ to the AMOC$-$in this case, a decrease in $SSD_S$ and AMOC weakening.

As SPNA $SSD_T$ is directly related to SPNA SST, this implies GISS-E2-1-G and MRI-ESM2-0 yield SPNA SST cooling (Supplementary Figures 9-10), in contrast to the expected warming under the large increase in $CO_2$ (i.e., a "warming hole"). UKESM1-0-LL and EC-Earth3-AerChem show SPNA SST warming, although this warming is weaker

than the surrounding ocean (Supplementary Figures 7-8). This is consistent with AMOC weakening and less poleward Atlantic ocean heat transport (OHT), which would act to offset or mute SPNA SST warming from the increase in $CO_2$. Poleward Atlantic OHT significantly decreases in all three AQ experiments at latitudes ranging from 0N up to 50N (Supplementary Figure 5). At 50N, for example, the decrease ranges from $-1.8$ to $-3.8$ TW year$^{-1}$ under weak AQ control, with similar changes under strong non-CH$_4$ and strong AQ control. The two models that have the largest AMOC weakening (GISS-E2-1-G and MRI-ESM2-0), as well as the increase in SSD$_T$ due to SPNA cooling, feature the largest decrease in poleward Atlantic OHT. In turn, the SST response impacts the net surface net freshwater flux (FF) through precipitation (P) and in particular, evaporation $(-E)$, which will impact SSD$_S$.

All models yield a 2015-2100 increase in SPNA FF (Supplementary Table 2; Supplementary Figures 7-10). This increase is largely related to an increase in $-E$, which is also a robust response across all models and AQ control experiments. For example, the SPNA MMM increase in $-E$ is 0.89, 0.93 and 0.81 mg m$^{-2}$ s$^{-1}$ per decade for weak, strong non-CH$_4$ and strong AQ control experiments. Larger increases in FF occur in GISS-E2-1-G and MRI-ESM2-0, which is related to larger increases in $-E$. This is despite a decrease in SPNA P in these two models, which acts to decrease FF, muting the overall increase in FF due to $-E$. UKESM1-0-LL and EC-Earth3-AerChem, however, feature increases in SPNA P, which reinforces the increase in FF due to increases in $-E$. All models also yield a decrease in freshwater flux due to sea ice thermodynamics (melt, M), which acts to mute the overall increase in FF. The decrease in M is consistent with AMOC weakening and less

poleward OHT. We also note in the case of some models (e.g., GISS-E2-1-G), differences exist between P−E+M and FF, suggesting another term may be important. Ultimately, the change in SPNA FF is largely controlled by −E. P is also important in EC-Earth3-AerChem and in particular, for UKESM1-0-LL where SPNA P trends exceed −E trends.

The SPNA change in P and −E is largely related to the change in SST (Supplementary Figures 7-10). The relatively large −E increase and P decrease is GISS-E2-1-G and MRI-ESM2-0 is consistent with SPNA SST cooling. Cooler SSTs would act to decrease evaporation (increase −E), and may also act to stabilize the atmosphere, inhibiting convection and atmospheric precipitation. −E increases in UKESM1-0-LL and EC-Earth3-AerChem also appears to be related to the lack of strong SST warming in the SPNA. Although SSTs do not cool here, like GISS-E2-1-G and MRI-ESM2-0, there is still a SPNA warming minimum. As discussed above, the atmosphere just above the surface warms more, due to atmospheric transport of heat from outside the SPNA (which warms substantially more). This reduces the vertical gradient in specific humidity, promoting an increase in −E (i.e., decrease in evaporation).

SPNA surface wind (WS) changes also show robust decreases (Supplementary Table 2), which are consistent with the increase in −E (i.e., a decrease in WS would promote a decrease in E). However, the spatial pattern of the WS decrease resembles the spatial pattern of the trends in SST (and −E; Supplementary Figures 7-10). Furthermore, the SPNA WS decrease is relatively uniform across the models ($-0.04$ to $-0.07$ m s$^{-1}$ per decade), whereas −E is not (using the same 3 models that have WS trends, −E trends range 0.47 to 1.54 mg m$^{-2}$ s$^{-1}$ per decade). Hence, the WS changes are likely related to

SSTs, and are not driving −E. SST cooling will stabilize the boundary layer and decrease mixing, which would promote a decrease in WS. Although UKESM1-0-LL and EC-Earth3-AerChem do not feature SPNA SST cooling, there is a warming minimum, which likely leads to less mixing due to more atmospheric warming aloft (via atmospheric transport of heat from the broader North Atlantic region, which warms substantially more).

To summarize, the AQ control experiments show strong and robust AMOC mechanisms, that are in general similar to those under the NTCF signals. SPNA SSD decreases, which implies a decrease in buoyancy anomalies which impact deep water formation. The decrease in SPNA SSD is largely consistent with a decrease in SSD$_S$, and this in turn is largely related to an increase in −E. Changes in −E appear to be largely related to changes in SPNA SSTs, and in particular, the SPNA SST change relative to the broader region of the North Atlantic. For two models (GISS-E2-1-G and MRI-ESM2-0), this is SPNA SST cooling; for the other two models (EC-Earth3-AerChem and UKESM1-0-LL), this is muted SPNA SST warming. We mention that the similar responses in EC-Earth3-AerChem and UKESM1-0-LL may be related to the fact they have a similar ocean model−NEMO3.6 and NEMO-HadGEM3-GO6.0. Significant AMOC-related feedbacks exist in these four models, largely consistent with AMOC-induced changes in poleward heat transport (weakening), which in turn impacts −E and SSD$_S$, both of which promote additional AMOC weakening. We are unable to diagnose cause and effect, and we do not suggest AMOC changes are driven by this mechanism. Our argument is consistent with [139], who showed AMOC-related salinity feedbacks act to reinforce the initial (largely thermally-forced) AMOC response.

### C.1.5  Additional Details on GISS-E2-1-G Under NMNTCF Mitigation

The GISS-E2-1-G model is an outlier (particularly for all-NTCF and $CH_4$ mitigation) as its AMOC response is larger than than predicted from the the NA cumulative ERF−as well as NA ERF−regressions (Fig. 4). This is also consistent with GISS-E2-1-G's large AMOC response under AQ control experiments (Supplementary Figures 1-2). Thus, GISS-E2-1-G AMOC response is very sensitive to GHGs. Although less obvious, the GISS-E2-1-G AMOC response under NMNTCF mitigation is also relatively large compared to the forcing−the AMOC trend is $-0.013$ Sv year$^{-1}$ (comparable to other models), but GISS-E2-1-G's NMNTCF cumulative NA ERF is quite small at 15.4 W m$^{-2}$ year. Similar results apply based on the NA ERF, which is also quite small at 0.002 W m$^{-2}$ year$^{-1}$ (Fig. 3).

We suspect that a strong AMOC response is a fundamental aspect of this model−due to any type forcing (GHGs or aerosols). For example, as discussed in the main text, this appears to be related to a strong AMOC-CLT feedback (Supplementary Figure 16). We also note that GISS-E2-1-G has a very large area with deep ($>$200 m) climatological MMLD, which spans the entire SPNA (not shown). The reason why GISS-E2-1-G lacks a (more obviously) larger AMOC response under NMNTCF mitigation may be related to a dynamical response in the first half of the 21st century, involving an increase in SPNA surface winds due to reduced sea level pressure (SLP) near Iceland and increased SLP near 30N in the Atlantic. This leads to an increase in SPNA evaporation and an increase in $SSD_S$, which would act to strengthen the AMOC (not shown). This dynamical response, however, is not present in the second half of the century, and here, there is a decrease in SPNA evaporation and $SSD_S$ (which is consistent with SPNA cooling associated with reduced poleward

Atlantic OHT). The other models do not exhibit this behavior. We also note this SLP and surface wind response is similar, but opposite to that under CMIP6 AA experiments from 1990-2020 [139]. Thus, to summarize, it appears GISS-E2-1-G yields a dynamical response under NMNTCF mitigation during the first half of the 21st century that acts to mute AMOC weakening. GISS-E2-1-G exhibits considerable multi-decadal variability in its AMOC times series, particularly under NMNTCF mitigation (Fig. 2); thus, the signal may be related to internal climate variability, as opposed to an externally forced response.

## C.2    Appendix C Tables

Table C.1: **Definition of coupled ocean-atmosphere-chemistry experiments and mitigation signals used in this study.**

| CMIP6 Experiment Name | Description | |
|---|---|---|
| SSP3-7.0 | Weak AQ Control | |
| SSP3-7.0-lowNTCF | Strong non-methane AQ Control | |
| SSP3-7.0-lowNTCFCH4 | Strong AQ control (with methane) | |
| Mitigation Signal | Description | Abbreviation |
| SSP3-7.0-lowNTCF−SSP3-7.0 | Non-methane NTCF Mitigation | NMNTCF Mitigation |
| SSP3-7.0-lowNTCFCH4−SSP3-7.0 | NTCF Mitigation (with methane) | all-NTCF Mitigation |
| SSP3-7.0-lowNTCFCH4−SSP3-7.0-lowNTCF | Methane Mitigation | CH4 Mitigation |

AQ = Air Quality

Table C.2: **2015-2100 model mean subpolar North Atlantic trends.** Trends for precipitation (P), negative of surface evaporation ($-E$), melt (M), surface net freshwater flux (FF), March mixed layer depth (MMLD) and surface wind speed (WS) for the (top table) three NTCF signals and (bottom table) AQ control experiments. Units for P, $-E$, M and FF are mg m$^{-2}$ s$^{-1}$ per decade; units for MMLD are m per decade; and units for WS are m s$^{-1}$ per decade. Model names have been abbreviated as: EC3 = EC-Earth3-AerChem; GISS = GISS-E2-1-G; MRI = MRI-ESM2-0; UKESM1 = UKESM1-0-LL. MMM is the multi-model mean. Bold trends are significant at the 95% confidence level, based on a standard t-test. n/a is not available.

| | Mitigation Signals | | | | | | | | |
| | P | | | $-E$ | | | M | | |
| Model | NMNTCF | all-NTCF | CH4 | NMNTCF | all-NTCF | CH4 | NMNTCF | all-NTCF | CH4 |
|---|---|---|---|---|---|---|---|---|---|
| EC3 | −0.03 | −0.001 | −0.02 | 0.07 | 0.09 | 0.02 | 0.07 | **0.12** | 0.05 |
| GISS | 0.05 | **0.32** | **0.28** | 0.07 | **−0.31** | **−0.38** | −0.01 | −0.01 | −0.01 |
| MRI | 0.003 | −0.001 | −0.004 | 0.07 | −0.02 | **−0.09** | 0.01 | 0.04 | **0.03** |
| UKESM1 | **0.16** | −0.05 | **−0.21** | **−0.09** | −0.05 | 0.04 | n/a | n/a | n/a |
| MMM | **0.05** | **0.06** | 0.009 | 0.03 | **−0.07** | **−0.10** | 0.02 | 0.05 | 0.02 |
| | FF | | | MMLD | | | WS | | |
| Model | NMNTCF | all-NTCF | CH4 | NMNTCF | all-NTCF | CH4 | NMNTCF | all-NTCF | CH4 |
| EC3 | 0.02 | **0.18** | 0.16 | **−3.1** | 1.1 | **4.2** | −0.010 | 0.013 | **0.023** |
| GISS | 0.07 | **−0.31** | **−0.38** | −4.8 | **16.8** | **21.6** | 0.002 | **0.015** | **0.013** |
| MRI | 0.07 | 0.01 | −0.05 | −2.1 | **3.0** | **5.1** | −0.005 | 0.007 | 0.013 |
| UKESM1 | 0.07 | **−0.12** | **−0.19** | **2.0** | **3.3** | **1.2** | n/a | **0.012** | n/a |
| MMM | **0.05** | **−0.07** | **−0.12** | **−1.96** | **5.9** | **7.9** | −0.004 | **0.012** | **0.016** |

| | Air Quality Control Experiments | | | | | | | | |
| | P | | | $-E$ | | | M | | |
| Model | Weak | Strong non-CH4 | Strong | Weak | Strong non-CH4 | Strong | Weak | Strong non-CH4 | Strong |
|---|---|---|---|---|---|---|---|---|---|
| EC3 | **0.14** | **0.16** | 0.11 | **0.47** | **0.54** | **0.58** | **−0.59** | **−0.52** | **−0.47** |
| GISS | **−0.67** | **−0.62** | **−0.32** | **1.48** | **1.54** | **1.10** | **−0.12** | **−0.13** | **−0.13** |
| MRI | **−0.34** | **−0.34** | **−0.35** | **1.32** | **1.40** | **1.31** | **−0.22** | **−0.21** | **−0.18** |
| UKESM1 | **0.36** | **0.52** | **0.29** | **0.31** | **0.22** | **0.26** | n/a | n/a | n/a |
| MMM | **−0.13** | **−0.07** | **−0.07** | **0.89** | **0.93** | **0.81** | **−0.31** | **−0.29** | **−0.26** |
| | FF | | | MMLD | | | WS | | |
| Model | Weak | Strong non-CH4 | Strong | Weak | Strong non-CH4 | Strong | Weak | Strong non-CH4 | Strong |
| EC3 | 0.10 | **0.25** | **0.30** | **−5.83** | **−7.0** | **−5.8** | **−0.07** | **−0.07** | **−0.05** |
| GISS | **1.33** | **1.39** | **0.95** | **−26.8** | **−26.5** | **−22.2** | **−0.06** | **−0.06** | **−0.04** |
| MRI | **0.73** | **0.82** | **0.74** | **−14.4** | **−15.0** | **−13.4** | **−0.06** | **−0.07** | **−0.06** |
| UKESM1 | **0.23** | **0.29** | **0.12** | **−5.2** | **−4.6** | **−4.3** | n/a | n/a | n/a |
| MMM | **0.60** | **0.69** | **0.53** | **−13.1** | **−13.3** | **−11.4** | **−0.06** | **−0.07** | **−0.05** |

Table C.3: **2015-2055 model mean subpolar North Atlantic trends.** Trends for precipitation (P), negative of surface evaporation (−E), melt (M), surface net freshwater flux (FF), March mixed layer depth (MMLD) and surface wind speed (WS) for the three NTCF signals. Units for P, −E, M and FF are mg m$^{-2}$ s$^{-1}$ per decade; units for MMLD are m per decade; and units for WS are m s$^{-1}$ per decade. Model names have been abbreviated as: EC3 = EC-Earth3-AerChem; GISS = GISS-E2-1-G; MRI = MRI-ESM2-0; UKESM1 = UKESM1-0-LL. MMM is the multi-model mean. Bold trends are significant at the 95% confidence level, based on a standard t-test. n/a is not available.

| | Mitigation Signals | | | | | | | | |
| | P | | | −E | | | M | | |
| Model | NMNTCF | all-NTCF | CH4 | NMNTCF | all-NTCF | CH4 | NMNTCF | all-NTCF | CH4 |
|---|---|---|---|---|---|---|---|---|---|
| EC3 | 0.11 | 0.25 | 0.15 | 0.09 | −0.07 | −0.16 | −0.023 | 0.003 | 0.026 |
| GISS | **0.44** | **0.24** | −0.19 | **−0.27** | −0.19 | 0.09 | −0.005 | **0.006** | **0.012** |
| MRI | −0.03 | 0.13 | 0.16 | 0.11 | −0.10 | −0.21 | 0.007 | **0.012** | 0.005 |
| UKESM1 | 0.17 | **0.26** | 0.09 | 0.08 | −0.11 | −0.19 | n/a | n/a | n/a |
| MMM | **0.17** | **0.22** | 0.05 | 0.001 | **−0.12** | −0.12 | −0.007 | 0.007 | 0.014 |
| | FF | | | MMLD | | | WS | | |
| Model | NMNTCF | all-NTCF | CH4 | NMNTCF | all-NTCF | CH4 | NMNTCF | all-NTCF | CH4 |
| EC3 | 0.03 | 0.32 | 0.29 | −5.7 | −2.4 | 3.4 | −0.014 | 0.022 | 0.036 |
| GISS | −0.30 | −0.17 | 0.13 | 8.8 | −1.5 | −10.3 | **0.046** | 0.026 | −0.020 |
| MRI | 0.10 | 0.13 | 0.02 | **−10.0** | 7.7 | **17.7** | 0.000 | 0.036 | 0.036 |
| UKESM1 | 0.28 | 0.13 | −0.15 | 2.9 | **7.4** | **4.5** | n/a | 0.015 | n/a |
| MMM | 0.03 | 0.11 | 0.08 | −1.0 | 2.8 | 3.8 | 0.011 | **0.025** | 0.017 |

Table C.4: **2015-2100 model mean subpolar North Atlantic sea surface density (SSD) trends.** Top half of table shows results for the three NTCF signals; bottom half of table shows results for the three air quality (AQ) control experiments. Units for SSD, $SSD_S$ and $SSD_T$ are kg m$^{-3}$ per decade. Model names have been abbreviated as: EC3 = EC-Earth3-AerChem; GISS = GISS-E2-1-G; MRI = MRI-ESM2-0; UKESM1 = UKESM1-0-LL. MMM is the multi-model mean. Bold trends are significant at the 95% confidence level, based on a standard t-test.

| | Mitigation Signals | | | | | | | | |
| | SSD | | | $SSD_S$ | | | $SSD_T$ | | |
| Model | NMNTCF | all-NTCF | CH4 | NMNTCF | all-NTCF | CH4 | NMNTCF | all-NTCF | CH4 |
|---|---|---|---|---|---|---|---|---|---|
| EC3 | **−0.064** | 0.014 | **0.078** | **−0.048** | −0.007 | **0.042** | **−0.015** | **0.020** | **0.036** |
| GISS | −0.013 | **0.026** | **0.040** | −0.016 | **0.042** | **0.058** | 0.003 | −0.015 | −0.019 |
| MRI | **−0.030** | 0.008 | **0.037** | **−0.026** | 0.002 | **0.028** | −0.004 | 0.005 | **0.009** |
| UKESM1 | −0.015 | **0.031** | **0.046** | −0.007 | **0.015** | **0.022** | −0.008 | **0.015** | **0.024** |
| MMM | **−0.030** | **0.019** | **0.050** | **−0.024** | **0.013** | **0.037** | −0.006 | **0.006** | **0.012** |

| | Air Quality Control Experiments | | | | | | | | |
| | SSD | | | $SSD_S$ | | | $SSD_T$ | | |
| Model | Weak | Strong non-CH4 | Strong | Weak | Strong non-CH4 | Strong | Weak | Strong non-CH4 | Strong |
|---|---|---|---|---|---|---|---|---|---|
| EC3 | **−0.20** | **−0.26** | **−0.18** | **−0.13** | **−0.17** | **−0.13** | **−0.07** | **−0.08** | **−0.05** |
| GISS | **−0.08** | **−0.09** | **−0.05** | **−0.12** | **−0.14** | **−0.08** | **0.04** | **0.05** | **0.03** |
| MRI | **−0.17** | **−0.20** | **−0.16** | **−0.19** | **−0.21** | **−0.19** | **0.02** | **0.01** | **0.02** |
| UKESM1 | **−0.22** | **−0.23** | **−0.20** | **−0.15** | **−0.15** | **−0.14** | **−0.07** | **−0.08** | **−0.06** |
| MMM | **−0.17** | **−0.20** | **−0.15** | **−0.15** | **−0.17** | **−0.13** | **−0.02** | **−0.03** | **−0.02** |

Table C.5: **2015-2055 model mean subpolar North Atlantic sea surface density (SSD) trends.** Results for the three NTCF signals. Units for SSD, $SSD_S$ and $SSD_T$ are kg m$^{-3}$ per decade. Model names have been abbreviated as: EC3 = EC-Earth3-AerChem; GISS = GISS-E2-1-G; MRI = MRI-ESM2-0; UKESM1 = UKESM1-0-LL. MMM is the multi-model mean. Bold trends are significant at the 95% confidence level, based on a standard t-test.

| | Mitigation Signals | | | | | | | | |
| | SSD | | | $SSD_S$ | | | $SSD_T$ | | |
| Model | NMNTCF | all-NTCF | CH4 | NMNTCF | all-NTCF | CH4 | NMNTCF | all-NTCF | CH4 |
|---|---|---|---|---|---|---|---|---|---|
| EC3 | **−0.044** | −0.016 | **0.028** | −0.018 | −0.013 | 0.005 | **−0.028** | −0.003 | **0.025** |
| GISS | 0.002 | 0.002 | 0.0003 | **0.009** | 0.003 | **−0.007** | **−0.008** | −0.0006 | 0.007 |
| MRI | **−0.023** | 0.013 | **0.036** | **−0.026** | −0.001 | **0.025** | 0.003 | **0.013** | **0.011** |
| UKESM1 | −0.016 | **0.040** | **0.056** | −0.019 | **0.033** | **0.053** | 0.003 | 0.007 | 0.004 |
| MMM | **−0.020** | 0.009 | **0.030** | **−0.013** | 0.005 | **0.019** | **−0.008** | 0.004 | **0.011** |

Table C.6: **Percentage of the subpolar North Atlantic sea surface density (SSD) trend due to SSD$_S$.** Top half of table shows results for the three NTCF signals; bottom half of table shows results for the three air quality (AQ) control experiments. Model names have been abbreviated as: EC3 = EC-Earth3-AerChem; GISS = GISS-E2-1-G; MRI = MRI-ESM2-0; UKESM1 = UKESM1-0-LL. MMM is the multi-model mean. Unit is percent.

| | Mitigation Signals | | |
| | SSD$_S$/SSD Trend | | |
| Model | NMNTCF | all-NTCF | CH4 |
|---|---|---|---|
| EC3 | 75 | $-50$ | 53 |
| GISS | 114 | 158 | 146 |
| MRI | 90 | 38 | 74 |
| UKESM1 | 47 | 48 | 48 |
| MMM | 83 | 70 | 76 |

| | Air Quality Control Experiments | | |
| | SSD$_S$/SSD Trend | | |
| Model | Weak | Strong non-CH4 | Strong |
|---|---|---|---|
| EC3 | 65 | 68 | 74 |
| GISS | 153 | 148 | 145 |
| MRI | 111 | 107 | 114 |
| UKESM1 | 67 | 65 | 70 |
| MMM | 88 | 87 | 90 |

## C.3   Appendix C Figures
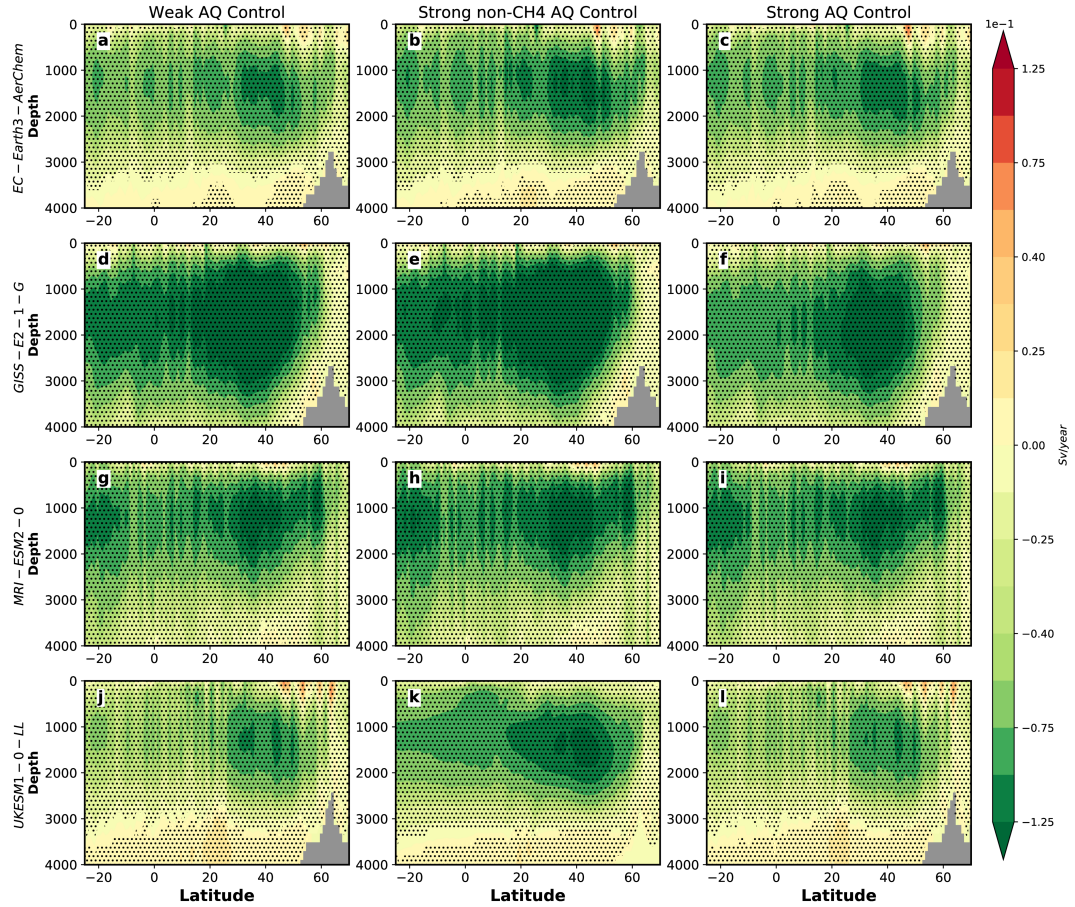


Figure C.1: **2015-2100 annual mean depth-latitude trends in the Atlantic meridional stream function for the three air quality experiments.** (a, d, g, j) Weak; (b, e, h, k) strong non-CH$_4$; and (c, f, i, l) strong air quality (AQ) control for (a-c) EC-Earth3-AerChem; (d-f) GISS-E2-1-G; (g-i) MRI-ESM2-0; and (j-l) UKESM1-0-LL. Trend units are $10^{-1}$ Sverdrups yr$^{-1}$, where Sverdrups (Sv) $= 10^6$ m$^3$ s$^{-1}$. Symbols designate trend significance at 95% confidence level based on a standard $t$-test. Strengthening of the circulation is represented by red shading; weakening is represented by green shading.
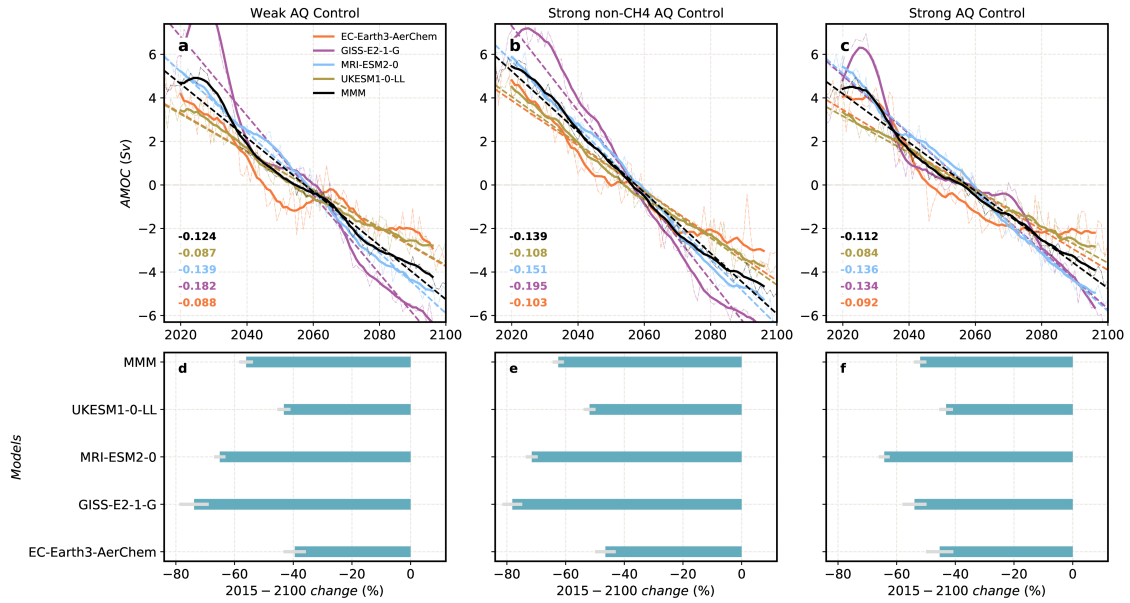
Figure C.2: **2015-2100 changes in the annual mean Atlantic Meridional Overturning Circulation (AMOC) for the three air quality experiments.** (a-c) Normalized (relative to the long-term 2015-2100 climatology) AMOC time series and trends; (d-f) AMOC percent change (relative to 2015) for each model, including the multi-model mean (MMM) for (a, d) weak; (b, e) strong non-$CH_4$; and (c, f) strong air quality (AQ) control. In (a-c), thick lines show the smoothed AMOC time series using a 10-year running mean. Also included in (a-c) is the slope of the least-squares trend line (units of Sv year$^{-1}$), color coded by model as defined in the legend. AMOC trends significant at the 95% confidence level are bold (all are significant here). In (d-f), AMOC weakening (strengthening) is shown with blue (red) bars. The gray thin lines over the percent change bars represent the 95% confidence level.
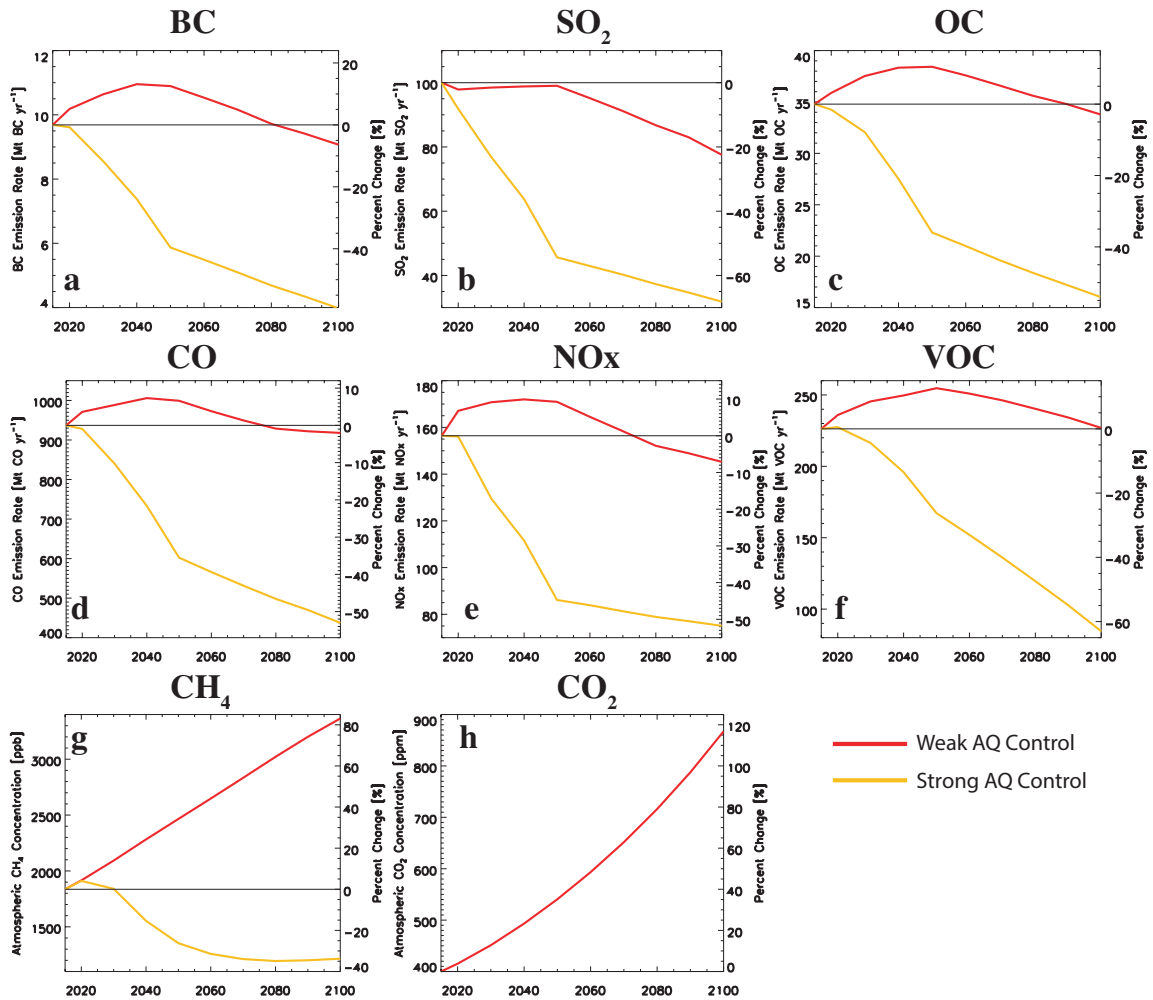
Figure C.3: **2015-2100 global annual mean $CO_2$ and $CH_4$ atmospheric concentrations and precursor gas emissions.** Panels show (a) black carbon (BC); (b) sulfur dioxide ($SO_2$); (c) organic carbon (OC); (d) carbon monoxide (CO); (e) nitrogen oxides ($NO_x$); and (f) volatile organic compounds (VOC) emissions, as well as atmospheric concentrations of (g) methane ($CH_4$); and (h) carbon dioxide ($CO_2$) for weak (red) and strong (gold) air quality control. Also included is the corresponding percent change (relative to 2015). Emission units for species X are Mt X $yr^{-1}$, where Mt is a megatonne, or $10^9$ kg. $CO_2$ and $CH_4$ units are parts per million by volume (ppm) and parts per billion by volume (ppb), respectively. Percent change units are %. Only weak air quality control $CO_2$ emissions are shown, as AerChemMIP simulations include the same change in $CO_2$ concentrations based on the weak air quality control scenario. Emissions data includes anthropogenic and biomass burning sectors, and comes directly from the CMIP6 forcing datasets which were downloaded from the input datasets for Model Intercomparison Project (input4MIPS).
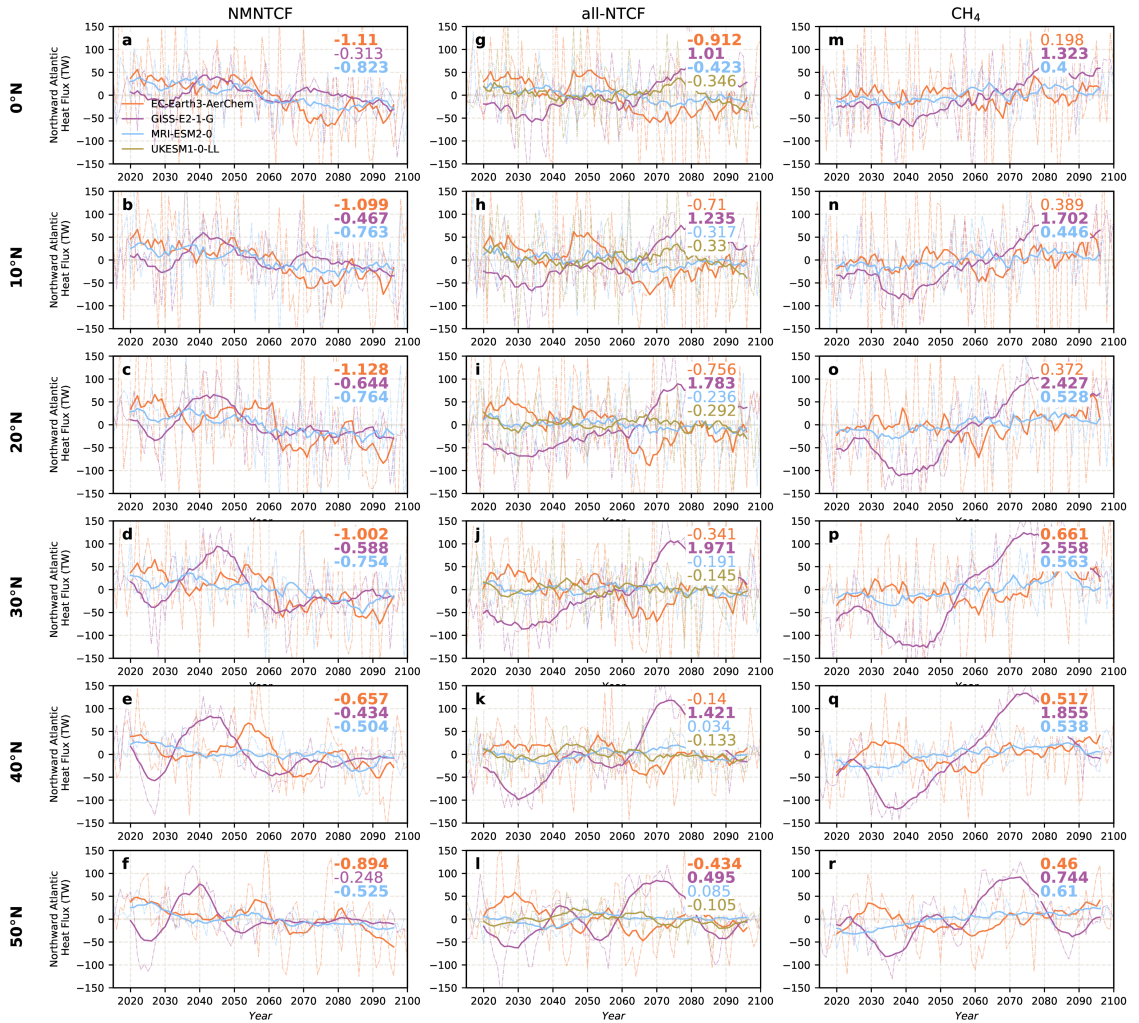
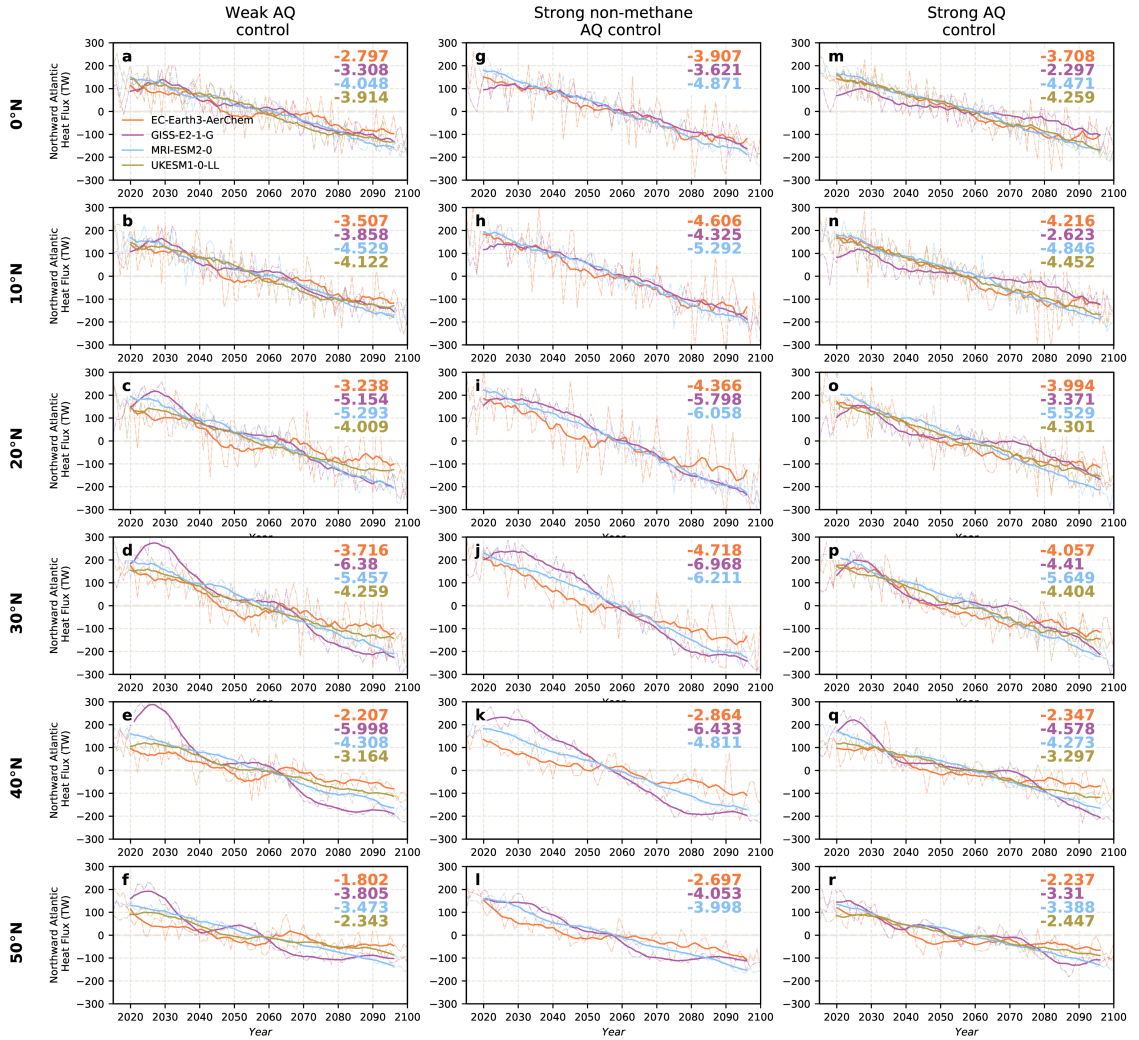Figure C.4: **2015-2100 annual mean poleward Atlantic ocean heat transport (OHT) for the three mitigation signals.** (left panels) NMNTCF; (middle panels) all-NTCF; and (right panels) $CH_4$ mitigation at (from top to bottom) 0N; 10N; 20N; 30N; 40N; and 50N. Models are color coded according to the legend (UKESM1-0-LL is not available for NMNTCF and $CH_4$ mitigation). Thick lines show the smoothed OHT time series using a 10-year running mean. Also included is the slope of the least-squares trend line, color coded by model as defined in the legend. OHT trends significant at the 95% confidence level are bold. Units are TW (i.e., $10^{12}$ W); trend units are TW $yr^{-1}$.

Figure C.5: **2015-2100 annual mean poleward Atlantic ocean heat transport (OHT) for the three air quality experiments.** (left panels) Weak; (middle panels) strong non-CH$_4$; and (right panels) strong air quality control experiment at (from top to bottom) 0N; 10N; 20N; 30N; 40N; and 50N. Models are color coded according to the legend (UKESM1-0-LL is not available for strong non-CH$_4$ AQ control). Thick lines show the smoothed OHT time series using a 10-year running mean. Also included is the slope of the least-squares trend line, color coded by model as defined in the legend. OHT trends significant at the 95% confidence level are bold. Units are TW (i.e., $10^{12}$ W); trend units are TW yr$^{-1}$.
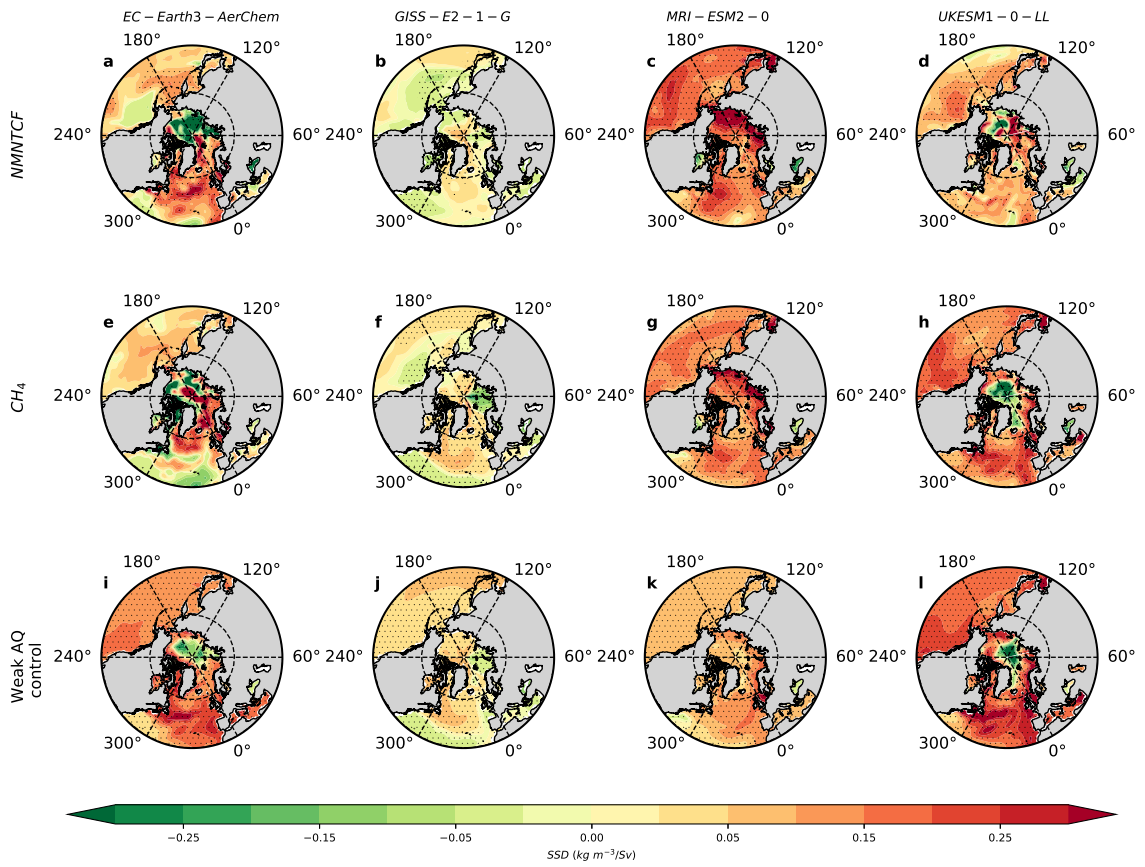
Figure C.6: **2015-2100 annual mean sea surface density (SSD) regression analysis.**
Spatial maps of the AMOC time series regressed onto SSD under (a-d) NMNTCF mitigation;
(e-h) CH$_4$ mitigation; and (i-l) the weak air quality (AQ) control experiment for (a, e, i)
EC-Earth3-AerChem; (b, f, j) GISS-E2-1-G; (c, g, k) MRI-ESM2-0; and (d, h, l) UKESM1-
0-LL. Units of kg m$^{-3}$ per Sv. Symbols denote significant at the 95% confidence level.
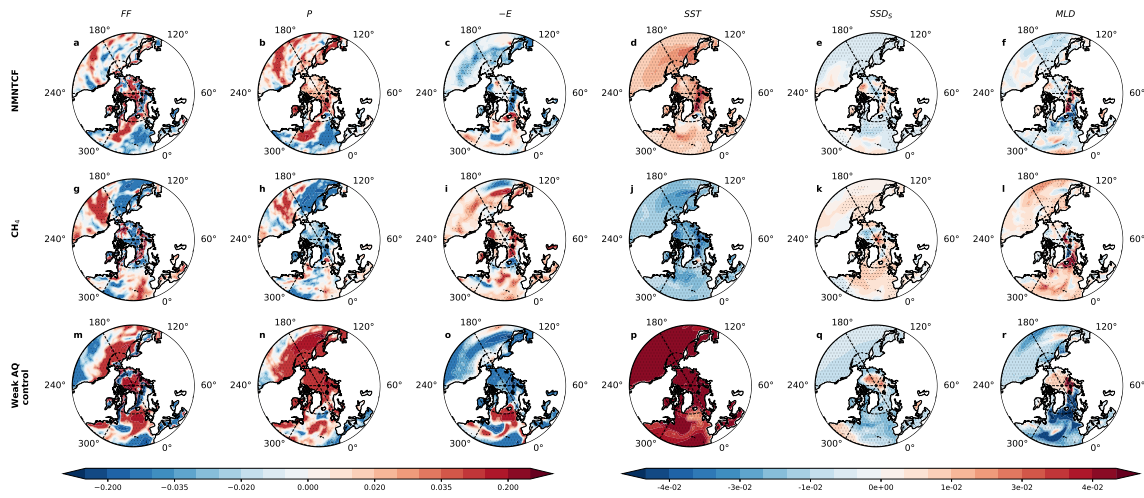
Figure C.7: **2015-2100 EC-Earth3-AerChem annual mean trend maps.** Trend of (a, g, m) surface net freshwater flux (FF; kg m$^{-2}$ s$^{-1}$ per year); (b, h, n) precipitation (kg m$^{-2}$ s$^{-1}$ per year); (c, i, o) negative of evaporation ($-$E; kg m$^{-2}$ s$^{-1}$ per year); (d, j, p) sea surface temperature (SST; °C per year); (e, k, q) SSD$_S$ (kg m$^{-3}$ per year); and (f, l, r) March mixed-layer depth (MMLD; dam per year) for (top row) NMNTCF mitigation; (middle row) CH$_4$ mitigation, and (bottom row) weak AQ control. Symbols denote trend significance at the 95% confidence level based on a standard $t$-test.
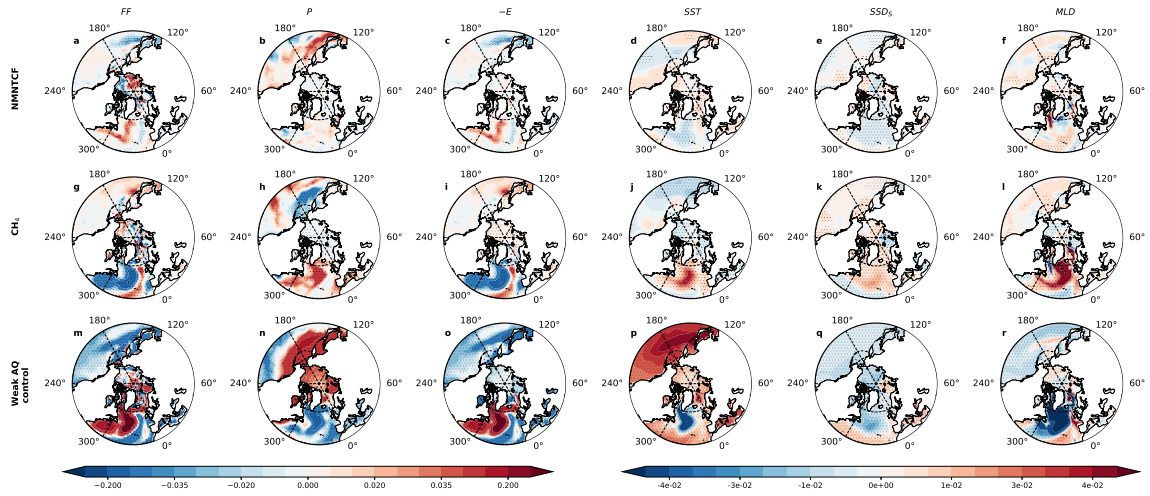
Figure C.8: **2015-2100 UKESM1-0-LL annual mean trend maps.** Trend of (a, g, m) surface net freshwater flux (FF; kg m$^{-2}$ s$^{-1}$ per year); (b, h, n) precipitation (kg m$^{-2}$ s$^{-1}$ per year); (c, i, o) negative of evaporation ($-$E; kg m$^{-2}$ s$^{-1}$ per year); (d, j, p) sea surface temperature (SST; $^{\circ}$C per year); (e, k, q) SSD$_S$ (kg m$^{-3}$ per year); and (f, l, r) March mixed-layer depth (MMLD; dam per year) for (top row) NMNTCF mitigation; (middle row) CH$_4$ mitigation, and (bottom row) weak AQ control. Symbols denote trend significance at the 95% confidence level based on a standard $t$-test.
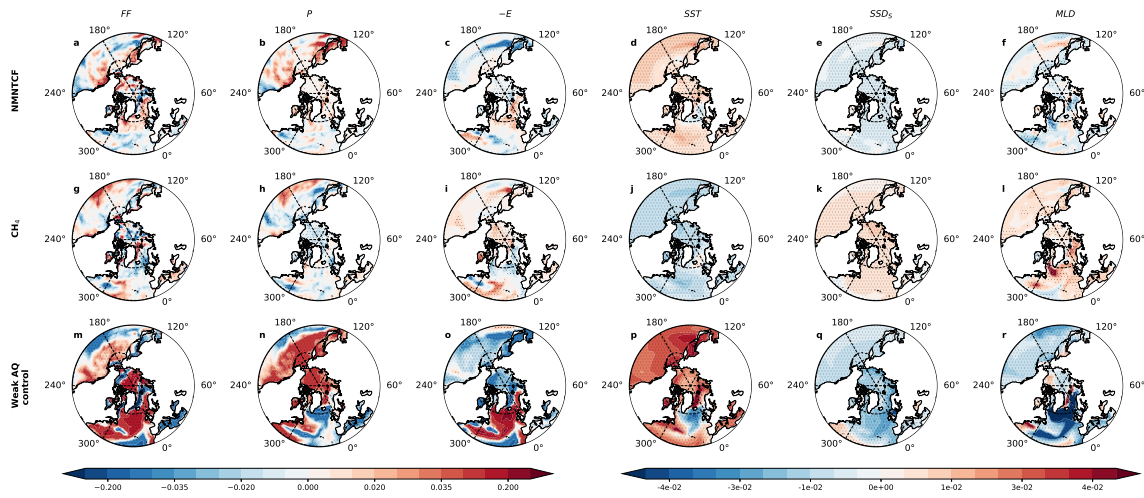
Figure C.9: **2015-2100 GISS-E2-1-G annual mean trend maps.** Trend of (a, g, m) surface net freshwater flux (FF; kg m$^{-2}$ s$^{-1}$ per year); (b, h, n) precipitation (kg m$^{-2}$ s$^{-1}$ per year); (c, i, o) negative of evaporation ($-E$; kg m$^{-2}$ s$^{-1}$ per year); (d, j, p) sea surface temperature (SST; $^{\circ}$C per year); (e, k, q) SSD$_S$ (kg m$^{-3}$ per year); and (f, l, r) March mixed-layer depth (MMLD; dam per year) for (top row) NMNTCF mitigation; (middle row) CH$_4$ mitigation, and (bottom row) weak AQ control. Symbols denote trend significance at the 95% confidence level based on a standard $t$-test.
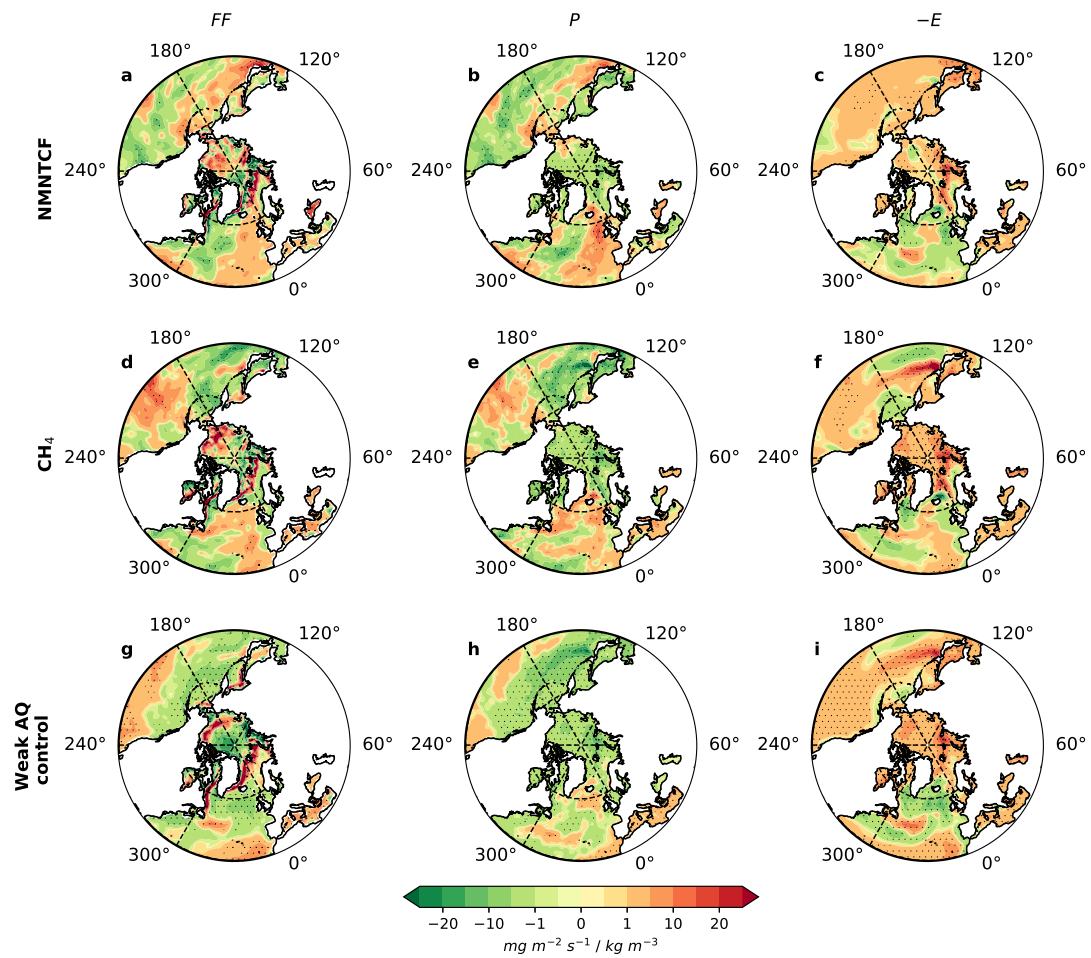
Figure C.10: **2015-2100 MRI-ESM2-0 annual mean trend maps.** Trend of (a, g, m) surface net freshwater flux (FF; kg m$^{-2}$ s$^{-1}$ per year); (b, h, n) precipitation (kg m$^{-2}$ s$^{-1}$ per year); (c, i, o) negative of evaporation (−E; kg m$^{-2}$ s$^{-1}$ per year); (d, j, p) sea surface temperature (SST; °C per year); (e, k, q) SSD$_S$ (kg m$^{-3}$ per year); and (f, l, r) March mixed-layer depth (MMLD; dam per year) for (top row) NMNTCF mitigation; (middle row) CH$_4$ mitigation, and (bottom row) weak AQ control. Symbols denote trend significance at the 95% confidence level based on a standard $t$-test.

Figure C.11: **2015-2100 EC-Earth3-AerChem annual mean hydrological regressions onto SPNA SSD$_S$.** (a, d, g) Surface net freshwater flux; (b, e, h) precipitation; and (c, f, i) negative of evaporation ($-E$) regressed onto SPNA SSD$_S$ for (a-c) NMNTCF mitigation; (d-f) CH$_4$ mitigation; and (g-i) weak AQ control. Symbols denote significance at the 95% confidence level, based on a standard $t$-test. Units are mg m$^{-2}$ s$^{-1}$ per kg m$^{-3}$.
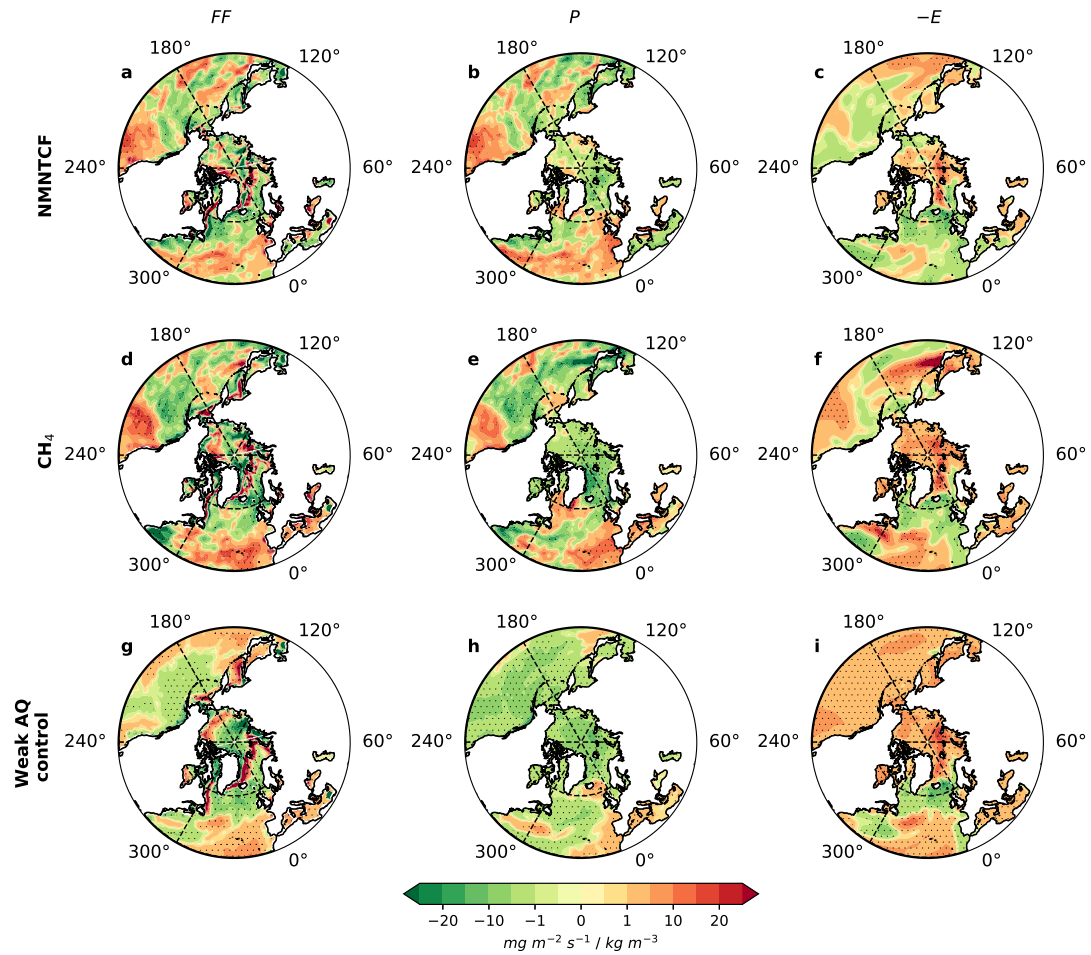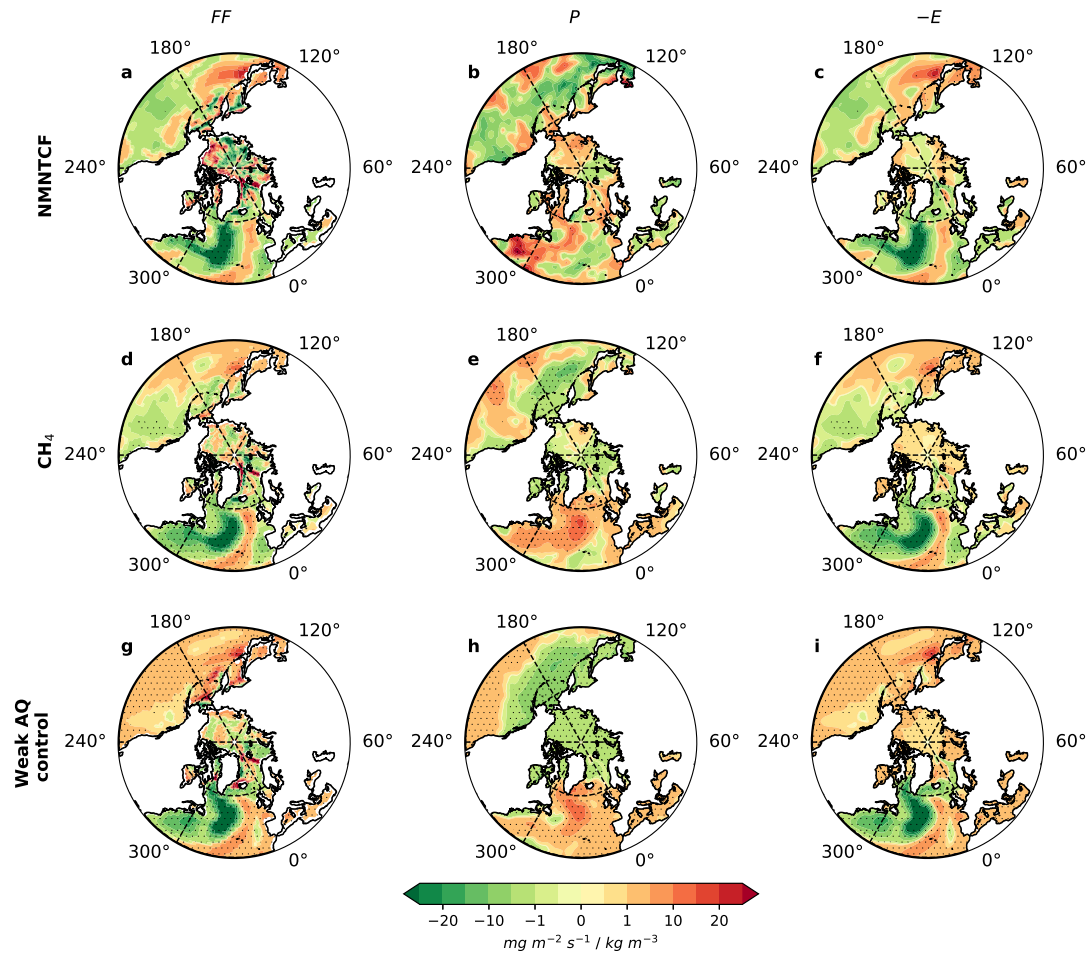
Figure C.12: **2015-2100 UKESM1-0-LL annual mean hydrological regressions onto SPNA SSD$_S$.** (a, d, g) Surface net freshwater flux; (b, e, h) precipitation; and (c, f, i) negative of evaporation ($-$E) regressed onto SPNA SSD$_S$ for (a-c) NMNTCF mitigation; (d-f) CH$_4$ mitigation; and (g-i) weak AQ control. Symbols denote significance at the 95% confidence level, based on a standard $t$-test. Units are mg m$^{-2}$ s$^{-1}$ per kg m$^{-3}$.

Figure C.13: **2015-2100 GISS-E2-1-G annual mean hydrological regressions onto SPNA SSD$_S$.** (a, d, g) Surface net freshwater flux; (b, e, h) precipitation; and (c, f, i) negative of evaporation ($-$E) regressed onto SPNA SSD$_S$ for (a-c) NMNTCF mitigation; (d-f) CH$_4$ mitigation; and (g-i) weak AQ control. Symbols denote significance at the 95% confidence level, based on a standard $t$-test. Units are mg m$^{-2}$ s$^{-1}$ per kg m$^{-3}$.
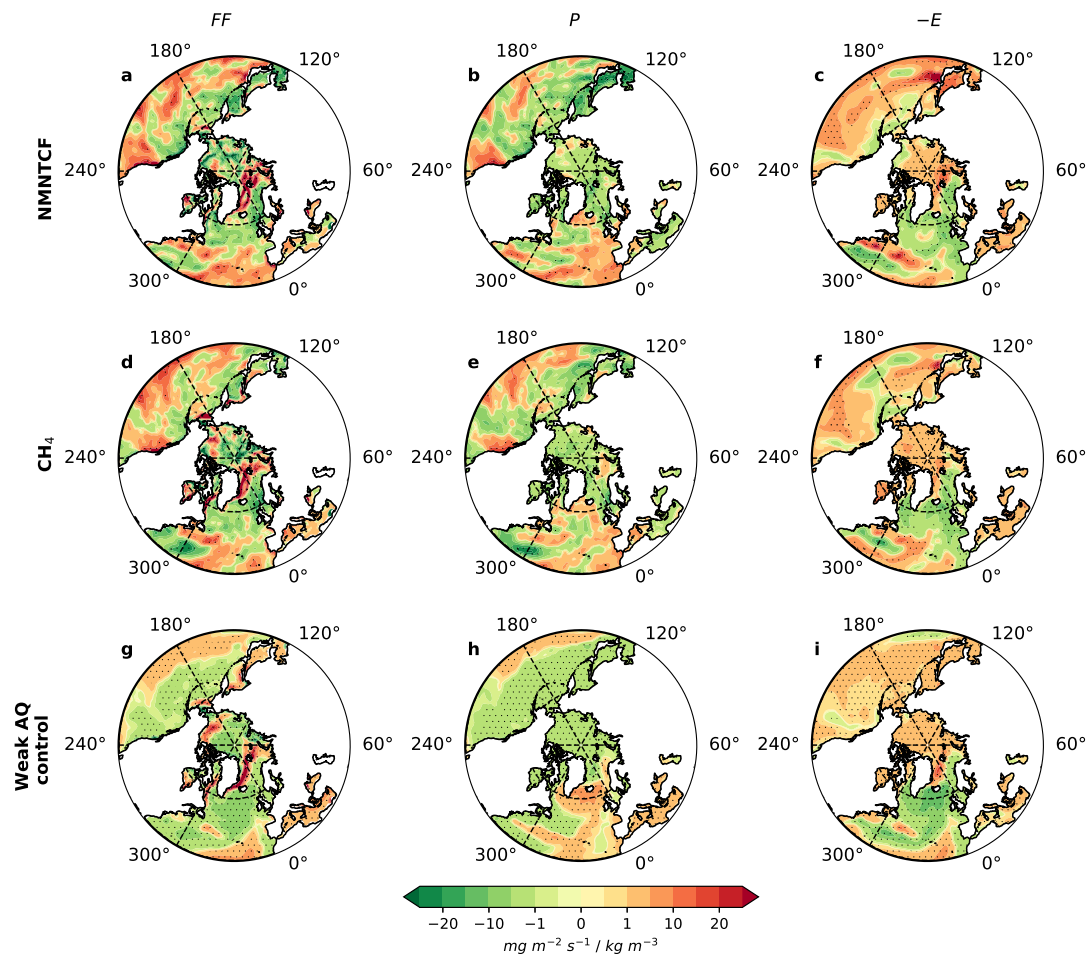
Figure C.14: **2015-2100 MRI-ESM2-0 annual mean hydrological regressions onto SPNA SSD$_S$.** (a, d, g) Surface net freshwater flux; (b, e, h) precipitation; and (c, f, i) negative of evaporation ($-$E) regressed onto SPNA SSD$_S$ for (a-c) NMNTCF mitigation; (d-f) CH$_4$ mitigation; and (g-i) weak AQ control. Symbols denote significance at the 95% confidence level, based on a standard $t$-test. Units are mg m$^{-2}$ s$^{-1}$ per kg m$^{-3}$.
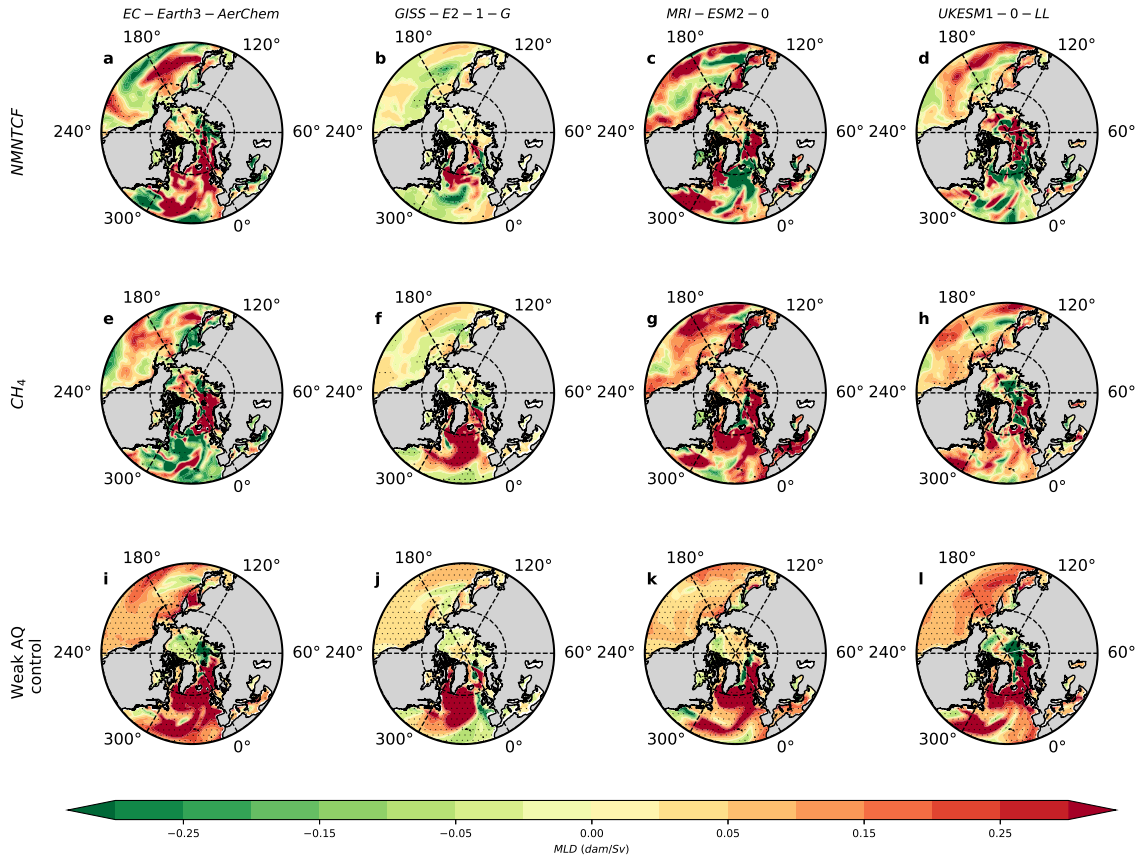
Figure C.15: **2015-2100 annual mean March mixed layer depth regression analysis.** Spatial maps of the AMOC time series regressed onto March mixed layer depth (MMLD) under (a-d) NMNTCF mitigation; (e-h) $CH_4$ mitigation; and (i-l) the weak air quality (AQ) control experiment for (a, e, i) EC-Earth3-AerChem; (b, f, j) GISS-E2-1-G; (c, g, k) MRI-ESM2-0; and (d, h, l) UKESM1-0-LL. Units are dam (i.e., $10^1$ m) per Sv. Symbols denote significant at the 95% confidence level.
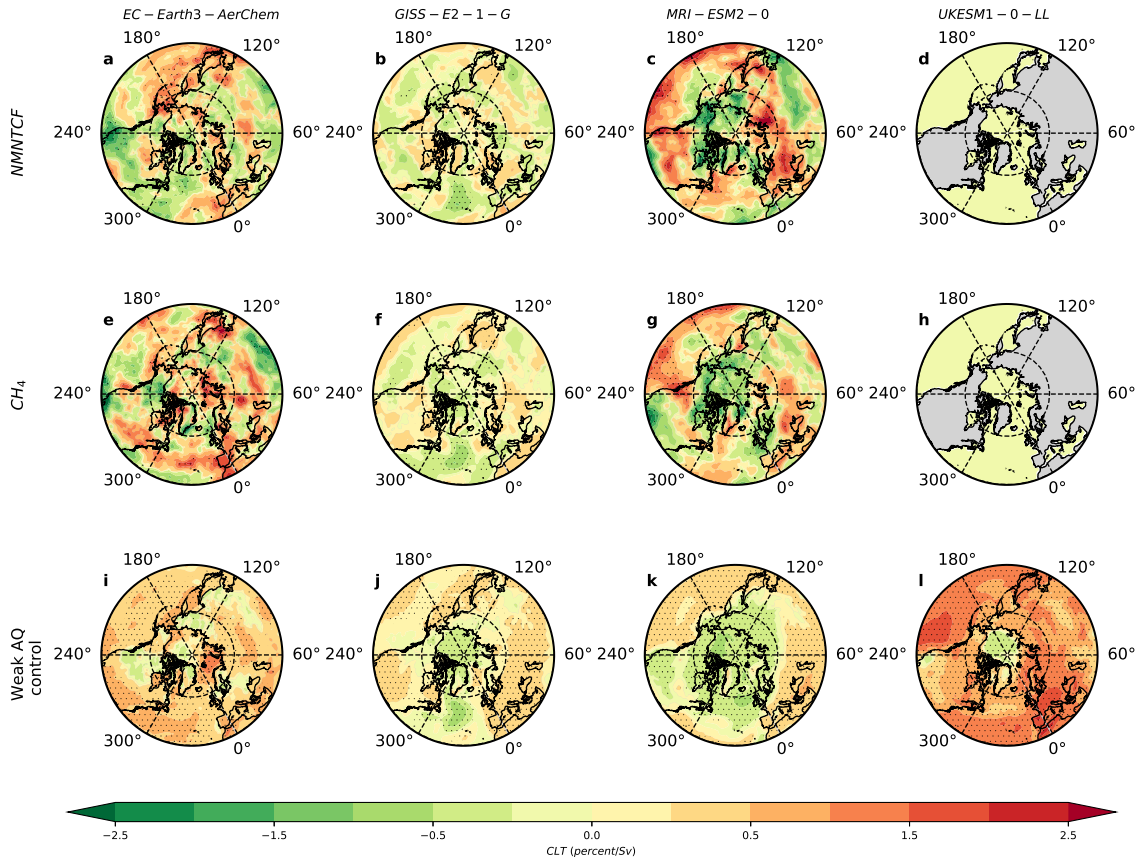
Figure C.16: **2015-2100 annual mean total cloud cover regression analysis.** Spatial maps of the AMOC time series regressed onto total cloud cover (CLT) under (a-d) NMNTCF mitigation; (e-h) $CH_4$ mitigation; and (i-l) the weak air quality (AQ) control experiment for (a, e, i) EC-Earth3-AerChem; (b, f, j) GISS-E2-1-G; (c, g, k) MRI-ESM2-0; and (d, h, l) UKESM1-0-LL. Units of % per Sv. Symbols denote significant at the 95% confidence level. UKESM1-0-LL is not available for NMNTCF and $CH_4$ mitigation.